

**EXPLORING THE PHOTOEXCITED CHARGE CARRIER
DYNAMICS OF PEROVSKITE NANOSTRUCTURES
THROUGH ULTRAFAST TRANSIENT ABSORPTION AND
TERAHERTZ SPECTROSCOPY**

AYUSHI SHUKLA

*A thesis submitted for the partial fulfillment of
the degree of Doctor of Philosophy*



Institute of Nano Science and Technology
Knowledge city, Sector-81, SAS Nagar, Manauli PO, Mohali
140306, Punjab, India.

Indian Institute of Science Education and Research, Mohali
Knowledge city, Sector 81, SAS Nagar, Manauli PO, Mohali
140306, Punjab, India.

February, 2024

Dedication

*To my family, my pillar of
strength...*

Declaration

The work presented in this thesis has been carried out by me under the guidance of Prof. Hirendra N. Ghosh and Dr. Ramendra S. Dey at the Institute of Nano Science and Technology, Mohali. This work has not been submitted in part or in full for a degree, a diploma, or a fellowship to any other university or institute. Whenever contributions of others are involved, every effort is made to indicate this clearly, with due acknowledgment of collaborative research and discussions. This thesis is a bona fide record of original work done by me, and all sources listed within have been detailed in the bibliography.

Ayushi Shukla

In my capacity as the supervisor of the candidate's thesis work, I certify that the above statements by the candidate are true to the best of my knowledge.

Prof. Hirendra N. Ghosh
(Co-Supervisor)

Dr. Ramendra S. Dey
(Supervisor)

Acknowledgment

As I embark on this remarkable academic journey, I'm deeply grateful for the incredible support and guidance I've received throughout my academic journey. This thesis represents the culmination of years of hard work and wouldn't have been possible without the invaluable contributions of some wonderful people in my life. I want to express my heartfelt thanks to all those who have played a part in this scholarly endeavor. Firstly, I offer my deepest gratitude to the **Almighty** for his unwavering presence and boundless blessings that have consistently provided me with the strength I needed throughout my journey.

At the outset of my journey, I would like to express my deepest gratitude to my Ph.D. supervisors **Prof. Hirendra N. Ghosh** and **Dr. Ramendra S. Dey** for their continuous support in my academic journey.

I want to thank **Prof. Hirendra N. Ghosh**, for his unconditional support, guidance, and mentorship throughout my doctoral journey. Without his invaluable assistance, this achievement would not have been possible. He has been an indispensable pillar of support and guidance throughout my academic journey. His expertise, dedication, and mentorship have not only shaped the direction of my research but have also empowered me with invaluable skills and insights. From the moment I started my Ph.D. journey, he has consistently been available and supportive. His untiring commitment ensured that our lab had all the necessary resources for our research endeavors. Whenever I encountered challenges, I could always turn to him, and he has never failed to provide the assistance I require. Among his numerous outstanding qualities, one that truly stands out is his approachable nature. He is consistently available and approachable, never hesitating to provide guidance or support whenever I need it. One remarkable aspect of Prof. H. N. Ghosh's mentorship is his willingness to empower students with the freedom to select their study areas in alignment with their interests. He granted me the freedom to select my research area and played a pivotal role in nurturing the researcher within me. His profound knowledge, scientific passion, and daily discussions, along with our collaborative paper writing, were instrumental in facilitating high-quality research. Indeed, his journey serves as a profound source of motivation and a valuable learning experience. Even in the most challenging times, he remains resolute in his determination and commitment towards his goals; it is an inspiring quality I aim to emulate. Even after his move to BARC, he remained

readily available whenever I needed his guidance and support. Furthermore, even when he assumed the role of Director at NISER, he continued to offer his guidance and remained consistently available and dedicated to our growth and development. Reflecting on my journey, I can clearly discern a greater sense of confidence and maturity in my own development, and this transformation undoubtedly underscores the impact of his mentorship. "Thank you, Sir, for everything. I am truly grateful to you for your role in transforming the student in me into a nurturing researcher."

I will take this opportunity to thank my research supervisor **Dr. Ramendra S. Dey**, I am deeply grateful for his continuous support and guidance during my Ph.D. tenure, which were instrumental in my successful completion of the program especially after Prof. Ghosh's rejoined BARC. He consistently offered a compassionate helping hand and assisted me in addressing every challenge with great efficiency and timeliness, offering suitable solutions. He shows passion and selflessness as a scientist, always ready to help. His constructive suggestions for my research significantly contributed to my continued growth. His dedication to science and constant availability for students are the qualities worth emulating. I am fortunate to have had such a dedicated and supportive supervisor by my side, and I owe a significant portion of my accomplishments to his guidance.

I would also like to extend my heartfelt thanks to my Ph.D. monitoring committee members, **Prof. Dipankar Mandal, Dr. Kiran S. Hazra, Prof. Abir De Sarkar and Dr. Tapasi Sen**, for their support. They have consistently devoted their valuable time to conduct yearly assessments and offering constructive suggestions for my research work. I am also grateful for their cooperation in all aspects of my academic journey.

I would like to thank **Prof. Deepa Ghosh, Prof. Debabrata Patra and Prof. Suvankar Chakravarty** for always backing us whenever needed.

I want to convey my heartfelt gratitude to all my collaborators, including **Dr. Ranjini Vishwannath, Dr. Sukhendu Mandal, Prof. Umesh Waghmare, Saptarshi, Akashdeep, Koyendrila, and Sarabjit**. Through these collaborations, I have gained invaluable knowledge and experiences, and I am truly thankful for the opportunity to learn and grow with each of you.

I'd like to extend my thanks to our laser engineers, **Arun Kumar P R from Laser Science Services (I) Pvt. Ltd., Arun kumar Singh from Trokut Solutions Pvt. Ltd.,** from **Laser Spectra Services**, for their timely support. Their assistance significantly contributed to the effective functioning of our laser systems, which are integral to the success of my PhD.

At the commencement of my journey, I wish to convey my deep appreciation to my lab colleagues, (**Members of Ultrafast Territory**). I am grateful to **Nandan Sir, Gurpreet Di, Tanmay Sir, Justice Sir, Dharmendra Sir, Sachin Sir, Palwinder Sir, Sourav Sir, Inderjeet Sir, Arshdeep, Himanshu, Ram Chandra Saha (RCS), Manvi, Nitika, Vikas, Anil and Samaresh Sir.** Your unconditional support, friendship, and teamwork have been indispensable during my academic endeavors. I am truly thankful for the privilege of working with such a dedicated and inspiring group of individuals. Our lab cultivates a unique friendly atmosphere, a rare find in academic settings, where each member is consistently willing to assist one another.

As my journey commenced in 2018, I, along with **Arshdeep and Liza**, became part of the Lab. We were truly fortunate to have the most incredible seniors in **Nandan Sir, Gurpreet Di, and Tanmay Sir** by our side. I vividly recall how, from the very first day, I would turn to **Gurpreet Di** with all my queries and doubts. She was more than just a senior colleague; she became a sister and a mentor to me. We began working together on my first project, and our partnership has been exceptional. Gurpreet Di has always been my go-to person whenever I had a new idea or faced any confusion, and she always gave me constructive suggestions. I remember those days when my faith weakened, she consistently pushed me forward in every way she could. The period when we were aligning Terahertz experiments could have been exhausting and frustrating, but it was her continuous support that helped us to persevere and progress together. Gurpreet Di has not only been a wonderful colleague but also a close friend in my personal life. I've leaned on her during emotional times, and she's been a steadfast source of support. I want to thank you, Gurpreet Di for always being there for me, both in our work and in my personal moments.

Justice Sir has been my guiding mentor throughout my Ph.D. journey, always offering continuous support and encouragement. As a physics student, I initially found the hot injection

synthesis process quite challenging. However, Justice Sir came to my aid and patiently taught me the intricacies of the synthesis. He not only motivated me but also imparted valuable lessons in research ethics. In addition to his scholarly guidance, Justice Sir brought laughter to our lab with his jokes and translated Tamil poetry. He even treated us with delicious homemade meals, including his very famous ginger tea. He always used to be there in my tough times, he has been a source of encouragement. I extend my heartfelt gratitude to Justice Sir for everything.

I want to thank **Arshdeep** for her support throughout my PhD. I truly admire her admirable qualities of effectively managing both family and work.

Tanmay Sir, Gurpreet Di, Himanshu, (Luchi and three others) lived together in Phase 10. We often went on outings and shared meals. These people in Mohali made me feel like a second home to me. They were an integral part of my days at INST filled with enjoyment and friendship. **Tanmay Sir** was more than a senior; he was like a big brother, always ready to help me. One valuable quality I've learned from him is effective management. Whether it's in the lab or during our trips, he excels at organizing and handling things smoothly. **Himanshu,** though my junior, was like a brother to me. Himanshu is someone you can always rely on in times of need. His discipline and dedication are qualities worth learning, and they have been a source of inspiration.

Manvi, Nitika, and Vikas, as my juniors, stood out as exceptional individuals who were always there to support me when needed them. They have been a great support, creating a friendly lab atmosphere where we share all our joyful moments. Their presence in all my challenging moments is priceless. Our shared tea breaks, hostel parties, late-night chats games, and outings were truly enjoyable, and these moments together created lasting memories. When I moved from Phase 10 to the hostel these people were always alongside me. All these moments have been some of the most beautiful moments spent in INST. All the moments spent with these wonderful people have been the most cherished experiences during my time at INST.

I thank my **Mahila Mandal** members for the 3B2 outings, parties, and fun-filled conversations.

Dharmendra Sir consistently emphasized the importance of dedication, not only to research but also to one's family. He derived genuine enjoyment from his research endeavors and set a

valuable example for all of us. These are the group of individuals who were like a family to me.

These people are not just my lab mates; they are family to me. I will deeply miss you all.

I extend my heartfelt thanks to my group, **Yariyaan, (Himadri, Liza, Anamika, Hari, Silky, Arshdeep, Akshay, and Archana, Suneera)** for the fun-filled outings together. I am thankful to **Silky** for her uplifting pep talks, enjoyable coffee outings, and the sharing my favorite pizza (although which she never liked). She has consistently been my reliable and go-to friend.

I would also like to extend my appreciation to everyone who provided assistance, whether it was through direct or indirect support during my time at INST: **Asmita, Ritika, Sakshi, Rejaoul, Raihan, Varun, Sourav, Chinmayee, Mamta, Neha Di, Preeti Di, Aniraban Sir, Rohit Sir, Mujeeb Sir, and Praveen Sir.**

Anamika is undoubtedly one of the best individuals I've encountered. She was not just my roommate but I found a best friend in her during my time at INST. She possesses a rare and beautiful soul, always by my side since we first met on my very first day at INST, together we have shared countless moments of joy. I find myself both fortunate and blessed to have discovered such a beautiful and lifelong connection during my time at INST. One invaluable trait I've learned from Anamika is her firm dedication and persistent drive to grow. Her sense of humor, along with her incredible jokes and the way she used to narrate stories, was truly delightful and unforgettable. Thank you, **Anamika (Ramu)**, for always being there for me, I'll deeply miss you, my dear friend, I pray you get all the happiness in life.

I want to thank **Neetu** (my childhood friend), **Alok bhaia, Anchal, Shivani, and Sucheta Di** for always being there for me. These wonderful people in my life have consistently supported me.

I would like to thank some of my beautiful relationships without whom this journey would have never been complete. **Nikita and Garima**, my best friends, have been my steadfast support. I can't recall a single instance when I needed them, and they didn't stand by my side. They are my constants in life, always there when I need them. I've learned the values of commitment to both work and family from them. **Shivam** is truly a remarkable individual, a gem of a person. He has consistently been there to provide motivation and guidance whenever

I've felt down. His persistent dedication and relentless hard work in pursuit of his dreams are two qualities that genuinely inspire me. His fun-filled nature lightens up my mood even when in tough times. He has continuously motivated me with his steadfast optimism, pushing me to work hard and never give up. I consider myself fortunate enough to be surrounded by such compassionate individuals.

I would acknowledge **my Family: where life begins and love never ends.** These are the most important people in my life, not just a support system; they are my pillars of strength. I want to thank my **Mummy, Papa** for always believing in me and giving me the wings to fly and fulfill my dreams. There were times when I faced self-doubt and uncertainty, but my family never wavered in their support. Their confidence in my abilities pushed me to overcome obstacles and never give up. It is their sacrifices, unshakeable belief, and continuous encouragement that made this journey possible for me. My family has been my constant source of motivation, their enduring inspiration and constant encouragement have filled my heart with a deep sense of purpose. It's their belief in me, that has been a guiding light, urging me to reach for excellence and pour my heart into every endeavor. Thank you for always being there for me, for believing in my dreams, and for helping me turn them into reality. I'd like to thank my brother, **Ayush**, for being a special person who lifts me up during my weakest moments. He reminds me that I can overcome any challenge and achieve my goals. He has been my partner in crime, my source of joy, and my constant companion in this journey. My family's love and support has shaped me into the person I am today, every ounce of my success is owed to them. I attribute all of my accomplishments to my family.!!

Ayushi Shukla

INST Mohali

Table of Content

List of Abbreviation	ix
Abstract	xii
List of Figures	xv
List of Tables.....	xxiv
Thesis Overview.....	xxvi
Chapter 1 Introduction	1
1.1 Motivation.....	1
1.2 From Discovery to Dominance: The Evolution of Perovskite and Its Structural Marvel	2
1.2.1. Dominance of Perovskite in Photovoltaics.....	2
1.2.2. Discovery of Perovskite.....	3
1.3 The Structure and Stability of Metal Halide Perovskites.....	5
1.3.1. Inorganic Lead Halide Perovskites.....	7
1.3.2. Phase Transitions in Inorganic Lead Halide Perovskites	10
1.3.3. Doping of Impurity Ions in Perovskites	12
1.4 Fundamental photo physical phenomena in perovskites.....	15
1.4.1. Electronic Band Structures	15
1.4.2. Quantum confinement	17
1.5 Carrier Relaxation Processes After Photoexcitation.....	20
1.5.1. Factors Affecting Carrier Cooling.....	21
1.5.1.1. Phonon Bottleneck Effect.....	21
1.5.1.2. Carrier Phonon Coupling.....	23
1.5.1.3. Auger Heating	25
1.5.1.4. Band filling at high carrier density.....	27
1.5.1.5. Defects.....	29
1.6 References.....	31
Chapter 2 Experimental Section	40
2.1. The hot injection technique used to synthesize the halide perovskites.....	40
2.2. Synthesis of perovskite nanostructures used in this thesis.....	43
2.2.1. The chemicals needed for all the synthesis conducted in this thesis.....	43
2.2.2. Preparation of Cs-oleate	43
2.2.3. Synthesis of CsPbBr ₃ NCs.....	44

2.2.4. Synthesis of CsPbBr ₃ NSs.....	44
2.2.5. Synthesis of Polyhedral Dodecahedron-CsPbBr ₃ NCs	44
2.2.6. Synthesis of CsPbCl ₃ NCs	45
2.2.7. Synthesis of Eu-CsPbCl ₃ NCs.....	45
2.2.8. Synthesis of Eu-CsPbBr ₃ NCs	46
2.3. Characterization techniques	46
2.3.1. X-Ray Diffraction (XRD)	46
2.3.1.1. Principle.....	46
2.3.1.2. Instrumentation.....	48
2.3.2. Transmission Electron Microscopy (TEM)	49
2.3.2.1. Working Principle	51
2.3.2.2. Instrumentation.....	52
2.3.3. Steady State Optical Studies	54
2.3.3.1. UV-Vis Absorption Spectroscopy.....	54
2.3.3.1.1. Principle	54
2.3.3.1.2. Instrumentation	55
2.3.3.2. Photoluminescence (PL) Spectroscopy	56
2.3.3.2.1. Principle	57
2.3.3.2.2. Instrumentation	58
2.3.4. Time Correlated Single Photon Counting (TCSPC) / Time Resolved Photoluminescence (TRPL) studies	59
2.3.4.1. Working Principle:	60
2.3.5. Transient Absorption (TA) Spectroscopy	62
2.3.5.1. Generation of Ultrafast Laser	67
2.3.5.1.1. Q Switching	68
2.3.5.1.2. Mode locking	71
2.3.5.2. Experimental Setup of Femtosecond Transient Absorption.....	74
2.3.5.2.1. Main Laser	74
2.3.5.2.1.1. Seed Laser	75
2.3.5.2.1.2. Pump Laser	76
2.3.5.2.1.3. Regenerative Ti: Sapphire Amplifier	76
2.3.5.2.2. Optical Parametric Amplifier (OPA).....	82
2.3.5.2.3. Transient Absorption spectrometer.....	88

2.3.5.2.3.1. Surface Xplorer™ software.....	89
2.3.6. Terahertz Spectroscopy	92
2.3.6.1. A Brief Introduction to the History behind Terahertz Spectroscopy.....	92
2.3.6.2. Terahertz Technique Introduction	94
2.3.6.3. Time-Resolved Terahertz Spectroscopy (TRTS)	95
2.3.6.3.1. THz Generation.....	96
2.3.6.3.2. Detection of THz	97
2.3.6.4. Experimental setup in our lab.....	98
2.3.6.4.1. Working of the Terahertz Time-domain Spectrometer (THz-TDS)	99
2.3.6.4.2. Data acquisition and calculations involved	101
2.4. References	103
Chapter 3 Effect of Confinement on the Exciton and Bi-exciton Dynamics in Perovskite 2D-Nanosheets and 3D-Nanocrystals.....	110
3.1 Introduction.....	111
3.2 Results and Discussion	112
3.2.1 Structural Analysis	112
3.2.2 Ultrafast Transient absorption studies	114
3.2.2.1 3D CsPbBr ₃ NCs	115
3.2.2.2 2D CsPbBr ₃ NSs	117
3.2.2.2.1 Near bandgap excitation (420 nm).....	117
3.2.2.2.2 Far Band gap excitation (300 nm).....	120
3.2.2.3 Hot carrier Cooling Dynamics.....	122
3.2.2.4 Bi-exciton Dynamics	124
3.3 Conclusion	128
3.4 References.....	128
Chapter 4 Fast Polaron Formation and Low Carrier Mobility in Defect Free Polyhedral CsPbBr₃ Perovskite Nanocrystals	133
4.1. Introduction.....	134
4.2. Result and Discussion	135
4.2.1. Optical Studies.....	136
4.2.2. Transient Absorption Studies	139
4.2.3. Low temperature photoluminescence	144
4.2.4. Low Temperature Transient Absorption Study	145

4.2.4.1.	Calculation of number of charge carriers (N) and polaron radius	149
4.2.5.	Carrier Mobility calculations.....	150
4.3.	Conclusion	152
4.4.	References.....	153
Chapter 5 Spectroscopic Investigation of Structural Perturbations in CsPbCl₃ Perovskite Nanocrystals: Temperature and Excitation Energy Dependent Study		159
5.1	Introduction.....	160
5.2	Result and Discussion.....	161
5.2.1.	Crystallographic studies and Morphological investigations	161
5.2.2.	Steady State Optical Properties.....	162
5.2.3.	Transient Absorption Study	164
5.2.3.1.	Temperature Dependent Carrier Cooling	164
5.2.3.2.	Temperature Dependent Exciton and Biexciton Transient Kinetics	166
5.2.3.3.	Effect of Phase Transition on Carrier Temperature and Energy Loss.....	171
5.2.3.4.	Excitation Energy Dependent Photoconductivity and Carrier Mobility....	173
5.3.	Conclusion	178
5.4.	References.....	179
Chapter 6 Defect interceded Cascading Energy Transfer and Underlying Charge Transfer in Europium Doped CsPbCl₃ Nanocrystals		185
6.1.	Introduction.....	186
6.2.	Results and discussion	187
6.2.1.	Structural and morphological studies of CsPbCl ₃ and Eu-CsPbCl ₃	187
6.2.2.	Optical Studies of CsPbCl ₃ and Eu-CsPbCl ₃	189
6.2.3.	Florescence Upconversion Studies of CsPbCl ₃ and Eu-CsPbCl ₃	192
6.2.4.	Transient Absorption Studies of CsPbCl ₃ and Eu-CsPbCl ₃	195
6.2.5.	Two photon Absorption Studies in CsPbCl ₃ and Eu-CsPbCl ₃	200
6.3.	Conclusion	202
6.4.	References.....	203
Chapter 7 Retarded Hot Carrier Relaxation and Augmented Photoconductivity in Europium doped CsPbBr₃ Nanocrystals.....		209
7.1	Introduction.....	210
7.2	Results and discussion	211
7.2.1	Structural and morphological studies	211

7.2.2	Optical Studies of CsPbBr ₃ and Eu-CsPbBr ₃ NCs.....	213
7.2.3	Transient Absorption Study of CsPbBr ₃ and Eu-CsPbBr ₃ NCs.....	213
7.2.3.1	Near Resonant Excitation	213
7.2.3.2.	Far Resonant Excitation.....	215
7.2.4	Low Temperature Transient Absorption Study	217
7.2.5	Photoconductivity and Mobility Calculations	221
7.3	Conclusion	224
7.4	References	224
Chapter 8	229
8.1.	Conclusion	229
8.2.	Future Prospects.....	233
List of Publications (Included in Thesis)	xxxii
List of Publications (Not included in thesis)	xxxii
Conferences attended/ Oral and Poster presentations	xxxiv
Copyright from Journals to Reuse the Content in Thesis	xxxv

List of Abbreviation

ABBREVIATION	DESCRIPTION
1 D	One-Dimensional
2D	Two-Dimensional
ADP	Ammonium Dihydrogen Phosphate
BBO	Barium Borate
BGR	Band Gap Renormalization
CB	Conduction Band
CBM	Conduction Band Minima
CPA	Chirp Pulse Amplification
CW	Continuous Wave
DFG	Difference Frequency Generation
DOS	Density of States
DSSC	Dye-Sensitized Solar Cells
EDS	Energy Dispersive X-Ray Spectroscopy
ESA	Excited State Absorption
FA	Formamidinium
FWHM	Full Width at Half Maximum
GSB	Ground State Bleach
GVD	Group Velocity Dispersion
ICDD	International Centre for Diffraction Data

IRF	Instrument Response Function
JCPDS	Joint Committee on Powder Diffraction Standards
KDP	Potassium Dihydrogen Phosphate
KLM	Kerr Lens Mode-Locking
LARP	Ligand-Assisted Reprecipitation Method
LBO	Lithium Triborate
LO	Longitudinal Optical
MA	Methyl Ammonium
MHP	Metal Halide Perovskites
N ₂	Nitrogen
NCs	Nanocrystals
NIR	Near-Infrared
NSs	Nano Sheets
O ₂	Oxygen
OA	Oleic Acid
ODE	1- Octadecene
OLM	Oleylamine
OPA	Optical Parametric Amplification
PB	Photo Bleaching
PC	Pockel Cell
PCE	Photo Conversion Efficiency
PIA	Photo Induced Absorption
PL	Photoluminescence

PLQY	Photoluminescence Quantum Yield
PV	Photovoltaics
QD	Quantum Dot
RB	Round Bottom
REGN	Regenerative Amplifier
SAED	Selected Area Electron Diffraction
SDG	Synchronization and Delay Generator
SE	Stimulated Emission
SEM	Scanning Electron Microscopy
SFG	Sum Frequency Generation
SHG	Second Harmonic Generation
STM	Scanning Tunneling Microscopy
TA	Transient Absorption
T _c	Carrier Temperature
TEM	Transmission Electron Microscopy
TFP	Thin Film Polarizer
THz	Terahertz
Ti:S	Titanium: Sapphire
VB	Valence Band
VBM	Valence band maxima
WLC	White Light Continuum
XRD	X-Ray Diffraction

Abstract

“Perovskites: Bridging the gap between efficiency and affordability in solar energy”

In the field of photovoltaics, inorganic metal halide perovskite solar cells have attracted a lot of attention because of their high power conversion efficiencies (PCE) and affordable manufacturing. The great potential of perovskite solar cell technology has attracted the attention of researchers and industry experts due to this extraordinary advancement. In 2009, these novel materials made their debut, displaying a PCE of 3.8%. Since that time, there has been no turning back, and a staggering rise in these numbers has been seen, with current developments raising the efficiency of organic-inorganic perovskite-based tandem cells to 31.25%. Rapid charge carrier recombination, which causes energy loss, poses a significant obstacle to their overall efficiency. To get around this obstacle, scientists are working tirelessly to find ways to control carrier cooling, which would make it possible to collect and use the surplus energy currently lost as heat. Since the inherent relaxation mechanisms pursued by the heated carriers have a significant influence on their behavior. Efficient carrier cooling is crucial in enhancing the performance of cutting-edge optoelectronic devices, as the intrinsic relaxation mechanisms pursued by the hot carriers profoundly impact their behavior. Therefore, gaining a comprehensive understanding of the dynamics of carrier cooling becomes imperative for making advancements in these fields. However, the thermalization and cooling of carriers occurs in a femtosecond time scale which could be understood using transient absorption spectroscopy. My thesis work is primarily focused on unraveling the photophysical properties of perovskite materials by employing two key techniques: transient absorption (TA) spectroscopy and terahertz (THz) spectroscopy. By delving deep into the dynamics of carriers within perovskite materials, we aimed to provide valuable insights that can contribute to the development of more efficient and reliable devices.

First work highlights that the shape of perovskite crystals can have a significant impact on carrier cooling in perovskite solar cells. The investigation reveals a captivating disparity in the hot carrier cooling rate between 2D Nanosheets (NSs) and 3D Nanocrystals (NCs), the carrier cooling is found to be faster in 2D NSs. However, this goes against the anticipated outcome since the cooling of the carrier was expected to be slow due to the decrease in the density of states in 2D NSs. The faster cooling rate observed in the 2D system can be attributed to the

reduction in Fröhlich interaction, facilitated by the system's higher surface-volume ratio which leads to easier dissipation of heat to the surrounding. In the next work, we tuned the facets and formed a newly synthesized dodecahedron cesium lead bromide (dodecahedron-CsPbBr₃) perovskite and compared its properties with conventional cube-CsPbBr₃ perovskite. Through transient absorption (TA) studies, we have observed that dodecahedron-CsPbBr₃ exhibits prolonged carrier cooling and a remarkable 20-30% enhancement in biexciton yield compared to cube-CsPbBr₃. Further, temperature-dependent TA studies revealed the rapid formation of polarons within 0.25 ps in dodecahedron-CsPbBr₃, leading to an increase in polaron size compared to cube-CsPbBr₃. Additionally, terahertz spectroscopic measurements have shown that the carrier mobility in dodecahedron-CsPbBr₃ at early time scales (few ps) is approximately 2 times lower than in cube-CsPbBr₃, further supporting the faster polaron formation in dodecahedron-CsPbBr₃. In the third work, we investigated cesium lead chloride (CsPbCl₃) which stands out for its remarkable blue emission. Also, the research carried out at low temperatures offers a more profound insight into the complex photophysical processes that are typically challenging to investigate at standard temperatures. This challenge arises from the increased system entropy caused by the phonon disorder. The underlying photophysics of CsPbCl₃ NCs is investigated using ultrafast TA and THz spectroscopy, focusing on temperature and excitation energy dependence. A direct dependence of carrier relaxation, carrier temperature, and energy loss on phase transition is observed. By analyzing the optical pump THz probe (OPTP) spectroscopy data, we have observed that decreasing the excitation energy leads to a slower decay in mobility, attributed to reduced auger recombination and increased penetration depth. As the absorption and PL of CsPbCl₃ is restricted in the UV region so, via doping the PL could be extended up to the VIS region. In the fourth work, we further doped rare earth ions (RE³⁺) i.e., Eu³⁺ (Europium ion) in the lattice of CsPbCl₃ as it has revolutionized the field of optoelectronics, offering exciting possibilities to explore and manipulate optical, magnetic, and charge carrier transport properties. Herein, we have investigated the intricate mechanistic transfer processes from the band edge of the host material, CsPbCl₃ to the dopant europium ion (Eu³⁺). We observe an intriguing defect-mediated cascading energy transfer phenomenon from CsPbCl₃ to Eu³⁺, accompanied by intriguing cross-relaxation interactions among different states of Eu³⁺ revealing two distinct characteristic traits. Additionally, we observed two-photon absorption in our study, and intriguingly, we

found no compromise in the efficiency of energy and charge transfer processes. In the final work, we prepared Eu-doped CsPbBr₃ in order to see how doping affects a different halide family member i.e., CsPbBr₃. In this study, we have investigated the spectroscopic properties of CsPbBr₃ and Eu-CsPbBr₃. Our findings reveal that the doped counterpart exhibits significantly slower cooling which was opposite to what was observed in the case of CsPbCl₃, while the formation and decay time of polaron remains unchanged. Low-temperature transient studies indicate that this is attributed to the absence of bound excitons resulting from the passivation of Br⁻ vacancies. Additionally, OPTP studies demonstrate that this phenomenon also impacts carrier mobility and photoconductivity, leading to higher photoconductivity and slower mobility in Eu-CsPbBr₃. The implications derived from our research indisputably demonstrate that the slower hot carrier cooling and enhanced photoconductivity in Eu-CsPbBr₃ positions it as a superior candidate for photovoltaic applications.

List of Figures

Figure 1.1 The schematic representation explaining the concept of a solar cell.	1
Figure 1.2 Best research-cell efficiency chart (U.S., National Renewable Energy Laboratory (NREL), https://www.nrel.gov/pv/assets/pdfs/pvefficiencychart.201812171.pdf).	3
Figure 1.3 Schematic representation of (A) Perovskite structure (ABX_3 where A stands at the corner position, (B) is present at the body center position and X is at faces), (C) octahedral sites.	5
Figure 1.4 Presents a map illustrating the tolerance factor-octahedral factor ($t-\mu$) relationship for several halide perovskite compounds.	6
Figure 1.5 Classification of perovskite system.....	7
Figure 1.6 (A) Under the illumination of a UV lamp, the colloidal solutions of $CsPbX_3$ NCs ($X = Cl, Br, I$) in toluene are visually depicted, (B) the PL spectra of $CsPbX_3$ NCs, (C) the optical absorption and PL spectra.....	8
Figure 1.7 (A) The schematic representation of the electronic structure of defect tolerant perovskite, both the VB and CB are created through antibonding orbitals, and (B) the band gap of all inorganic lead halide perovskites i.e., $CsPbX_3$ ($X=Cl, Br, I$).....	9
Figure 1.8 The crystal structures of different phases of perovskites (A) Cubic, (B) Orthorhombic, (C) Monoclinic, and (D) Tetragonal.....	11
Figure 1.9 Schematic representation of the possible doping sites in ABX_3 Perovskites and their impact on the intrinsic properties of the material.....	12
Figure 1.10 The metal elements which can be doped in perovskites and their main roles in altering lead halide perovskites..	13
Figure 1.11 The schematic illustrated energy diagrams of metal, insulator, and semiconductors.	16
Figure 1.12 The quantum confinement effect in semiconducting NCs, showcasing the increase in the energy bandgap of NCs with confinement.	18
Figure 1.13 Schematic illustration of the density of states in the differently confined materials.	19
Figure 1.14 The time-dependent carrier relaxation processes in perovskites.....	20
Figure 1.15 Factors affecting the carrier cooling.....	21

Figure 1.16 The schematic illustration of polaron formation in the lattice. Polaron is a quasiparticle arising as a result of coupling between an electron or hole and its surrounding lattice vibrations (phonons). When an electron or hole moves through a crystal lattice, it causes a local distortion or deformation in the lattice structure. Due to this distortion, a charge carrier (electron or hole) is dressed or surrounded by a cloud of lattice vibrations giving rise to a polaron. 23

Figure 1.17 The schematic illustration of the relaxation process of hot electrons, showcasing effect of both LO phonon emission and Auger recombination. These processes contribute to the deceleration of hot electron cooling. (It is important to note that a similar relaxation process also occurs for hot holes, although it is not shown in the schematic for clarity) 26

Figure 1.18 The Schematic representation explaining the Burstein-Moss effect. 28

Figure 1.19 Schematic representation illustrating the trapping of electrons and holes in trap states within a semiconductor QDs, which leads to a delayed carrier cooling process. 30

Figure 2.1 The schematic representation of the HI method used to synthesize perovskite NCs. 40

Figure 2.2 A schematic illustration depicting the sequential changes in atomic concentration within a classical LaMer mechanism across its three reaction phases. 41

Figure 2.3 Schematic illustration depicting the Diffraction of Incident X-rays by a crystal. X-rays are scattered by the crystal lattice, and their diffraction angles are governed by Bragg's Law, for the determination of crystal structure. 47

Figure 2.4 A schematic illustration of XRD setup. 48

Figure 2.5 Generation of rays and electrons as a consequence of the interaction between the incoming electron beam and the sample. 50

Figure 2.6 The schematic illustration of the experimental setup for TEM. 52

Figure 2.7 The schematic representation of the absorption phenomenon. 54

Figure 2.8 The basic experimental setup of a steady state absorbance spectrometer. 56

Figure 2.9 The experimental setup of the PL spectrometer consisting of its various components. 58

Figure 2.10 The schematic representation of a TCSPC setup. 60

Figure 2.11 The principle involved in TCSPC measurement. 61

Figure 2.12 Illustrates the core concept of a pump-probe experimental setup in a schematic manner.	64
Figure 2.13 A schematic representation of the various processes that occur subsequent to photoexcitation typically includes the following stages.....	65
Figure 2.14 (A) The schematic representation explaining how Q-switching works with an electro-optic modulator (Pockels or Kerr cell), demonstrating the setup, (B) depicts the strong laser pulses (giant pulses) produced by Q-switching.	69
Figure 2.15 Q-switching using Pockels cell for producing short, high-energy laser pulses...	70
Figure 2.16 The schematic representation of the resulting electric field intensity acquired after the superposition of (A) randomly oriented phased modes, and (B) modes with identical phase configurations within a laser cavity.....	72
Figure 2.17 The resulting pulse, obtained by superimposing different number of modes, i.e., 4, 8, and 60 modes, illustrates a reduction in pulse width as the number of incorporated modes increases.....	73
Figure 2.18 Schematic representation illustrating the configuration of the Chirped Pulse Amplification (CPA) system.	77
Figure 2.19 Schematic representation illustrating the negative and positive dispersion.	78
Figure 2.20 Schematic representation of the REGEN unit.....	80
Figure 2.21 (A) illustrates the overall concept of the optical parametric amplifier (OPA) process, Energy level diagram depicting, (B) the energy conservation, and (C) momentum conservation in OPA process.....	83
Figure 2.22 (A) The schematic representation of Sum Frequency Generation the resultant photon is the sum of the incident photon frequencies (B) Difference Frequency Generation process where the output frequency is the difference of the incident frequencies.	84
Figure 2.23 Schematic representation of the Opera Solo parametric amplifier setup showing all optical components of the parametric amplifier.	86
Figure 2.24 illustrates the schematic representation of the Helios-FIRE spectrometer.....	89
Figure 2.25(A) Different type of signals which are observed in TA and (B) Schematic illustrating their respective origins.	91
Figure 2.26 A visualization of the electromagnetic spectrum, highlighting the various regions based on frequency.	93

Figure 2.27 THz radiation is present in the region of the electromagnetic spectrum that comprises rotational, vibrational, and electronic transition frequencies.	94
Figure 2.28 Schematic depiction of Time-Resolved THz Spectroscopy.	96
Figure 2.29 The schematic representation of THz generation by two color plasma.	96
Figure 2.30 Electro optic detection setup in THz-TDS	97
Figure 2.31 The schematic layout of Newport Terahertz Time Domain spectrometer.	98
Figure 3.1 XRD patterns of CsPbBr ₃ NCs and NSs.	112
Figure 3.2 (A) HR-TEM images of (a, b) CsPbBr ₃ NCs and (c, d) NSs (Inset: corresponding FFT patterns). (B) Optical absorbance and PL studies for (a,b) CsPbBr ₃ NCs and (c, d) CsPbBr ₃ NSs. (Inset: Schematic representation of the splitting in the valence band due to increased spin-orbit coupling in NSs)	113
Figure 3.3 (A, B) TA spectra of CsPbBr ₃ NCs at different time delays after exciting the samples at 420 nm and 300 nm laser light respectively. (C) Bleach recovery kinetics monitored at 510 nm for both the 420 nm (green: open circles) and 300 nm excitation (red: closed circles), (D) Schematic representation of the photoexcited charge carrier cooling involved after the pump excitation.	116
Figure 3.4 (A) TA Spectra for 2D CsPbBr ₃ NSs under 420 nm pump excitation (B) Comparative kinetic traces for system probed at probe wavelength $\lambda = 474$ nm and 487 nm; Inset: schematic representation of carrier cooling process in 2D CsPbBr ₃ NSs.....	118
Figure 3.5 Early time (0.3 ps) TA spectra of (A) CsPbBr ₃ NC and (B) CsPbBr ₃ NSs matches with the second derivative of steady-state absorption for CsPbBr ₃ (inset), which clearly signifies the biexciton-induced Stark effect in the TA spectra.....	118
Figure 3.6 (A) TA spectra for CsPbBr ₃ NSs at different time delays after exciting at 300 nm laser light. (B) Comparative kinetic traces at different probe wavelength i.e., 400 nm, 474nm and 487 nm.	120
Figure 3.7 (A, C) Normalized TA spectra under pump excitation (300 nm) for probe delays (from 500fs to 2 ps for NCs and 300fs to 2 ps for NSs); the dashed boxes drawn to show the high-energy tail region on which MB fitting has been done. (B,D) Change in carrier temperature T_c with time for NCs and NSs respectively.	123
Figure 3.8 Schematic representation illustrating (A) the hot biexciton formation by the coulombic interaction between pump induced hot exciton and probe induced exciton. (B)	

biexciton (thermalized pump induced exciton and probe induced exciton) formed as the band gap is renormalized due to the bi-excitonic induced stark effect. 125

Figure 3.9 (A) Normalized kinetic traces for CsPbBr₃ NCs probed at probe wavelength $\lambda = 525$ nm at (a) 420nm and (b) 300 nm pump excitation, **(B)** Normalized kinetic traces for CsPbBr₃ NSs probed at probe wavelength $\lambda = 498$ nm (positive band) for both (a) 420 nm and (b) 300 nm pump excitation..... 127

Figure 4.1 (a, b) HR-TEM images of dodecahedron and cube-CsPbBr₃ atomic model showing orthorhombic phase of dodecahedron-CsPbBr₃ having (200), (112) facets (right panel of Figure 4.1a), and cube- CsPbBr₃ having (110), (002) facets (left panel of Figure 4.1b); (Diamond software version 4.5.3 with ICSD 97851 for CsPbBr₃ was used for the formation atomic models), the models and ligands were designed as per the previous reported literature.¹⁹ ... 135

Figure 4.2 HR-TEM images of (a) dodecahedron-CsPbBr₃ (Inset: generated FFT pattern from green rectangle), (b) cube-CsPbBr₃, (c) XRD pattern of cube and dodecahedron-CsPbBr₃ along with orthorhombic CsPbBr₃ PDF line are also shown in the bottom (PDF: 01-072-7929). . 136

Figure 4.3 Steady state absorption and corresponding PL spectra ($\lambda_{ex} = 420$ nm) of (a) dodecahedron- CsPbBr₃ and (b) cube-CsPbBr₃ (inset: Time-correlated single photon counting (TCSPC) study of dodecahedron and cube-CsPbBr₃ after exciting the sample at 402 nm and monitoring at emission peak position, and laser pulse (IRF) blue line). 137

Figure 4.4 XPS spectra of dodecahedron- CsPbBr₃ (a) survey scan; and high-resolution scans of (b) Cs_{3d}, (c) Pb_{4f}, (d) Br_{3d} and (e) N_{1s}. 138

Figure 4.5 TA spectra of (a) dodecahedron-CsPbBr₃ and (c) cube-CsPbBr₃ at different time delays in hexane after exciting the samples at 350 nm, (b) Comparison of bleach kinetics monitored at 510 and 506 nm for dodecahedron -CsPbBr₃ and cube-CsPbBr₃ respectively, (d) Comparison of bi-exciton kinetics monitored at 528 and 524 nm for dodecahedron -CsPbBr₃ and cube-CsPbBr₃ respectively. Inset: change in ratio of bi-exciton signal and excitonic bleach intensity with laser power for both dodecahedron-CsPbBr₃ and cube-CsPbBr₃. 140

Figure 4.6 (a,b) Early time TA spectra (0.3 ps) of cube-CsPbBr₃ and dodecahedron-CsPbBr₃ which matches with the second derivative of steady-state absorption for (c) cube and (d) dodecahedron-CsPbBr₃, which clearly indicate the biexciton-induced stark effect in the TA spectra..... 141

Figure 4.7. (a) Normalized temperature-dependent PL plots for dodecahedron-CsPbBr₃ film. (b) Representative shift in the PL peak position maxima and the FWHM line monitored as a

function of temperature (300 – 5K), (c) PL spectra of cube-CsPbBr₃ at 300 and 5 K under 350 nm excitation (the contribution of bound (blue) and free exciton (violet) at 527 and 510 nm respectively in the PL spectrum were deconvoluted with non- Lorentzian fit in the cube-CsPbBr₃ at 5 K also plotted), (d,f) Orthorhombic crystal structure of dodecahedron and cube-CsPbBr₃ and (e,g) corresponding schematic representation of bound exciton and free exciton formation in dodecahedron and cube-CsPbBr₃ respectively. 145

Figure 4. 8 (a, d) TA spectra of dodecahedron-CsPbBr₃ with the temperature of 300 and 5 K under 350 nm pump excitation; **(b, c, e)** Bleach, polaron and bi-exciton kinetics at different temperature for dodecahedron- CsPbBr₃ monitored at 514, 530 and 620 nm probe wavelength respectively; and **(f)** Carrier temperature at 300 and 5 K as a function of time delay obtained by Maxwell-Boltzmann fitting of the high energy region of the TA spectra. 146

Figure 4. 9 Schematic representation portraying **(a,c)** the defect free nature of dodecahedron CsPbBr₃ and the traditional CsPbBr₃ nanocubes accounting for the absence of bound exciton in the former system; **(b,d)** reveal the contrasting polaron dynamics of dodecahedron and traditional cube-CsPbBr₃ illustrating the relatively fast polaron formation in dodecahedron (0.25 ps) than nanocubes (0.55 ps). These two factors together are liable for the retarded carrier cooling dynamics observed for dodecahedron CsPbBr₃. 148

Figure 4.10 (a) FE-SEM images of the as-deposited dodecahedron-CsPbBr₃ over the glass substrate and **(b)** corresponding the thickness of the sample. 149

Figure 4.11 (a) THz-TDS waveforms transmitted through the air, polystyrene, cube-CsPbBr₃ and dodecahedron-CsPbBr₃ over polystyrene, **(b)** Normalized comparative photoinduced THz transmissions versus pump–probe delay for 480 nm pump and **(c)** Calculated time dependent effective mobility for both cube-CsPbBr₃ and dodecahedron-CsPbBr₃. 151

Figure 5.1 (A) XRD pattern of as-prepared CsPbCl₃ NCs film. The standard JCPDS data of cubic CsPbCl₃ is also shown as lines at the bottom, **(B)** TEM and **(C)** HR-TEM images of CsPbCl₃ NCs. 161

Figure 5. 2 (A) The absorption spectra of CsPbCl₃ NCs, **(B)** Deconvoluted PL spectrum of CsPbCl₃ NCs at 5K, **(C)** The band-edge PL peak intensity and PL line width plotted against the temperature, and **(D)** Schematic representation of various PL transitions taking place at 5K. 163

Figure 5.3 (A) The PL spectrum of CsPbCl₃ NCs in the temperature range of 300 to 5K, **(B)** deconvoluted PL spectrum of CsPbCl₃ NCs at 300 K. 164

Figure 5.4(A-D) TA spectra of CsPbCl₃ NCs spreading over the temperature range 300K to 5K under 3.54 eV pump excitation, **(E)** The deconvoluted transient spectra at 5 ps corresponding to 5K depicting exciton, biexciton stimulated and defect emission, **(F)** The Plot of bleach maximum intensity and FWHM as a function of Temperature (T)..... 165

Figure 5.5 Comparative ground state excitonic bleach kinetic traces of CsPbCl₃ NCs film monitored for the energy corresponding to bleach maximum in the temperature range of **(A)** 300 K to 200 K, **(B)** 200 K to 5 K **(C)** The normalized kinetics at the position of biexciton maxima at two extreme temperature ends (300K and 5K), **(D)** The bleach growth time is plotted as a function of the temperature, and **(E)** Schematic representation of phase transition experienced by CsPbCl₃ NCs (The crystal structure of orthorhombic and monoclinic CsPbCl₃ models were designed using Vesta software from CIF file with ICSD code of 243734).³⁷..167

Figure 5.6 The plots for carrier temperature were calculated for **(A)** 300 K, **(B)** 200 K, and **(C)**5K. The energy loss is calculated as a function of T_c corresponding to the different lattice temperatures i.e., **(D)** 300 K, **(E)** 200 K, and **(F)** 5K. 171

Figure 5.7 (A) The relative carrier temperature plots, **(B)** The comparative energy loss vs carrier temperature plots of CsPbCl₃ NCs for the various lattice temperatures. 172

Figure 5.8 (A) The THz-TDS waveforms transmitted through the N₂, polystyrene (PS), and polystyrene CsPbCl₃ NCs (PS+ CsPbCl₃ NCs), **(B)** The THz transients of CsPbCl₃ NCs at 2.95, 3.26 and 3.54 eV pump excitation, **(C)** The time-dependent photoconductivity trace of CsPbCl₃ NCs at 2.95, 3.26 and 3.54 eV pump excitation, **(D)** Comparative normalized mobility trace versus pump-probe delay, **(E)** The transient excitonic bleach of CsPbCl₃ NCs at 3.26, 3.54, and 4.13 eV pump excitation, and **(F)** Schematic representation of the excitation energy dependent photophysical processes taking place in CsPbCl₃ NCs..... 175

Figure 5.9 The temporal evolution of transient THz spectra at different carrier densities of CsPbCl₃ NCs..... 176

Figure 6.1 (A) TEM and HR-TEM images of (a, b) CsPbCl₃ NCs, (c, d) Eu-CsPbCl₃ NCs; **(B)** XRD pattern of (a) CsPbCl₃ NCs, and (b) Eu-CsPbCl₃ NCs; **Inset:** shows the enlarged comparative XRD pattern of (101) plane. 187

Figure 6.2 The Energy dispersive spectra for Eu-CsPbCl₃ NCs; inset table shows different atomic percent of elements. 188

Figure 6.3 (A) The comparative absorption spectra for both (a) CsPbCl₃ and (b) Eu-CsPbCl₃ NCs; Inset: shows the enlarged absorbance near band edge; **(B)** The comparative PL spectra of both (a) CsPbCl₃ and (b) Eu-CsPbCl₃ NCs; Inset: illustrates the PL transitions of Eu³⁺. **(C)** TRPL decay traces of CsPbCl₃ (403 nm), Eu-CsPbCl₃ (406 nm), and Eu-CsPbCl₃ (468 nm) after exciting at 375 nm and **(D)** PL decay traces of Eu-CsPbCl₃ NCs monitoring Eu³⁺ D-F emissions at 592 nm (⁵D₀-⁷F₁), 616 nm (⁵D₀-⁷F₂) and 700 nm (⁵D₀-⁷F₄) after exciting the sample at 375 nm. Interestingly, PL lifetime of Eu transition peaking at 592 nm which is MD transition is much lower in comparison to the 616 and 700 nm (both are ED transitions). 189

Figure 6.4 PL upconversion decay comparative kinetic traces of both (a) CsPbCl₃ and (b) Eu-CsPbCl₃ dispersed in toluene upon probing 440 nm after exciting both the samples at 390 nm. 193

Figure 6.5 (A) PL upconversion decay traces of Eu-CsPbCl₃ dispersed in toluene after monitoring at (a) 440 nm, (b) 468 nm, (c) 592 nm, and (d) 616 nm after exciting at 390 nm and **(B)** Schematic representation of the cascading energy transfer processes in photo-excited Eu-CsPbCl₃ manifested by the PL decay traces where the recovery component of one transition is in good agreement with the growth of succeeding transition portraying the defect mediated transfer from CsPbCl₃ to Eu³⁺ and further transfer mechanism taking place among Eu³⁺ transition states. 194

Figure 6.6 TA spectra of (A) CsPbCl₃ and (B) Eu-CsPbCl₃ NCs at different time delays, inset: The transient bleach observed due to the defect state; (C) Transient bleach kinetics and corresponding fitted data for (a) CsPbCl₃ and (b) Eu- CsPbCl₃ NCs probed at 400 nm and 403 nm, respectively with pump excitation of 350 nm and (D) Comparative transient biexciton signal for (a) CsPbCl₃ NCs, (b) Eu-CsPbCl₃ NCs probed at 410 and 413 nm, respectively. 196

Figure 6.7 Pseudo contour plots of both (A) CsPbCl₃ and (B) Eu- CsPbCl₃ after exciting with 350 nm pump excitation. 197

Figure 6.8 Deconvoluted absorption spectra of (A) CsPbCl₃ into the excitonic peak and the continuum peak and (B) Eu- CsPbCl₃ into the excitonic, absorption due to defect state and the continuum peak. 198

Figure 6.9 Normalized transient kinetics of both CsPbCl₃ and Eu- CsPbCl₃ monitored at 418 nm (defect) after exciting with 350 nm pump. 199

Figure 6.10 PL spectra for both CsPbCl₃ and Eu-CsPbCl₃ upon exciting at 750 nm (Inset: Schematic representation of the TPA in Eu-CsPbCl₃); TA spectra of **(B)** CsPbCl₃ and **(C)** Eu-CsPbCl₃ at different time delay after exciting at 700 nm laser light and **(D)** Comparative decay traces of bleach monitored for **(a)** CsPbCl₃ and **(b)** Eu- CsPbCl₃..... 201

Figure 7.1 TEM and HR-TEM images of **(a)** CsPbBr₃ and **(b)** Eu-CsPbBr₃ NCs, **(c)** XRD pattern of CsPbBr₃ and Eu-CsPbBr₃ NCs, **(d)** optical absorbance of CsPbBr₃ and Eu-CsPbBr₃ **(e)** photoluminescence spectra of CsPbBr₃ and Eu-CsPbBr₃ NCs and **(f)** TCSPC study of CsPbBr₃ and Eu-CsPbBr₃ NCs after exciting at 3.08 eV and monitoring at the band edge emission. 212

Figure 7.2 **(a)** The structure representation of the pump probe spectroscopy for Eu-CsPbBr₃ NCs; Transient absorption (TA) spectra of **(b)** CsPbBr₃, **(c)** Eu-CsPbBr₃, under 2.58 eV pump excitation and **(d)** comparative bleach decay kinetics of CsPbBr₃ and Eu-CsPbBr₃ probed at the bleach minima..... 214

Figure 7.3 **(a, b)** Transient absorption spectra of CsPbBr₃ and Eu-doped CsPbBr₃ respectively after 3.54 eV pump excitation, **(c)** comparative transient bleach kinetics of CsPbBr₃ and Eu-doped CsPbBr₃ NCs and **(d)** comparative polaron kinetics probed at 2.0 eV. 216

Figure 7.4 The transient absorption spectra of Eu-CsPbBr₃ in the temperature range of **(a-d)** 200 K-5K upon 3.54 eV pump excitation, **(e)** The normalized transient bleach recovery kinetics for all the temperatures under consideration, and **(f)** schematic representation of bound exciton formation in both systems..... 219

Figure 7.5 **(a)** THz waveforms transmitted through air, quartz, CsPbBr₃, and Eu-CsPbBr₃, the time-dependent traces of **(b)** THz conductivity, **(c)** effective mobility, and **(d)** Normalized effective mobility plot for CsPbBr₃, and Eu-CsPbBr₃ upon 2.58 eV pump excitation..... 222

List of Tables

Table 3.1 Kinetics Fitting Parameters for CsPbBr ₃ NCs Dispersed in n-hexane after exciting the Samples at 420 nm and 300 nm.	117
Table 3.2. Kinetics fitting parameters for CsPbBr ₃ NSs at different wavelengths dispersed in n-hexane after exciting the samples at 420 nm.	119
Table 3.3 Kinetics fitting parameters for CsPbBr ₃ NSs dispersed in n-hexane after exciting the samples at 300 nm.	121
Table 3.4 Kinetics fitting parameters for CsPbBr ₃ NCs and NSs dispersed in n-hexane after exciting the samples at 300 nm and 420 nm respectively.	126
Table 4. 1 PL quantum yield calculation	137
Table 4.2 Details of PL-decay fitting parameters of prepared samples.	138
Table 4.3 Kinetics of fitting parameters at bleach position after exciting the samples at 350 nm laser pulse.	142
Table 4.4 Kinetics fitting parameters bi-excitonic peak position of cube-CsPbBr ₃ and dodecahedron-CsPbBr ₃ after exciting the samples at 350 nm laser pulse.	143
Table 4.5 Kinetic fitting parameters at excitonic bleach position for dodecahedron-CsPbBr ₃ deposited over a glass substrate at different temperature under 350 nm pump excitation. ...	147
Table 5.1 Kinetic fitting parameters upon fitting the band edge bleach for CsPbCl ₃ NCs for different lattice temperature under 4.41 eV pump excitation.	168
Table 5.2 Biexciton formation and decay components obtained upon fitting the Biexciton maxima for CsPbCl ₃ NCs for different lattice temperature under 4.42 eV pump excitation.	169
Table 5.3 Kinetic fitting parameters upon fitting THz transient kinetics for CsPbCl ₃ NCs for different pump excitation energy.	177
Table 5.4 Kinetic fitting parameters upon fitting THz transient kinetics for CsPbCl ₃ NCs for different carrier density (fluence).	178
Table 6.1 Fitting parameters of PL decay of both CsPbCl ₃ and Eu-CsPbCl ₃ after exciting samples at 375 nm.	191
Table 6.2 Fitting parameters of PL decay of Eu- CsPbCl ₃ after exciting samples at 375 nm and monitoring the Eu ³⁺ transitions.	191
Table 6.3 Fitting parameters of florescence upconversion study for both CsPbCl ₃ and Eu-CsPbCl ₃ after exciting samples at 390 nm.	195

Table 6.4 Kinetics fitting parameters of transient absorption for both CsPbCl₃ and Eu- CsPbCl₃ after exciting samples at 350 nm. 199

Table 6.5 Kinetics fitting parameters of transient absorption data for both CsPbCl₃ and Eu- CsPbCl₃ after exciting samples at 350 nm monitoring the signal due to defect state. 200

Table 7. 1 Kinetic fitting parameters at bleach position for CsPbBr₃ and Eu-CsPbBr₃ under 2.58 eV pump excitation. 215

Table 7.2 Kinetic fitting parameters at bleach position for CsPbBr₃ and Eu-CsPbBr₃ under 3.54 eV pump excitation. 217

Table 7.3 Kinetic fitting parameters at bleach position for Eu-CsPbBr₃ at different temperature under 3.54 eV pump excitation. 220

Thesis Overview

All inorganic perovskite solar cells (ABX_3) have made significant advancements, with the current efficiency record already nearing 31 %. Lead-halide perovskites have undergone extensive research into their photo physics and carrier dynamics recently due to their potential performance in conventional solar devices. Metal halide perovskites (MHPs) have quickly gained popularity because of their outstanding optoelectronic properties, which include high optical absorption, high PLQY, defect-tolerant nature, and cost-effectiveness. To further enhance the PCE of perovskite solar cells, researchers have been consistently striving for improvements. One approach involves **slowing down the carrier cooling process** to effectively **increase the extraction time** for the charge carriers. Consequently, understanding the dynamics involved in carrier cooling is crucial for improving photovoltaic performance.

Nevertheless, the important factor is that the carrier cooling processes occur on a very short time scale, particularly within femtoseconds. The photophysical properties of perovskite nanostructures have been deeply studied using two vital techniques: **TA spectroscopy** and **THz spectroscopy**. Moreover, to understand the behavior of these photo-generated charge carriers at low temperatures, temperature dependent TA studies have been performed. Understanding the behavior of the carriers upon varying the lattice temperature is one of the crucial factors, as during real-time application the devices have to go through various temperatures. Our aim is to provide valuable insights for the enhancement of more efficient and reliable devices by delving deep into the dynamics of carriers within perovskite materials. To tune the carrier cooling, a variety of strategies can be employed. These include modifying dimensionality, altering morphology, substituting cations, doping the lattice with impurity ions to enhance lattice properties, and synthesizing heterostructures. I have explored some of these strategies in my thesis work.

Chapter 1 emphasizes the prominence of solar energy and the rapid advancements in the realm of photovoltaic devices. It provides a comprehensive overview of the historical trajectory of perovskites and their meteoric rise within a condensed timeframe. Moreover, the chapter delves into the various classifications of perovskite materials, with particular attention given to Lead Halide Perovskites (LHPs). The discussion encompasses the profound influence of phase transitions and doping on the structural configuration of perovskites, thereby imparting distinct

properties to the materials. Through an exploration of these phenomena, the chapter aims to establish a comprehensive comprehension of the intricate relationship linking perovskite structures, phase transitions, and doping effects. Furthermore, this chapter presents an exhaustive and intricate elucidation of the manifold factors that govern carrier cooling processes. It delves into the intricacies associated with parameters such as polaron formation, carrier-phonon coupling, Auger heating, and defect states, meticulously delineating their impact on the efficacy of carrier cooling.

Chapter 2 provides a thorough exploration of the synthesis strategies and instrumental techniques used in this study. It covers various experimental approaches for characterizing the synthesized halide perovskite nanocrystals, including X-ray diffraction, UV spectroscopy, PL, time-correlated single-photon counting, and transmission electron microscopy. The chapter also focuses on a detailed discussion of the femtosecond transient absorption and terahertz time-domain spectroscopy setups, which are central to this thesis. By highlighting the importance of these techniques, the chapter establishes a solid foundation for the subsequent analyses and findings.

Chapter 3 shows that the shape of perovskite crystals can have a significant impact on carrier cooling in perovskite solar cells. We investigated the difference in the cooling mechanisms in differently confined materials and found that the exciton and biexciton dynamics are faster in 2D NSs in contrast to 3D NCs, due to less efficient charge screening by the Fröhlich interaction in the low-dielectric medium. By exciting the samples at varying wavelengths, a comprehensive comparison has been made to illuminate the underlying mechanisms. Moreover, the charge carrier dynamics, encompassing both exciton and biexciton dynamics, exhibit a slowed response at higher energy excitations in both 2D and 3D systems. This phenomenon arises from the injection of carriers into higher energy states, necessitating relaxation time towards the band-edge position. The study sheds light on intriguing differences in the rate of hot carrier cooling between 2D nanosheets (NSs) and 3D nanocrystals (NCs). The reduced Fröhlich interaction, due to the increased surface-volume ratio and lower dielectric constant, is the cause of the 2D system's faster cooling rate. This intriguing characteristic enables efficient dissipation of energy to the surrounding medium. This profound exploration not only enhances our fundamental understanding of the impact of dimensionality on charge carrier relaxation dynamics but also paves the way for the development of cutting-edge

optoelectronic devices. The remarkable observation of faster hot carrier relaxation in 2D perovskite systems holds immense promise for advancing technologically advanced optoelectronics based on these materials.

The facets have been modified and a novel synthesized polyhedral dodecahedron was synthesized in the next study, **Chapter 4**. In our study, we synthesized the perovskite dodecahedron-CsPbBr₃ and compared its properties to those of the more conventional cube-CsPbBr₃ perovskite. We have discovered through transient absorption (TA) investigation that dodecahedron-CsPbBr₃ exhibits slower carrier cooling and a striking 20–30% increase in biexciton yield in comparison to cube-CsPbBr₃. As per the low-temperature photoluminescence (PL) investigations, where no additional PL emission associated with bound exciton was identified, thus the slower carrier cooling in dodecahedron-CsPbBr₃ can be attributed to the absence of bound exciton. Furthermore, polarons in dodecahedron-CsPbBr₃ rapidly form within 0.25 ps, resulting in larger polarons than in cube-CsPbBr₃. The slower bleach growth and decay dynamics are a result of the increase in polaron size from 34.7 Å in cube-CsPbBr₃ to 39.6 Å in dodecahedron-CsPbBr₃. Further evidence for the slower carrier cooling in the dodecahedron-CsPbBr₃ comes from terahertz spectroscopic studies, which revealed that the carrier mobility is around two times lower in the dodecahedron-CsPbBr₃ at early time scales (few ps) than in the cube-CsPbBr₃. Overall our studies clearly indicate that the dodecahedron CsPbBr₃ is a better alternative for photovoltaic applications as compared to the cube system.

In **Chapter 5**, we investigated CsPbCl₃, which has been under continuous attention for its ability to emit blue light and has the potential to be doped or stacked with another complementary material. A direct dependence of carrier relaxation, carrier temperature, and energy loss on phase transition is observed, which makes CsPbCl₃ an intriguing material for understanding the behavior of carriers upon phase transition and excitation energy. In the field of photovoltaic research, inorganic lead halide perovskites have emerged as a cutting-edge material for solar cell applications, particularly as an absorbing layer. Within this group of perovskite materials, CsPbCl₃ is particularly notable for its exceptional blue emission. However, the understanding of its photophysical properties in relation to temperature and phase transitions is still limited. In this study, we have investigated the underlying photophysics of

CsPbCl₃ NCs using ultrafast transient absorption (TA) and terahertz (THz) spectroscopy, upon varying the temperature and excitation energy dependence. Our findings have revealed the significant impact of phase transitions on carrier relaxation, carrier temperature, and energy loss in CsPbCl₃ NCs. By analyzing the optical pump THz probe spectroscopy data, we have observed that decreasing the excitation energy leads to a slower decay in mobility, attributed to reduced Auger recombination and increased penetration depth. Additionally, our investigation using low-temperature TA and optical pump THz probe spectroscopy has provided insights into the optical properties of CsPbCl₃ NCs. At lower lattice temperatures, multiple peaks in the PL spectrum have been observed, accompanied by an increase in PL intensity due to reduced thermal perturbations. The temperature-dependent behavior of carriers across the orthorhombic to monoclinic phase transition has been elucidated, which is crucial for understanding the performance of photovoltaic devices under varying operating temperatures. Furthermore, the excitation energy and temperature-dependent relaxation processes uncovered in this study offer valuable insights for the development of advanced optoelectronic devices based on CsPbCl₃ perovskite NCs.

In **Chapter 6**, we expanded our research by introducing rare earth ions (RE³⁺) into the lattice of CsPbCl₃. This innovative use of RE³⁺ doping in CsPbCl₃ has brought about a transformative shift in the field of optoelectronics, presenting exciting opportunities to explore and manipulate optical, magnetic, and charge carrier transport properties. CsPbCl₃ is known for its limited absorption and PL capabilities in the UV region. Through impurity ion doping, we extended the PL into the visible (VIS) region, observing distinct and sharp PL peaks at 598, 616, and 700 nm. Our investigation focused on understanding the mechanistic transfer processes from the band edge of the host material, CsPbCl₃, to the dopant europium ion (Eu³⁺), utilizing advanced techniques like femtosecond fluorescence upconversion and transient absorption (TA) spectroscopy. We observed a fascinating defect-mediated cascading energy transfer from CsPbCl₃ to Eu³⁺, along with intriguing cross-relaxation interactions among different states of Eu³⁺, revealing two distinct characteristics. One of these characteristics, arising from magnetic dipole-assisted (MD) decay, exhibited rapid growth at 592 nm. The other, attributed to electric dipole (ED) transition, displayed slower growth at 616 nm. Additionally, our TA studies provided compelling evidence of charge transfer occurring from the band edge of CsPbCl₃ to shallow defect states induced by the Eu³⁺ doping. Notably, our study observed two-photon

absorption without compromising the efficiency of energy and charge transfer processes. This result indicates that Eu-CsPbCl₃ not only exhibits PL in the visible region but also has the potential to harness the solar energy spectrum within this range. By effectively utilizing visible and UV wavelengths, this material holds significant promise for advancing solar energy conversion and driving substantial progress in optoelectronic applications.

In **Chapter 7**, our focus shifted to Eu-doped CsPbBr₃, exploring how doping affects a different halide family member, namely CsPbBr₃. This investigation involved a comprehensive analysis of the spectroscopic properties of CsPbBr₃ and Eu-CsPbBr₃. In this study, we conducted an excitation energy-dependent study and observed that the doped counterpart exhibited significantly slower cooling and recombination, in contrast to what was observed in the case of CsPbCl₃. It's interesting that the polaron's formation and decay times weren't affected. The low-temperature transient studies suggested that this slow cooling was an outcome of absent bound excitons as a result of Br⁻ vacancy passivation. Studies using optical pumps and THz probes showed that this phenomenon also had an impact on carrier mobility and photoconductivity; as a result, we observed increased photoconductivity and slower transient carrier mobility in Eu-CsPbBr₃. The conclusions gathered from our study show that Eu-CsPbBr₃ is a better contender for photovoltaic applications due to its slower hot carrier cooling and improved photoconductivity.

Chapter 8 concludes the thesis and presents future perspectives for enhancing perovskite-based photovoltaic devices. The findings of this study pave the way for advancements in solar cells, photodetectors, ultrafast devices, and photo-transistors. These insights into photophysics will definitely assist in the development of improved technologies in the field, offering exciting possibilities for further research and innovation.

Chapter 1

Introduction

1.1 Motivation

“The future of energy generation is being written by photovoltaics, where solar power becomes the norm, not the exception.”

The global energy demand has witnessed an exceptional surge, reaching new heights with each passing year. This exponential increase in energy consumption has become a defining characteristic of our modern world. As populations grow, industries expand, and technology advances, the thirst for energy becomes insatiable. Energy has become an integral part of our daily lives, from powering our homes and businesses to fueling transportation.^{1,2}

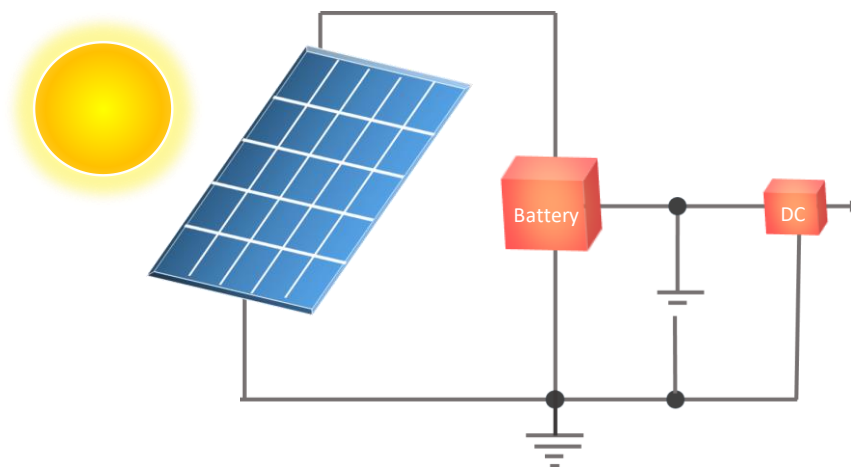


Figure 1.1 The schematic representation explaining the concept of a solar cell.

This escalating demand presents us with both challenges and opportunities as we strive to meet the growing energy needs while ensuring a sustainable and secure future for generations to come. Unleashing the supremacy of the sun, solar energy arises as the driving force behind a greener and brighter future.^{3,4} With a growing urgency for renewable resources, our motivation to

embrace solar power knows no bounds. It's a revolution fueled by the desire to break free from traditional energy restraints and embrace the boundless potential of the sun. With every ray of sunlight harnessed (**Figure 1.1**), we take a step closer to a sustainable tomorrow, where clean energy powers our homes, fuels our industries, and illuminates our world.⁵⁻¹²

The pursuit of a sustainable energy future hinges on the energy efficiency, financial viability, and environmental implications of photovoltaic technology, driving the motivation behind ongoing research. While crystalline silicon cells currently dominate the market with their high power conversion efficiencies, further improvements are limited, and their production entails significant energy consumption and greenhouse gas emissions. Therefore, the search for alternative light-absorbing materials that are cost-effective and require less energy input has become paramount. Exploring innovative concepts like tandem cells holds the promise of achieving even higher efficiencies. Hybrid metal halide perovskites, in particular, offer great potential for advancing the performance and reducing the cost of photovoltaic devices, paving the way for a brighter and more sustainable future.^{13,14}

1.2 From Discovery to Dominance: The Evolution of Perovskite and Its Structural Marvel

Perovskites: Redefining what's possible in solar energy

1.2.1. Dominance of Perovskite in Photovoltaics

From a visionary breakthrough to soaring efficiency: witness the astounding journey of organic-inorganic lead halide perovskite solar cells (PSCs) in the realm of photovoltaics (PV).¹⁵⁻²⁰ Since the first ground breaking research in 2009,²¹ from experiments dating back to 2005, PSCs have skyrocketed in power conversion efficiency (PCE), hitting a staggering 31.25 % (as per the national renewable energy laboratory (NREL), **Figure 1.2**) a feat on par with silicon based solar cells. But it's not just the remarkable performance; it's the game-changing, cost-effective, solution-based processes used in their creation that unlock the boundless potential of PSCs as the PV technology of tomorrow. The remarkable appeal of perovskite solar cells extends far beyond their exceptional performance. Their unique ability to combine high efficiency with cost-effective solution-based fabrication processes sets them apart from other solar cell materials.²²⁻²⁴ This captivating combination underscores the immense potential of perovskites as the future of photovoltaic technology.²⁵⁻³⁰

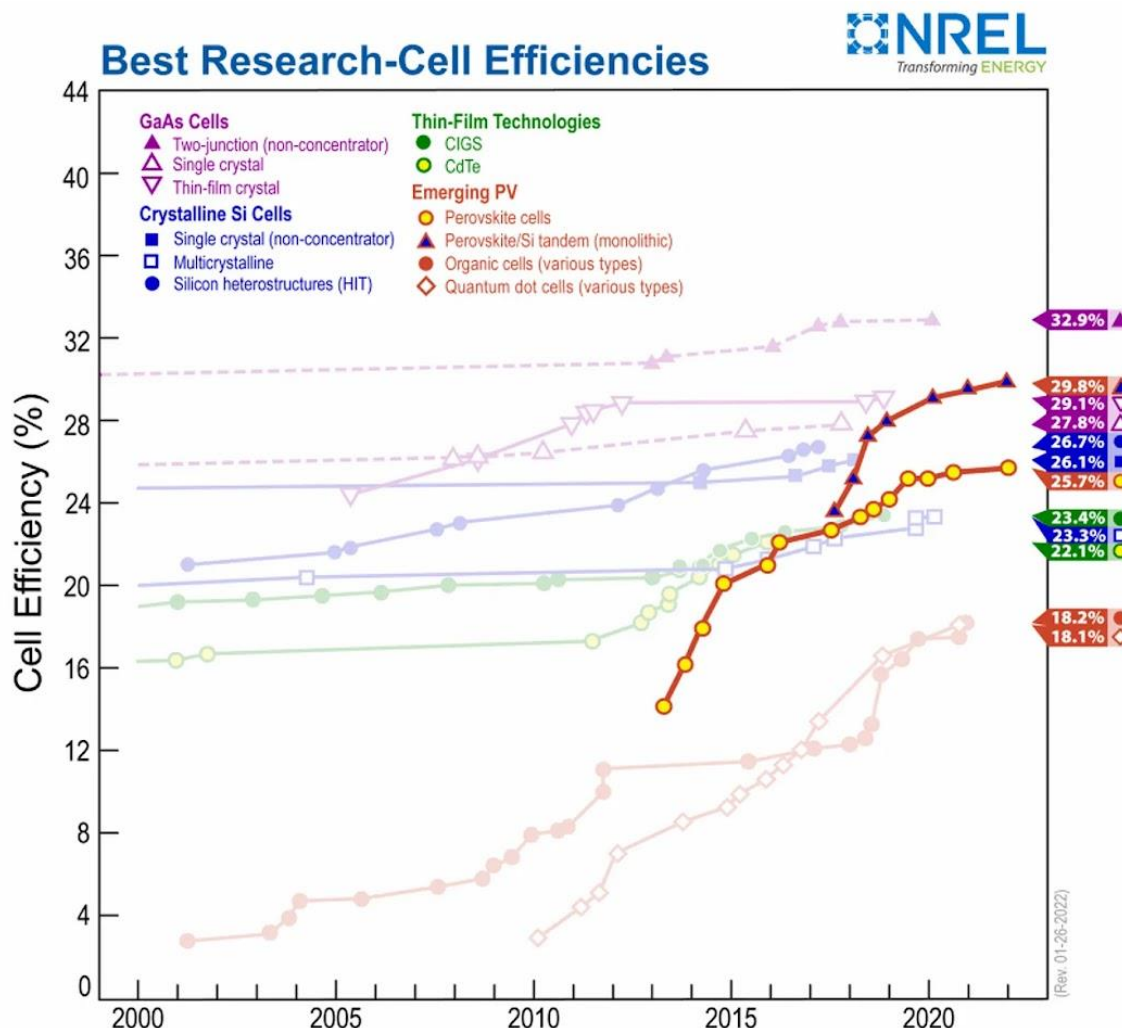


Figure 1.2 The solar cell efficiency chart (U.S., National Renewable Energy Laboratory (NREL), <https://www.nrel.gov/pv/assets/pdfs/pvefficiencychart.201812171.pdf>).

By leveraging their affordability and remarkable performance, perovskite solar cells hold the key to unlocking a new era of sustainable energy generation. Thus, understanding the origin and basics of perovskite becomes essential.^{31,32}

1.2.2. Discovery of Perovskite

The journey of perovskite research commenced in 1839, as Gustav Rose, a Prussian mineralogist, discovered perovskite calcium titanate (CaTiO_3), in a piece of chlorite-rich skarn, marking its introduction in the field of minerals.³³ The mineral was named in honor of the distinguished Russian mineralogist Count Lev A. Perovski upon the request of a eminent Russian mineral collector, August Alexander Kammerer.^{2,34} In general, perovskite crystal

exhibits the chemical formula ABX_3 , where A and B represented cations, and X represented an anion. The ideal cubic structure of perovskite consisted of the B cation surrounded by an octahedron of anions, with 6-fold coordination. The A cation, on the other hand, had 12-fold cuboctahedral coordination. In the cubic unit cell, A cations are present at the corner positions, B cations sat at the body-center position, and X anions occupied the face-centered positions. The exploration of "halide perovskites," another member of the perovskite family, commenced with notable studies in the 1890s. Wells et al. conducted an extensive investigation in 1893, exploring the synthesis of lead halide compounds.³⁵ They experimented with solutions containing lead halide and cesium ($CsPbX_3$) where X represents Cl, Br, or I.³⁶ In 1957, C. K. Møller made noteworthy advancements in the field, unveiling that compounds such as $CsPbCl_3$ and $CsPbBr_3$ displayed the perovskite structure.³⁷ Notably, these compounds existed in a tetragonally distorted form, which underwent a transformation into a pure cubic phase at elevated temperatures. However, despite this breakthrough, these compounds initially did not receive much attention. It was not until the remarkable advancements in perovskite solar cell performance that the field of perovskite research gained continuous attention and began to flourish. Fast forward to 2005, the term "perovskite solar cell" was still unfamiliar to most people. However, it was during this year that the exploration to PV applications of halide perovskites began at the Miyasaka laboratory at Toin University, Yokohama, Japan. Since 2005, the understanding and research on perovskite solar cells have progressed significantly, and in 2009, Miyasaka and his colleagues made a pioneering breakthrough by showcasing the application of perovskite materials in solar cells. They utilized $CH_3NH_3PbX_3$ as a sensitizer in dye-sensitized solar cells (DSSC), achieving an impressive power conversion efficiency (PCE) of 3.81%.²¹ This demonstration marked an important milestone in the utilization of perovskite materials for solar energy conversion.³⁵ Since that pivotal breakthrough, the progress of perovskite solar cells has been nothing short of remarkable. In a relatively short span of time, by the year 2023, the efficiency of perovskite solar cells has skyrocketed to approximately 31.25% (according to the records accessed from NREL).³⁸ This achievement places perovskite solar cells on par with traditional crystalline silicon-based solar cells in terms of efficiency. Such remarkable growth in the performance of perovskites has positioned them as standout contenders in the arena of photovoltaics. The unprecedented growth in the performance of perovskite solar cells sparked immense interest and accelerated research efforts in the field.

1.3 The Structure and Stability of Metal Halide Perovskites

The perovskite structure can be described by its chemical formula ABX_3 (X- Cl, Br, and I) (**Figure 1.3 A**), where, the B cations are enclosed by an octahedral arrangement of X anions. These octahedra share corners, creating a three-dimensional network or framework (as depicted in **Figure 1.3 B**). The A cations are located in the spaces between these octahedra. One way to visualize the perovskite structure is as a framework of BX_6 octahedra with A cations occupying the voids within this framework. BX_6 octahedral network in perovskite materials plays a vital role in determining their phase transitions, bandgap characteristics, and transport properties.³⁹

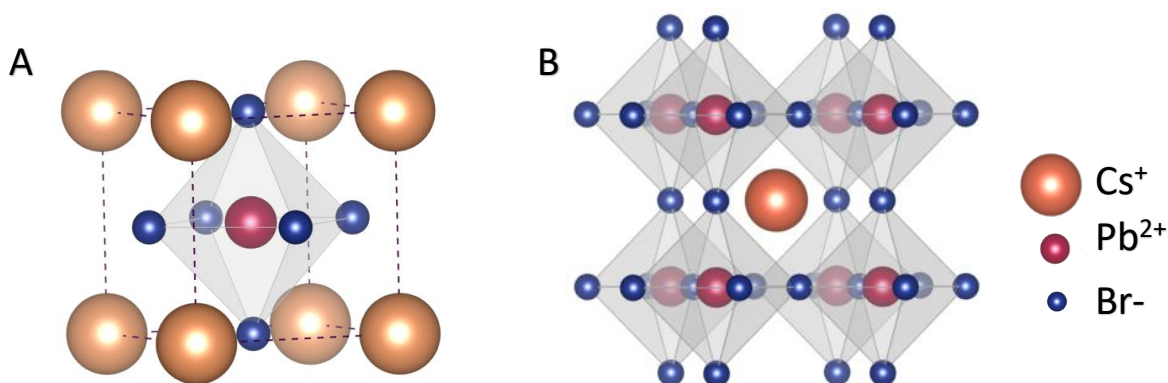


Figure 1.3 Schematic representation of (A) Perovskite structure (ABX_3 where A stands at the corner position, B is present at the body center position and X is at faces), (B) octahedral sites.

By manipulating and engineering the octahedral arrangement, the properties of perovskites can be easily tailored to enhance their performance in various applications. Perovskite semiconductor materials are produced by introducing substitutions and variations in the molecular stoichiometry of each component during synthesis. To assess the structural integrity of perovskite materials, two key empirical parameters are considered: The Goldschmidt tolerance factor (t) and the octahedral factor (μ). These parameters provide valuable insights into the stability and characteristics of perovskite structures.^{39,40}

$$t = \frac{R_A + R_X}{\sqrt{2}(R_B + R_X)} \quad \text{Eq.1.1}$$

$$\mu = \frac{R_B}{R_X} \quad \text{Eq.1.2}$$

here r_A , r_B , and r_X denote the corresponding ionic radii of ions A, B, and X. In an ideal perovskite with a cubic structure, t is equal to 1. Perovskites can generally be formed within the range of $0.8 < t < 1.0$. To provide a clearer understanding of the formation of ABX_3 perovskites a tolerance factor and octahedral factor can be plotted on 't- μ ' graphs (Figure 1.4) to assess the stability of a perovskite structure, and it was concluded that the stable region for halide perovskite falls within the ranges of $0.813 < t < 1.107$ and $0.377 < \mu < 0.895$.³⁹ The tilting of BX_6 octahedra in perovskite structures plays a crucial role in determining the crystal symmetry and properties of the material. Small deviations from the ideal perovskite structure, typically within the range of $t = 0.8$ to 1.1, can still maintain the typical perovskite ionic coordination. However, these deviations result in a lowering of symmetry, leading to tetragonal, orthorhombic, or monoclinic unit cells.

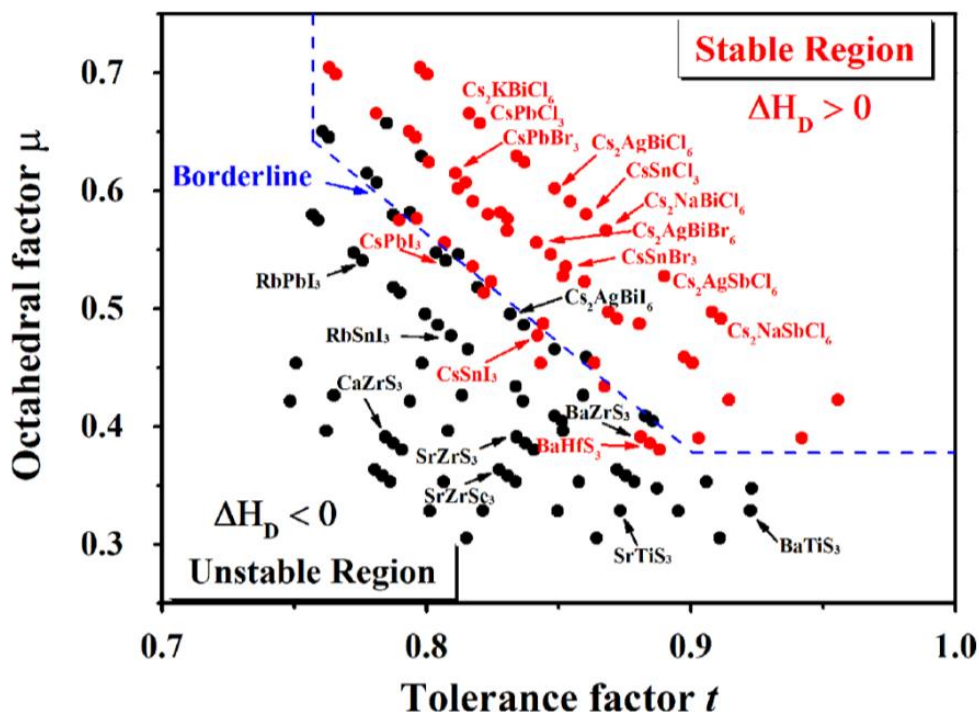


Figure 1.4 Presents a map illustrating the tolerance factor-octahedral factor (t - μ) relationship for several halide perovskite compounds. "Reprinted (adapted) with permission from ref {39} copyright {2017} American Chemical Society."

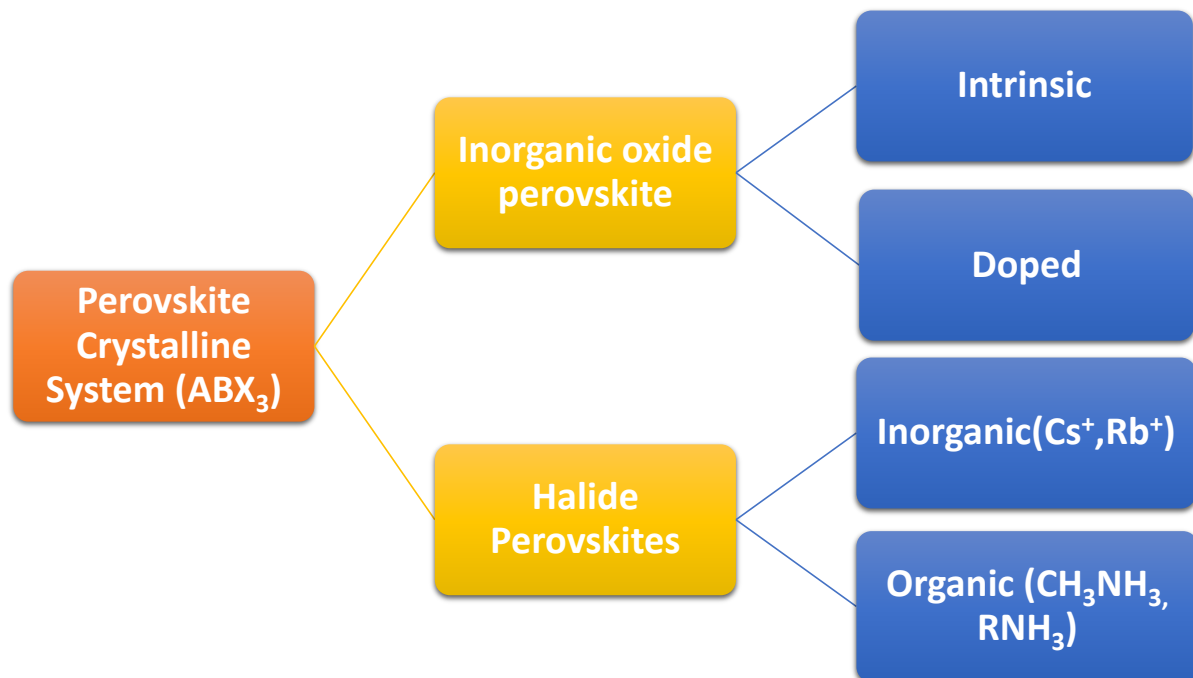


Figure 1.5 Classification of perovskite system

Halide perovskites are indeed considered to be both organic and inorganic in nature (**Figure 1.5**). They are classified as hybrid materials due to their composition, which includes both organic and inorganic components. The organic component typically consists of small organic cations, including methyl ammonium (MA) or formamidinium (FA), while the inorganic component comprises metal cations and halide anions.⁴¹ Moisture and temperature can cause rapid degradation of these perovskite materials.^{42,43} The central difficulty in the usage of these organic perovskites is their tendency to degrade, which poses a significant obstacle to achieving long-term stability. To overcome this problem, an alternative approach is proposed, which involves substituting to all-inorganic cesium lead halide (CsPbX_3) perovskites. By using all-inorganic perovskites, it becomes possible to combine high optoelectronic performance, such as achieving solar cell PCE ~21%,^{44,45} with a significant improvement in environmental stability. In this thesis, the focus was on investigating the properties and characteristics of inorganic cesium lead halide perovskites.

1.3.1. Inorganic Lead Halide Perovskites

In the realm of scientific exploration, the journey of all-inorganic CsPbX_3 perovskites began in the depths of the 1890s. It wasn't until the 1950s when Muller shed light on their crystal structure and photoconductivity, unraveling their hidden mysteries.³⁹ The choice of the

inorganic lead halide cation can be either Cs or Rb. The relatively smaller size of the Rb as compared to the Cs results in a reduced tolerance factor. Consequently, perovskites that incorporate Cesium cation at the A-site exhibit significantly higher stability than those with Rb cation.

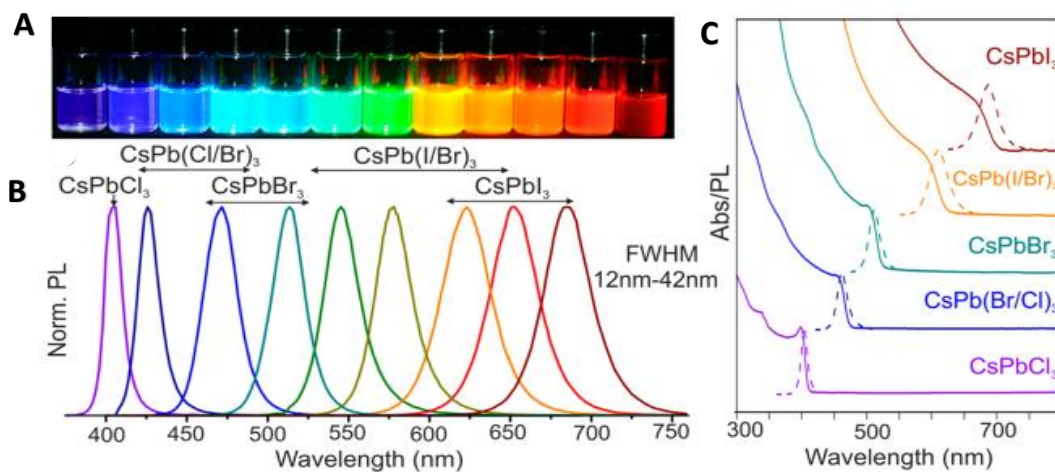


Figure 1.6 (A) Under the illumination of a UV lamp, the colloidal solutions of CsPbX₃ NCs (X = Cl, Br, I) in toluene are visually depicted, (B) the PL spectra of CsPbX₃ NCs, (C) the optical absorption and PL spectra. “Adapted from ref {46} *Nano Lett.* 2015, 15, 6, 3692–3696. © 2015, American Chemical Society”.

Moving forward in 2005, Kovalenko and his collaborators pioneered a groundbreaking feat and pioneered the synthesis of all-inorganic cesium lead halide colloidal NCs,⁴⁶ steering a new era of precision and control over the nano-sized perovskite structures. These NCs exhibit remarkable characteristics, including an astounding photoluminescence quantum yield (PLQY) of up to 90%. Not only can their PL be finely tuned across the entire visible spectrum, but their emission bandwidth is also significantly reduced through ingenious composition modulation, as vividly illustrated in **Figure 1.6. (A, B)**. While the manipulation of nanocrystal size allows to alter the bandgap (as shown in **Figure 1.6. C**) within the realm of quantum confinement, the ability to precisely vary the bandgap across the full visible range represents a remarkable opportunity in the field of photovoltaics. This newfound capability opens up exciting possibilities for pushing the boundaries of optical applications and unlocking the true potential of these all-inorganic cesium lead halide colloidal NCs. Within the group of inorganic lead halide perovskites, three significant perovskite materials are CsPbCl₃, CsPbBr₃, and

CsPbI₃. Under standard conditions, CsPbI₃ exhibits an orthorhombic structure with a tolerance factor (t) of 0.81, CsPbBr₃ adopts an orthorhombic structure with a tolerance factor of 0.86, and CsPbCl₃ maintains its stability in a cubic phase and exhibits a tolerance factor of 0.87. The Bohr diameters and binding energies for the Wannier-Mott excitons in CsPbCl₃, CsPbBr₃, and CsPbI₃ are as follows: CsPbCl₃ (5 nm and 75 meV), CsPbBr₃ (7 nm and 40 meV), and CsPbI₃ (12 nm and 20 meV).⁴⁶ The energy band gap (E_g) amid the valence and CBs determines the material's electrical properties. The variation in the band gap of lead halide perovskites (**Figure 1.7 A**) can be attributed to the alterations in the binding energies of the halide p-orbitals. In the case of lead halide perovskites, the valence band (VB) is mainly composed of the atomic orbitals of the halide ions, specifically the p orbitals. These orbitals overlap with the 6p and 6s orbitals of the lead (Pb) ions (**Figure 1.7 B**). On the other hand, the conduction band (CB) is formed by the combination of certain hybridized orbitals. In particular, the Pb 6p - I 5s σ^* and Pb 6p - I 5p π^* orbitals contribute to the formation of the CB (**Figure 1.7 A**).^{47,48} By altering the halide precursors stoichiometry, the composition of the perovskite can be modified, leading to changes in the binding energies of the halide orbitals. These changes affect the separation between the VB and CB, thereby altering the band gap as shown in **Figure 1.7**.

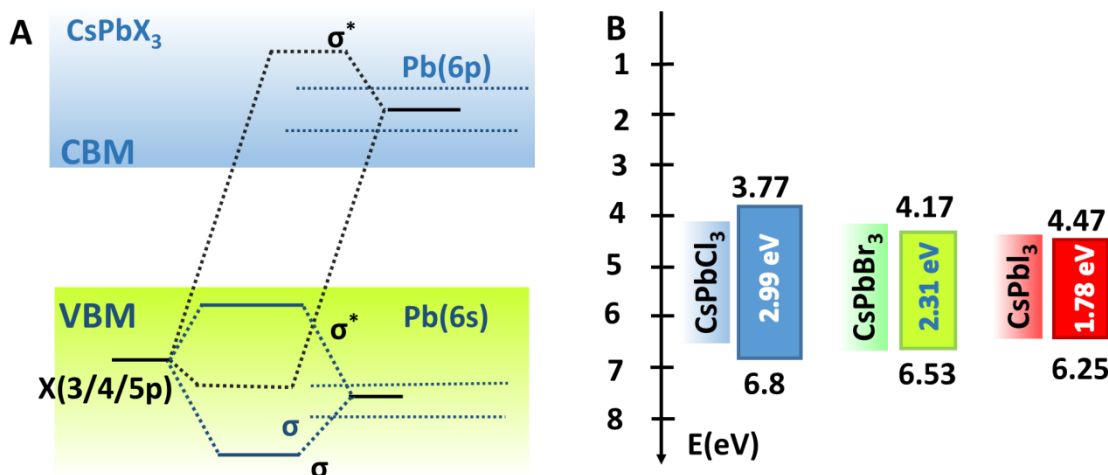


Figure 1.7 (A) The schematic representation of the electronic structure of defect tolerant perovskite, both the VB and CB are created through antibonding orbitals, and **(B)** the band gap of all inorganic lead halide perovskites i.e., CsPbX₃ (X-Cl, Br, I)

The larger Goldschmidt tolerance factor of CsPbCl₃ compared to CsPbBr₃ and CsPbI₃ contributes to its cubic phase stability.⁴⁹ Despite CsPbCl₃ having a high band gap, it holds

significant promise for integration with complementary materials. Additionally, doping with impurity ions could greatly extend its PL into regions beyond the ultraviolet (UV) spectrum, thus rendering it suitable for utilization in photovoltaic applications. While CsPbBr₃ is a robust perovskite material that maintains stability in the presence of air and moisture, along with efficient absorption across a wide range of solar radiation wavelengths. Although CsPbI₃ possesses the narrowest band gap compared to other perovskite counterparts, it holds immense promise as an excellent candidate for solar cells due to its well-suited band gap that enables the effective harnessing of a broad solar spectrum. However, CsPbI₃ encounters obstacles stemming from its low tolerance factor (0.81) and degrades quickly with moisture or fluctuations in temperature.^{50,51} Thus, CsPbBr₃ and CsPbCl₃ perovskite materials have received substantial consideration in the field of optoelectronic devices due to their thermal and moisture stability. As a result, they hold great promise for applications in devices operating under challenging thermal conditions or in humid environments.

1.3.2. Phase Transitions in Inorganic Lead Halide Perovskites

The thermal expansion causes a continuous change in the volume of the perovskite unit cell by altering the lengths of internal bonds at different rates.^{52,53} This thermal response imposes limitations on the temperature ranges in which a stable perovskite phase can exist. Specifically, for a given composition, the formation of a stable perovskite phase is restricted to certain temperature ranges.^{54–56} The perovskites NCs exhibit different phases (**Figure 1.8**) i.e., cubic, orthorhombic, monoclinic, and tetragonal.

At room temperature, perovskite materials typically exist in either the cubic or tetragonal form. However, as the temperature changes, several factors come into play, leading to phase transitions within the material. One crucial factor is the tilting of octahedra within the perovskite structure.⁵⁷ The size and arrangement of the atoms within the crystal lattice cause the octahedra to tilt, affecting the overall symmetry of the material. As temperature increases or decreases, the tilting of the octahedra can become more pronounced or less pronounced, respectively. Moreover, as the temperature is lower, the thermal energy reduces, resulting in the softening of phonons. This softening refers to a decrease in the energy required to excite these vibrational modes. Thus, such factors lead to a temperature-dependent phase transition in perovskite. Such transition is observed in CsPbCl₃, above 200 K, the phase transitions

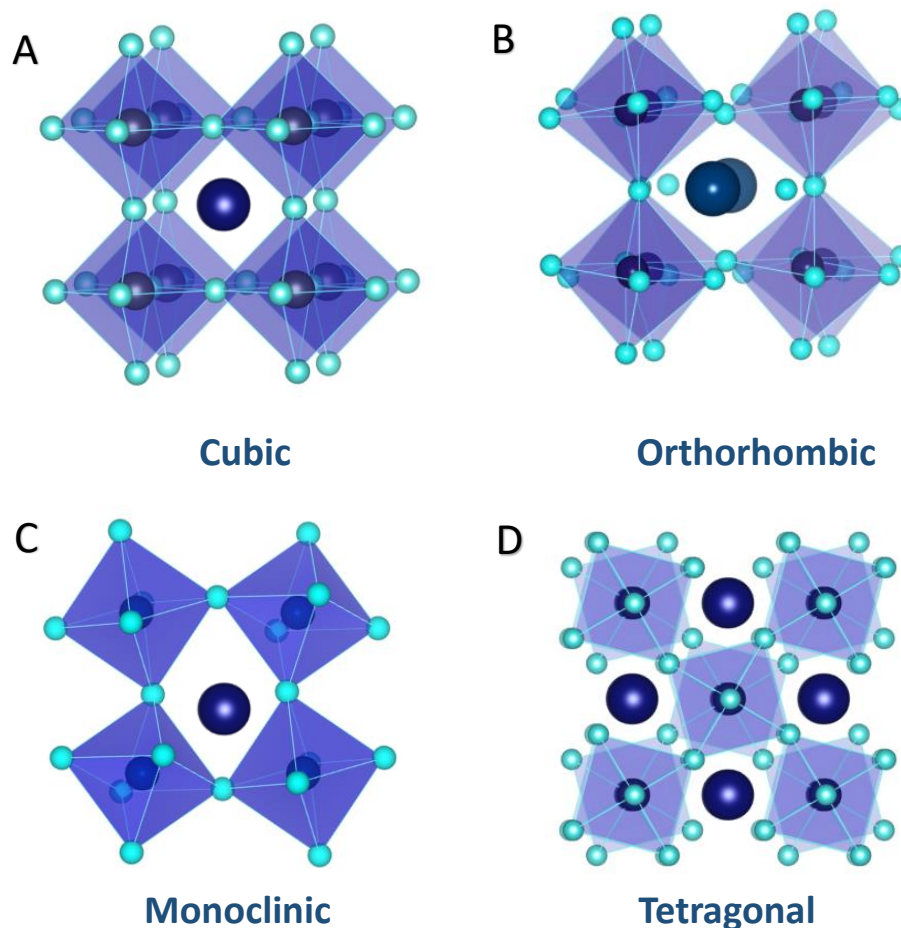


Figure 1.8 The crystal structures of different phases of perovskites (A) Cubic, (B) Orthorhombic, (C) Monoclinic, and (D) Tetragonal.

observed in CsPbCl_3 are classified as first-order transitions, which arise from the condensation of rotational modes of PbCl_6 . However, when the temperature reaches 200 K, a second-order phase transition occurs in CsPbCl_3 .⁵⁸ This transition is characterized by the participation of an elastic soft mode. As the temperature is further lowered to 200 K, CsPbCl_3 undergoes a distinct phase transition, transitioning from the orthorhombic phase to the monoclinic phase.⁵⁹ In CsPbI_3 the transition temperatures between the characteristic low-temperature (LT) non-perovskite (yellow in color) and the high-temperature (HT) perovskite phase (black in color) for CsPbBr_3 phase transition occurs at temperatures well above room temperature (RT), specifically above 315 °C.

1.3.3. Doping of Impurity Ions in Perovskites

Doping the lattice of MHP with impurity ions has emerged as a powerful tool, going beyond structural perfection and differences in composition, to modify numerous properties of halide perovskites while preserving their intrinsic properties.^{60–65} In recent years, there has been a significant advancement in our understanding of doped halide perovskites.

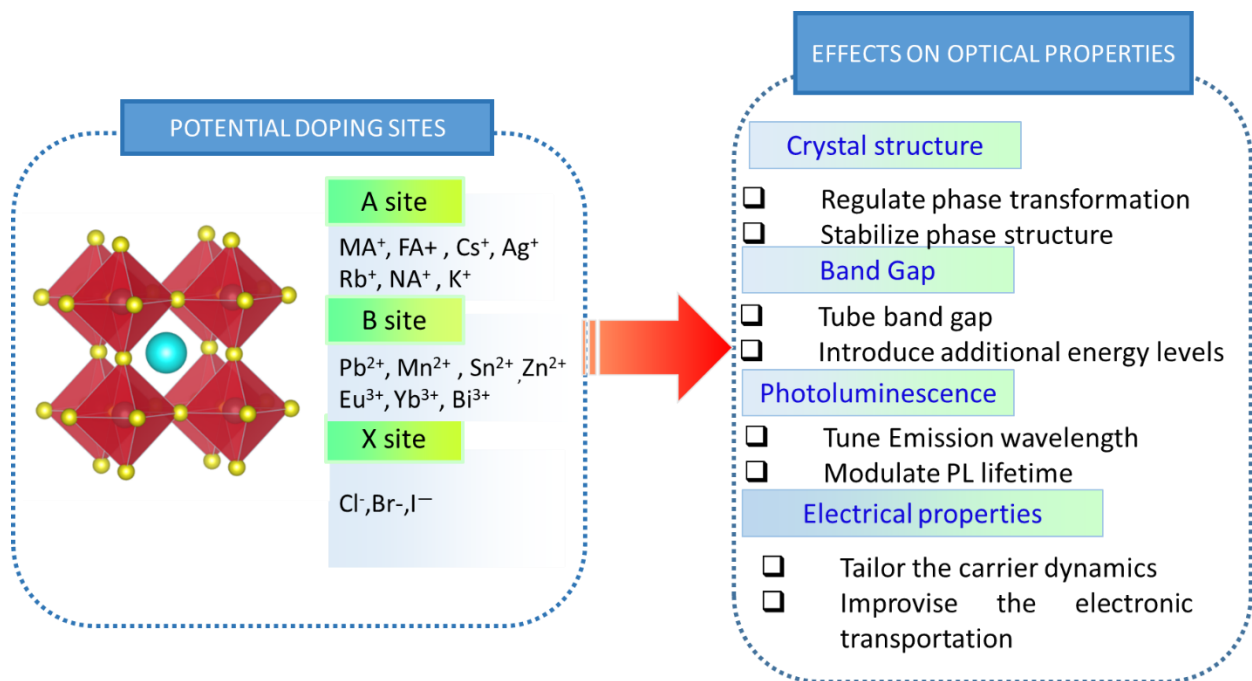


Figure 1.9 Schematic representation of the possible doping sites in ABX₃ Perovskites and their impact on the intrinsic properties of the material.

These doped materials display unique optical and electronic characteristics compared to their undoped counterparts, resulting in enhanced performance of perovskite optoelectronic devices. As we delve into the topic of doping in MHP, important questions emerge: What are the most effective doping frameworks for altering the density of carriers in hybrid organic/inorganic perovskites? How does the doping in MHPs differ from traditional purely organic or inorganic systems? In MHPs, doping can be categorized as substitutional or alloying, depending on the position of the dopant impurity ion on the A, B, or X sites as shown in **Figure 1.9**. The choice of halide or pseudo-halide affects the band structures, while A-site cations have deeper positions in the bands while B-site doping allows for tuning carrier concentration and Fermi level.^{66,67} The effect of doping at B-site effects the electronic structure, especially near the CB and VB edges, and is a crucial factor for effective doping.⁶⁸

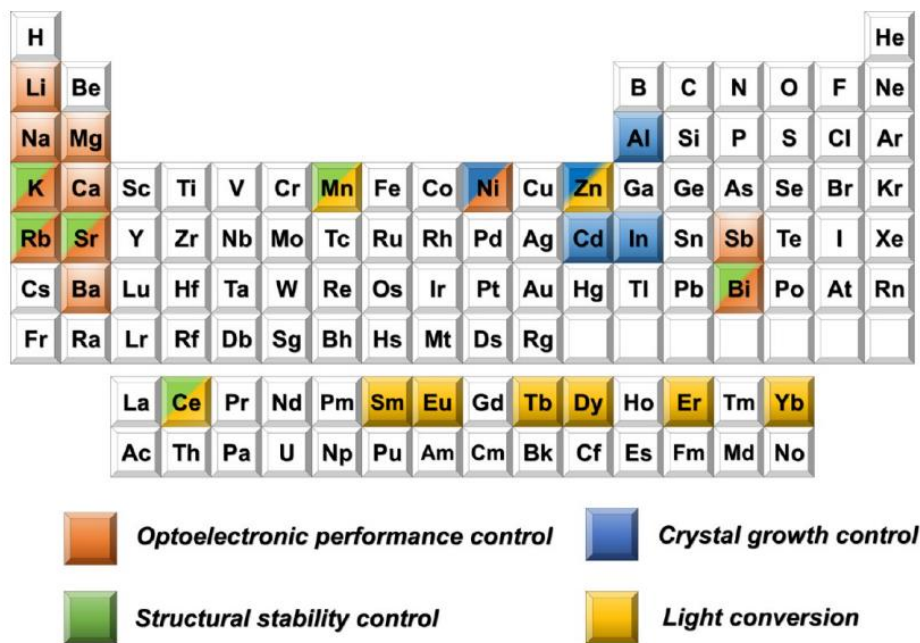


Figure 1.10 The metal elements which can be doped in perovskites and their main roles in altering lead halide perovskites. “Adapted from ref {60} Copyright Chem. Mater. 2018, 30, 6589-6613 American Chemical Society”.

Figure 1.10 of the periodic table showcases the metallic elements that have been incorporated as dopants in halide perovskites. These elements are categorized by different colors: orange, blue, green, and yellow. Each color assigned here represents a specific function related to performance in photovoltaic devices, growth of crystal, stability of structure, and light conversion in lead halide perovskites, respectively. Recent advancements have allowed us to differentiate these metals based on their main roles. Notably, metallic elements like Mn, Sr, Rb and Bi, which are manifested with two colors, are effective as dopants in halide perovskites.^{69–77}

A-site doping

The selection of A-site cations in MHP is vital for maintaining the integrity of the [BX₆] framework.^{64,65,69,70,77,78} An imbalance in the size of the cations, whether they are too large or too small, can lead to distortions or even a complete breakdown of the cubic-like crystal structure. Generally, the universal A-site cation consists of organic MA⁺ (methylammonium, 2.70 Å), FA⁺ (formamidinium, 2.79 Å), and inorganic Cs⁺ (cesium, 1.88 Å). According to equation 1.1, it is evident that the size of MA⁺ cation is reasonably ideal for the cubic perovskite

structure in contrast to FA^+ and Cs^+ . Nonetheless, perovskite structures based on MA^+ often exhibit inadequate thermal stability due to the inclusion of organic components. To address this issue, all-inorganic perovskite NCs have been developed by incorporating Cs^+ as an inorganic cation. Introducing other inorganic ions with smaller radii, such as Rb^+ or K^+ , does not solve the stability problem. The combination of larger and smaller ions as mixed A-site cations shows promise in achieving a balanced and stable perovskite structure.^{79,80}

B-site doping

Unleashing the potential of B-site cations in lead halide perovskites is a tantalizing challenge, where they must meet the criteria of tolerance (t) and octahedral factors (μ). While exploring alternatives to lead, options for three-dimensional structures remain limited. Yet, the right cationic substitution not only ensures structural stability but also ignites a captivating interplay of luminescence and electronic properties. Despite the challenges in developing lead-free perovskites, the incorporation of small amounts of dopants has shown promising results in enhancing stability and optical properties. Furthermore, it has been vividly known over years, various metal ions, including Mn^{2+} , Bi^{3+} , Sn^+ , and rare earth ions such as Ce^{3+} , Tb^{3+} , and Eu^{3+} ,^{73–75,81–83} have been successfully doped into halide perovskites, leading to the emergence of various properties such as high PL lifetime, introduced defect states, improvised PLQY. In contrast to the A-site, the process of doping the B-site in perovskite lattices presents more obstacles and holds a crucial role in determining phase stability as it directly alters the octahedra $[\text{BX}_6]$.

X-site doping/exchange

By tuning the halogen in the X-site, a wide array of light emissions can be achieved in perovskite materials. Formation of deep trap states in MHPs is challenging due to their significantly higher formation energy. Instead, shallow defects related to vacancies are more prevalent, characterized by antibonding in the VB (involving 3/4/5p orbitals of halide and 6s orbital of Pb) and effect of spin-orbit in the CB (dominated by Pb 6p orbitals). As chloride or bromide-based perovskites emit blue light, bromine-based perovskites emit green light, and iodine or iodine/bromine-based perovskites emit red light.⁴⁶ The combination of A-site and X-site regulation offers abundant possibilities for controlling and fine-tuning light emission properties. Furthermore, surface defects are commonly found in MHP NCs, and to mitigate their impact, alternative strategies frequently employed is X-site doping. These

approaches help in surface passivation and reduction of nonradioactive states. The X-site doping leads to passivation of the halide vacancies which in turn increases the PL lifetime.

1.4 Fundamental photo physical phenomena in perovskites

To comprehend the photophysics of perovskites, it is crucial to establish a solid understanding of their electronic band structure. The electronic band structure dictates the behavior of electrons within a material, specifically their energy levels and allowed transitions. The electron energy levels in solids exhibit distinct characteristics compared to those of single atoms due to the crystal's periodicity and the involvement of a large number of atoms. This leads to the formation of a band structure consisting of a range of energy states rather than discrete levels. The VB and CB, among the various bands present, play a significant role in defining the electronic and optical properties of a material. The VB accommodates tightly bound electrons, while the CB represents energy levels that allow for greater electron mobility. These bands collectively govern the majority of electronic and optical behavior observed in materials. Although the following description primarily applies to crystalline solids, it still holds valid qualitative implications for other types of solids. Understanding the band structure is crucial for comprehending the electronic characteristics of materials and serves as the foundation for developing advanced electronic devices and technologies.

By delving deeper into the intricate details of their band structure, researchers can uncover the underlying mechanisms behind the photophysical phenomena exhibited by perovskite materials.⁸⁴⁻⁹⁴ This knowledge serves as a solid foundation for further exploration and advancement of perovskite-based devices and applications, ultimately driving the progress of renewable energy, lighting, and optoelectronics fields.

1.4.1. Electronic Band Structures

To describe electron properties in a solid, the time-dependent Schrödinger equation is solved under a periodic potential $V(r)$. This potential, varying periodically in space, influences the behavior and energy levels of electrons, revealing insights into the electronic structure of solids.⁹⁵

$$H\Psi(r) = \left(-\frac{\hbar^2}{2m}\Delta^2 + V(r)\right)\Psi(r) = E\Psi(r) \quad \text{Eq 1.3}$$

Where H represents the Hamiltonian operator associated with the total energy of the system, ψ corresponds to the wave function, \hbar denotes the reduced Planck constant, "m" denotes the mass of the electron, and "E" represents the energy associated with the electron.

It is important to switch from the real-space coordinate system to the reciprocal space, also known as k-space, in order to accurately solve the Schrödinger equation. During this transition, a real-space lattice is subjected to a Fourier transformation, producing a lattice representation in reciprocal space. A vector $G = hg_1 + kg_2 + lg_3$ represents the reciprocal lattice, where g_i stands for the base vectors and h, k, and l are the Miller indices related to this lattice structure.^{95,96}

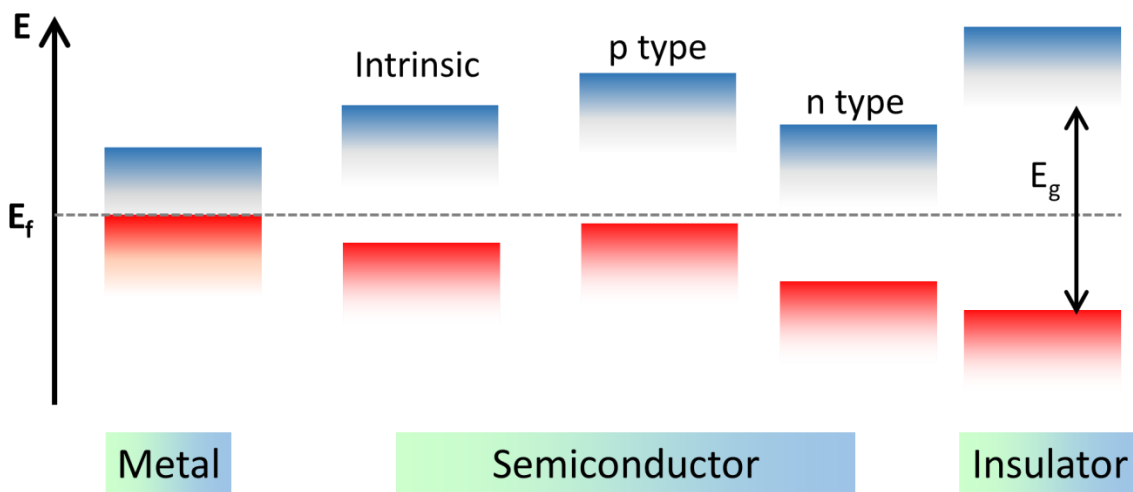


Figure 1.11 The schematic illustrated energy diagrams of metal, insulator, and semiconductors.

In the context of a periodic potential, a solution to the Schrödinger equation manifests as a modulated plane wave, commonly known as a Bloch wave.

$$\Psi(\mathbf{k}) = \Psi_{\mathbf{k}}(\mathbf{r})e^{i\mathbf{k}\cdot\mathbf{r}} \quad \text{Eq 1.4}$$

where $\Psi(\mathbf{k})$ represents a periodic function which exhibits the periodicity of the lattice and $\exp(i\mathbf{k} \cdot \mathbf{r})$ is a plane wave with wavevector \mathbf{k} . where \mathbf{k} is the wave vector, which varies depending on the values of $k_i = 0, 2\pi/L, 4\pi/L, \dots$ with $i = x, y, \text{ and } z$, and L is the crystal's macroscopic dimension, The voltage $V(\mathbf{r})$ is described by $\Psi_{\mathbf{k}}(\mathbf{r}) = \Psi_{\mathbf{k}}(\mathbf{r} + \mathbf{r}_n)$ which also represents the periodicity of the lattice.

Further, due to the periodicity of the lattice equation 1.3 can be restated as:

$$E(\mathbf{k})_k = E(\mathbf{k})_{k+G} = H_k = H_{k+G} \quad \text{Eq 1.5}$$

Given that $E(\mathbf{k})$ and $E(\mathbf{k}+G)$, or its periodicity, are equivalent, so in order to investigate the entire periodic lattice, it is enough to study $E(\mathbf{k})$ in the first Brillouin zone with bounds $G = \pm 2\pi/L$. The most appropriate term for the energy surface $E(\mathbf{k})$ is the electronic band structure. The characteristics of a solid, whether it exhibits metallic, insulating, or semi-conducting behavior, are determined by the occupancy of the energy bands at a specific temperature and energy gap, as depicted in **Figure 1.11**.

1.4.2. Quantum confinement

Quantum confinement is basically the spatial restriction of electron, hole, or electron-hole pair wave functions to the extent that at least one dimension becomes smaller than the bohr radius. When electrons or holes are confined to a thin semiconductor layer, their behavior undergoes a significant and remarkable change due to the reduction in dimensionality. Further, with the advent of photoexcitation in any system, an array of energy is unleashed, generating an interplay between electrons and holes. These excited electrons and holes bind together and form an exciton. This bound state exhibits similarities to a hydrogen-like system, allowing us to estimate the separation distance between the constituents using the Bohr radius approximation. The exciton Bohr radius (a_e) is the term commonly used to describe this critical equilibrium distance, and it can be quantitatively expressed as:

$$a_B = \frac{ma_0}{\mu} \varepsilon \quad \text{Eq 1.6}$$

where, the symbol a_0 represents the Bohr radius of a hydrogen atom, μ denotes the reduced mass, m signifies the mass of the electron, and ε corresponds to the permittivity. In confined materials, the exciton Bohr radius (a_B) varies for electrons (a_e), holes (a_h), and excitons (a_{ex}). At its core, the concept of spatial confinement suggests that when an electron and a hole are confined within a smaller volume, their likelihood of interacting increases. In bulk materials, energy bands arise from a vast collection of atoms and molecules, resulting in a continuum of states as their energy levels merge. However, in confined NC, the scenario is notably distinct. The reduced size and altered electronic structure of nanostructures give rise to distinct energy levels. With fewer molecular orbitals (MOs) in the crystal, the electronic structure transitions

from a delocalized quasi-continuous band to discrete, separate states, a phenomenon known as quantum confinement.

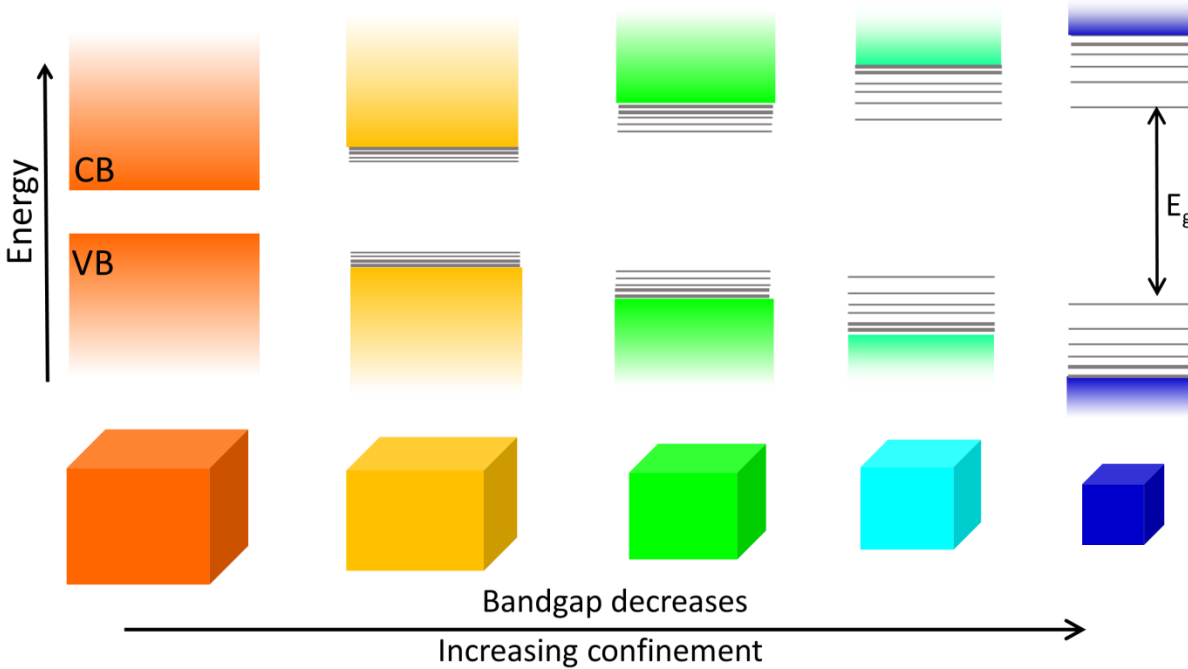


Figure 1.12 The quantum confinement effect in semiconducting NCs, showcasing the increase in the energy bandgap of NCs with confinement.

As depicted in **Figure 1.12** quantum confinement manifests as an increased bandgap and enhanced energy separation of states, particularly at the edges of the energy bands. Therefore, confined materials exhibit a reduced density of states compared to bulk materials.

Density of states (DOS) refers to the quantity of the available energy states within a material or system. It represents the distribution of energy levels and provides insight into the population and accessibility of these states for particles such as electrons. Essentially, DOS (**Figure 1.13**) describes how densely packed the energy levels are in relation to the energy range considered. In bulk semiconductors, the DOS is continuous and exhibits a strong dependence on energy, with the following relation

$$g_{3D}(E) \propto E \tag{Eq 1.7}$$

However, in two-dimensional (2D) quantum confinement or quantum well structures, the DOS is independent of energy. In the case of one-dimensional (1D) quantum wires, the DOS decreases as the energy increases, following the given equation

$$g_{1D}(E) \propto 1/E$$

Eq 1.8

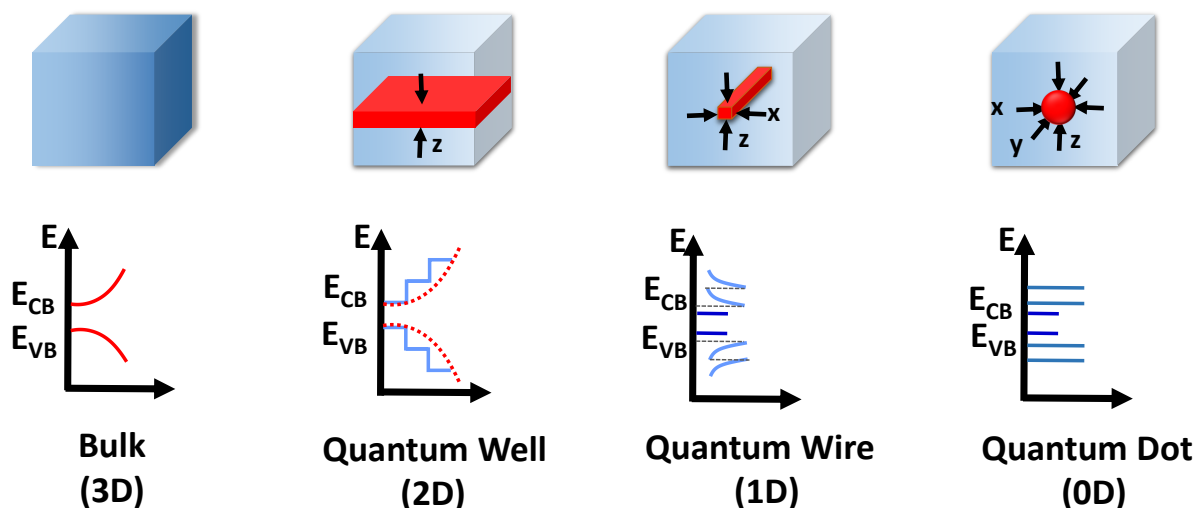


Figure 1.13 Schematic illustration of the density of states in the differently confined materials.

Furthermore, different confinement regions for these confined NCs can be defined based on their size relative to the exciton Bohr radius and the effective radius of each carrier in that particular system (a_h and a_e). In the strong confinement regime, the NC radius (r) is smaller than all three Böhr radii ($r < a_e, a_h, a_e$), resulting in both charge carriers being tightly confined within the NC volume. In the weak confinement regime ($a_e, a_h < r < a_e$), only the motion of the exciton is confined. An intermediate confinement regime occurs when ($a_e < r < a_h, a_e$) either an electron or a hole is strongly confined here.

Low-dimensional nanostructures serve as a bridge between the bulk and molecular domains, offering novel opportunities to harness the intrinsic properties of materials. What sets these nanostructures apart is the ability to modify their intrinsic properties by simply altering the particle size. The NCs with tunable band gap, increased absorption coefficient, high exciton binding energy making them better than bulk counterparts. The confined NCs, with their customizable optical and electronic properties, hold greater demand than bulk materials for a harnessing and manipulating light and electricity in various technological applications.

1.5 Carrier Relaxation Processes After Photoexcitation

As a perovskite absorbs solar radiation in a photovoltaic application, it instigates the generation of electron-hole pairs with energies surpassing the band edge. During the initial stages, these excited charge carriers exist in a non-equilibrium state and undergo a cascade of relaxation processes in order to attain equilibrium near the band edge, as shown in **Figure 1.14**. The process of initial charge carrier relaxation involves multiple stages, each playing a crucial role in the efficient extraction of these carriers. A comprehensive understanding of the behavior and dynamics of charge carriers in this context is of utmost importance.

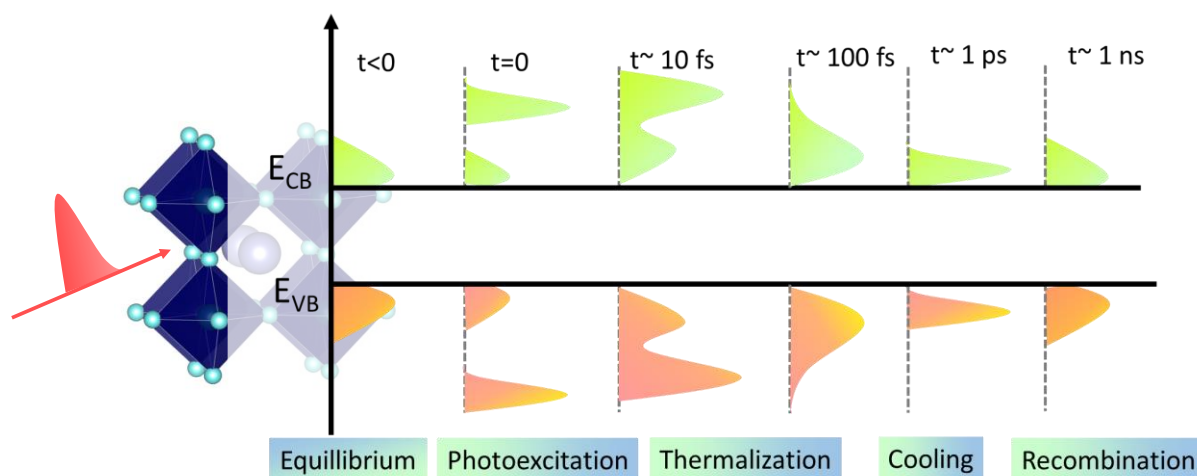


Figure 1.14 The time-dependent carrier relaxation processes in perovskites.

- Following photoexcitation, the photoexcited electron-hole pairs give rise to polarization in the material. Initially, this polarization maintains a coherent phase relationship with different photogenerated states. However, over time, this coherence diminishes due to scattering processes, such as collisions between charge carriers or interactions with phonons. These scattering events disrupt the fixed-phase relationship, ultimately resulting in the loss of coherence within the system.
- After photoexcitation, the initially created nonequilibrium distribution of charge carriers will quickly (with in few picoseconds) undergo relaxation within the electronic bands through carrier-phonon and carrier-carrier scattering. As a result, a thermalized Maxwell distribution will be established, described by carrier temperature (T_c).

- While T_c remains higher in contrast to the lattice temperature, the carriers are considered "hot."
- After the process of thermalization, the high-energy carriers lose excess energy and reach a thermal equilibrium state, the carriers continue to thermalize and equilibrate their temperatures before recombination takes place.

1.5.1. Factors Affecting Carrier Cooling

Carrier relaxation is one of the most decisive factor that significantly influences the performance of devices. To optimize device performance, it is essential to understand and effectively address carrier relaxation. This involves tailoring various factors (**Figure 1.15**) that can impact carrier relaxation dynamics. The carrier cooling process depends on various factors which are detailed here

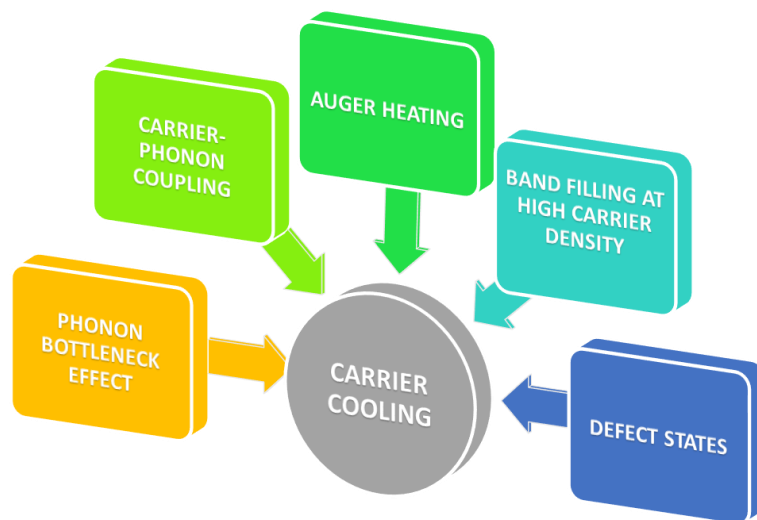


Figure 1.15 Factors affecting the carrier cooling.

1.5.1.1. Phonon Bottleneck Effect

The phonon bottleneck effect (PBE) refers to a phenomenon when the relaxation of hot carriers (excited charge carriers with excess energy) is hindered by the slow thermalization of phonons.⁹⁷ In the PBE, the carrier cooling process is delayed due to the inefficient energy transfer from the hot carriers to the lattice vibrations. The phonon bottleneck effect comes into play when the energy difference amid quantized levels is higher than the longitudinal optical (LO)

phonon. In the process of undergoing thermalization the excited carriers dissipate then energy in form of phonons. However, a non-equilibrium optical phonon population is established if the emission rate of optical phonons by carriers exceeds the decay rate of LO phonons. Consequently, there is an increased likelihood of phonon reabsorption by carriers rather than phonon decay taking place. Consequently, the overall emission rate of phonons decreases, leading to a reduction in the energy loss from the carriers inform of LO phonons.⁹⁷⁻⁹⁹

Table 1.1 Factors affecting the phonon bottleneck effect and their respective mechanism

FACTOR	MECHANISM
1.	CARRIER DENSITY
	Carrier density effects the rate of carrier-carrier and carrier-phonon scattering processes through Fröhlich interaction, decreasing the overall rate of phonon emission. ¹⁰⁰
2.	ELECTRONIC STRUCTURE
	In certain bulk semiconductors, there can be a phenomenon called slow intervalley scattering (IVS) through phonon emission. This IVS process can lead to the trapping of a portion of excited carriers in side valleys, resulting in a reduction of the overall phonon emission rate. ¹⁰¹
3.	PHONONIC STRUCTURE
	A significant phononic bandgap plays a crucial role in partially or completely obstructing the primary Klemens and secondary Ridley decay processes. This obstruction leads to the enhancement or establishment of the Power Balance Efficiency (PBE). ⁸⁸
4.	DIMENSIONALITY ¹⁰²
	The confinement of carriers and phonons in material directly affects the density of states, which, in turn, influences carrier relaxation dynamics. The interplay between confinement, the density of states, and the phonon bottleneck significantly impacts carrier relaxation processes.

In conventional semiconductors, the decay mechanisms of LO phonons to lower-energy acoustic phonons are commonly attributed to the *symmetric Klemens*-decay and *anti-symmetric Ridley*-decay processes.⁹⁸

- The LO phonon will undergo a process called the *Klemens decay*, where it splits into two longitudinal acoustic (LA) phonons. Both these phonons have equal energy but exhibit opposite kinetic momentum. However, this decay is an irreversible dissipation of energy.⁹⁸
- An alternative decay mechanism arises when the LO phonon converts into an LA phonon (longitudinal acoustic) and a TO phonon (transverse optical) via the *Ridley decay*. Although the manifestation of Ridley decay is less probable than the Klemens decay owing to the dissimilarities in energy and momentum between LA and TO phonons, its significance in accelerating the thermalization rate of carriers cannot be dismissed. Therefore, it remains essential to acknowledge the impact of Ridley decay on carrier dynamics and the overall thermalization process.⁹⁹

1.5.1.2. Carrier Phonon Coupling

The interaction among the carriers (i.e., electrons and holes) and lattice vibrations (phonons) is a crucial factor in the carrier cooling phenomena within semiconductors.¹⁰² This interaction, known as carrier-phonon scattering, significantly influences the relaxation of photo-excited semiconductors and the transport properties of these materials. When semiconductors are excited by light, carriers are generated and can exchange energy and momentum with the lattice vibrations.

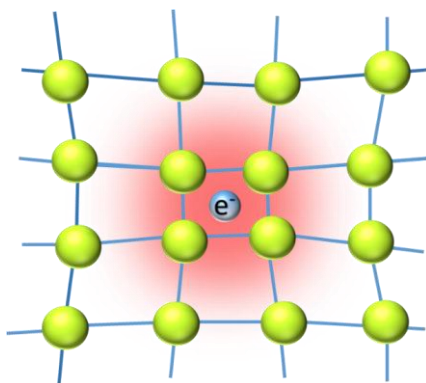


Figure 1.16 The schematic illustration of polaron formation in the lattice. Polaron is a quasiparticle arising as a result of coupling between an electron or hole and its surrounding lattice vibrations (phonons). When an electron or hole moves within a crystal lattice, it causes a local distortion or deformation in the lattice structure. Due to this distortion, a charge carrier (electron or hole) is dressed or surrounded by a cloud of lattice vibrations giving rise to a polaron.

This exchange occurs through electron-phonon and hole-phonon scattering mechanisms. Such scattering processes determine the time it takes for carriers to return to equilibrium and affect phenomena like thermalization, conductivity, and thermal conductivity in semiconductors. In polar semiconductor materials, the presence of LO phonons leads to the generation of a macroscopic electric field, which interacts with the excited carriers. This long-range coupling is referred to as the Frohlich interaction. When an electron interacts with LO phonons, it gives rise to a quasi-particle called a polaron. This phenomenon arises from the profound periodic deformations of the lattice structure caused by the carriers' presence. The strength of this interaction is quantified by a dimensionless parameter known as the Frohlich coupling constant. The general concept of polarons (**Figure 1.16**) was introduced by Landau in 1933¹⁰³ as charge carriers traverse a crystal lattice, their movement is characterized by a gradual pace, accompanied by the corresponding motion of the surrounding atoms. Later, Landau and Pekar further explored the self-energy and effective mass of polarons in 1951.¹⁰⁴⁻¹⁰⁷ It was subsequently demonstrated by Fröhlich in 1954 that the behavior described by Landau and Pekar corresponds to the strong-coupling regime of polarons. The polaron theory, first proposed by Fröhlich and expanded upon by Feynman, has been extensively utilized to understand the interaction of charge carriers with optical phonons.^{108,109} An important parameter in this theory is the Fröhlich parameter $\alpha_{(e-ph)}$, which quantifies the degree of coupling between the carriers and LO phonons, which can be expressed mathematically as:

$$\alpha_{e-ph} = \frac{1}{2} \left(\frac{1}{\epsilon_{\infty}} - \frac{1}{\epsilon_0} \right) \frac{k_e e^2}{\hbar \omega_{LO}} \sqrt{\frac{2m^* \omega_{LO}}{\hbar}} \quad \text{Eq 1.9}$$

Here, ϵ_{∞} represents the dielectric constant at high frequencies, while ϵ_0 represents the static dielectric constant. \hbar denotes Planck's constant, $\hbar\omega_{LO}$ refers to the energy of the LO phonon mode, and m^* represents the effective mass of either an electron or a hole.

In III-V bulk semiconductors, the polar coupling with LO phonons facilitate an efficient relaxation mechanism where the carriers transfer their initial kinetic energy to the lattice. MHPs, due to the high polarizability of soft lattice along with their ionic nature and high dielectric constant, are more prone to polaron formation compared to covalent semiconductors. Polarons play a crucial role in understanding various phenomena in condensed matter physics, such as charge transport, conductivity, and optical absorption in materials. Both experimental observations and computational calculations reveal that the deformation of the $[\text{PbBr}_3]^-$ sublattice plays a significant role in the formation of polarons in both perovskites.¹⁰² Polaron

formation specifically reduces the rate at which carriers cool down and is more relevant at low carrier densities. As at higher densities, the mutual repulsion between polarons makes them unstable. The polarons reduce the effectiveness of Coulombic screening, causing a delay in the scattering of charge carriers with other species and extending their overall lifespan and diffusion length. Additionally, the dressing of carriers with a phonon cloud increases the effective mass and thus reduces their mobility, resulting in slower relaxation dynamics.

Polaron formation is governed by two essential interaction potentials. The first one is the long-range Coulomb potential (V_{LR}), which describes the interaction between the excess charge and the lattice ions. The another one is the short-range deformation potential (V_{SR}), which relates the electronic energy to the strain in the lattice. When the V_{SR} potential dominates, a small polaron is formed, characterized by a coherence length (L_{coh}) that is smaller than the dimension of a single unit cell. In contrast, when the V_{LR} potential becomes more significant, a large polaron is formed, with L_{coh} exceeding the size of more than a unit cell. A large polaron exhibits delocalization over multiple unit cells, leading to coherent and band-like transport and the carrier mobility (μ) of a large polaron decreases with increasing temperature (T), as indicated by the negative derivative of mobility with respect to temperature ($d\mu/dT < 0$). On the other hand, a small polaron remains localized to a single unit cell and its transport follows thermally activated hopping. In this case, the derivative of mobility with respect to temperature is positive ($d\mu/dT > 0$), indicating that the mobility increases with increasing temperature. Understanding the impact of polaron formation on carrier cooling is crucial for optimizing the thermal management and performance of electronic devices and materials. By mitigating the effects of polarons, it is possible to enhance the cooling efficiency and overall thermal properties of the system.

1.5.1.3. Auger Heating

Auger heating is one of the key factors that significantly influence the cooling mechanism of carriers. It involves the non-radiative recombination of an excited electron and hole, leading to the transfer of excess energy to another electron or hole within the system (**Figure 1.17**). Unlike photon emission, this energy transfer adds to the heating of the system.¹¹⁰ The process of Auger heating has a notable influence on the cooling rate of carriers, as it raises the average energy of electron-hole pairs, potentially slowing down the relaxation dynamics. In perovskite systems, when the carrier densities are increased above 10^{19} cm^{-3} , the cooling process can be significantly influenced by the Auger heating along with the hot-phonon bottleneck.

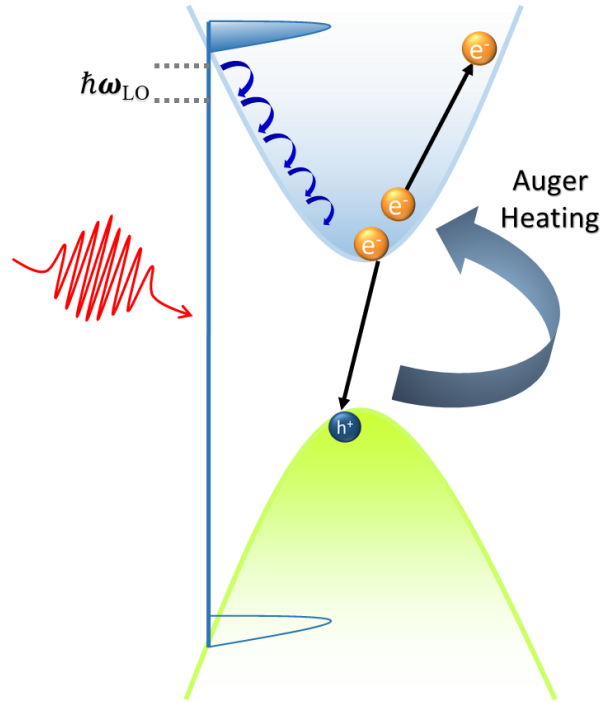


Figure 1.17 The schematic illustration of the relaxation process of hot electrons, showcasing effect of both Auger recombination and LO phonon emission. These processes contribute to the slow hot electron cooling. (It is important to note that a similar relaxation process also occurs for hot holes, although it is not shown in the schematic for clarity)

The energy transferred during recombination to the electronic system is directly proportional to $(E_g + E)$.⁸⁴ The influence of Auger heating on carrier-cooling dynamics can be accurately described using the following expression.¹¹¹

$$\left\langle \frac{dE}{dt} \right\rangle_{(tot)} = \left\langle \frac{dE}{dt} \right\rangle_{(e-ph)} + k_3 n^2 (E_g + E) \quad \text{Eq 1.10}$$

$$\frac{dn}{dt} = -k_1 n - k_2 n^2 - k_3 n^3 \quad \text{Eq 1.11}$$

Where k_1 represents the monomolecular recombination coefficient; k_2 denotes the bimolecular recombination coefficient for free carriers; and k_3 denotes the coefficient of auger recombination and n is the concentration of carriers. It is important to note that the Auger recombination coefficient (k_3) tends to be larger for materials with smaller bandgaps and higher carrier temperatures. The cumulative energy loss of carriers depends on two distinct factors as depicted in equation (1.10), the first one denotes the energy loss rate via electron- LO phonon interaction, whereas the second one signifies the impact of Auger-heating.

In bulk semiconductors, Auger heating does not play a vital role due to the limitations imposed by energy and momentum conservation. However, in quantum-confined semiconductor NCs, auger processes can become highly competent. This is primarily due to the relaxation in momentum conservation and the obligatory overlay of carrier wavefunctions induced due to the increased quantum confinement.¹¹⁰ As a result, the Auger heating effect is particularly pronounced in perovskite nanostructures. Moreover, As per Fermi's golden rule, the Auger recombination rate is described by the equation:

$$k_3 \propto \sqrt{E_g} \exp\left(-\frac{m_e}{m_e+m_h} \cdot \frac{E_g}{k_B T}\right) \quad \text{Eq 1.12}$$

where m_e and m_h represents the effective mass of the electron and hole respectively, K_B is Boltzmann constant and, T_c is carrier temperature. Also, the auger recombination rate is dependent on both the band gap and T_c thus semiconductors with their relatively reduced band gap and the prevalence of the hot-phonon effect contribute to the strong Auger heating observed at high excitation densities. The Hot carrier (HC) cooling, which takes into account both hot phonon bottleneck effect and Auger heating effect. At high carrier densities, the non-equilibrium population of LO phonons predominantly influences HC cooling during the initial few ps (~ 2 ps) while Auger heating takes over in further HC relaxation.¹¹¹ Auger heating is considered one of the most significant factors that can lead to a retardation of carrier cooling. This phenomenon plays a decisive role in influencing the dynamics of carrier relaxation and can have a significant impact on device efficiency. By slowing down the cooling process, Auger heating allows for an efficient utilization of carrier energy, which can be beneficial for improving device performance.

1.5.1.4. Band filling at high carrier density

After photoexcitation, both electrons and holes are indeed excited to higher energy states within the semiconductor's energy bands. These higher energy states are often referred to as "hot carriers" because they have excess energy compared to their equilibrium (non-excited) counterparts. As these hot carriers undergo thermalization, they lose their excess energy and return to the conduction and VB edges, eventually reaching a thermal equilibrium state. This occupation of states near the band edges results in the promotion of higher-energy optical transitions, which is a direct consequence of the Pauli Exclusion Principle. This phenomenon is depicted schematically in **Figure 1.18**. The shift in the semiconductor's optical properties

due to carrier-induced band filling can be described using the following mathematical expression:¹¹²

$$\Delta E_g^{BM} = - \left(\frac{\hbar^2}{2m_{eh}^*} \right) (3\pi^2 n)^{2/3} \quad \text{Eq 1.13}$$

In this equation, ΔE_g^{BM} represents the change in the optical bandgap, attributable to the Burstein–Moss band filling effect, m_{eh}^* stands for the reduced effective mass, which is calculated as the sum of the effective electron mass (m_e) and effective hole mass (m_h^*), and \hbar represents the reduced Planck constant.

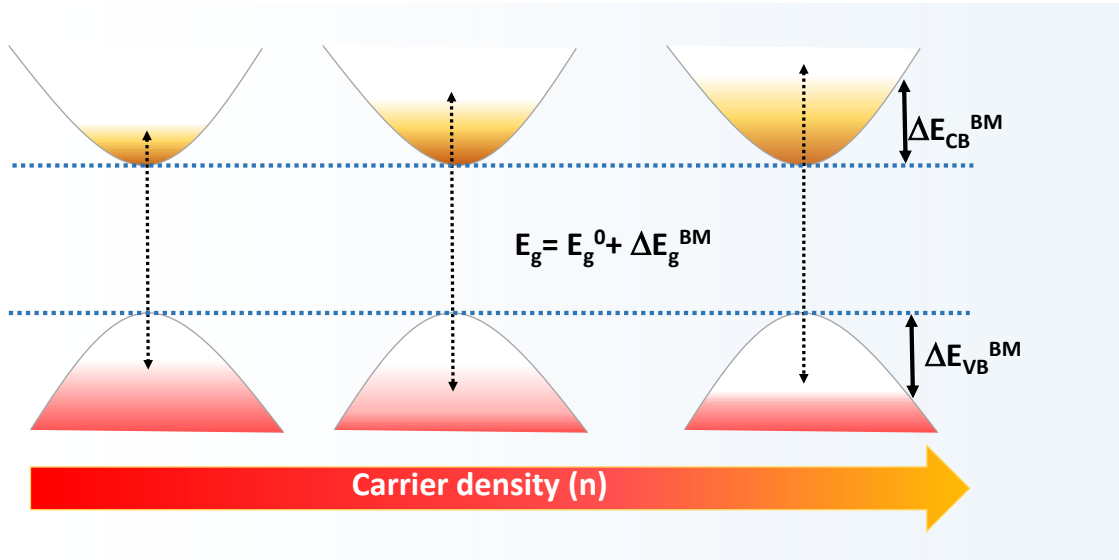


Figure 1.18 The Schematic representation explaining the Burstein-Moss effect.

The total optical transition energy (E_g) can then be defined as the sum of the intrinsic bandgap energy (E_g^0) and the change in bandgap energy due to the Burstein–Moss effect (ΔE_g^{BM}). The Burstein-Moss shift can therefore be described by the equation $\Delta E_g^{BM} = \Delta E_{CB}^{BM} + \Delta E_{VB}^{BM}$. The mathematical model provided calculates the change in the optical bandgap subsequent to the Burstein–Moss band-filling, offering insights into the semiconductor's optical transition properties.

In the study conducted by Loi and co-workers, they observed unexpectedly long lifetimes of PL emitted by hot carriers in formamidinium tin triiodide, lasting for a few nanoseconds.¹¹² Furthermore, significant blue shift is observed in the time-resolved PL as the excitation power is increased. In conclusion, they found that both the slow relaxation of hot carriers and the filling of band edge states are responsible for this observation. Furthermore, slow HC emission

becomes more pronounced at higher excitation intensities and can even be observed at low temperatures of 24 K.

Further, Chen and co-workers the band filling effect, has a notable impact not only on the ground state bleaching but also on the excited state absorption. This influence is evident observed in the transient signal for both ground state bleaching and excited state absorption.¹¹³

Fu *et.al.* found that the bandgap of perovskite is notably affected by two competing carrier-density-dependent processes i.e., the Burstein–Moss effect and band gap renormalization (BGR).¹¹¹ The BGR tends to cause a redshift in the bandgap, meaning the energy levels shift toward longer wavelengths. On the other hand, the Burstein–Moss effect contributes to a blueshift in the bandgap, indicating a shift toward shorter wavelengths. Due to the interplay of these two effects, the photobleaching (PB) peak is observed to be slightly redshifted. Also, they observe that the slope of the hot carrier (HC) cooling curve becomes less steep at high carrier densities, indicating a lower rate of energy loss. Furthermore, when the carrier takes more than 1 ps to reach equilibrium with the lattice. This extended timescale suggests a sluggish cooling of HC at higher carrier concentrations. This observation aligns with the slower rise time of the band-edge PB signal at higher pump fluence. So, the efficient harvesting of these hot carriers, while maintaining them at their highest temperatures, remains a key challenge for achieving maximal efficiencies in HC solar cells.¹¹⁴

1.5.1.5. Defects

Defects can indeed play a crucial role in the hot carrier cooling process in semiconductors.

- ✓ **Trapping and Scattering:** Defects in a semiconductor lattice can act as trapping centers for hot carriers. When a hot carrier encounters a defect, it can become trapped at that site as shown in **Figure 1.19**, preventing it from relaxing and losing its excess energy. This trapping process can significantly delay the cooling of hot carriers.¹⁰
- ✓ **Auger Recombination:** Certain defects can facilitate Auger recombination, which is a process where an energetic electron or hole transfers its energy to another carrier, causing them to both lose energy and cool down. This can enhance the hot carrier cooling rate by promoting energy transfer from hot carriers to the surrounding carriers through defect-mediated Auger processes.

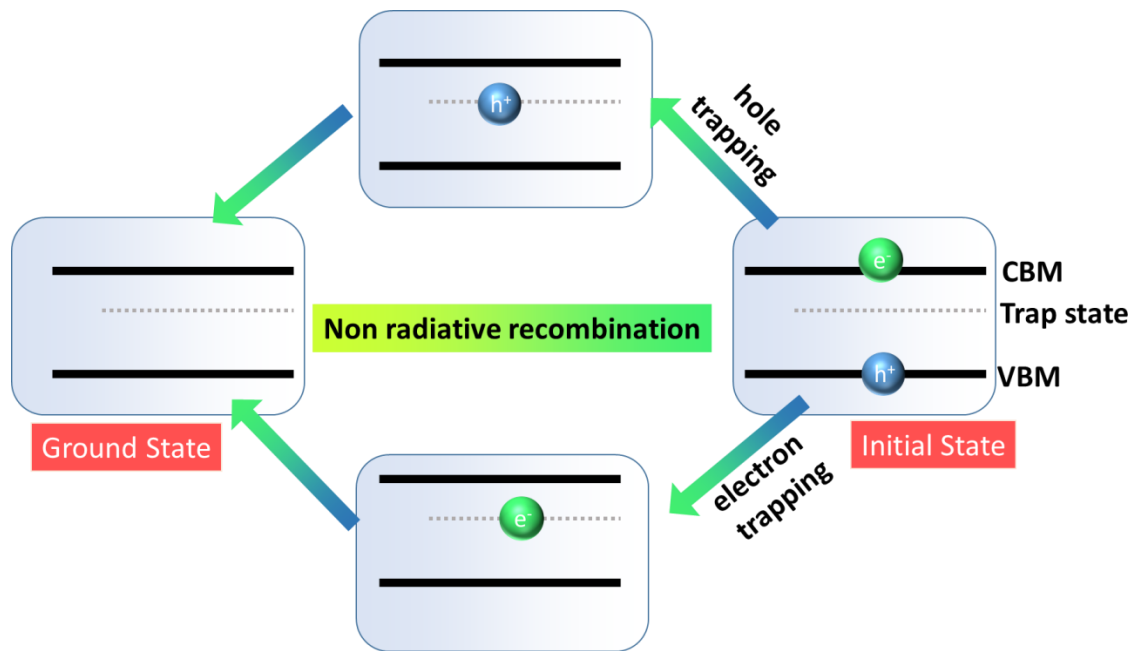


Figure 1.19 Schematic representation illustrating the trapping of electrons and holes in trap states within a semiconductor QDs, which leads to a delayed carrier cooling process.

- ✓ **Non-Radiative Recombination:** Defects can also contribute to non-radiative recombination, where carriers recombine without emitting photons. This process leads to energy dissipation as heat and contributes to the cooling of hot carriers.
- ✓ **Carrier Localization:** Defects can create localized electronic states within the bandgap of a semiconductor. When hot carriers become localized near these defect states, their energy can be dissipated more slowly compared to when they are free to move throughout the crystal lattice.
- ✓ **Impact on Material Properties:** The type and concentration of defects in a semiconductor can influence its electronic properties, including carrier mobility and recombination rates. These properties, in turn, affect how quickly hot carriers lose their excess energy.
- ✓ **Engineering for Hot Carrier Devices:** In some cases, defects may be intentionally introduced or controlled in semiconductor materials to engineer specific hot carrier behavior. This can be doping the perovskite system with any impurity ions in order to tune its properties. This is particularly relevant in the development of hot carrier solar cells and other optoelectronic devices where controlling hot carrier dynamics can enhance device efficiency.

1.6 References

- (1) Mortimer, N. D. Energy Analysis of Renewable Energy Sources. *Energy Policy* **1991**, *19* (4), 374–385.
- (2) Woldeyohannes, A. D.; Woldemichael, D. E.; Baheta, A. T. Sustainable Renewable Energy Resources Utilization in Rural Areas. *Renew. Sustain. Energy Rev.* **2016**, *66*, 1–9.
- (3) Elavarasan, R. M. The Motivation for Renewable Energy and Its Comparison with Other Energy Sources: A Review. *Eur. J. Sustain. Dev. Res.* **2019**, *3* (1), em0076.
- (4) Qazi, A.; Hussain, F.; Rahim, N. A. B. D.; Hardaker, G.; Alghazzawi, D.; Shaban, K.; Haruna, K. Towards Sustainable Energy: A Systematic Review of Renewable Energy Sources, Technologies, and Public Opinions. *IEEE Access* **2019**, *7*, 63837–63851.
- (5) Kannan, N.; Vakeesan, D. Solar Energy for Future World: - A Review. *Renew. Sustain. Energy Rev.* **2016**, *62*, 1092–1105.
- (6) Devabhaktuni, V.; Alam, M.; Shekara Sreenadh Reddy Depuru, S.; Green, R. C.; Nims, D.; Near, C. Solar Energy: Trends and Enabling Technologies. *Renew. Sustain. Energy Rev.* **2013**, *19*, 555–564.
- (7) Lewis, N. S.; Crabtree, G.; Nozik, A. J.; Wasielewski, M. R.; Alivisatos, P.; Kung, H.; Tsao, J.; Chandler, E.; Walukiewicz, W.; Spitler, M.; Ellingson, R.; Overend, R.; Mazer, J.; Gress, M.; Horwitz, J.; Ashton, C.; Herndon, B.; Shapard, L.; Nault, R. M. *Basic Research Needs for Solar Energy Utilization. Report of the Basic Energy Sciences Workshop on Solar Energy Utilization, April 18-21, 2005*; United States, 2005.
- (8) Crabtree, G. W.; Lewis, N. S. Solar Energy Conversion. *Phys. Today* **2007**, *60* (3), 37–42.
- (9) Fthenakis, V.; Mason, J. E.; Zweibel, K. The Technical, Geographical, and Economic Feasibility for Solar Energy to Supply the Energy Needs of the US. *Energy Policy* **2009**, *37* (2), 387–399.
- (10) Li, W.; Liu, J.; Bai, F.-Q.; Zhang, H.-X.; Prezhdo, O. V. Hole Trapping by Iodine Interstitial Defects Decreases Free Carrier Losses in Perovskite Solar Cells: A Time-Domain Ab Initio Study. *ACS Energy Lett.* **2017**, *2* (6), 1270–1278.
- (11) Turner, J. A. A Realizable Renewable Energy Future. *Science* **1999**, *285* (5428), 687–689.
- (12) Gielen, D.; Boshell, F.; Saygin, D.; Bazilian, M. D.; Wagner, N.; Gorini, R. The Role of Renewable Energy in the Global Energy Transformation. *Energy Strateg. Rev.* **2019**, *24*, 38–50.
- (13) Ameri, T.; Dennler, G.; Lungenschmied, C.; Brabec, C. J. Organic Tandem Solar Cells: A Review. *Energy Environ. Sci.* **2009**, *2* (4), 347–363.
- (14) Ameri, T.; Li, N.; Brabec, C. J. Highly Efficient Organic Tandem Solar Cells: A Follow up Review. *Energy Environ. Sci.* **2013**, *6* (8), 2390–2413.

- (15) Green, M. A.; Ho-Baillie, A.; Snaith, H. J. The Emergence of Perovskite Solar Cells. *Nat. Photonics* **2014**, *8* (7), 506–514.
- (16) Kim, J. Y.; Lee, J.-W.; Jung, H. S.; Shin, H.; Park, N.-G. High-Efficiency Perovskite Solar Cells. *Chem. Rev.* **2020**, *120* (15), 7867–7918.
- (17) Noel, N. K.; Stranks, S. D.; Abate, A.; Wehrenfennig, C.; Guarnera, S.; Haghighirad, A.-A.; Sadhanala, A.; Eperon, G. E.; Pathak, S. K.; Johnston, M. B.; Petrozza, A.; Herz, L. M.; Snaith, H. J. Lead-Free Organic–Inorganic Tin Halide Perovskites for Photovoltaic Applications. *Energy Environ. Sci.* **2014**, *7* (9), 3061–3068.
- (18) Tonui, P.; Oseni, S. O.; Sharma, G.; Yan, Q.; Tessema Mola, G. Perovskites Photovoltaic Solar Cells: An Overview of Current Status. *Renew. Sustain. Energy Rev.* **2018**, *91*, 1025–1044.
- (19) Christians, J. A.; Manser, J. S.; Kamat, P. V. Best Practices in Perovskite Solar Cell Efficiency Measurements. Avoiding the Error of Making Bad Cells Look Good. *J. Phys. Chem. Lett.* **2015**, *6* (5), 852–857.
- (20) Snaith, H. J. Present Status and Future Prospects of Perovskite Photovoltaics. *Nat. Mater.* **2018**, *17* (5), 372–376.
- (21) Kojima, A.; Teshima, K.; Shirai, Y.; Miyasaka, T. Organometal Halide Perovskites as Visible-Light Sensitizers for Photovoltaic Cells. *J. Am. Chem. Soc.* **2009**, *131* (17), 6050–6051.
- (22) Tang, H.; He, S.; Peng, C. A Short Progress Report on High-Efficiency Perovskite Solar Cells. *Nanoscale Res. Lett.* **2017**, *12* (1), 410.
- (23) Seo, J.; Noh, J. H.; Seok, S. II. Rational Strategies for Efficient Perovskite Solar Cells. *Acc. Chem. Res.* **2016**, *49* (3), 562–572.
- (24) Zhang, F.; Yao, Z.; Guo, Y.; Li, Y.; Bergstrand, J.; Brett, C. J.; Cai, B.; Hajian, A.; Guo, Y.; Yang, X. Polymeric, Cost-Effective, Dopant-Free Hole Transport Materials for Efficient and Stable Perovskite Solar Cells. *J. Am. Chem. Soc.* **2019**, *141* (50), 19700–19707.
- (25) Bella, F.; Griffini, G.; Correa-Baena, J.-P.; Saracco, G.; Grätzel, M.; Hagfeldt, A.; Turri, S.; Gerbaldi, C. Improving Efficiency and Stability of Perovskite Solar Cells with Photocurable Fluoropolymers. *Science* **2016**, *354* (6309), 203–206.
- (26) Sha, W. E. I.; Ren, X.; Chen, L.; Choy, W. C. H. The Efficiency Limit of $\text{CH}_3\text{NH}_3\text{PbI}_3$ Perovskite Solar Cells. *Appl. Phys. Lett.* **2015**, *106* (22), 221104.
- (27) Jiang, Q.; Chu, Z.; Wang, P.; Yang, X.; Liu, H.; Wang, Y.; Yin, Z.; Wu, J.; Zhang, X.; You, J. Planar-Structure Perovskite Solar Cells with Efficiency beyond 21%. *Adv. Mater.* **2017**, *29* (46), 1703852.
- (28) Rong, Y.; Liu, L.; Mei, A.; Li, X.; Han, H. Beyond Efficiency: The Challenge of Stability in Mesoscopic Perovskite Solar Cells. *Adv. Energy Mater.* **2015**, *5* (20), 1501066.

- (29) Jeong, M.; Choi, I. W.; Go, E. M.; Cho, Y.; Kim, M.; Lee, B.; Jeong, S.; Jo, Y.; Choi, H. W.; Lee, J.; Bae, J.-H.; Kwak, S. K.; Kim, D. S.; Yang, C. Stable Perovskite Solar Cells with Efficiency Exceeding 24.8% and 0.3-V Voltage Loss. *Science* **2020**, *369* (6511), 1615–1620.
- (30) Correa-Baena, J.-P.; Saliba, M.; Buonassisi, T.; Grätzel, M.; Abate, A.; Tress, W.; Hagfeldt, A. Promises and Challenges of Perovskite Solar Cells. *Science* **2017**, *358* (6364), 739–744.
- (31) Hou, Y.; Du, X.; Scheiner, S.; McMeekin, D. P.; Wang, Z.; Li, N.; Killian, M. S.; Chen, H.; Richter, M.; Levchuk, I. A Generic Interface to Reduce the Efficiency-Stability-Cost Gap of Perovskite Solar Cells. *Science* **2017**, *358* (6367), 1192–1197.
- (32) Sharma, R.; Sharma, A.; Agarwal, S.; Dhaka, M. S. Stability and Efficiency Issues, Solutions and Advancements in Perovskite Solar Cells: A Review. *Sol. Energy* **2022**.
- (33) Jena, A. K.; Kulkarni, A.; Miyasaka, T. Halide Perovskite Photovoltaics: Background, Status, and Future Prospects. *Chem. Rev.* **2019**, *119* (5), 3036–3103.
- (34) Chakhmouradian, A. R.; Woodward, P. M. Celebrating 175 Years of Perovskite Research: A Tribute to Roger H. Mitchell. *Physics and Chemistry of Minerals*. Springer 2014, pp 387–391.
- (35) Wells, H. L. Über Die Cäsium-und Kalium-bleihalogenide. *Zeitschrift für Anorg. Chemie* **1893**, *3* (1), 195–210.
- (36) Wells, H. L. ART. XVI. On the Coesium-and the Potassium-Lead Halides. *Am. J. Sci.* **1893**, *45* (266), 121.
- (37) Møller, C. K. The structure of perovskite-like Caesium Plumbotrihalides. *Mat.-Fys. Medd. Dan. Vid. Selsk* **1959**, *32*, 2.
- (38) NREL, Best Research-Cell Efficiency Chart, <https://www.nrel.gov/pv/cell-efficiency.html> (Last accessed: August 8, 2023).
- (39) Sun, Q.; Yin, W.-J. Thermodynamic Stability Trend of Cubic Perovskites. *J. Am. Chem. Soc.* **2017**, *139* (42), 14905–14908.
- (40) Jiang, S.; Hu, T.; Gild, J.; Zhou, N.; Nie, J.; Qin, M.; Harrington, T.; Vecchio, K.; Luo, J. A New Class of High-Entropy Perovskite Oxides. *Scr. Mater.* **2018**, *142*, 116–120.
- (41) Saparov, B.; Mitzi, D. B. Organic–Inorganic Perovskites: Structural Versatility for Functional Materials Design. *Chem. Rev.* **2016**, *116* (7), 4558–4596.
- (42) Duan, L.; Uddin, A. Defects and Stability of Perovskite Solar Cells: A Critical Analysis. *Mater. Chem. Front.* **2022**, *6* (4), 400–417.
- (43) Zhao, X.; Park, N.-G. Stability Issues on Perovskite Solar Cells. In *Photonics*; MDPI, 2015; Vol. 2, pp 1139–1151.
- (44) Jiang, J.; Jin, Z.; Gao, F.; Sun, J.; Wang, Q.; Liu, S. (Frank). CsPbCl₃-Driven Low-Trap-Density Perovskite Grain Growth for >20% Solar Cell Efficiency. *Adv. Sci.* **2018**, *5* (7), 1800474.

- (45) Wang, J.; Che, Y.; Duan, Y.; Liu, Z.; Yang, S.; Xu, D.; Fang, Z.; Lei, X.; Li, Y.; Liu, S. 21.15%-Efficiency and Stable Γ -CsPbI₃ Perovskite Solar Cells Enabled by an Acyloin Ligand. *Adv. Mater.* **2023**, *35* (12), 2210223.
- (46) Protesescu, L.; Yakunin, S.; Bodnarchuk, M. I.; Krieg, F.; Caputo, R.; Hendon, C. H.; Yang, R. X.; Walsh, A.; Kovalenko, M. V. Nanocrystals of Cesium Lead Halide Perovskites (CsPbX₃, X = Cl, Br, and I): Novel Optoelectronic Materials Showing Bright Emission with Wide Color Gamut. *Nano Lett.* **2015**, *15* (6), 3692–3696.
- (47) du Fossé, I.; Mulder, J. T.; Almeida, G.; Spruit, A. G. M.; Infante, I.; Grozema, F. C.; Houtepen, A. J. Limits of Defect Tolerance in Perovskite Nanocrystals: Effect of Local Electrostatic Potential on Trap States. *J. Am. Chem. Soc.* **2022**, *144* (25), 11059–11063.
- (48) Brandt, R. E.; Poindexter, J. R.; Gorai, P.; Kurchin, R. C.; Hoye, R. L. Z.; Nienhaus, L.; Wilson, M. W. B.; Polizzotti, J. A.; Sereika, R.; Žaltauskas, R.; Lee, L. C.; MacManus-Driscoll, J. L.; Bawendi, M.; Stevanović, V.; Buonassisi, T. Searching for “Defect-Tolerant” Photovoltaic Materials: Combined Theoretical and Experimental Screening. *Chem. Mater.* **2017**, *29* (11), 4667–4674.
- (49) Wang, B.; Navrotsky, A. Thermodynamics of Cesium Lead Halide (CsPbX₃, X= I, Br, Cl) Perovskites. *Thermochim. Acta* **2021**, *695*, 178813.
- (50) Li, G.; Wang, H.; Zhu, Z.; Chang, Y.; Zhang, T.; Song, Z. Shape and Phase Evolution From CsPbBr₃ Perovskite Nanocubes To Tetragonal CsPb₂Br₅ Nanosheets With An Indirect Bandgap. *Chem. Comm.* 2016, *52*, 11296–11299.
- (51) Fu, X.; Li, W.; Zeng, X.; Yan, C.; Peng, X.; Gao, Y.; Wang, Q.; Cao, J.; Yang, S.; Yang, W. Structurally Tolerance-Factor-Tuned Metal Halide Nanocrystals for Environmentally Stable and Efficient Red Light-Emitting Diodes. *J. Phys. Chem. Lett.* **2022**, *13* (9), 2217–2225.
- (52) Bruce, A. D.; Cowley, R. A. Structural Phase Transitions. **1981**.
- (53) Domb, C. *Phase Transitions and Critical Phenomena*; Elsevier, 2000.
- (54) Redfern, S. A. T. High-Temperature Structural Phase Transitions in Perovskite. *J. Phys. Condens. Matter* **1996**, *8* (43), 8267.
- (55) Dutta, A.; Behera, R. K.; Dutta, S. K.; Das Adhikari, S.; Pradhan, N. Annealing CsPbX₃ (X= Cl and Br) Perovskite Nanocrystals at High Reaction Temperatures: Phase Change and Its Prevention. *J. Phys. Chem. Lett.* **2018**, *9* (22), 6599–6604.
- (56) Angel, R. J.; Zhao, J.; Ross, N. L. General Rules for Predicting Phase Transitions in Perovskites Due to Octahedral Tilting. *Phys. Rev. Lett.* **2005**, *95* (2), 25503.

- (57) Steele, J. A.; Lai, M.; Zhang, Y.; Lin, Z.; Hofkens, J.; Roeffaers, M. B. J.; Yang, P. Phase Transitions and Anion Exchange in All-Inorganic Halide Perovskites. *Accounts Mater. Res.* **2020**, *1* (1), 3–15.
- (58) Cohen, M. I.; Young, K. F.; Chang, T.; Brower, W. S. Phase Transitions in CsPbCl₃. *J. Appl. Phys.* **1971**, *42* (13), 5267–5272.
- (59) Hirotsu, S. Experimental Studies of Structural Phase Transitions in CsPbCl₃. *J. Phys. Soc. Japan* **1971**, *31* (2), 552–560.
- (60) Zhou, Y.; Chen, J.; Bakr, O. M.; Sun, H.-T. Metal-Doped Lead Halide Perovskites: Synthesis, Properties, and Optoelectronic Applications. *Chem. Mater.* **2018**, *30* (19), 6589–6613.
- (61) Zhang, X.; Li, L.; Sun, Z.; Luo, J. Rational Chemical Doping of Metal Halide Perovskites. *Chem. Soc. Rev.* **2019**, *48* (2), 517–539.
- (62) Wang, J. T.-W.; Wang, Z.; Pathak, S.; Zhang, W.; deQuilettes, D. W.; Wisnivesky-Rocca-Rivarola, F.; Huang, J.; Nayak, P. K.; Patel, J. B.; Yusof, H. A. M. Efficient Perovskite Solar Cells by Metal Ion Doping. *Energy Environ. Sci.* **2016**, *9* (9), 2892–2901.
- (63) Su, B.; Zhou, G.; Huang, J.; Song, E.; Nag, A.; Xia, Z. Mn²⁺-doped Metal Halide Perovskites: Structure, Photoluminescence, and Application. *Laser Photon. Rev.* **2021**, *15* (1), 2000334.
- (64) Jia, S.; Wang, J.; Zhu, L. Enhancing the Photovoltaic Performance of Perovskite Solar Cells by Potassium Ions Doping. *J. Mater. Sci. Mater. Electron.* **2019**, *30*, 2057–2066.
- (65) Swarnkar, A.; Mir, W. J.; Nag, A. Can B-Site Doping or Alloying Improve Thermal-and Phase-Stability of All-Inorganic CsPbX₃ (X= Cl, Br, I) Perovskites? *ACS Energy Lett.* **2018**, *3* (2), 286–289.
- (66) Saliba, M.; Matsui, T.; Domanski, K.; Seo, J.-Y.; Ummadisingu, A.; Zakeeruddin, S. M.; Correa-Baena, J.-P.; Tress, W. R.; Abate, A.; Hagfeldt, A. Incorporation of Rubidium Cations into Perovskite Solar Cells Improves Photovoltaic Performance. *Science*. **2016**, *354* (6309), 206–209.
- (67) Kubicki, D. J.; Prochowicz, D.; Hofstetter, A.; Zakeeruddin, S. M.; Grätzel, M.; Emsley, L. Phase Segregation in Cs-, Rb- and K-Doped Mixed-Cation (MA)_x(FA)_{1-x}PbI₃ Hybrid Perovskites from Solid-State NMR. *J. Am. Chem. Soc.* **2017**, *139* (40), 14173–14180.
- (68) Petrozza, A. Doping of Soft Semiconductors. *ACS Energy Letters*. **2022**, *7*, 3, 1101–1102.
- (69) Bouich, A.; Marí-Guaita, J.; Soucase, B. M.; Palacios, P. Bright Future by Enhancing the Stability of Methylammonium Lead Triiodide Perovskites Thin Films through Rb, Cs and Li as Dopants. *Mater. Res. Bull.* **2023**, *163*, 112213.
- (70) Syzgantseva, O. A.; Saliba, M.; Grätzel, M.; Rothlisberger, U. Stabilization of the Perovskite Phase of Formamidinium Lead Triiodide by Methylammonium, Cs, and/or Rb Doping. *J. Phys. Chem. Lett.* **2017**, *8* (6), 1191–1196.

- (71) Hou, L.; Zhu, Y.; Zhu, J.; Li, X.; Zeng, F.; Yang, T.; Gong, Y.; Shen, J.; Li, C. Synthesis of Gram-Scale Ultrastable Mn-Doped 2D Perovskites for Light-Emitting Diodes. *Adv. Mater. Interfaces* **2021**, *8* (7), 2002175.
- (72) Yu, R.; Wang, C.; Chen, J.; Wu, Y.; Li, H.; Ma, H. Photoluminescence Characteristics of Eu³⁺-Doped Double-Perovskite Phosphors. *ECS J. Solid State Sci. Technol.* **2014**, *3* (3), R33.
- (73) Jing, X.; Zhou, D.; Sun, R.; Zhang, Y.; Li, Y.; Li, X.; Li, Q.; Song, H.; Liu, B. Enhanced Photoluminescence and Photoresponsiveness of Eu³⁺ Ions-Doped CsPbCl₃ Perovskite Quantum Dots under High Pressure. *Adv. Funct. Mater.* **2021**, *31* (31), 2100930.
- (74) Bispo-Jr, A. G.; de Moraes, A. J.; Calado, C. M. S.; Mazali, I. O.; Sigoli, F. A. Lanthanide-Doped Luminescent Perovskites: A Review of Synthesis, Properties, and Applications. *J. Lumin.* **2022**, 119406.
- (75) Kachhap, S.; Singh, S.; Singh, A. K.; Singh, S. K. Lanthanide-Doped Inorganic Halide Perovskites (CsPbX₃): Novel Properties and Emerging Applications. *J. Mater. Chem. C* **2022**, *10* (10), 3647–3676.
- (76) Das Adhikari, S.; Dutta, A.; Dutta, S. K.; Pradhan, N. Layered Perovskites L₂(Pb_{1-x}Mn_x)Cl₄ to Mn-Doped CsPbCl₃ Perovskite Platelets. *ACS Energy Lett.* **2018**, *3* (6), 1247–1253.
- (77) Pansa-NGat, P.; Nakajima, H.; Supruangnet, R.; Suwanna, S.; Pakawatpanurut, P.; Sahasithiwat, S.; Kanjanaboos, P. Phase Evolution in Lead-Free Cs-Doped FASnI₃ Hybrid Perovskites and Optical Properties. *J. Phys. Chem. C* **2021**, *125* (31), 16903–16912.
- (78) Liang, F.; Wang, J.; Zhang, Z.; Wang, Y.; Gao, Y.; Luo, L. Broadband, Ultrafast, Self-driven Photodetector Based on Cs-doped FAPbI₃ Perovskite Thin Film. *Adv. Opt. Mater.* **2017**, *5* (22), 1700654.
- (79) Liu, Y.; Pan, G.; Wang, R.; Shao, H.; Wang, H.; Xu, W.; Cui, H.; Song, H. Considerably Enhanced Exciton Emission of CsPbCl₃ Perovskite Quantum Dots by the Introduction of Potassium and Lanthanide Ions. *Nanoscale* **2018**, *10* (29), 14067–14072.
- (80) Protesescu, L.; Yakunin, S.; Kumar, S.; Bär, J.; Bertolotti, F.; Masciocchi, N.; Guagliardi, A.; Grotevent, M.; Shorubalko, I.; Bodnarchuk, M. I. Dismantling the “Red Wall” of Colloidal Perovskites: Highly Luminescent Formamidinium and Formamidinium–Cesium Lead Iodide Nanocrystals. *ACS Nano* **2017**, *11* (3), 3119–3134.
- (81) Mir, W. J.; Sheikh, T.; Arfin, H.; Xia, Z.; Nag, A. Lanthanide Doping in Metal Halide Perovskite Nanocrystals: Spectral Shifting, Quantum Cutting and Optoelectronic Applications. *NPG Asia Mater.* **2020**, *12* (1), 9.
- (82) Pan, G.; Bai, X.; Yang, D.; Chen, X.; Jing, P.; Qu, S.; Zhang, L.; Zhou, D.; Zhu, J.; Xu, W. Doping Lanthanide into Perovskite Nanocrystals: Highly Improved and Expanded Optical Properties. *Nano Lett.* **2017**, *17* (12), 8005–8011.

- (83) Ma, J.-P.; Chen, Y.-M.; Zhang, L.-M.; Guo, S.-Q.; Liu, J.-D.; Li, H.; Ye, B.-J.; Li, Z.-Y.; Zhou, Y.; Zhang, B.-B. Insights into the Local Structure of Dopants, Doping Efficiency, and Luminescence Properties of Lanthanide-Doped CsPbCl₃ Perovskite Nanocrystals. *J. Mater. Chem. C* **2019**, *7* (10), 3037–3048.
- (84) Li, M.; Fu, J.; Xu, Q.; Sum, T. C. Slow Hot-Carrier Cooling in Halide Perovskites: Prospects for Hot-Carrier Solar Cells. *Adv. Mater.* **2019**, *31* (47), 1–17.
- (85) Chen, J.; Messing, M. E.; Zheng, K.; Pullerits, T. Cation-Dependent Hot Carrier Cooling in Halide Perovskite Nanocrystals. *J. Am. Chem. Soc.* **2019**, *141* (8), 3532–3540.
- (86) Wu, J.; Cha, H.; Du, T.; Dong, Y.; Xu, W.; Lin, C.-T.; Durrant, J. R. A Comparison of Charge Carrier Dynamics in Organic and Perovskite Solar Cells. *Adv. Mater.* **2022**, *34* (2), 2101833.
- (87) Fu, J.; Xu, Q.; Han, G.; Wu, B.; Huan, C. H. A.; Leek, M. L.; Sum, T. C. Hot Carrier Cooling Mechanisms in Halide Perovskites. *Nat. Commun.* **2017**, *8* (1), 1300.
- (88) Conibeer, G. J.; König, D.; Green, M. A.; Guillemoles, J. F. Slowing of Carrier Cooling in Hot Carrier Solar Cells. *Thin Solid Films* **2008**, *516* (20), 6948–6953.
- (89) Conibeer, G.; Ekins-Daukes, N.; Guillemoles, J.-F.; König, D.; Cho, E.-C.; Jiang, C.-W.; Shrestha, S.; Green, M. Progress on Hot Carrier Cells. *Sol. Energy Mater. Sol. Cells* **2009**, *93* (6), 713–719.
- (90) Leheny, R. F.; Shah, J.; Fork, R. L.; Shank, C. V; Migus, A. Dynamics of Hot Carrier Cooling in Photo-Excited GaAs. *Solid State Commun.* **1979**, *31* (11), 809–813.
- (91) Rosenwaks, Y.; Hanna, M. C.; Levi, D. H.; Szymyd, D. M.; Ahrenkiel, R. K.; Nozik, A. J. Hot-Carrier Cooling in GaAs: Quantum Wells versus Bulk. *Phys. Rev. B* **1993**, *48* (19), 14675–14678.
- (92) Wehrenfennig, C.; Liu, M.; Snaith, H. J.; Johnston, M. B.; Herz, L. M. Charge-Carrier Dynamics in Vapour-Deposited Films of the Organolead Halide Perovskite CH₃NH₃PbI_{3-x}Cl_x. *Energy Environ. Sci.* **2014**, *7* (7), 2269–2275.
- (93) Yang, B.; Han, K. Charge-Carrier Dynamics of Lead-Free Halide Perovskite Nanocrystals. *Acc. Chem. Res.* **2019**, *52* (11), 3188–3198.
- (94) Bartesaghi, D.; Slavney, A. H.; Gélvez-Rueda, M. C.; Connor, B. A.; Grozema, F. C.; Karunadasa, H. I.; Savenije, T. J. Charge Carrier Dynamics in Cs₂AgBiBr₆ Double Perovskite. *J. Phys. Chem. C* **2018**, *122* (9), 4809–4816.
- (95) Ibach, H.; Lüth, H. *Solid-State Physics: An Introduction to Principles of Materials Science*; Springer Science & Business Media, 2009.
- (96) Efros, A. L.; Rosen, M. The Electronic Structure of Semiconductor Nanocrystals. *Annu. Rev. Mater. Sci.* **2000**, *30* (1), 475–521.

- (97) Inoshita, T.; Sakaki, H. Electron-Phonon Interaction and the so-Called Phonon Bottleneck Effect in Semiconductor Quantum Dots. *Phys. B Condens. Matter* **1996**, 227 (1–4), 373–377.
- (98) Yang, J.; Wen, X.; Xia, H.; Sheng, R.; Ma, Q.; Kim, J.; Tapping, P.; Harada, T.; Kee, T. W.; Huang, F.; Cheng, Y.-B.; Green, M.; Ho-Baillie, A.; Huang, S.; Shrestha, S.; Patterson, R.; Conibeer, G. Acoustic-Optical Phonon up-Conversion and Hot-Phonon Bottleneck in Lead-Halide Perovskites. *Nat. Commun.* **2017**, 8 (1), 14120.
- (99) Srivastava, G. P. Origin of the Hot Phonon Effect in Group-III Nitrides. *Phys. Rev. B* **2008**, 77 (15), 155205.
- (100) Piyathilaka, H. P.; Sooriyagoda, R.; Esmailpour, H.; Whiteside, V. R.; Mishima, T. D.; Santos, M. B.; Sellers, I. R.; Bristow, A. D. Hot-Carrier Dynamics in InAs/AlAsSb Multiple-Quantum Wells. *Sci. Rep.* **2021**, 11 (1), 10483.
- (101) Clady, R.; Tayebjee, M. J. Y.; Aliberti, P.; König, D.; Ekins-Daukes, N. J.; Conibeer, G. J.; Schmidt, T. W.; Green, M. A. Interplay between the Hot Phonon Effect and Intervalley Scattering on the Cooling Rate of Hot Carriers in GaAs and InP. *Prog. Photovoltaics Res. Appl.* **2012**, 20 (1), 82–92.
- (102) Miyata, K.; Meggiolaro, D.; Trinh, M. T.; Joshi, P. P.; Mosconi, E.; Jones, S. C.; De Angelis, F.; Zhu, X.-Y. Large Polarons in Lead Halide Perovskites. *Sci. Adv.* 2017, 3 (8), e1701217.
- (103) Landau, L. D. Electron Motion in Crystal Lattices. *Phys. Z. Sowjet.* **1933**, 3, 664.
- (104) Pekar, S. Local Quantum States of Electrons in an Ideal Ion Crystal. *Zhurnal Eksp. I Teor. Fiz.* **1946**, 16 (4), 341–348.
- (105) Landau, L. D.; Pekar, S. I. Effective Mass of a Polaron. *Zh. Eksp. Teor. Fiz* **1948**, 18 (5), 419–423.
- (106) Landau, L. D. Über Die Bewegung Der Elektronen in Kristalgitter. *Phys. Z. Sowjetunion* **1933**, 3, 644–645.
- (107) Pekar, S. Issledovaniya Po Èlektronnoi Teorii Kristallov, Gostekhizdat, Moscow, 1951. *Transl. as Res. electron theory crystals, US At. Energy Com., Oak Ridge, TN* **1963**.
- (108) Fröhlich, H. Electrons in Lattice Fields. *Adv. Phys.* **1954**, 3 (11), 325–361.
- (109) Fröhlich, H.; Pelzer, H.; Zienau, S. XX. Properties of Slow Electrons in Polar Materials. *London, Edinburgh, Dublin Philos. Mag. J. Sci.* **1950**, 41 (314), 221–242.
- (110) Achermann, M.; Bartko, A. P.; Hollingsworth, J. A.; Klimov, V. I. The Effect of Auger Heating on Intraband Carrier Relaxation in Semiconductor Quantum Rods. *Nat. Phys.* **2006**, 2 (8), 557–561.
- (111) Fu, J.; Xu, Q.; Han, G.; Wu, B.; Huan, C. H. A.; Leek, M. L.; Sum, T. C. Hot Carrier Cooling Mechanisms in Halide Perovskites. *Nat. Commun.* **2017**, 8 (1).

- (112) Manser, J. S.; Kamat, P. V. Band Filling with Free Charge Carriers in Organometal Halide Perovskites. *Nat. Photonics* **2014**, 8 (9), 737–743.
- (113) Fang, H.-H.; Adjokatse, S.; Shao, S.; Even, J.; Loi, M. A. Long-Lived Hot-Carrier Light Emission and Large Blue Shift in Formamidinium Tin Triiodide Perovskites. *Nat. Commun.* **2018**, 9 (1), 243.
- (114) Li, M.; Fu, J.; Xu, Q.; Sum, T. C. Slow Hot-Carrier Cooling in Halide Perovskites: Prospects for Hot-Carrier Solar Cells. *Adv. Mater.* **2019**, 31 (47), 1802486.

Chapter 2

Experimental Section

2.1. The hot injection technique used to synthesize the halide perovskites

It is widely recognized that the choice of synthetic route employed in the fabrication of LHP NCs profoundly influences their characteristics, especially their optical properties. The way in which surface bonds are terminated and the stoichiometric ratio of the ions composing the perovskite structure are the primary factors responsible for this diversity. Hot injection (HI) method, is considered the most effective method for producing high-quality NCs.

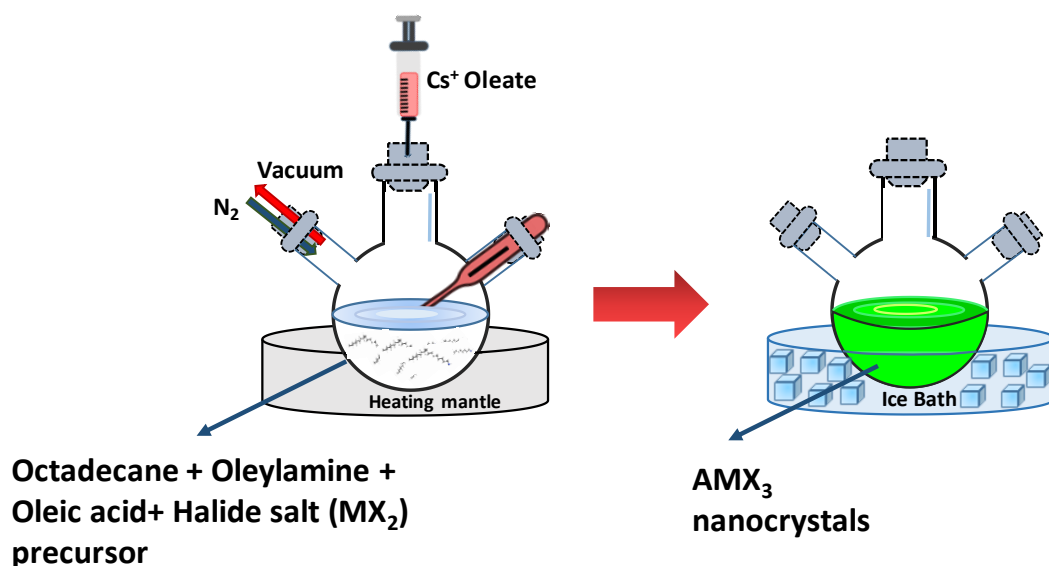


Figure 2.1 The schematic representation of the HI method used to synthesize perovskite NCs.

It is recognized for its ability to precisely synthesize nanoparticles or NCs and regulate both size and composition as shown in **Figure 2.1**. Originally pioneered by Alivisatos and Bawendi for the synthesis of materials like II-VI chalcogenide quantum dots (QDs) by HI method, is fundamentally grounded in the principles elucidated by LaMer and Dinegar.¹⁻³ Their work

reveals the manner in which the formation of finely dispersed colloidal NCs relies upon the rapid nucleation and subsequent controlled growth of existing nuclei. Following Lamer's model, the entire process of NC formation can be categorized into three primary phases (as depicted in **Figure 2.2**).

- **Generation:** In the initial phase, soluble atoms are generated within the solution.
- **Self-nucleation:** The subsequent stage marks the onset of nucleation, wherein the atomic concentration exceeds the critical supersaturation level ($C_{\text{min nucleation}}$). This breach of the nucleation energy barrier initiates the formation of atomic clusters.
- **Growth:** Following nucleation, as the atomic concentration decreases and falls below $C_{\text{min nucleation}}$ but remains greater than the saturation concentration (C_s), the growth process commences. During this phase, smaller nuclei grow into larger ones, facilitated by diffusion processes.

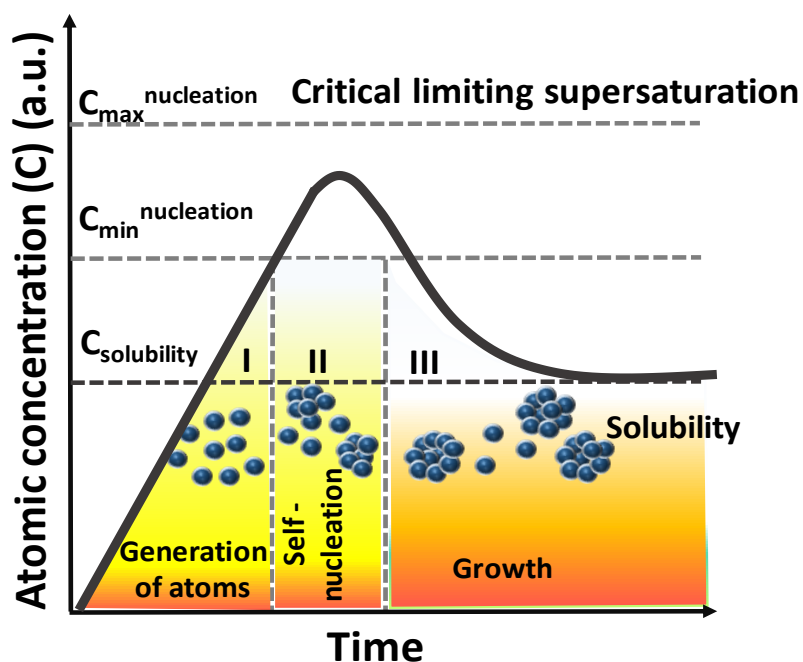
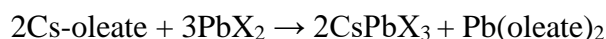


Figure 2.2 A schematic illustration depicting the sequential changes in atomic concentration within a classical LaMer mechanism across its three reaction phases.

This method involves the prompt injection of a precursor solution, typically containing metal salts and coordinating ligands, into another hot solvent or reaction medium. The injection leads to a sudden increase in temperature and triggers the nucleation and growth of nanoparticles.

Although the synthesis procedure, crystallography studies, and photoconductivity of direct bandgap CsPbX₃ materials were documented over 50 years ago, their utilization in the form of colloidal nanomaterials has remained unexplored.⁴ In 2013, Schmidt and his team succeeded in synthesizing MAPbBr₃ NCs through a solution-based colloidal method. In their pioneering work, they achieved a noteworthy PLQY of around 20 % for the CsPbX₃ NCs.⁵ However, in 2015 Protesescu and his colleagues presented an uncomplicated colloidal synthesis method for producing monodisperse CsPbX₃ NCs characterized by their cubic shape and cubic perovskite crystal structure, with sizes ranging from 4 to 15 nm.⁶ They achieved this using the traditional HI synthesis method, a technique commonly employed for the preparation of conventional colloidal QDs like CdS and PbS.^{7,8} The PL properties of CsPbX₃ NCs are marked by narrow emission line widths, ranging from 12 to 42 nm, high PLQY between 50 % and 90 %, and PL radiative lifetimes ranging from 1 to 29 ns. By altering the halide precursors (from Cl to I), and the level of confinement the resulting NCs can be tuned to exhibit a variable band gap spanning a wide range, typically from 410 to 700 nm. As the degree of confinement increases, the band gap tends to increase.⁹ The HI synthesis of CsPbX₃ NCs comprises two fundamental steps. The initial stage involves the preparation of Cs-oleate, while the second stage involves creating a lead (II)-halide-based precursor into which a suitable amount of Cs-oleate is rapidly injected. Due to the nature of the underlying ionic mechanism, which accounts for their extraordinarily rapid nucleation and growth kinetics, with growth occurring within a mere few seconds, the reaction flask is quickly immersed in a cold bath to quench the reaction and yield CsPbX₃ NCs. The underlying reaction driving this process can be summarized as follows:¹⁰⁻¹²



Nonetheless, alongside the HI technique, other liquid-phase strategies, including ligand-assisted reprecipitation (LARP) method and solvothermal synthesis, have also been deployed for producing MHP NCs and are frequently utilized.¹³ These alternative synthesis methods unquestionably yield high-quality and luminescent NCs. In conclusion, conventional two-step HI method is the most established approach for synthesizing the high quality, uniformly sized perovskite NCs. As a result, the HI synthesis route was designated for the synthesis of all the inorganic nanostructures considered in this thesis.

2.2. Synthesis of perovskite nanostructures used in this thesis

The perovskite synthesis consists of a two-step process: first, the preparation of Cs-oleate, followed by the injection of Cs-oleate into the Pb-precursor solution. So, we begin with the preparation of Cs-oleate, which is a common step in all the synthesis procedures.

2.2.1. The chemicals needed for all the synthesis conducted in this thesis

- ✓ **Chemicals and reagents:** Cesium carbonate (Cs_2CO_3 , 99 % trace metals basis), Lead (II) bromide (PbBr_2 , 99.99 % trace metals basis), Lead (II)chloride (PbCl_2 , 99.99 % trace metals basis) %), Lead (II) oxide (PbO , 99.999%), 2-bromoacetophenone ($\text{C}_6\text{H}_5\text{COCH}_2\text{Br}$, 98%), $\text{EuCl}_3 \cdot 6\text{H}_2\text{O}$ (99.9%), Europium(III) chloride hexahydrate ($\text{EuCl}_3 \cdot 6\text{H}_2\text{O}$, 99.9%), $\text{EuBr}_3 \cdot 6\text{H}_2\text{O}$ (99.9%), Europium(III) bromide hexahydrate ($\text{EuBr}_3 \cdot 6\text{H}_2\text{O}$, 9.9%) and Trioctylphosphine (TOP, 97 %) were purchased from Sigma-Aldrich.
- ✓ **Capping Agents:** 1-octadecene (ODE, tech, 90%), Oleylamine (OLM, tech, 70 %) and Oleic acid (OA, tech, 90) were purchased from Sigma-Aldrich and used without further purification.
- ✓ **Solvents:** Ethyl acetate (EtOAc, 99.5%), methyl acetate (MeOAc, 99.5%), Anhydrous dichloromethane (DCM) ($\geq 99.8\%$), toluene (ACS reagent, $\geq 99.5\%$) and n-hexane was purchased from Sigma-Aldrich and used without further purification.

2.2.2. Preparation of Cs-oleate

In a 50 mL three-neck round-bottomed (RB) flask, a mixture consisting of 1.25 mmol (approximately 0.41 g) of Cs_2CO_3 , 20 mL of ODE, and 4 mmol (~1.4 mL) of OA was loaded. The mixture was continuously stirred was alternately degassed and purged with nitrogen (N_2), for a duration of 30 min, at a temperature of 120°C. This procedure was iterated to effectively eliminate any dissolved oxygen (O_2) and moisture from the flask. Afterwards, the mixture was heated to 150 °C within a N_2 atmosphere, in order to completely dissolve of Cs_2CO_3 . The full dissolution of Cs_2CO_3 is indicative of the formation of cesium oleate. The Cs-oleate solution was reheated to 120 °C, before injecting into the Pb precursor solution to synthesize the perovskite nanostructures.

2.2.3. Synthesis of CsPbBr₃ NCs

The colloidal CsPbBr₃ NCs were synthesized following a previously reported synthesis methodology with minor modifications.⁶ In a 25 mL three-neck RB flask, PbBr₂ (0.188 mmol), 5 mL of ODE, 0.7 mL of OA, and 0.7 mL of OLM were added. The resulting mixture underwent stirring under vacuum conditions for 30 min at a temperature of 120 °C. Subsequently, the mixture was alternately degassed and purged with N₂ for duration of 30 min. The temperature was then raised to 160 °C, and a solution of Cs-oleate (approximately 0.4 mL) was rapidly injected into the mixture. Within a span of 10 s, the reaction mixture was promptly cooled in an ice bath. Following this, the crude solution underwent centrifugation at 10,000 rpm for 10 minutes to eliminate any unreacted precursors. The supernatant obtained after centrifugation was transferred, and the resulting NCs were dispersed in n-hexane.

2.2.4. Synthesis of CsPbBr₃ NSs

The colloidal CsPbBr₃ NSs were synthesized following a previously reported synthesis methodology with minor modifications.⁹ In a three-neck RB flask, a mixture comprising 69 mg of PbBr₂ (equivalent to 0.188 mmol), 5 mL of ODE, 0.7 mL of OA, and 1.4 mL of OLM was introduced and subsequently subjected to vacuum drying at 120°C for a duration of 1 hour. Following this step, the temperature was elevated to 140°C, at which point 0.5 mL of the Cs-oleate precursor was rapidly injected into the reaction mixture. The reaction was maintained at the specified temperature for a period of 30 minutes and then quenched in an ice bath. The crude solution was dissolved with 5 mL of anhydrous DCM, and then centrifugation was carried out at 10,000 rpm for 10 min. The supernatant was discarded and the precipitated NSs were re-dispersed in 5 mL of anhydrous n-hexane.

2.2.5. Synthesis of Polyhedral Dodecahedron-CsPbBr₃ NCs

Polyhedral CsPbBr₃ nanostructures, with a dodecahedral shape, were synthesized using a previously established procedure reported by Pradhan and co-workers,¹⁴ with slight modifications. To outline the synthesis process, 0.4 mmol of PbO, 1.2 mmol of 2-bromoacetophenone, 2 ml of OA, 2 ml of OLM and 10 ml of ODE were loaded into a 50 mL RB flask. This mixture was subjected to stirring within a N₂ atmosphere and degassed at 120 °C for duration of 45 min, while continuously purging with N₂ gas. It is noteworthy that the initially yellow solution gradually transitioned to a red during this phase. Subsequently, the

temperature was elevated to 210 °C, resulting in the solution's color shifting to a faint yellow shade after 1 h. Under these reaction conditions, 1 mL of Cs-oleate was swiftly injected into the solution. Following the introduction of the Cs-oleate solution, the reaction mixture was kept for 15 min, followed by rapid cooling in ice-bath. At this stage, a distinct bright green color was observed in the reaction mixture. The raw colloidal solution was centrifuged at 8000 rpm for 10 min. Subsequently, the resulting precipitate was collected and re-dispersed in hexane, while the supernatant solution was cautiously removed. For further purification, the precipitate was dispersed in a hexane: methyl acetate mixture (with a ratio of 4:1) and subjected to another round of centrifugation at 6000 rpm for 5 minutes. Finally, the dodecahedron-CsPbBr₃ NCs were obtained as a precipitate and re-dispersed in hexane for the further experiments.

2.2.6. Synthesis of CsPbCl₃ NCs

CsPbCl₃ NCs were synthesized with small alterations to the previously published method.⁶ PbCl₂ (0.2 mmol), ODE (10 mL), OA (1 mL), 1ml TOP and OLM (1 mL) were loaded into a 3-neck RB flask, and the reaction mixture was continuously stirred under vacuum for 30 min at 120 °C. The mixture was stirred under vacuum at 120°C for 30 min, followed by continuous purging with N₂. Further, the temperature was raised up to 160 °C and ~1 mL of Cs-oleate solution was swiftly injected. Then the reaction mixture was cooled down within 10 s in an ice bath. The obtained crude solution was subjected to centrifugation at 6000 rpm for 10 min. The supernatant obtained after centrifugation was discarded, and the isolated CsPbCl₃ NCs were washed and dispersed in toluene /hexane for further characterization.

2.2.7. Synthesis of Eu-CsPbCl₃ NCs

Europium doped CsPbCl₃ NCs (Eu-CsPbCl₃ NCs) were synthesized with minor modifications to the formerly reported method.¹⁵ To start, 0.188 mmol of EuCl₃ was dissolved in 10 ml of ODE, OLM (1 mL), and OA (1 mL), at a temperature of 160 °C for 1 h and the degassed while purging with N₂ for 30 min. Subsequently, 0.376 mmol of PbCl₂ was added to the solution, and the mixture was continuously heated at 160 °C for 1 h. Once both Europium and lead chlorides were completely dissolved, the temperature was raised to 240 °C under N₂ purging. At this point, Cs-oleate was injected into the precursor solution, and within 30 s, the solution was rapidly cooled in an ice bath. The resulting NCs were centrifuged at 8000 rpm for 10 min, and

the supernatant was discarded. The NCs were then dispersed in toluene and was centrifuged again at 8000 rpm for 10 min. Finally, the resulting NCs were re-dispersed in toluene for further use.

2.2.8. Synthesis of Eu-CsPbBr₃ NCs

Europium doped CsPbBr₃ NCs (Eu-CsPbBr₃ NCs) were synthesized with minor modifications to the formerly reported method.¹⁵ In a 25 mL three-neck RB flask, 0.188 mmol of EuBr₃ was dissolved in 10 ml of ODE, OLM (1.2 mL), and OA (1.2 mL). This mixture was heated to 80 °C and maintained at that temperature for 1 h while being degassed by purging with N₂ for 30 min. Afterward, PbBr₂ (0.188 mmol) was added to the solution. The temperature of resulting mixture was increased to 120 °C under continuous stirring, and then was degassed under N₂ purging for 30 min at a temperature of 120 °C. The temperature was then raised to 200 °C, and a solution of Cs-oleate (approximately 0.4 mL) was rapidly injected into the mixture. Within a span of 10 s, the reaction mixture was promptly cooled in an ice bath. Following this, the reaction mixture was promptly cooled in an ice bath. After cooling, the crude solution was centrifuged at 10,000 rpm for 10 min to remove any unreacted precursors. The supernatant obtained after centrifugation was transferred, and the resulting NCs were dispersed in n-hexane.

2.3. Characterization techniques

This section presents a comprehensive review of all the characterization techniques employed for conducting the experiments in this thesis.

2.3.1. X-Ray Diffraction (XRD)

Max von Laue's discovery in 1912 revealed that crystalline substances perform as three-dimensional diffraction gratings for X-ray wavelengths analogous to the spacing of planes within a crystal lattice. This discovery laid the foundation for XRD, which has become a common technique for studying crystal structures and atomic arrangements.

2.3.1.1. Principle

XRD works on the principle of constructive interference of monochromatic X-rays when they interact with a crystalline sample.^{16,17} The X-rays are first produced using a cathode ray tube, filtered to ensure they are of a single wavelength, and then focused into a concentrated beam before being directed at the sample.¹⁸

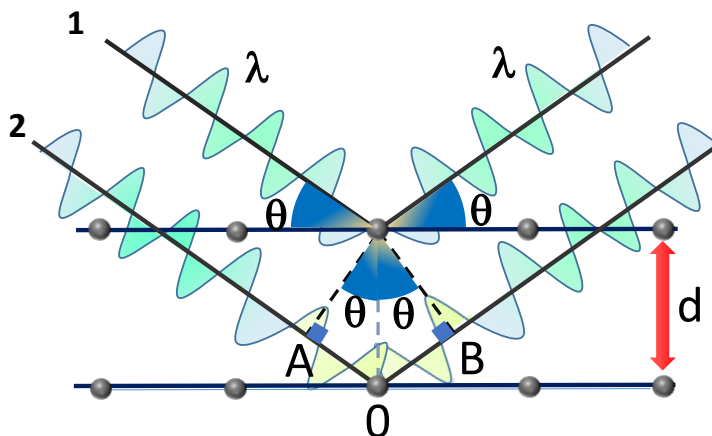


Figure 2.3 Schematic illustration depicting the Diffraction of Incident X-rays by a crystal. X-rays are scattered by the crystal lattice, and their diffraction angles are governed by Bragg's Law, for the determination of crystal structure.

The intriguing aspect lies in the fact that the interatomic distances within crystalline systems approximate the wavelengths of X-rays, typically a few Angstroms. This alignment allows the crystal lattice planes to function as diffraction gratings, especially when X-rays strike them (as shown in **Figure 2.3**) at a glancing angle thus, the angle of reflection will be θ . As it can be clearly seen in **Figure 2.3**, the two waves transverse different paths. The 2nd wave has to travel an additional path length corresponding to “AO+ OB”. So, when these incident X-rays interact with the sample, they create constructive interference (leading to a diffracted ray). To ensure the same phase of both these waves after reflection by the atoms and to facilitate constructive interference, it is imperative that the path difference between the two waves corresponds to an integer multiple of their respective wavelengths. The governing principles for this phenomenon are encapsulated in the well-established "Bragg's equation," which was articulated by William Henry Bragg and William Lawrence Bragg.¹⁶ The Bragg's Law is a central principle in X-ray crystallography that describes the relationship between the angle of incidence (θ), the wavelength of X-rays (λ), and the spacing between atomic planes (d) in a crystal lattice.

Mathematically, Bragg's Law is expressed as

$$n\lambda = 2d\sin\theta \quad \text{Eq.2.1}$$

Where, n is an integer (1, 2, 3, ...) signifying the order of the diffraction peak, λ is the wavelength of the incident X-rays, d is the spacing between adjacent atomic planes in the

crystal lattice, θ is the angle between the incident X-ray beam and the direction of the diffracted X-ray beam.

When the path difference traveled by X-rays reflecting off different planes of atoms within the crystal is an integer multiple of the wavelength ($n\lambda$), the waves reinforce each other, leading to a diffraction peak. By measuring the angles at which diffraction peaks occur and knowing the wavelength of the incident X-rays, the d-spacing within the crystal lattice can be determined. This information is crucial for determining the crystal's structure and is widely used in several scientific fields, including chemistry, materials science, and biology, to study the arrangement of atoms or molecules in crystalline substances.

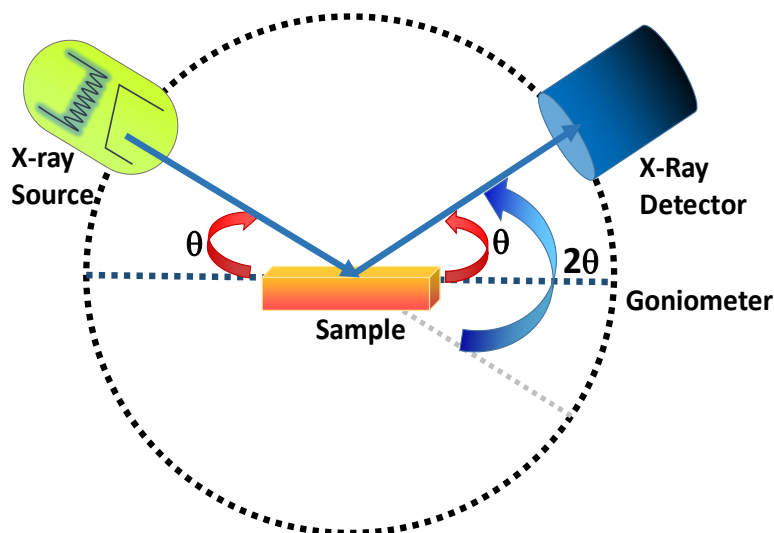


Figure 2.4 A schematic illustration of XRD setup.

The average particle size can also be calculated by applying Scherrer's equation and considering the width of the XRD peak which is stated as:¹⁹

$$\tau = \frac{k\lambda}{\beta \cos\theta} \quad \text{Eq.2.2}$$

In this equation, " τ " represents the average particle size in Angstroms (\AA), "k" is the shape factor (typically close to 1), " β " denotes the Full Width at Half Maximum (FWHM) of the peak, and " θ " stands for the diffraction angle

2.3.1.2. Instrumentation

A typical X-ray diffractometer setup comprises three fundamental components: An X-ray source, a goniometer, and a detector (as shown in **Figure 2.4**).²⁰⁻²² X-rays are produced by directing high-energy electrons from the cathode onto the anode, typically made of materials

like copper (Cu) or manganese (Mn). X-ray diffractometers are traditionally designed using a goniometer, ensuring that for every angle θ by which the sample holder rotates in the direction of the incident X-ray beam, the detector, mounted on an arm for collecting the diffracted rays, moves by twice that angle (2θ). In X-ray diffraction, three crucial spectral lines are generated, known as $K_{\alpha 1}$, $K_{\alpha 2}$, and K_{β} . $K_{\alpha 1}$ and $K_{\alpha 2}$ are very close in energy and form what's called a K_{α} doublet, as $K_{\alpha 1}$ is twice as intense as $K_{\alpha 2}$. The most commonly used X-ray diffraction radiation is Cu K_{α} , which has a wavelength of 1.54 Å, and is suitable for studying a wide range of materials. By applying appropriate biasing, these electrons are accelerated toward the anode, which acts as the target source for X-ray emission. When these electrons strike the anode's surface with sufficient energy, they can displace inner shell electrons of the anode material. This process generates characteristic X-ray spectra. It then strikes the sample surface at an incident angle θ . After interacting with the sample, the diffracted X-ray beam exits at an angle of 2θ . During the experiment, the intensity of the reflected X-rays is measured. The results are then recorded and processed by the detector, which converts the collected signal into a count rate. This information is typically sent to a device, such as a computer monitor, for further analysis. In this thesis, we collected diffraction data using a Bruker D8 advance X-ray diffractometer, utilizing Cu K_{α} X-ray radiation with a wavelength of 1.54178 Å. The scanning range was set from 10 to 80° with a scanning rate of $\sim 0.005^{\circ}$ per second. The X-ray source operated at an accelerating voltage of 40 kV and a current of 25 mA. Samples were prepared as thin films on glass substrates. The crystal structure of the samples was confirmed by comparing their diffraction patterns to the standard database provided by the International Centre for Diffraction Data (ICDD) database, formerly known as the Joint Committee on Powder Diffraction Standards (JCPDS).

2.3.2. Transmission Electron Microscopy (TEM)

Over the years, there has been significant development and research in the field of microscopic techniques for the analysis and characterization of materials. Microscopes come with varying specifications, including magnification and resolution, and these differences impact the range of applications they can effectively serve. In 1897, Ferdinand Braun developed the cathode ray oscilloscope (CRO).²³ In 1928, Max Knoll headed a group of researchers dedicated to further improve the CRO technique at the Technical University of Berlin. Further in 1931, it was the collaborative effort of Max Knoll and Ernst Ruska that led to a major breakthrough as they

successfully produced magnified images of mesh grids. The significance of their achievement became evident in 1939 when the very first commercial electron microscope was installed in the Department of Physics at IG-Farben-Werke.²⁴

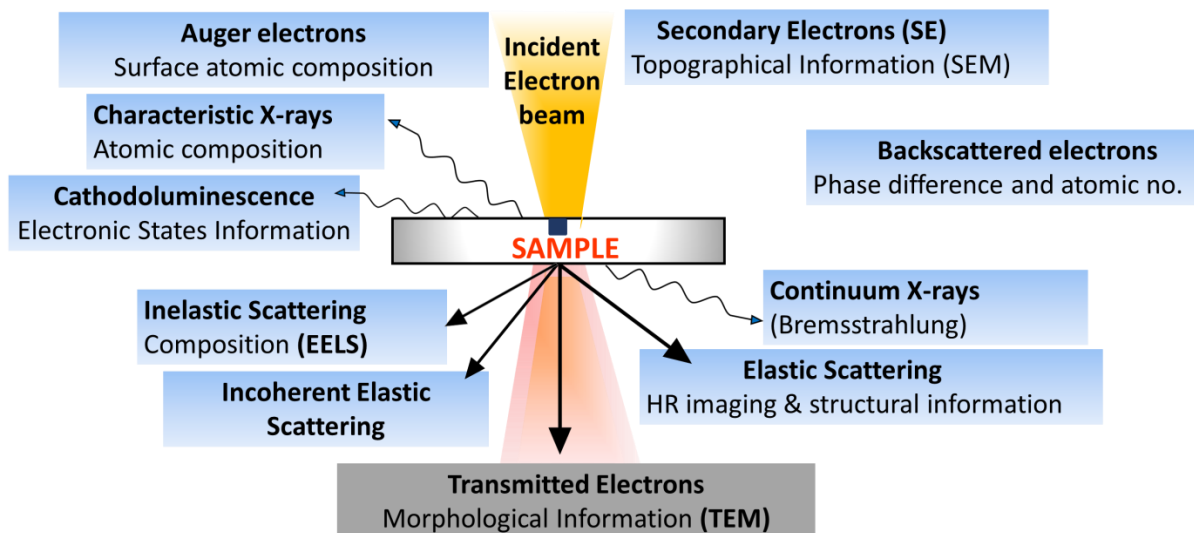


Figure 2.5 Generation of rays and electrons as a consequence of the interaction between the incoming electron beam and the sample.

An electron microscope (EM) closely resembles a conventional optical microscope commonly used to enlarge images of small specimens.²⁵ The primary distinction lies in the equipment and its remarkably high resolution capabilities. Instead of visible light, EM employs an electron beam as its source of illumination, which is directed onto the specimen using electromagnets (in contrast to lenses used for focusing visible light in an optical microscope).²⁶ The electrons hold an exceptionally low effective wavelength, EM enables the visualization of extremely tiny objects, such as atoms. There are primarily three distinct EM techniques: Transmission Electron Microscopy (TEM), Scanning Electron Microscopy (SEM), and Scanning Tunneling Microscopy (STM). Each operates differently, but in this discussion, we will focus exclusively on TEM. TEM stands out as the most potent electron microscopy technique currently known, offering a resolution approaching 1 nm. TEM finds extensive use across various scientific fields for observing the structure, morphology, defects, and other characteristics of materials. TEM extends beyond just imaging samples; it is used for quantitative material analysis. Energy dispersive x-ray spectroscopy (EDS) studies the X-rays emitted from a material when bombarded with electron beams, providing information about the elements present in the

material. The selected area electron diffraction (SAED) technique utilizes diffracted electrons to examine the crystal structure and phase exhibited by the material.

2.3.2.1. Working Principle

The fundamental principle of TEM revolves around directing a highly accelerated electron beam through the specimen. This procedure initiates a sequence of interactions that gives comprehensive information about the sample's morphology, size, and composition.^{26–28} When the sample is bombarded by the high-intensity electron beam, the sample's atoms act as scatterer, giving rise to several types of scattering processes. The interaction of electrons with the specimen is depicted in **Figure 2.5**. These processes include characteristic X-ray emission, backscattering of electrons, inelastic and elastic scattering processes, affecting the energy and trajectory of the electrons, and secondary electron emission.^{27,28}

The resolution of an optical microscope depends on the photon energy used for probing and the numerical aperture of the system. The maximum achievable resolution (d) can be determined using the following equation:²⁹

$$d = \frac{\lambda}{(2n\sin\alpha)} \quad \text{Eq.2.3}$$

Here, n represents the refractive index of the medium, and α is the half-angle of the light cone. However, for electron microscopy, the wavelength of electrons is governed by the De-Broglie equation, and the electron beam is emitted from an electron gun with high speed.

Taking relativistic effects into account, the wavelength can be expressed as:²⁹

$$\lambda_e = \frac{h}{\sqrt{2m_0E\left(1 + \frac{E}{2m_0c^2}\right)}} \quad \text{Eq.2.4}$$

In this equation, h is Planck's constant, m_0 is the mass of the electron, and E is the kinetic energy of the accelerated electron.

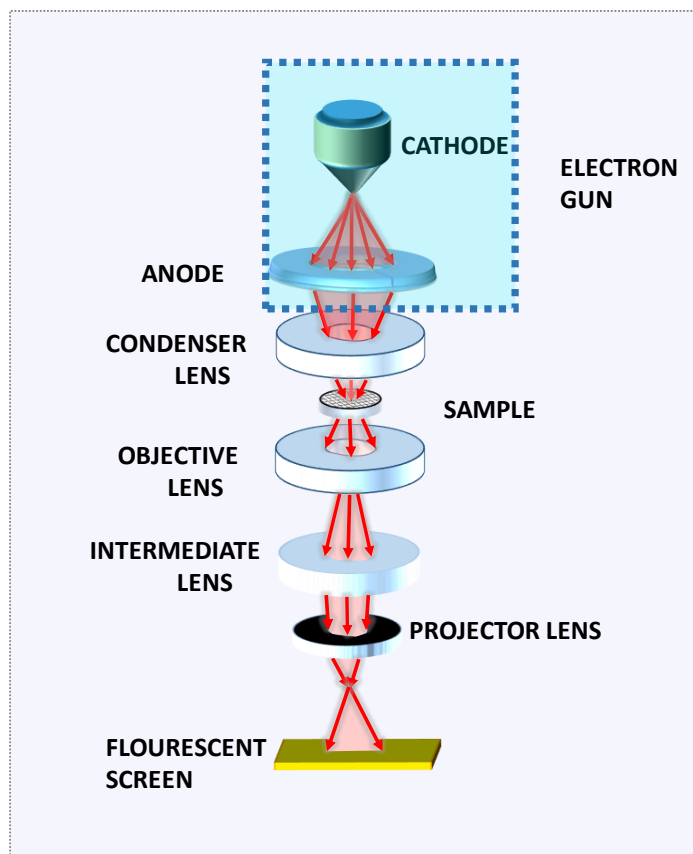


Figure 2.6 The schematic illustration of the experimental setup for TEM.

2.3.2.2. Instrumentation

The TEM setup is a multifaceted system composed of various components, as illustrated in **Figure 2.6**.^{29,30}

(i) Electron Gun: The electron source is placed at the top of the TEM column. A cathode, typically using a filament, is connected to a voltage source in order to generate and accelerate electrons. In TEM, electron speed plays a critical role because electrons that move at higher speeds display shorter wavelengths, which ultimately results in enhanced resolution. These accelerated electron beams are released from the gun through an anode plate and travel downward within the instrument. There are various types of filaments available, including tungsten (W) and LaB₆. These filaments are heated to temperatures of 2700 K and 1700 K for tungsten (W) and LaB₆, respectively. In comparison to the tungsten (W) filament, the LaB₆ filament is ten times brighter and boasts a longer operational lifespan.

(ii) Electromagnetic Coil: The electromagnetic coils placed in the setup basically acts as lenses for the electron beam (in the same way as the optical lenses act for light). In the TEM column, there are four electromagnetic coils in operation. The initial lens, referred to as the **condenser lens**, is responsible for converging the initially parallel electron beam emitted from the gun into a tightly concentrated beam. Another condenser lens then focuses the electrons onto the sample as required. Subsequently, the second, third, and fourth lenses, known as the **objective, intermediate, and projector lenses**, collectively aid in refining and precisely focusing the transmitted electron beams onto the fluorescence screen.

(iii) Aperture: Apertures are small metallic plates designed to exclude scattered or diffracted electrons from reaching the projector. They allow control over the intensity of the electron beams.

(iv) Sample Stage: Samples are typically placed on a copper grid and inserted between the condenser and objective lenses.

(v) Vacuum System: TEM operates in a high vacuum environment because electrons cannot travel effectively in air. Proper vacuum conditions minimize electron scattering caused by interactions with air particles. It also prevents contamination of the specimen and maintains electron gun efficiency. Proper vacuum maintenance is crucial for high-resolution imaging TEM.

(vi) Imaging: Transmitted electron beams are projected onto a fluorescence plate, which generates an image of the sample area under investigation. Beneath this plate, a charge coupled detector (CCD) camera records the images and transmits them to a computer as micrographs. The detector collects signals, which are digitized and processed by dedicated electronics for display on cathode ray tubes or monitors. Different detectors (scintillation-photomultiplier tubes, semiconductors, CCDs) are used depending on the imaging mode (STM, EELS, EDS) which is chosen.

In this thesis, the TEM and high- resolution TEM (HR-TEM) images of the perovskite nanostructures were taken using a JEOL model 2100 instrument with an operating voltage of 200 kV. This voltage choice improves resolution and does not damage the inorganic samples. The prepared NCs were diluted and drop-casted onto holey carbon films on 300 mesh copper grids for TEM sample preparation.

2.3.3. Steady State Optical Studies

Steady-state optical investigations include a collection of experimental methods such as UV-Vis absorption spectroscopy and PL spectroscopy, which are employed for examining the optical characteristics of nanomaterials when is no temporal variation. This provides insights into electronic transitions induced by optical radiation. These experiments are generally carried out in a consistent and unchanging state, in contrast to dynamic or time-resolved experiments.

2.3.3.1. UV-Vis Absorption Spectroscopy

The absorption spectroscopy is a study to understand the processes that occur when a material absorbs light at different wavelengths. The fundamental concept behind this method is that materials can absorb light, leading to the occurrence of electronic transitions where electrons move from the ground state to higher energy states.^{31,32} An optical spectrometer quantitatively measures a material's absorption or transmission. The absorbance data is represented as an absorbance (A) vs. wavelength, thus termed an absorption spectrum and covers the UV to NIR regions of the electromagnetic spectrum. Each material possesses distinct absorption characteristics that can serve as a unique identifier (similar to a fingerprint) assisting in their identification. This technique is commonly employed to gain insights into the ground state absorption properties, excitation coefficients, and the material's band gap.³³

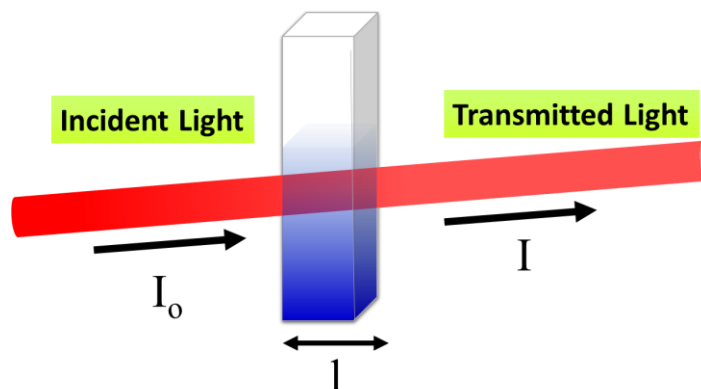


Figure 2.7 The schematic representation of the absorption phenomenon.

2.3.3.1.1. Principle

Absorbance is a measure of how much incident electromagnetic radiation from a source is absorbed compared to the transmitted electromagnetic radiation detected by a detector.

If the intensity of incident monochromatic light on the sample is I_0 and the intensity of light transmitted through the sample as I , (**Figure 2.7**) the absorbance of the material can be defined as:

$$A = \log (I_0 / I) \quad \text{Eq.2.5}$$

Beer-Lambert's law³⁴ provides insights into material absorption properties. As per the Lambert's law the absorbance 'A' of monochromatic light increases proportionally with the path length (' ℓ ') i.e., $A \propto \ell$. While, the Beer's law³⁵ establishes a direct relationship between the absorbance 'A' of light and the concentration ('c') of a solution i.e., $A \propto c$. Combining Beer and Lambert's laws, the Beer-Lambert law asserts that the absorbance 'A' of a monochromatic beam is directly proportional to both the concentration 'c' of the solution and the path length ' ℓ '.^{36,37}

$$A = \varepsilon . c . \ell \quad \text{Eq.2.6}$$

Here, ' ε ' represents the molar extinction coefficient.

2.3.3.1.2. Instrumentation

The fundamental configuration of an absorption spectrometer comprises four primary components: a light source, a monochromator, a sample stage, and a detector (as depicted in **Figure 2.8**).³⁸

1. **Light Source:** Typically, a single xenon lamp is employed to cover both the UV and Vis wavelength ranges, offering a broad spectral coverage. However, xenon lamps are costlier and have stability challenges. So, in order to cover entire UV and Vis region two light sources are employed, a deuterium arc lamp that serves as the preferred UV light source due to its reliability in the UV region. In contrast, tungsten or halogen lamps are used as a source in the visible light range, delivering consistent performance for various spectroscopic applications.
2. **Monochromator:** Monochromatic light can be produced by employing dispersion devices, such as prisms or holographic gratings. These devices disperse light into its various wavelengths at specific angles. When combined with an exit slit, a particular wavelength can be selected from the continuous light source, resulting in monochromatic illumination. In some instances, other types of filters or a combination of monochromator and filters may also be used.

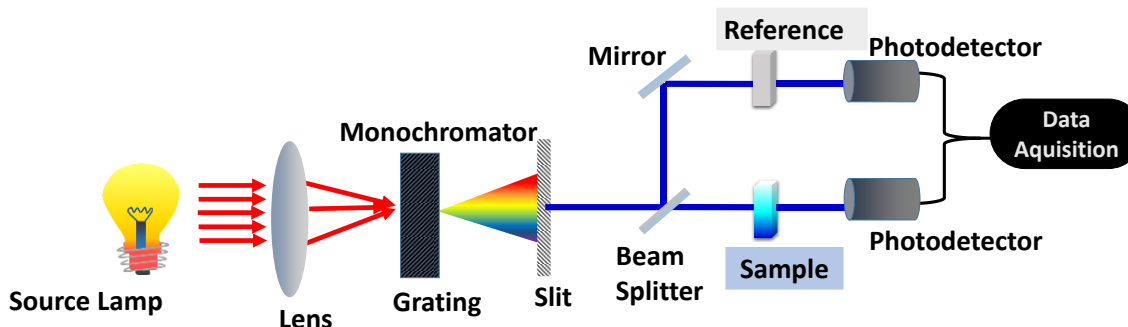


Figure 2.8 The basic experimental setup of a steady state absorbance spectrometer

3. **Sample Stage:** Following wavelength selection, the light passes through the sample under investigation. It is essential to perform a scan for the reference sample, often referred to as a "blank." This reference sample consists of a cuvette filled with the same solvent as that in which the sample is dispersed. The instrument automatically uses this reference signal to correct for any solvent-related effects on the absorption measurements, providing the absolute absorbance of the sample.
4. **Detector:** The transmitted beams from both reference and sample are directed to the detector, which converts changes in absorption due to the sample into an electronic signal, subsequently transmitted to a computer for analysis. An absorption spectrometer generally employs photomultiplier as a detector.

In this thesis, the absorbance of perovskite nanostructures across UV-VIS spectrum has been measured using a Shimadzu UV-2600 spectrometer with an operational range spanning from 200 nm to 900 nm. The light sources used in this spectrometer are: A Deuterium lamp for the ultraviolet (UV) range and a halogen lamp for the visible domain.

2.3.3.2. Photoluminescence (PL) Spectroscopy

The PL spectroscopy is a commonly employed method for understanding the optical characteristics of materials.^{39,40} After absorbing electromagnetic radiation, the photoexcited charge carriers within the material tend to recombine. During this process, they release their energy in the form of either light or heat, following either radiative or non-radiative pathways, respectively. PL spectroscopy, as illustrated in **Figure 2.9**, is employed to investigate these radiative phenomena.⁴¹

2.3.3.2.1. Principle

In order to emit photons, the photo excited carriers firstly need to relax to the least energetic vibrational state within the excited state. This explains the underlying reason for the observed redshift (i.e., stokes shift) in PL spectra in contrast to the lowest absorption peak.^{42,43} PL can be formally classified into two main categories: fluorescence and phosphorescence, and the categorization is based on the characteristics of the excited state:

1. **Fluorescence:** In fluorescence, the excited electrons return to their ground state relatively quickly, usually within nanoseconds. During this process, they emit photons, producing visible light. Fluorescence is typically characterized by its short-lived emission and is commonly observed in various everyday applications, such as fluorescent lighting and certain biological assays.
2. **Phosphorescence:** Phosphorescence, on the other hand, involves a longer delay between the excitation and emission of photons. In this case, the excited electrons remain in an excited state for a longer period, sometimes ranging from microseconds to hours, before they return to the ground state and emit photons. This delay in emission distinguishes phosphorescence from fluorescence. A well-known example of phosphorescence is the glow-in-the-dark materials or objects that continue to emit light after the light source is removed.

This technique provides valuable insights into various material characteristics, size distribution, band gap, energy transfer, charge transfer, and defect states.

One of the critical photophysical characteristics studied for perovskites in optoelectronic applications is the PLQY. The PLQY (Φ) is commonly used to assess how effectively a material emits absorbed photons through fluorescence phosphorescence, expressed as the ratio of emitted photons to absorbed photons.^{44,45}

$$\Phi = (N_{emitted}/N_{absorbed}) \quad \text{Eq.2.7}$$

Typically, PLQY is expressed as a percentage, although it is quantified on a scale ranging from 0 to 1.0. However, when dealing with unidentified samples, PLQY (Φ_s) is determined relative to a previously identified, a previously characterized and highly luminescent fluorophore reference. (Φ_r) using the following equation:

$$\Phi_s = \Phi_r \frac{I_s}{I_r} \frac{OD_r \eta_s^2}{OD_s \eta_r^2} \quad \text{Eq.2.8}$$

In this equation, I_s and I_r represent the area under the curves for the sample and reference, respectively. OD denotes the value of optical densities at the excitation wavelength, and η represents the refractive indices of their respective solvents.

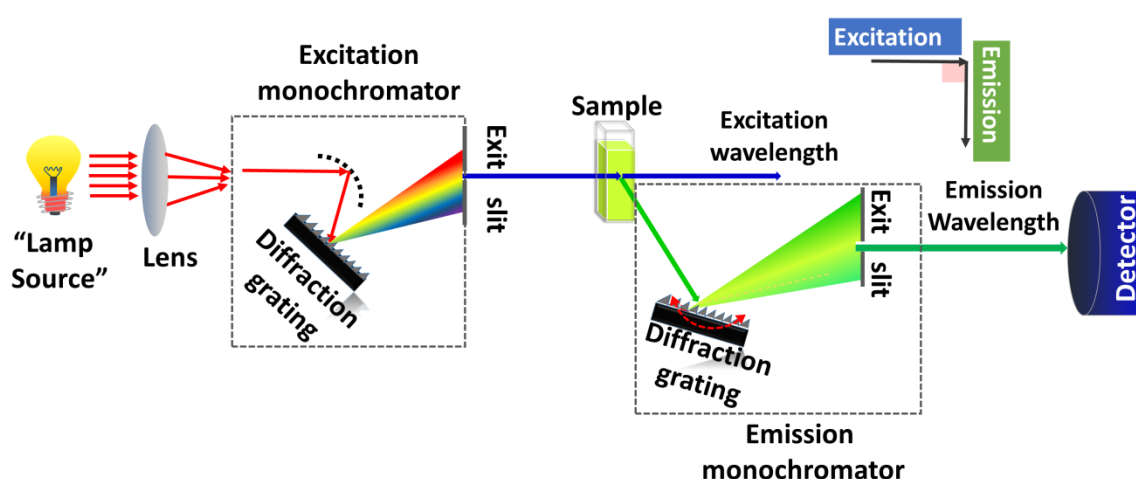


Figure 2.9 The experimental setup of the PL spectrometer consisting of its various components.

2.3.3.2.2. Instrumentation

The instrumental setup used for PL measurement is depicted in **Figure 2.9**. While the design of fluorometers may vary among different instruments, they share common elements that make up their basic configuration. These elements include:

Light Source: Fluorometers incorporate a steady light source, often a continuous xenon lamp. Xenon lamps are preferred because they emit intense white light across a wide wavelength range, spanning from the ultraviolet (UV) to the near-infrared region of the electromagnetic spectrum.

Excitation Monochromator: A monochromator assembly is used to select the desired excitation wavelength. This component is crucial for precisely tuning the excitation of the sample to a specific wavelength. It functions similarly to the first section of a steady-state absorption spectrometer.

Sample Holder: A sample holder is used to position and contain the sample being studied. This is where the sample is exposed to the excitation light, leading to radiative emission of photons.

Emission Monochromator: After emission from the sample, the emitted light is passed through another monochromator, known as the emission monochromator. This component selects only the relevant emission wavelengths while blocking out the excitation light.

Detector: The detector is responsible for collecting the emitted light from the emission monochromator. Typically, a photomultiplier tube (PMT) is used as the detector due to its low noise-to-signal ratio. In PL spectroscopy setups, the emitted radiation scatters in all directions. Unlike steady-state absorption instruments where the detector is positioned in line with the source, in PL spectroscopy, the detector is usually not aligned with the source to prevent the high-intensity excitation wavelength from reaching the detector unnecessarily. Instead, the detector is often positioned at a 90° angle to the incident beam to avoid overlap between the excitation and emission signals, as these wavelengths can be quite close to each other.

In this thesis the Edinburgh FS5 spectrofluorometer is used to measure the PL spectra of the perovskite nanostructures, which employs a 150 W continuous-wave (CW) ozone-free xenon arc lamp as its light source. This spectrofluorometer enables excitation at wavelengths ranging from 230 nm to 1000 nm and the monitoring of emitted light in the range from 200 nm to 900 nm. The emission detector in this setup is a photomultiplier PMT-900 with a spectral range of 200 nm to 900 nm.

2.3.4. Time Correlated Single Photon Counting (TCSPC) / Time Resolved Photoluminescence (TRPL) studies

Time-resolved PL spectroscopy is a tool that is frequently employed method for assessing fluorescence decay in the temporal domain for quantifying fluorescence lifetimes of luminous materials.⁴⁵ For the lifetime measurements, time correlated single photon counting (TCSPC) is used for data acquisition. To explore the initial processes occurring shortly after photoexcitation, such as carrier relaxation and recombination, in diverse perovskite nanostructures, we can employ two experimental techniques: TA methods, which will be discussed in greater detail later, and TRPL studies.⁴⁶⁻⁴⁸ As we specifically focus on the radiative recombination leading to the PL phenomenon, it becomes essential to employ a precise and accurate method to determine PL lifetimes. TA spectroscopy, while a powerful

technique, is not well-suited for measuring PL lifetimes across this entire range. The reason is that covering such timescales would require an impractically long translation stage, approximately 10 to 15 meters in length. Thus, TCSPC is one such technique used to quantify the average time a photon spends in the excited state before returning to the ground state during PL.

2.3.4.1. Working Principle:

In TCSPC instrument, the measurement of single photon arrival times is based on the laser excitation pulse which is termed as a reference signal. This reference pulse functions as the starting point, or "start" signal, for the time measurement. Simultaneously, the PL emitted from the sample acts as the stopping point, or "stop" signal.^{49,50}

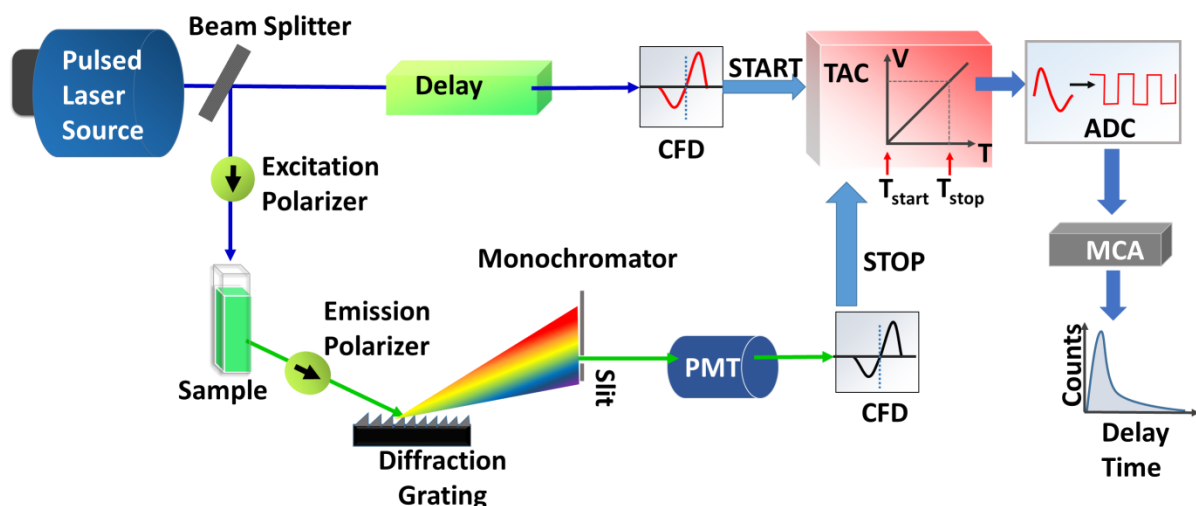


Figure 2.10 The schematic representation of a TCSPC setup.

The electronic system then calculates the time gap between the excitation and emission events. Each successful START-STOP sequence adds to a histogram in memory, where the x-axis represents different time intervals for completing these sequences. However, it's crucial to ensure that only one photon event is counted for each light flash due to statistical considerations. Failure to do this can lead to multiple photon events, resulting in inaccurate data, often known as the "pulse-pile up issue." To obtain reliable data, a single excitation-emission measurement cycle isn't enough. Instead, millions of these START-STOP sequences are needed. This process creates a histogram over time, showing how the PL intensity of the

sample evolves over various time intervals. Therefore, the most practical and effective option is to utilize TCSPC techniques, for accurate measurement of PL lifetimes and provides valuable insights into the dynamics of radiative recombination processes in perovskite nanostructures. A typical TCSPC system includes the following key components⁵¹: a pulsed laser light source, a timing control device, a single photon detector, and a monochromator (as depicted in **Figure 2.10**). The laser pulse originating from the excitation source is split into two segments: one portion is used to excite the sample, while the other is directed towards a photodiode, responsible for generating an electrical signal for the constant fraction discriminator (CFD). The signal from the detector is channeled to the CFD, which triggers a voltage rise in the TAC. The START signal pulse, initiated by the detection event, commences the charging of the TAC's capacitor. Charging continues until the STOP signal pulse, generated by the laser source as a synchronization trigger, upon photo-excitation, the sample emits photons, which are collected at right angles to the excitation source. Subsequently, these emitted photons pass through a monochromator before reaching the PMT for detection.

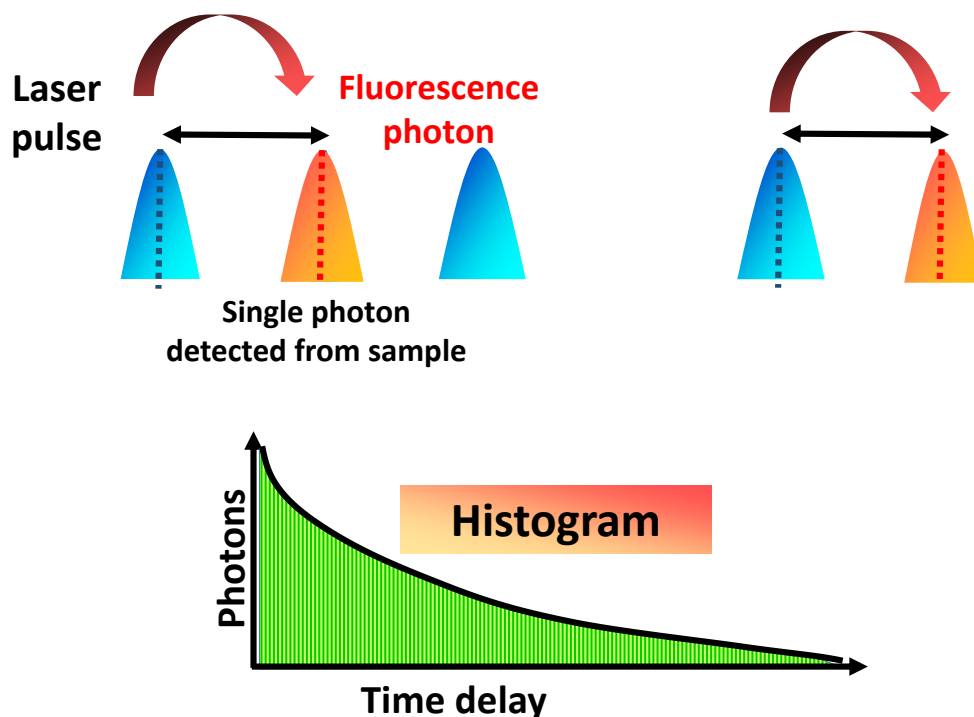


Figure 2.11 The principle involved in TCSPC measurement.

The signal from the PMT is sent to the CFD, followed by the TAC, which serves as the **Stop signal**. The signal from the TAC, corresponding to the time difference between the start and stop signals, is directed to the multi-channel analyzer (MCA), which provides the numerical value of the time delay through an analog-to-digital converter (ADC). The final output consists of counts plotted against channels, with each channel representing a distinct time delay as shown in **Figure 2.11**. To ensure high-quality decay curve recordings, the PL from the sample is detected at a specific angle known as the "magic angle" (54.7°) to mitigate any potential anisotropy effects. The maximum count threshold is set at 10000, and the decay is recorded within the range of ns to ms, as per the sample being analyzed. A picosecond photon detection (PPD) module is utilized, a compact device housing necessary electronics, including a pre-amplifier, CFD, PMT, and a suitable power supply.

In this thesis, PL lifetime of prepared perovskite nanostructures was attained using the Deltaflex Modular Fluorescence Lifetime System, provided by HORIBA Scientific. This spectrofluorometer is a fully integrated instrument with a standard 90° layout, specifically designed for measuring excited state lifetimes. It has the capability to measure lifetimes ranging from 1 nanosecond to well over 1 second. Commonly used wavelengths in the study include 280 nm, 365 nm and 402 nm. The 280 nm excitation source is a pulsed LED with a pulse width (instrument response function - IRF) of less than 1 ns, while the 365 nm and 402 nm wavelength source is a pulsed laser diode with an IRF < 200 ps. To streamline the measurement process, the system incorporates a compact PPD module. This module consolidates all the essential electronics, including a pre-amplifier, CFD, PMT, and the necessary power supply, into a single, compact device. This integration simplifies TRPL measurements and ensures precise data collection.

2.3.5. Transient Absorption (TA) Spectroscopy

"Shedding light on the invisible: Pump-probe spectroscopy reveals hidden secrets."

Numerous natural events, including the atomic motion during chemical reactions, vibrations of molecules, absorption and emission of photon, and several scattering phenomena, take place within very short time scales.⁵² Even in time periods as short as a few picoseconds (10^{-12} s) or femtoseconds (10^{-15} s), some of these events can be witnessed. Understanding the dynamics of the many excitations in matter entails observation of these prompt processes, which has spurred significant improvements in the precision of time-resolved measurements during the past

several decades. The uncertainty in timing must be less than the process's time scale in order to quantify ultrafast processes accurately, necessitating a temporal resolution of about 10^{-15} s. However, due to the limitations of detectors such as fast photodiodes and in stroboscopic oscilloscopes, which have a temporal resolution of just 10^{-10} s. A radically alternative methodology proposed is pump-probe spectroscopy, which necessitates indirectly detecting a process using a "probe beam" i.e., laser pulse. Pump-probe spectroscopy has expanded its popularity as a method for time-resolved research and has contributed to advances in diverse scientific disciplines. Let's first explore the inception and evolution of this technique in order to comprehend the origin of time-resolved studies. The high-speed photography experiments carried out by Eadweard Muybridge in 1878 are principally accredited with giving an upsurge to time-resolved optical research.⁵³ Muybridge was able to record distinct phases of a horse's motion on the Palo Alto racecourse using many cameras with rapid shutters that allowed exposure times of the order of 10^{-3} s. He captured the galloping phase of the horse's motion in a slow-motion video and resolved the motion in real-time. Alto racecourse, capturing the running phase in slow motion and capturing precisely what happens when all four hooves are lifted off the ground. Following this significant finding, advancements in technical capabilities for producing ever-shorter light flashes were linked to improvements in the time resolution of high-speed photography.^{53,54} Harold E. Edgerton developed stroboscopic photography in the middle of the twentieth century, which reduced the time resolution to a few microseconds.⁵⁵ Another noteworthy Revolution in Photography was observed by MIT Press, 1979: Short light pulses can be used to start a dynamic process as well as to monitor it. The "pump-probe" approach, developed by Abraham and Lemoine in 1899, uses two synchronized light pulses: an excitation or "pump" pulse that initiates a photo-induced phenomenon and a delayed "probe" pulse that detects a time-dependent modification of an optical phenomenon.⁵⁶ This important discovery led to the connection between gains in high-speed photography's time resolution and improvements in the technical ability to produce ever-shorter light flashes. Later, in 1988, Ahmed Zewail used fs laser pulses to explore the transient reaction dynamics and monitored the transition states, and for that he was awarded the Nobel Prize in 1999.⁵⁷ This groundbreaking work has ignited a revolution in the realm of pump-probe spectroscopy. Time-resolved absorption spectroscopy (TAS) has emerged as the go-to technique for unraveling the transient behavior of charge carriers and unraveling the inner photophysics of diverse

materials. In my thesis endeavor, I harnessed the short femtosecond (fs) laser pulses, with pulse widths of 50-100 fs, to understand the ultrafast photophysical processes within a myriad of halide perovskites.

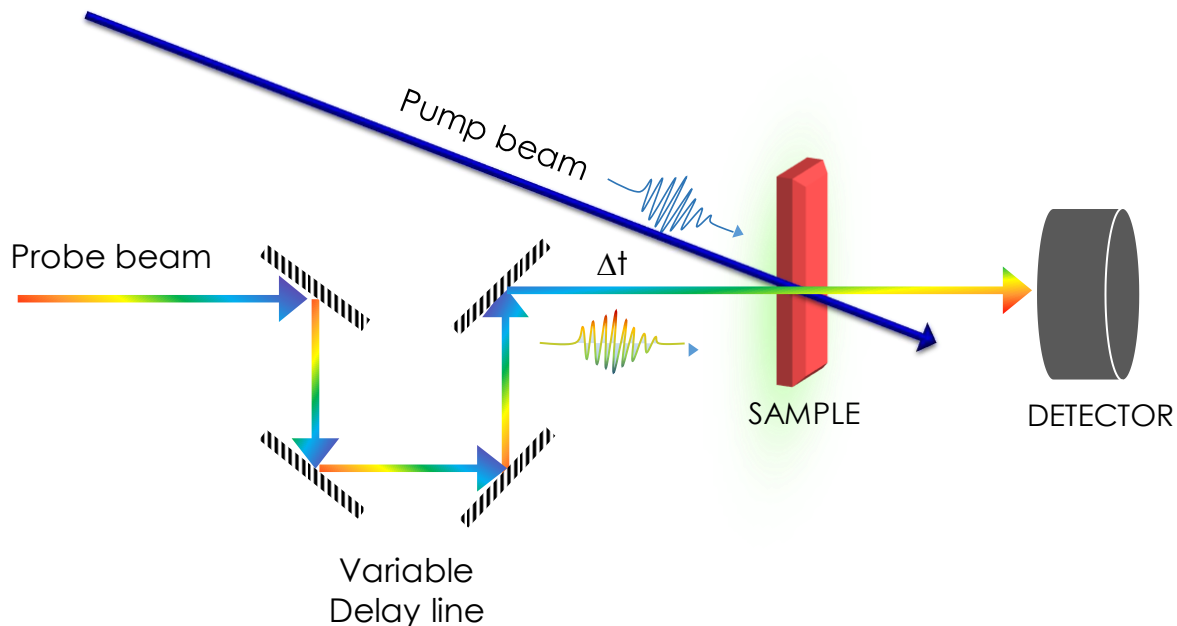


Figure 2.12 Illustrates the core concept of a pump-probe experimental setup in a schematic manner.

To accurately track the fluctuations in a material's transmission after photoexcitation, it is crucial to measure the material's transmission prior to and at specific time points following the excitation. This is typically achieved by employing a pump-probe experimental setup similar to the one illustrated in **Figure 2.12**. The pump beam serves as the catalyst, stimulating the sample and inducing changes in its absorption properties. Following this excitation, the probe beam comes into play, directed at the sample with an adjustable delay (Δt) relative to the pump beam. The probe beam's purpose is to carefully scrutinize any alterations in sample absorption caused by the pump beam, allowing us to explore deeper into the dynamics at play. After excitation, a fascinating array of phenomena unfolds at incredibly short time scales. Carrier cooling, where the excess energy of excited carriers is dissipated through interactions with the surrounding environment, takes place rapidly. The interplay between polarons (localized electron or hole states coupled to lattice vibrations) and phonons (quantized vibrations of the crystal lattice) becomes crucial in understanding energy transfer and relaxation processes.⁵⁸ All

of these occurrences occur over incredibly short spans of time (**Figure 2.13**), making their investigation challenging but essential for comprehending the intricate dynamics of materials and systems. TA spectroscopy with ultrafast lasers enables us to delve into these rapid processes and gain valuable insights into carrier dynamics, exciton behavior, and the intricate interplay between polarons and phonons.⁵⁸⁻⁶⁰

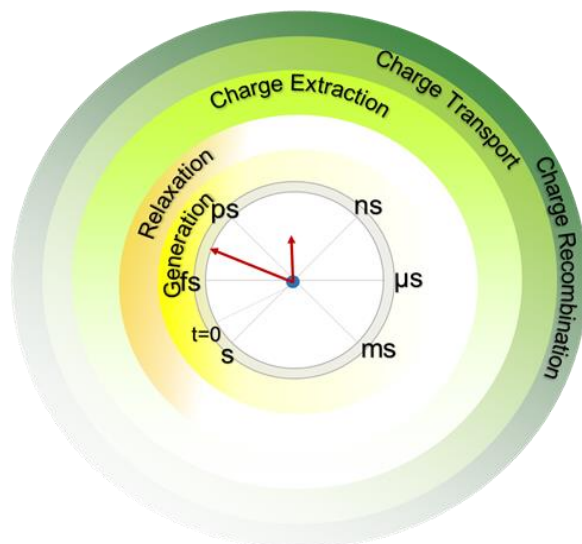


Figure 2.13 A schematic representation of the various processes that occur subsequent to photoexcitation typically includes the following stages

In the quest to unravel the photophysical properties of perovskite materials, in my thesis, I have primarily utilized these two instrumental techniques: TA spectroscopy, and terahertz spectroscopy. To effectively follow ultrafast processes, an experimental setup requires a time resolution that matches or exceeds the speed of the phenomenon being studied.^{61,62} In TA spectroscopy, this time resolution is achieved through the use of femtosecond lasers. TA spectroscopy, with its intense and ultrafast femtosecond lasers, allows us to capture and understand rapid changes in ground-state populations that traditional methods struggle to detect.⁵⁸ By perturbing the sample with a "pump" beam, we alter the population difference and decrease the absorption coefficient of the corresponding transition. This leaves the system in a non-equilibrium state, exciting a significant portion of the population to higher energy levels. The resulting changes in optical absorption are then examined using a delayed "probe" beam. By comparing the probe light's absorption in the presence and absence of the pump, we can determine the pump-induced change in absorption. In essence, TA spectroscopy provides

valuable insights into the dynamics and kinetics of the system under study, shedding light on transient states and rapid processes. The pump-induced change in absorption is determined by comparing the probe light's absorption in the presence and absence of the pump, denoted as:

$$\Delta A_{(\text{probe})} = \Delta A_{\text{pump on}} - \Delta A_{\text{pump off}} \quad \text{Eq. 2.9}$$

During a typical TA study, two distinct features are observed: a positive feature and a negative feature, often referred to as a "bleach." These features provide valuable insights into the dynamics of the system under investigation. The positive feature arises when the absorption of the probe increases in the presence of a pump pulse, indicating the presence of excited states or population transfer to higher energy levels. On the other hand, the negative feature, or bleach, occurs due to the depletion of the ground-state population.^{58,63,64} Bleach kinetics provides useful information about the interplay of the population between the ground state and excited states. By closely analyzing both the positive and negative features, the photophysical processes occurring within the system can be understood, shedding light on the energy transfer, relaxation dynamics, and transient phenomena at play.

Before introducing the details of the experimental setup, it is crucial to establish a foundation of the core principles involved in generating ultrafast lasers. As the heart of ultrafast laser technology lies in the ability to generate laser pulses with short durations, in particular femtoseconds (10^{-15} s). This remarkable achievement has opened up new avenues for studying and manipulating ultrafast phenomena in various scientific disciplines. The key principle behind femtosecond laser generation is mode-locking, a technique that ensures the generation of ultrafast pulses at regular intervals.⁶⁴ By carefully controlling the properties of the laser cavity and employing nonlinear optical effects, ultrafast pulses have been successfully generated. These ultrafast laser pulses have revolutionized fields such as spectroscopy, microscopy, and laser machining, offering exceptional temporal resolution and the ability to explore phenomena that unfold on incredibly short-time scales.⁶⁵ The continuous advancements in ultrafast laser technology, researchers can investigate deeper into the dynamics of chemical reactions, unravel the mysteries of quantum processes, and push the boundaries of our understanding of the fundamental principles of nature.

2.3.5.1. Generation of Ultrafast Laser

Lasers can be categorized into different types based on the basis of their emission characteristics including continuous wave (CW) and pulsed Lasers. CW lasers emit a constant beam of laser light with respect to time. They operate steadily, providing a constant output power over an extended period. While, in a pulsed laser, the light emitted is a short pulse. They offer precise control, high peak power, and short pulse durations. Back in 1960, the generation of laser pulses was indeed limited to durations of around 10 milliseconds (ms) with a peak power of approximately 1 kilowatt (kW). However, the introduction of Q-switching revolutionized laser technology by significantly reducing pulse durations and increasing peak power. Q-switching, a technique developed in the 1960s, allowed for pulse durations to be reduced by a factor of 10^4 , reaching the nanosecond (ns) range. This means that pulse durations were reduced to approximately 10^{-9} s.⁶⁶⁻⁶⁸ Additionally, the peak power of the laser pulses was increased to around 1 megawatt (MW), a significant improvement from the previous limit of 1 kW.⁵² While Q-switching facilitated a remarkable advancement in pulse duration reduction and peak power increase, it was primarily limited to generating nanosecond pulses. The technique itself was not capable of achieving pulse durations shorter than the nanosecond range. In 1964, a breakthrough in laser technology occurred with the introduction of a new technique called mode-locking.⁶⁹ This technique allowed for the generation of laser pulses with extremely short durations, on the order of picoseconds (10^{-12} s), and significantly increased the peak power of the pulses, reaching up to gigawatts (GW) of power.⁷⁰ This revolution was further enhanced by the advent of chirped pulse amplification (CPA), which enabled the generation of even shorter and more powerful laser pulses. These advancements have greatly expanded the capabilities of lasers and their applications in various scientific and technological fields.

Ultrafast pulses can be generated using two established techniques:

- Q switching
- Mode locking

2.3.5.1.1. Q Switching

Q-switching is a method used to generate short energetic laser pulses. It involves manipulating the cavity losses and the laser resonator's quality factor (Q factor). By modulating the losses, the laser is prevented from emitting light, allowing energy to accumulate in the gain medium. When the desired energy level is reached, the losses are rapidly reduced, enabling the stored energy to be released as a high-intensity pulse. This technique is useful for applications requiring high peak power pulses. Q switching could be achieved using two techniques i.e., active Q-switching and passive Q-switching. Active and passive Q-switching are two techniques used in laser systems to generate short and intense pulse of light. Both methods involve controlling the quality factor (Q-factor) of the laser cavity to achieve pulsed operation, but they differ in how they modulate the Q-factor.^{70,71}

- Passive Q-switching utilizes a saturable absorber, a material that becomes transparent at high light intensities. Initially, the saturable absorber blocks the laser light, but as the intensity increases, it saturates and allows the light to build up rapidly. This results in a short and high-energy pulse. Passive Q-switching doesn't require active control and is commonly used in solid-state lasers.
- On the other hand, In active Q-switching, the Q-factor is initially kept high to prevent lasing. The laser is continuously pumped to accumulate energy in the gain medium. When a pulse is desired, the Q-factor is rapidly reduced by applying a high-voltage pulse to the Electro optic modulator (EOM) or Acoustic optic modulator (AOM). This sudden decrease in the Q-factor allows the stored energy in the laser medium to be released as a short and intense pulse. The Q-factor is then quickly restored to its high value, and the process can be repeated.

Active Q-switching provides precise control over the pulse duration, repetition rate, and pulse energy. It is commonly used in diode-pumped solid-state lasers and fiber lasers. The pulse duration achieved through active Q-switching can range from nanoseconds down to picoseconds or even femtoseconds, depending on the laser configuration and the type of Q-switch used.

The laser setup comprises essential components as shown in **Figure 2.14 (A)**. In a laser system, the **gain medium** (e.g., solid crystal or gas-filled tube) amplifies light. The **active element**

(EOM/AOM), like controls losses and modulates the laser output. The **output coupler**, often a mirror, extracts output pulses while allowing some light to exit. These components enable precise control for diverse applications.⁷²

The laser operation involves a dynamic interplay of the above elements involved:

1. Active Element and Initial State:

An active element (EOM or AOM) is positioned between the laser gain medium and the output coupler. In the "on" state, the active element introduces high losses, preventing lasing and maintaining the laser system in a non-lasing state. Potassium dihydrogen phosphate (KDP) and lithium niobate (LiNbO₃) are commonly used for optical modulators. These crystals can change the polarization of light passing through them when an external voltage is applied.

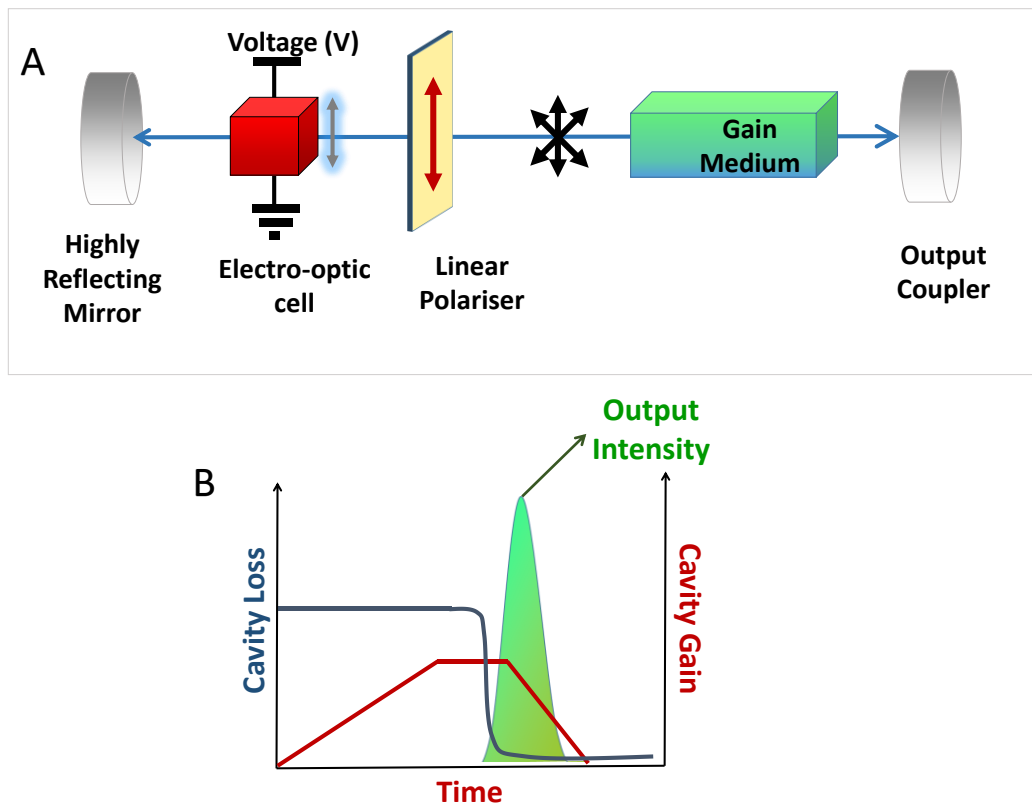


Figure 2.14 (A) The schematic representation explaining how Q-switching works with an electro-optic modulator (Pockels or Kerr cell), demonstrating the setup, (B) depicts the strong laser pulses (giant pulses) produced by Q-switching.

In this schematic, the key components of the active Q-switched laser system are depicted.

2. Polarization Control:

To control the laser's polarization when using these modulators, you can add a separate polarizer in the optical cavity or align the gain medium at specific Brewster angles. Applying an external voltage to the Pockels cell (an optical modulator) rotates the incoming light's polarization by 45° . After reflection from a highly reflective mirror, the light passes through the cell again, undergoing another 45° polarization rotation, effectively restoring its original polarization state as shown in **Figure 2.15**.

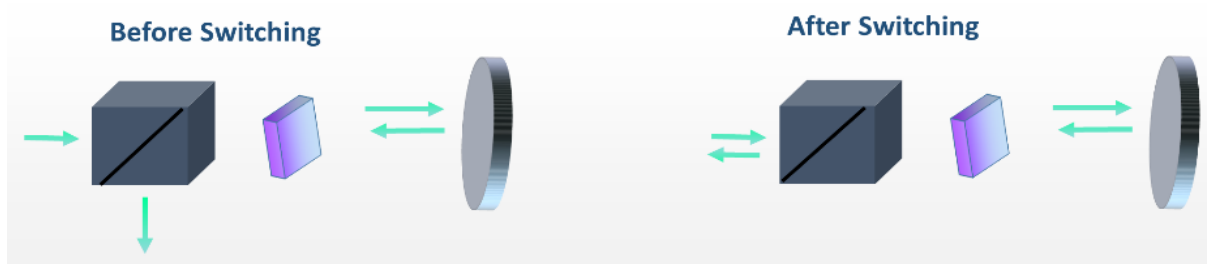


Figure 2.15 Q-switching using Pockels cell for producing short, high-energy laser pulses

Polarization Rotation and Laser Operation

- **Voltage Turned On:**

When the voltage is turned on, the electro-optic cell rotates the beam's polarization by 45° with each pass through the cell. After one round trip in the cavity, the total rotation accumulates to 90° . This causes the beam's polarization to become crossed with the linear polarizer, leading to reflection from the cavity and significant cavity loss.

- **Voltage Turned Off:**

When the voltage is turned off, the electro-optic cell does not change the polarization state of the incident beam. The beam passes through the cell without alteration, and there is no cavity loss.

3. Energy Accumulation:

- In the "on" state, the gain medium continues to be pumped with energy, leading to an accumulation of energy within the medium.

4. Rapid Switch to "Off" State:

- When the desired energy level is reached, the active element (EOM or AOM) is rapidly switched to the "off" state, typically triggered by an external control signal like an applied voltage (in the case of an EOM).

- This switching reduces intracavity losses significantly.

5. Pulse Formation:

- The sudden reduction in losses allows the stored energy within the gain medium to be released as a high-intensity pulse.
- The pulse has a short duration, determined by the rate at which the stored energy is depleted (**Figure 2.14 (B)**).

6. Repetition and Control:

- After the pulse is emitted, the active element is switched back to the "on" state with high losses, preventing further lasing until the next pulse is generated.
- This repetition process enables the production of a train of high-energy pulses at a controlled repetition rate.

Active Q-switching offers precise control over pulse characteristics, including pulse duration, energy, and repetition rate. It is widely used in laser technologies for applications such as laser marking, micromachining, and other areas requiring high-intensity, short-duration pulses.

2.3.5.1.2. Mode locking

Mode locking is a laser technique that creates ultra-short, high-power light pulses. Unlike continuous wave (CW) lasers that emit constant-intensity light, mode locking generates a series of very brief pulses in picoseconds (10^{-12} s) or femtoseconds (10^{-15} s).⁷³ This approach stands out compared to Q-switching, where the intense pulses have nanosecond durations. Mode locking excels in producing ultrashort femtosecond pulses, making it a superior choice for applications requiring such rapid time scales. The primary goal is to establish a coherent phase relationship among the longitudinal modes residing within the laser's resonant cavity. Within a laser cavity, a gain medium is enclosed between two mirrors. Light, behaving as a wave, interacts with these mirrors, resulting in reflection and subsequent interference phenomena.⁷⁴ These interactions give rise to the formation of stationary waves, also known as longitudinal modes.

The laser emissions do not exhibit perfect monochromaticity; instead, they manifest as a range of wavelengths with a limited bandwidth. These individual modes operate independently, behaving like a group of distinct lasers, each emitting light at slightly different frequencies.

However, when these modes become phase-locked, meaning they synchronize their spatial phase relationships and undergo constructive interference at regular intervals, they produce powerful, periodic pulses. This synchronized output is termed "phase-locked" or "mode-locked" as shown in **Figure 2.16**.⁷⁵

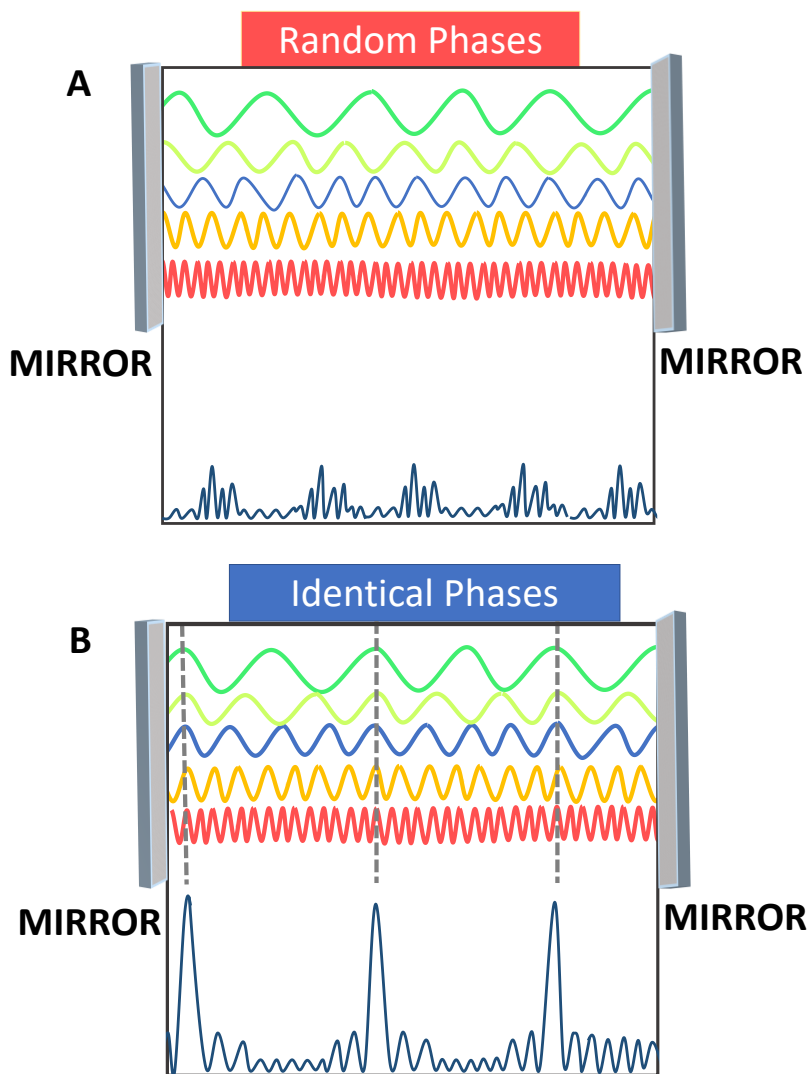


Figure 2.16 The schematic representation of the resulting electric field intensity acquired after the superposition of (A) randomly oriented phased modes, and (B) modes with identical phase configurations within a laser cavity.

Two key factors that define a mode-locked pulse are the interval between two successive pulses (Δt_{sep}) and the duration of the pulse (Δt_{p}).⁷⁶

$$\Delta t_{sep} = \frac{2\eta d}{c} \quad \text{Eq.2.10}$$

$$\Delta t_p = \frac{1}{\Delta\nu N} = \frac{1}{\text{Gain bandwidth}} \quad \text{Eq.2.11}$$

Here, c is the speed of light, d is the intracavity distance, η is the refractive index of the gain medium, and $\Delta\nu$ is the distance between two consecutive emitted frequencies.

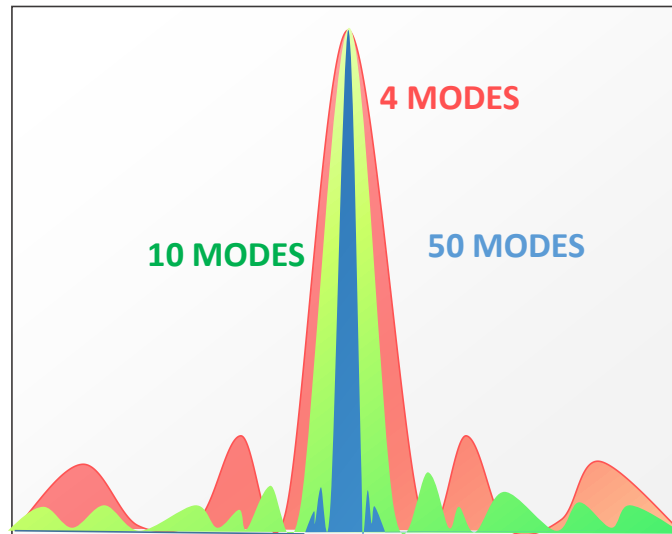


Figure 2.17 The resulting pulse, obtained by superimposing different number of modes, i.e., 4, 8, and 60 modes, illustrates a reduction in pulse width as the number of incorporated modes increases.

According to the above Eqn 2.10 and 2.11 the number of modes that the laser cavity can accommodate is proportional to the duration of a mode-locked pulse. Additionally, a wider bandwidth in the laser gain medium, which denotes the existence of a large no of modes, results in a mode-locked pulse with a shorter pulse width, as shown in **Figure 2.17**.

This mode-locking technique relies on the utilization of the Kerr effect, a non-linear optical phenomenon.⁷⁷ The Kerr effect, also recognized as the quadratic electro-optic effect in optics that leads to change of the refractive index in a medium due to the presence of a modulating electric field generated by the illuminating light beam itself. The change induced in the refractive index by the Kerr effect is linearly proportional to the incident intensity (I).⁷⁷⁻⁷⁹

$$n = n_0 + n_2 I \quad \text{Eq.2.12}$$

A laser system's light beam typically adopts a Gaussian distribution, with stronger intensity near the beam's centre and gradually decreasing intensity as it moves outward. The refractive

index changes from being higher at the centre to being lower at the edges when such a beam travels through a medium that can exhibit the Kerr effect. When laser modes are locked or phase-aligned self-focusing is more effective, contrasting to when there is no phase alignment or when the output resembles that of a continuous-wave (CW) laser.

There are two primary methods for achieving mode locking in lasers:

1. **Active Mode Locking:** In active mode locking, an external device like an EOM or AOM is employed to actively manipulate the phase and amplitude of the laser beam. This modulator introduces a time-varying phase shift to the light, causing the laser modes to synchronize and generate short pulses. Active mode locking offers precise control over pulse duration and repetition rate.⁸⁰
2. **Passive Mode Locking:** Passive mode locking relies on the inherent properties of the laser cavity to produce ultrashort pulses. A common approach is to incorporate a saturable absorber, such as a semiconductor or a dye solution, within the laser cavity. The saturable absorber transmits light at high intensities while absorbing light at low intensities. As a pulse builds up in the cavity, the saturable absorber becomes transparent, allowing the pulse to pass through. It then quickly becomes opaque, preventing further light from exiting the cavity. This cyclic process results in the emission of short pulses, creating a train of mode-locked pulses.⁸¹

2.3.5.2. Experimental Setup of Femtosecond Transient Absorption

Our Setup consists of basically 3 major parts namely

- Main laser
- Optical Parametric Amplifier (OPA)
- Spectrometer

2.3.5.2.1. Main Laser

In this thesis, we utilize the "Astrella Ultrafast Laser system" by Coherent Inc, it generates laser pulses with a wavelength of 800 nm, a pulse width of around 50 fs, a repetition rate of 1 kHz, and an energy output of roughly 5 mJ per pulse. This advanced system combines a femtosecond oscillator and a regenerative amplifier, operating through the synergy of Modelocking and Q-switching techniques. We delve into the specifics of each module,

exploring their principles and functions, and unveiling the potential of this laser system. In the thesis, we have employed a Coherent Astrella laser system.

The main laser system consists of three essential components:

- Seed Laser
- Pump Laser
- Regenerative Ti: Sapphire Amplifier

Each component plays a crucial role in generating and amplifying laser pulses with specific characteristics.

2.3.5.2.1.1. Seed Laser

The seed laser has a vital function within the laser system, serving as the primary source of laser light. It emits laser pulses with low power but specific attributes like wavelength, pulse duration, and coherence. The seed laser acts as the initial optical signal that sets the foundation for the amplification process. It provides the starting point for generating more intense laser pulses and plays a crucial role in shaping and defining the desired characteristics of the laser output. The Astrella system employs a mode-locked Titanium: Sapphire (Ti:S) laser oscillator, specifically the Coherent Vitara-T. The seed laser is powered by a continuous-wave (CW) diode laser known as the Verdi-G series, which utilizes optically pumped semiconductor laser (OPSL) technology to operate at a power level of 5W. The Verdi-G laser serves as the primary pump source for the Titanium-Sapphire (Ti³⁺ ions doped Al₂O₃) oscillator cavity. The Verdi-G laser produces output in the near-infrared (NIR) region, with a central wavelength of 1064 nm. The Verdi-G laser undergoes intracavity second harmonic generation (SHG) to convert its output into 532 nm visible light, as the TiS can only be pumped within the range of 514 nm to 532 nm only. The generated laser beam (532 nm) is then employed to pump the TiS crystal into the laser system. Kerr lens mode-locking is a technique used to generate ultrashort laser pulses. It involves placing a TiS gain medium inside a cavity between mirrors to trap the laser for a specific time. When a highly intense laser beam passes through the TiS medium, the refractive index of the medium changes non-linearly according to the equation

$$\eta(\nu) = \eta_0(\nu) + \eta_2(\nu)I \quad \text{Eq.2.13}$$

With each round trip through the Kerr medium, the laser beam experiences this intensity-dependent loss, resulting in pulsed laser generation. This process is known as Kerr lens mode-

locking or self-mode-locking, as the medium itself contributes to the focusing process. The Ti:S crystal is preferred because of the broad PL bandwidth, capable of generating extremely short pulses (< 6 fs). However, the laser beam experiences group velocity dispersion (GVD) during its multiple travels within the cavity. This dispersion is compensated by placing prisms inside the cavity. Additionally, the birefringent property of the Ti:S medium affects the laser's polarization, which is corrected by placing the crystal at the Brewster angle. The output pulses are ultrafast mode-locked pulses with a tunable wavelength range of 750-860 nm and a maximum gain of 800 nm. These pulses have a narrow bandwidth of 30-125 nm and a pulse width of ~ 20 fs. They have a horizontal polarization and a repetition rate of 80 MHz, corresponding to a time difference of 12.5 ns between consecutive pulses. The resulting output is referred to as the "Seed laser," which will undergo additional amplification in the multipass amplifier system.

2.3.5.2.1.2. Pump Laser

The Astrella assembly utilizes the "Revolution laser" from Coherent Inc. as the pump laser, which serves the purpose of achieving population inversion in the gain medium. The pump laser comprises a diode-pumped Q-switched laser (Nd: YLF) and a second harmonic generator, which generates an output at 527 nm with a repetition rate of 1 kHz. Each pulse from this module delivers approximately 40 mJ of power with a pulse width of less than 150 ns. The Revolution pump laser is selected not only for its ability to provide the necessary pulse energy to surpass the lasing threshold of the Ti^{3+} : Sapphire cavity, which serves as the gain medium in the regenerative amplifier assembly, but also for its output wavelength that aligns well with the optimal performance range of Ti^{3+} : Sapphire cavities. The pump laser is focused on the crystal at the same spot as the seed laser.

2.3.5.2.1.3. Regenerative Ti: Sapphire Amplifier

The seed laser pulses derived from the oscillator exhibit a low intensity, rendering them unsuitable for pump-probe experiments. Consequently, there arises a need to amplify the intensity of these laser pulses (nJ to mJ per pulse). So, with the assistance of this setup, we amplify the power of the seed pulse and reduce the repetition rate (MHz to kHz). The peak power of the initial pulse emitted by the oscillator is extremely high, measured in gigawatts (GW). This high energy per pulse and short pulse width can potentially cause damage to the optics of the regenerative amplifier. To address this issue, a pulse stretcher is integrated into

the system, which elongates the seed pulse into the picosecond range from its original femtosecond duration and reduces the peak power. Subsequently, after the amplification process, the ultrafast pulses are compressed back into femtosecond pulses. This component effectively utilizes the chirped pulse amplification (CPA) method to reduce the peak power.

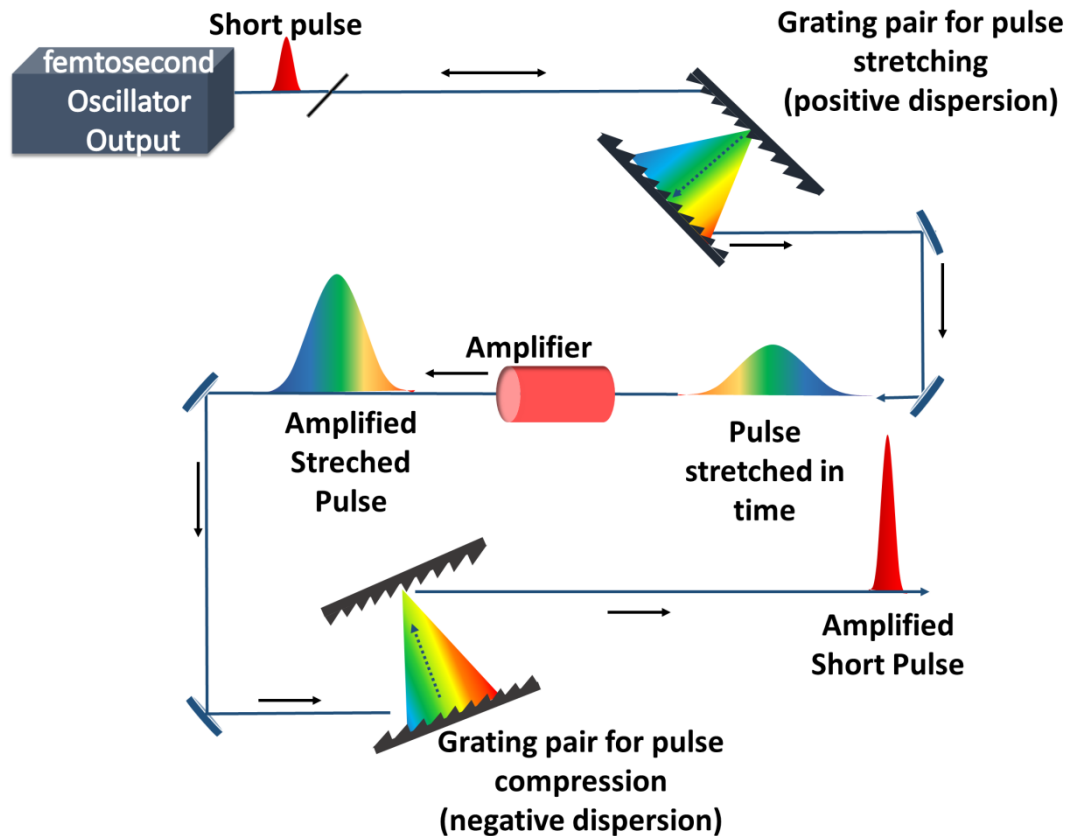


Figure 2.18 Schematic representation illustrating the configuration of the Chirped Pulse Amplification (CPA) system.

In a CPA unit, the typical components involved are the stretcher, pulse picker, gain medium, and compressor as shown in **Figure 2.18**. The initial stage of CPA involves the mode-locked pulses with a width of a few femtoseconds, generated by the femtosecond oscillator or seed laser (VITARA), undergo temporal expansion using the **stretcher** unit increasing their pulse width to hundreds of picoseconds. From the pulses delivered by the oscillator, the **pulse picker** selects only one pulse from 8000 pulses for further processing. The selected pulse is directed into the **gain medium**, where it undergoes amplification. Following amplification, the pulse is compressed back to a few femtoseconds by passing through the **compressor unit**. Finally, the

compressed pulse is coupled to the output window for subsequent use or transmission. The function of each of these units is detailed below.

□ Stretcher

The seed laser initially undergoes a crucial step by passing through a pulse stretcher. This device stretches the ultrafast femtosecond laser pulses into picosecond pulses. The stretching procedure employed relies on the concept of Group Velocity Dispersion (GVD). GVD is a phenomenon in which different spectral components of a light pulse travel at different velocities through a medium.

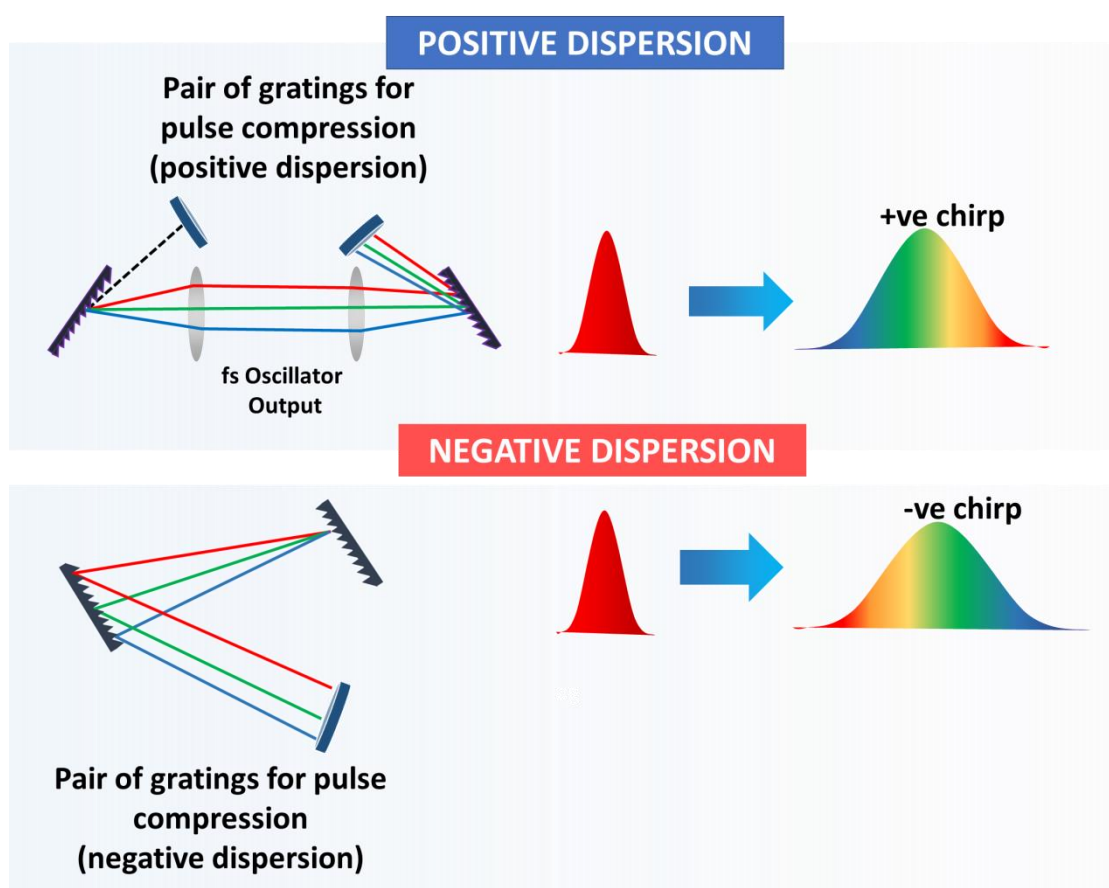


Figure 2.19 Schematic representation illustrating the negative and positive dispersion.

There are two types of GVD processes: positive and negative. The stretcher unit functions by utilizing positive GVD, utilizing a diffraction grating, the pulse spectrum is spread out, while carefully designed mirror configurations guide the beam path as shown in **Figure 2.19**. This arrangement causes the bluer components of the pulse (shorter wavelength) to travel a longer

distance compared to the other components. As a result, the red beams exit the stretcher earlier than the blue beams, effectively stretching the pulses in time. To achieve further spatial reconstruction of the stretched beam, a vertical retroreflector redirects the stretched pulses back into the stretcher, allowing for multiple passes. The stretcher unit operates is responsible for the stretching of the seed pulses, ensuring they have a longer temporal duration

□ Pulse Picker and Synchronization and Delay Generator

Before reaching the amplifier, the stretched pulses are directed through the pulse picker to lower the repetition rate from 80-90 MHz to 1 kHz. This process relies on the electro-optical effect of Pockel cells. Pockel cell is made up of a non-linear material such that by applying a high voltage (~ 4 kV to 6 kV) to the crystal, an electric field can be induced along different directions. This electric field causes a change in the refractive index of the crystal, resulting in a change in its optical properties. The crystal is generally made of materials including potassium dihydrogen phosphate (KDP), ammonium dihydrogen phosphate (ADP), or barium borate (BBO). In our system, two Pockels cells (PC1 and PC2) are strategically positioned as quarter-wave plates, altering the polarization by $\lambda/4$ when voltage is applied. These Pockels cells i.e., PC1 and PC2 serve as the entry and exit gates respectively for the seed pulse, ensuring the desired amplification. When no voltage is applied to the Pockels cell, the pulses are discarded without undergoing any amplification. However, when voltage is applied to the Pockels cell, the polarization of the input pulse changes from horizontal to vertical enabling them to pass through the polarizer and proceed for further amplification. This vertically polarized pulse can then pass through the polarizer and is utilized as the seed pulse for subsequent amplification processes. Synchronization electronics precisely control the voltage application on the Pockels cells, selectively choosing the pulses for amplification. The SDG (Synchronization and Delay Generator) Elite unit governs these electronics, maintaining accurate timing and adjusting the applied voltage to achieve the desired delay between the Pockels cells. To assure that only one pulse is allowed to enter into the cavity, the PC1 should every time be switched at the same time as the seed pulses.

Regenerative Amplifier

Components of REGEN unit

Before delving into the working of the REGN (Regenerative Amplifier) unit's operation, it is essential to understand the fundamental components involved:

- ❑ **Brewster's Angle:** When a light pulse with horizontal polarization strikes a medium at Brewster's angle, it undergoes total internal reflection, leading to its reflection from the surface. Conversely, if the incident pulse has vertical polarization, it propagates into the medium without reflection.
- ❑ **Quarter-Wave Plate ($\lambda/4$):** This optical component converts linearly polarized light to circularly polarized light by introducing a phase shift in the polarization state.
- ❑ **PC1 (Pockel Cell 1):** PC1 controls the admission of the seed pulse into the gain medium of the amplifier. By selectively switching PC1 on or off, the pulse can be directed either toward the gain medium for amplification or elsewhere for alternate routing.
- ❑ **Gain Medium:** The gain medium refers to the active material within the amplifier responsible for providing amplification to the seed pulse. As the pulse traverses through this medium, it undergoes energy amplification.

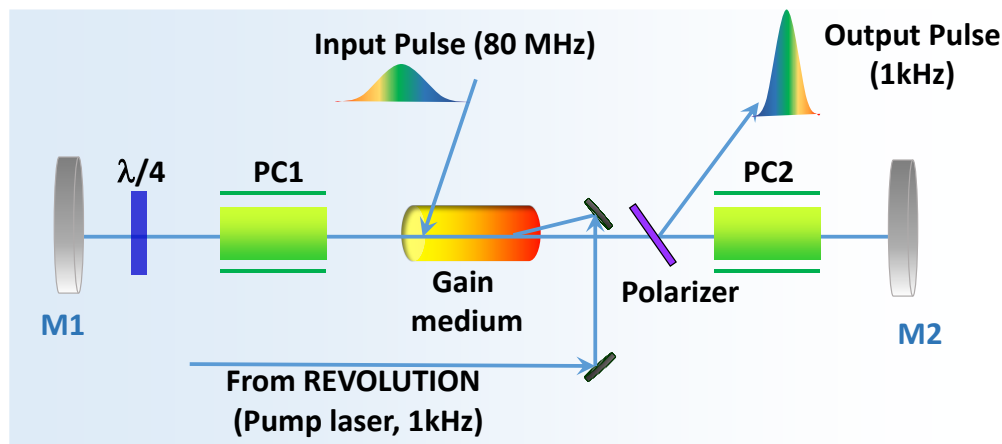


Figure 2.20 Schematic representation of the REGEN unit.

- ❑ **PC2 (Pockels Cell 2):** PC2 governs the ejection of the amplified pulse from the amplifier cavity. By selectively activating or deactivating PC2, the pulse can either be transmitted through or reflected from the gain medium.

- **THP (Thin Film Polarizer):** Working in conjunction with the Pockels cells, plays a crucial role in manipulating the polarization state of the pulses. It transmits or blocks the pulse depending on its polarization of incident pulses.

In the context of the optical arrangement (**Figure 2.20**) of the REGN, the horizontally polarized seed pulse from the stretcher unit is incident on the gain medium at Brewster's angle, so that it propagates towards PC1 instead of into the active medium as the seed pulse is horizontally polarized. If the PC1 is off, the light pulse passes through it towards the $\lambda/4$ plate without any change in its polarization state due to PC1. Further, as it passes twice through the $\lambda/4$ plate and once directly and secondly after reflecting from M1, its polarization is rotated by 90 degrees. Now that the seed pulse which was horizontally polarized becomes vertically polarized, it further travels through the gain medium and is amplified through the active medium. In case PC2 is also off at this time, the pulse exiting the amplifier will pass through the thin film polarizer (TFP) towards M2 and is reflected back. Since it is still vertically polarized, the pulse transmits through the gain medium again and undergoes further amplification. Now, two cases are possible if the pulse reaches PC1 and it is still off, the beam undergoes an additional 90° rotation of polarization, becoming horizontally polarized. In this case, the pulse is reflected back by TFP and is rejected. However, if PC1 is ON prior to the arrival of the seed pulse, the combined influence of the quarter-wave plate and PC1 results in a comprehensive polarization change of λ . This ensures that the polarization state of the pulse remains unaltered, maintaining its vertical polarization. As a consequence, the beam can undergo further amplification unhindered. Once the desired level of amplification (10^6), is attained, a suitable voltage is applied across PC2, switching it ON. Subsequently, the pulse traverses PC2, undergoes reflection from mirror M2, and returns through PC2. This sequential process induces a polarization change equivalent to $\lambda/4 + \lambda/4 = \lambda/2$. Consequently, the beam is reflected from the surface of the gain medium and precisely directed into the compressor unit.

Pump Laser

The gain medium Ti:S of REGN is excited by a highly intense pump laser beam, operating at the same repetition rate. This pump laser, known as the Revolution laser, is a diode-pumped Q-switched Nd:YLF laser. It emits pulsed laser light at a wavelength of 527 nm, with a repetition rate of 1 kHz, a pulse width of ~200 ns, and an average power of around 40 W. The generation of nanosecond pulses is facilitated by an acousto-optical Q-switch, which ensures

the desired temporal characteristics. To achieve the desired output, a temperature-controlled oven consists of a Lithium Triborate (LBO) crystal, maintaining it at a precisely regulated temperature of 324°F. This controlled temperature environment optimizes the performance and reliability of the LBO crystal within the system.

Pulse compressor

To enable pump-probe experiments, it is crucial to have femtosecond pulses. Consequently, the amplified pulses obtained from the REGN output, which initially span over a picosecond duration, undergo temporal compression to restore their femtosecond pulse width. This compression occurs within the compressor unit, where the chirping effect is eliminated. In contrast to the stretcher unit, the compressor unit employs the principle of negative GVD as shown in **Figure 2.19**. The lower wavelengths are compelled to travel shorter distances than the higher wavelengths, resulting in negative GVD. This compensates for the positive GVD experienced by the pulses prior to the gain stage. The final output of the pulse compressor is obtained as the final output that is utilized for pump-probe studies. This output pulse has a central wavelength of 800 nm (within the range of 780 nm to 820 nm), a repetition rate of 1 kHz, a pulse width of ~ 35 fs, and an energy per pulse of 5 mJ. These parameters meet the requirements for conducting precise pump-probe experiments and enable detailed analysis in spectroscopic investigations.

2.3.5.2.2. Optical Parametric Amplifier (OPA)

The Astrella laser system emits a coherent light beam centered at 800 nm wavelength. Yet, for scientific investigations involving systems sensitive to wavelengths outside this range, the flexibility to access a wide spectrum of wavelengths becomes crucial. This requisite tunability of wavelengths can be accomplished by harnessing non-linear optical effects. By exploiting these effects, researchers gain the capacity to tune the laser's output wavelength, allowing them to precisely excite and explore various materials and phenomena with exceptional scientific versatility. The selective excitation of material can be achieved by tuning the frequency through a fascinating optical phenomenon called optical parametric amplification (OPA), as demonstrated by the pioneering works of Giordmaine and Miller in 1965, and Baumgartner and Byer in 1979.⁸²

In the process of OPA, a suitable nonlinear crystal serves as the stage for transferring energy from a high-frequency and strongly intense beam (the pump beam) to a lower frequency with lower intensity beam (the signal beam), which undergoes significant amplification.^{83,84}

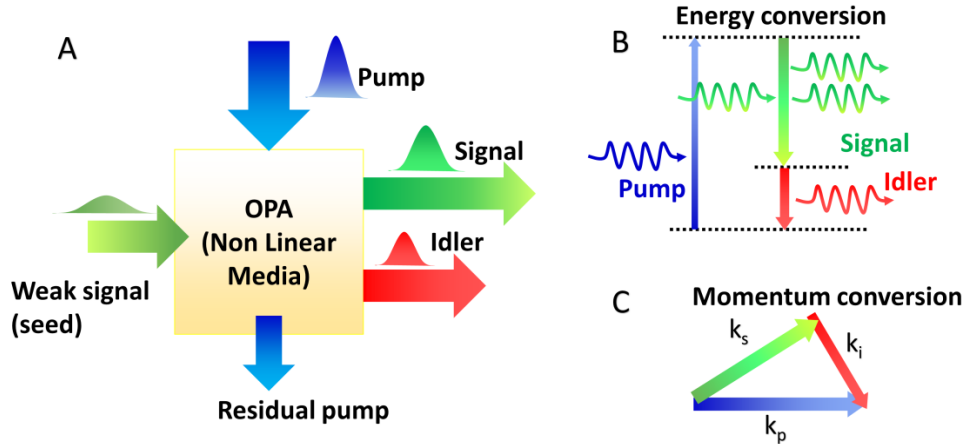


Figure 2.21 (A) illustrates the overall concept of the optical parametric amplifier (OPA) process, Energy level diagram depicting, (B) the energy conservation, and (C) momentum conversion in OPA process.

Notably, this process also generates a third beam, referred to as the idler beam, operating at frequency, thus ensuring energy conservation. A simple yet illuminating interpretation of the OPA process is depicted in **Figure 2.21**, a photon with frequency ω_3 is absorbed by a virtual level within the material, stimulating the emission of two photons of frequencies ω_1 and ω_2 . This interaction follows the fundamental principle of energy conservation, expressed as

$$\hbar\omega_3 = \hbar\omega_1 + \hbar\omega_2 \quad \text{Eq.2.14}$$

In any medium when an electric field is applied the connection between the polarisation (P) and applied electric field (E) can be represented through a power series expression:

$$P = \epsilon_0 (\chi^{(1)} E + \chi^{(2)} E^2 + \chi^{(3)} E^3 + \dots) \quad \text{Eq.2.15}$$

In this context, $\chi^{(n)}$ represents the nth-order dielectric susceptibility of the material and ϵ_0 signifies the permittivity of vacuum.

Moreover, the electric field of an electromagnetic (EM) wave can be represented as:

$$E = E_0 e^{i(kz - \omega t)} \quad \text{Eq. 2.16}$$

Substituting the expression for electric field Eq. 2.16 into Eq. 2.15 reveals that under such circumstances, the material can exclusively generate a single frequency denoted as ' ω '. However, when intense electric fields are subjected over these materials, the significance of the second term in Eq. 2.15 ($P \propto e^{2i(kz - \omega t)}$) becomes apparent. This suggests that the material exhibits a notable output at the frequency 2ω . Consequently, through the utilization of higher electric field strengths, additional higher harmonics of the incident light frequency can be generated.

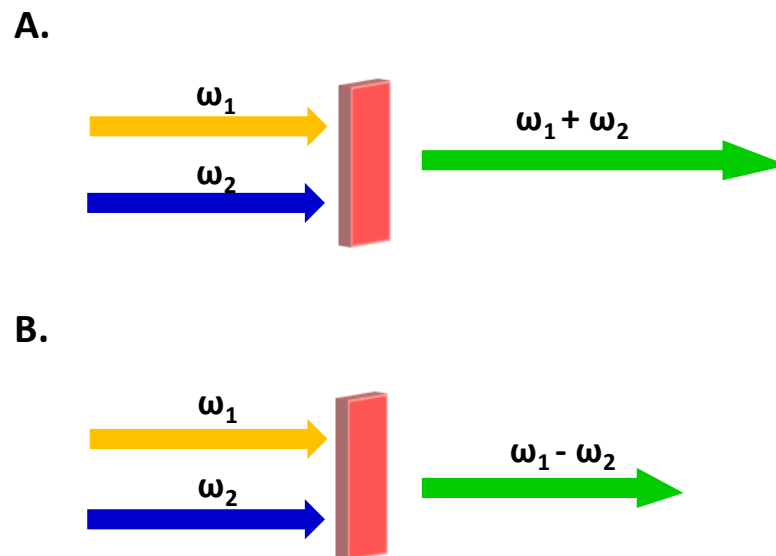


Figure 2.22 (A) The schematic representation of Sum Frequency Generation the resultant photon is the sum of the incident photon frequencies (B) Difference Frequency Generation process where the output frequency is the difference of the incident frequencies.

In this process, the incoming photon (often referred to as the "pump") is dismantled, and simultaneously, two outgoing photons ($\omega_P \rightarrow \omega_S + \omega_I$) are formed. The photon produced with the higher frequency is denoted as the "SIGNAL" (ω_S), while the one with the lower frequency is labeled as the "IDLER". Throughout this interaction, the principle of energy conservation remains upheld. The frequencies of these idler and signal photons, which arise due to OPG, are significantly influenced by the phase-matching condition. As these harmonics traverse through

a medium, they can interact either with each other or with the fundamental frequency. This interaction can yield the summation of the incoming frequencies, known as Sum Frequency Generation (SFG), or their difference, referred to as Difference Frequency Generation (DFG), as depicted in **Figure 2.22**. In the case of SFG, when two lower frequency photons (ω_1 and ω_2) are combined, a higher frequency photon ω_3 ($\omega_1 + \omega_2 \rightarrow \omega_3$) is generated. This also encompasses the special case of SFG known as the Second Harmonic Generation (SHG). On the other hand, in DFG (also denoted to as Parametric Down Conversion), a single photon is produced through the subtraction of the incident frequencies ($\omega_1 - \omega_2 \rightarrow \omega_3$) (**Figure 2.22**).

Generating White Light Continuum (WLC)

The idea of generating WLC, useful in time-resolved spectroscopy, comes from the same relationship between light intensity and refractive index and is given by^{74,77}

$$(n = n_0 + n_2 I) \quad \text{Eq.2.17}$$

It is also called the Kerr nonlinearity and the process relies on the optical Kerr effect, also called the self-focusing effect. The link between the phase of the electric field and the refractive index (nonlinear effect) is the key.^{85,86} This relationship, shown in Eq. 2.16, means that the wave vector (k) is proportionally related to the refractive index. Consequently, a wave moving through such a material gets its phase changed based on its own electric field's strength. Further, it is a known fact that the frequency is the time derivative of phase. Consequently, modulation in phase is equivalent to modulation in frequency. So, when a material has non-zero cubic dielectric susceptibility, a passing wave will experience self-phase modulation.⁸⁷ All these nonlinear optical effects, work together to widen the spectrum of a super short pulse of light (femtosecond pulse) as it goes through such a nonlinear material thus creating a white light supercontinuum.⁸⁸ This expanded spectrum is used as a probing light in time-resolved spectroscopy devices and as initial pulses in Optical Parametric Amplifiers.

Experimental Setup in our lab

In my thesis, we employed the "OPERA SOLO" apparatus developed by "Light Conversion" to generate a widespread range of tunable wavelengths, spanning from 280 nm to 2600 nm. OPERA-SOLO is a two-stage parametric amplifier that consists of several modules, including optics for pump beam delivery and beam splitting, a white light continuum generator (WLG), and pre-amplifiers (PA1, PA2). This apparatus is under computer control, allowing precise manipulation of the translational and rotational positions of all optical elements. Additionally,

the computer command enables the adjustment of the output wavelength across an extensive range. The comprehensive configuration of the OPERA-SOLO parametric amplifier is depicted in **Figure 2.23**. The pump beams are directed to the OPERA-SOLO system and first undergo amplification, the pump laser beam is divided into two segments using a beam splitter. The lower-energy segment passes through a sapphire crystal which generates a WLC. This WLC, in conjunction with the other segment serving as a pump, is then concentrated onto a non-linear crystal. These two components, which play the roles of WLC generation and pump, are aligned in a non-collinear manner, both spatially and temporally.

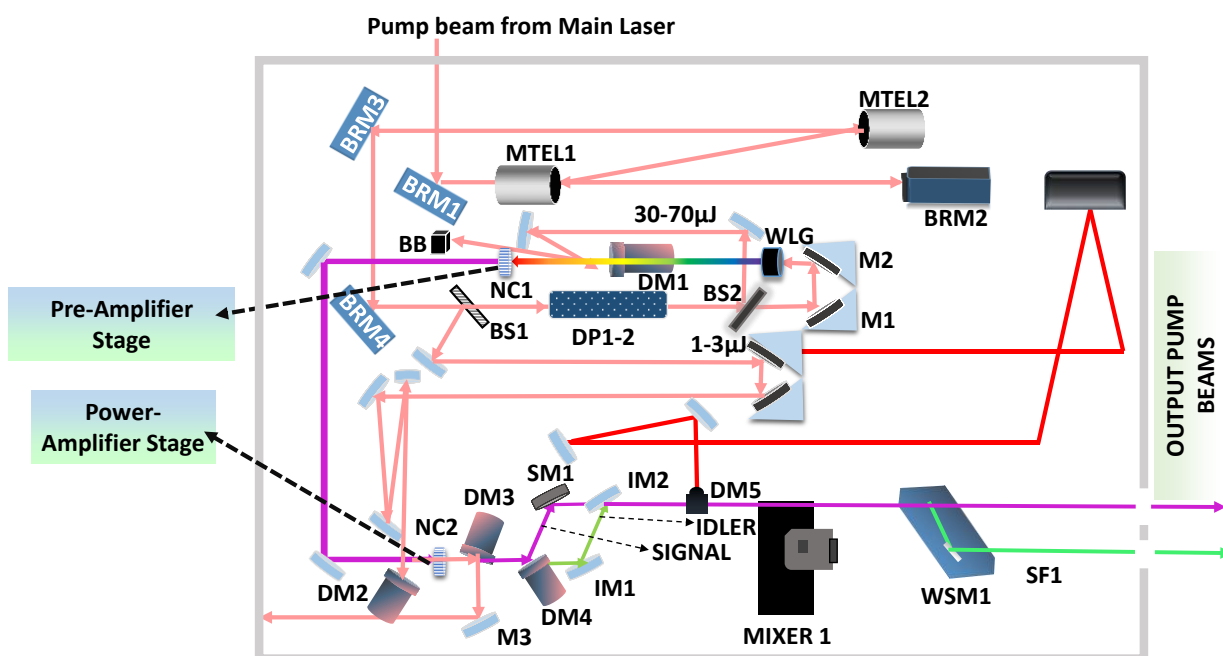


Figure 2.23 Schematic representation of the Opera Solo parametric amplifier setup showing all optical components of the parametric amplifier.

The setup encompasses optical elements for beam splitting and pump beam transmission, a crystal for generating the WLC, a pre-amplifier stage (also referred to as the first amplifier stage), an expander-collimator to adjust beam size, and a power amplifier stage (functioning as the second amplifier stage). This setup is under computer control, allowing us to accurately manage the translational and rotational positions of all optical elements.⁸⁹ Furthermore, we can adjust the output wavelength extensively by changing computer commands. **Figure 2.23** provides an overview of the layout of the OPERA-SOLO parametric amplification segment.

The 800 nm output originating from ASTRELLA is initially directed towards the beam splitter BS1. At this point, the incident pump beam undergoes bifurcation, with the transmitted component containing the residual energy amounting to 20%, while the reflected component carries approximately 80% of the energy. The transmitted beam subsequently impinges on another beam splitter, BS2, leading to a secondary division into two distinct segments. A small portion of this transmitted light beam, with significantly low energy levels in the range of approximately 1-3 μJ , is directed onto a sapphire plate (WLG). This interaction culminates in the generation of a WLC, functioning as the seed source. The WLC generated in this manner, coupled with another segment of the transmitted pump beam possessing energy levels ranging from 30-70 μJ , is then directed to NC1s. At this juncture, meticulous arrangements are made to ensure a non-collinear overlap between these two beams within the crystal. This specialized arrangement triggers the phenomenon of parametric amplification within the crystal, leading to the emergence of distinct SIGNAL and IDLER frequencies.

It is noteworthy that the SIGNAL frequency is intricately linked to the frequency of the WLC that coincides with the pump beam. These include the manipulation of the relative delay between the white-light pulse and the initial pump pulse, facilitated through the utilization of software-controlled Brewster angled plates DP1-2, along with the precise manipulation of adjustable mirrors M1 and M2. All of these components are mounted on a computer-controlled delay stage. Fine-tuning the crystal angle also plays a pivotal role in achieving optimal phase matching, thereby contributing to the achievement of wavelength tuning during this preamplifier stage. The beam transverses through a nonlinear setup to separate the various frequencies in the intensified SIGNAL beam. After passing through the NC1 crystal, a beam blocker (BB) stops the IDLER beam and any residual pump. The beam then goes to the power amplifier (NC2), which is the second stage of amplification. This amplifier is powered by the remaining part of the input beam, which bounces off the BS1 splitter. This reflection is a significant portion, more than what's used for WLC generation. To achieve high intensity, the beam size is reduced using a lens-mirror telescope. The pump and SIGNAL beams are then overlapped at the second non-linear crystal (NC2), resulting in OPA (Optical Parametric Amplification) and generating more focused SIGNAL and IDLER beams. These focused beams are directed at DM3, which reflects the pump beam onto M3. This mirror then redirects the pump beam to a beam dump. Using another dichroic mirror, DM4, after DM3, the signal

and idler beams are separated, allowing them to follow different paths and be collected at separate output ports of the OPERA SOLO device. Mirrors IM1 and IM2, known as golden mirrors, are detachable. They are typically not in the path when only the SIGNAL beam is needed, but they can be positioned to direct the IDLER beam if necessary. By adjusting the preamplifier's wavelength and optimizing the angle of the second nonlinear crystal (NLC), along with the delay of the SIGNAL beam in relation to the second pump beam, the power amplifier's tuning is achieved. To expand the range of wavelengths that OPERA-SOLO can cover, frequency mixers are used, including second harmonic generators (SHG) and sum frequency generators for both SIGNAL and IDLER beams. These mixers cover a broad range of wavelengths from ultraviolet (UV) to near-infrared (NIR). For generating sum frequencies of the SIGNAL or IDLER beams, pump pulses are combined with the corresponding SIGNAL or IDLER pulses (SFS, SFI). Type-1 phase-matching BBO crystals are used for SHG and SFG. These mixing processes are computer-controlled and produce blended frequency outputs. Following the mixer, a wavelength separator (WSM) is utilized to isolate the specific frequency we want from the rest. These monochromatic frequency outputs act as the pump beam for the TA studies.

2.3.5.2.3. Transient Absorption spectrometer

A TA spectrometer uses two types of light pulses, called pump and probe pulses, to perform the TA study which is termed pump-probe spectroscopy. The specific pump pulse is generated by OPA thereby directed towards the spectrometer, while the probe pulse enters the instrument directly. The layout of the Helios-FIRE spectrometer is shown in **Figure 2.24**. The probe pulse, at 800 nm, is sent through a set of mirrors to create different light ranges in UV-Vis, Vis, and NIR regions. The configuration permits the exploration of transients across three spectral regions: 350 nm to 750 nm, 450 nm to 800 nm, and 800 nm to 1600 nm. Correspondingly, in order to generate probe light in these different domains distinct crystals are employed, i.e., CaF₂ for UV, Sapphire for VIS, and Yt³⁺: Garnet for NIR - generate the probe light in different domains. The setup integrates two detectors: a CMOS sensor for the UV/Vis region and an InGaAs sensor for NIR detection. These crystals can be placed accurately using software control. The light produced passes through a filter and reaches the sample. Both the pump and probe beams hit the same spot on the sample, and this spot can be rotated for films or stirred for solutions. The pump beam passes through the chopper in order to reduce its repetition rate

from 1 KHz to 500 Hz. To establish periodic "PUMP ON" and "PUMP OFF" phases, the chopper synchronizes with the laser's output. The Instrument Response Function (IRF), around 100 fs, is approximately 1.4 times the laser pulse duration. The pump beam's size is 250 μm , whereas the probe beam is $\sim 100 \mu\text{m}$. This pump-probe size asymmetry ensures even excitation and circumvents any potential artifacts arising from delays. To mitigate undesired interactions, either the magic angle setting of 54.7° for both pump and probe beam polarizations or a preceding depolarizer is employed. Data collection, crystal motion, translation of the sample holder (to prevent damage), and delay stage operation are facilitated by the HeliosTM software, with subsequent data analysis performed using the Surface XplorerTM software, which also provides chirp correction capabilities.

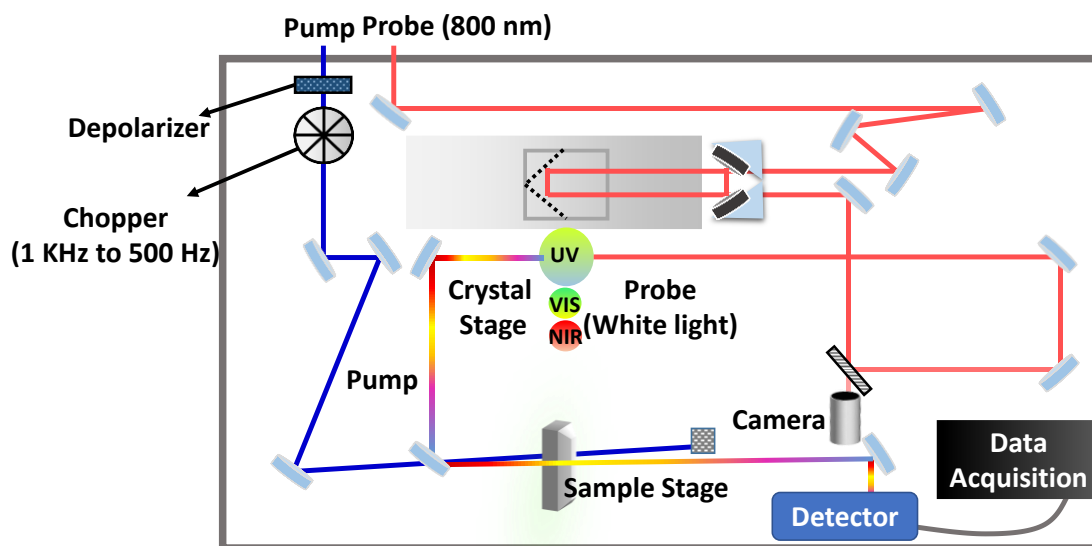


Figure 2.24 illustrates the schematic representation of the Helios-FIRE spectrometer.

2.3.5.2.3.1. Surface XplorerTM software

Surface Xplorer is a software application based on LabVIEW that is employed for fitting transient kinetic traces, denoted as $S(t)$, at specific wavelengths using a combination of convoluted exponentials:

$$S(t) = e^{-\left(\frac{t-t_0}{t_p}\right)^2} * \sum_i A_i e^{-\frac{t-t_0}{t_i}} \quad \text{Eq.2.18}$$

$$t_p = \frac{IRF}{2 \cdot \ln 2} \quad \text{Eq.2.19}$$

In the above equation, IRF refers to the Instrument Response Function, t_0 represents the time zero, and $*$ denotes the convolution function. The software also provides the relative amplitudes (A_i) corresponding to each fitted time constant.

Analyzing and understanding the TA data's spectral signatures:

When light travels through a substance that absorbs some of its energy, we can quantify the extent of absorption using Beer-Lambert's equation. The Beer-Lambert law states that the absorbance of a given solution is directly proportional to both the concentration of the substance and the optical path length (L) of the sample.

$$A = \log\left(\frac{I_0}{I}\right) = \epsilon c L \quad \text{Eq.2.20}$$

Here, ϵ represents the molar absorption coefficient, c signifies the molar concentration of the solution, and L quantifies the length of the optical path.

The TA Spectroscopy, the process employs two laser pulses - the pump and probe pulses – passing through the substance with a controllable delay. Initially, the pump laser excites the sample, pushing it into higher energy states. Subsequently, the probe laser monitors the subsequent relaxation and recombination processes occurring within the sample. The detector then analyzes the changes in the intensity of the probe beam in the presence and absence of the pump beam, resulting in a signal known as differential absorption (ΔA). The TA investigations yield two distinct types of signals based on whether ΔA has a **positive or negative value**. As mentioned previously, ΔA essentially represents the difference in probe absorption between " $\Delta A_{\text{pump On}}$ " and " $\Delta A_{\text{pump Off}}$." By incorporating this into Beer Lambert's equation, we can reformulate this expression for " ΔA " as follows:

$$\Delta A = \log\left(\frac{I_0^{\text{Probe}}(\lambda)}{I^{\text{Probe}}(\lambda, \Delta t)}\right)_{(PUMP\ ON)} - \log\left(\frac{I_0^{\text{Probe}}(\lambda)}{I^{\text{Probe}}(\lambda)}\right)_{(PUMP\ OFF)} \quad \text{Eq. 2.21}$$

$$\therefore \Delta A = \log\left(\frac{I^{\text{Probe}}(\lambda)_{(PUMP\ OFF)}}{I^{\text{Probe}}(\lambda, \Delta t)_{(PUMP\ ON)}}\right) \quad \text{Eq.2.22}$$

This equation serves as the fundamental cornerstone of Time-Resolved Absorption Spectroscopy (TAS) as it governs the generation of signals during TAS measurements. The resulting ΔA value can exhibit both positive and negative characteristics, giving rise to signals known as **ground state bleach (GSB)** and **photoinduced absorption (PIA)** or **excited state absorption (ESA)**.

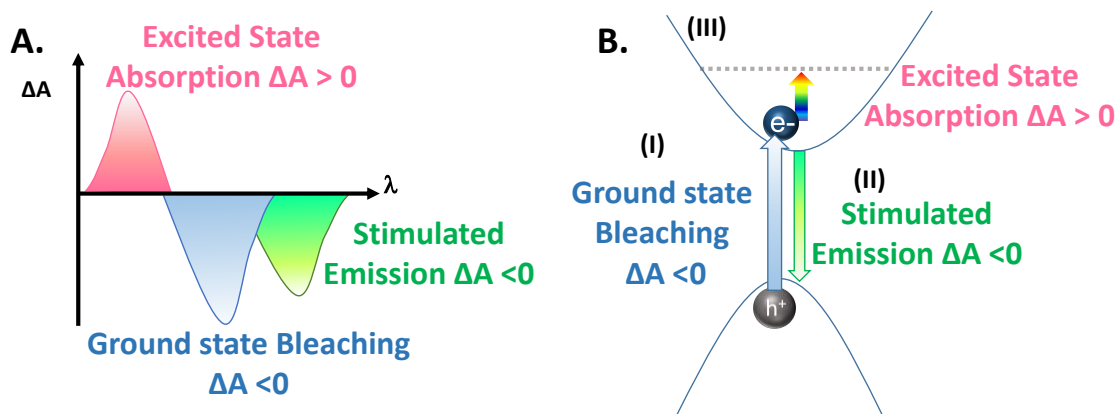


Figure 2.25 (A) Different type of signals which are observed in TA and (B) Schematic illustrating their respective origins.

- In instances where ΔA is negative, it signifies that $I(\lambda) < I(\lambda, \Delta t)$, indicating that the probe beam has a higher intensity in the presence of the pump beam or that the probe experiences reduced absorption when the pump is active. This situation arises when there is **GSB or stimulated emission (SE)** for the particular transition under investigation. In the context of GSB, the pump pulse elevates the carriers to higher energy states, thereby diminishing the probe pulse's absorption within the same transition region. Consequently, the probe pulse exhibits lower absorption in the presence of the pump. In case of SE, a photon from the incoming probe pulse triggers the emission of another photon from excited state to the ground state. The emitted photon possesses slightly lower energy and is emitted in the same direction as the incoming probe photon, resulting in an elevation of the transmitted probe intensity. The SE causes an augmented probe light intensity to reach the detector, and thus in turn it generates a negative ΔA signal, as illustrated in **Figure 2.25 (A)**.
- Conversely, ΔA becomes positive when $I(\lambda) > I(\lambda, \Delta t)$, indicating that the pump contributes to an enhanced absorption of the probe pulse. It involves the absorption of the probe beam, causing transitions from lower excited states to higher excited states as shown in the **Figure 2.25 (B)**. Since the probe beam gets absorbed in this process, the transmitted probe intensity will be relatively lower compared to when the pump beam is present.

2.3.6. Terahertz Spectroscopy

THz spectroscopy investigates how matter interacts with electromagnetic radiation within the frequency range of ~ 0.1 THz to ~ 10 THz. THz spectroscopy encompasses the spectral range spanning approximately 3 cm^{-1} to about 600 cm^{-1} (**Figure 2.26**), which is commonly referred to as the far-infrared (far-IR) region of the electromagnetic spectrum. In terms of frequency, this range corresponds to approximately 0.1 to 20 THz, with 1 THz equivalent to 33.33 cm^{-1} . Nevertheless, recent developments over the past decade have refined the implications of this terminology, particularly in the context of "THz time-domain spectroscopy" or "time-resolved THz spectroscopy." In this context, THz spectroscopy implies the generation and detection of THz pulses in a synchronized and coherent routine via visible or near-IR laser pulses. Although THz waves were known as far back as the 19th century, our understanding of this frequency band was severely limited due to the absence of suitable scientific methods for generating and detecting them, resulting in what is commonly called the "THz gap." It wasn't until the emergence of ultrafast laser technology and advancements in semiconductor technology that we gained the capability to both generate and detect THz waves effectively. This breakthrough marked the commencement of extensive research, exploration, and practical applications involving THz waves. As our knowledge of THz waves deepened, we began uncovering many of their distinct characteristics. THz spectroscopy proves valuable for analyzing lattice vibrations and intraband transitions in semiconductors. THz spectroscopy serves as a valuable tool for gaining insights into the electrical and optical properties of perovskites, and THz-TDS experiments will be conducted on a different perovskite nanostructure to gain insights into their photo carrier dynamics.

2.3.6.1. A Brief Introduction to the History behind Terahertz Spectroscopy

The timeline of THz technology is marked by significant milestones and breakthroughs. In 1995, the introduction of THz time-domain spectroscopy sparked significant interest and catalyzed the rapid expansion of THz technology.⁹⁰⁻⁹³ By 2002, the European Space Agency's Tiger Team at Rutherford Appleton Laboratory achieved a remarkable milestone by producing the first image of a human hand using THz, demonstrating the potential of THz imaging. In 2004, ThruVision Ltd. achieved a major breakthrough by showcasing the world's inaugural compact THz camera designed for security screening.⁹⁴ This groundbreaking system proved effective in detecting concealed firearms and explosives hidden beneath clothing. In mid-2007,

a collaborative effort involving scientists from the U.S. Department of Energy's Argonne National Laboratory, as well as partners in Turkey and Japan, resulted in the creation of a portable THz source. This innovative device harnessed high-temperature superconducting crystals and the Josephson effect to generate THz radiation, making it a significant development for portable THz technology. In 2008, engineers at Harvard University achieved a transformative milestone by enabling the emission of coherent THz radiation at room temperature using a semiconductor source. In 2009, researchers made a serendipitous discovery that peeling adhesive tape produced THz radiation known as T-waves. This revelation provided valuable insights into the mechanisms behind THz radiation generation. In 2011, Rohm, a Japanese electronic parts manufacturer, in collaboration with a research team at Osaka University, successfully developed a chip capable of transmitting data using THz radiation, showcasing the potential for high-speed communication in the THz range. Later in 2013, researchers at the Georgia Institute of Technology and the Polytechnic University of Catalonia introduced a groundbreaking method to create graphene antennas tailored for THz frequencies.⁹⁴ This innovation opened up exciting new possibilities and applications in the field of THz technology. Overcoming various technical challenges, scientists have made significant progress in generating and detecting THz radiation, leading to the emergence of a new field in spectroscopy (**Figure 2.26**). One notable advantage of THz radiation is its non-ionizing nature, making it safe for applications like detecting hidden explosives, and narcotics, and its utilization in medical fields for pharmaceutical testing and medical imaging.⁹²

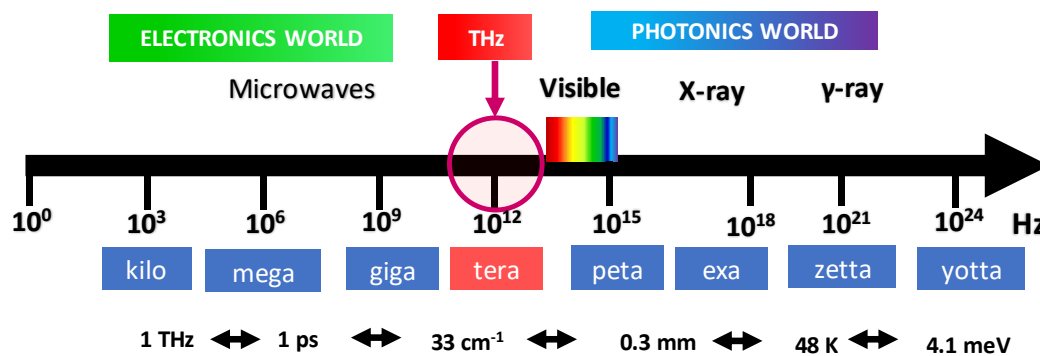


Figure 2.26 A visualization of the electromagnetic spectrum, highlighting the various regions based on frequency.

THz-based spectroscopic investigations are typically categorized into three primary types: (i) THz Time Domain Spectroscopy (TDS), (ii) Time-Resolved THz Spectroscopy (TRTS), and

(iii) THz Emission Spectroscopy.⁹¹ While TDS and TRTS are used for analyzing static and transient properties of the nanostructures, respectively. THz Emission Spectroscopy essentially functions as a TDS setup with the sample acting as the THz emitter. In this thesis, TRTS is employed to investigate the time-dependent mobility and photoconductivity response of the perovskite nanostructures.

Moreover, employing laser pulses for THz generation enables the implementation of pump-probe experiments. In these experiments, a sample is initially stimulated by an optical pulse (UV, VIS, IR), and subsequently, it's probed with a delayed THz pulse. This technique is employed to investigate ultrafast processes occurring on timescales spanning from fractions of picoseconds to nanoseconds.

2.3.6.2. Terahertz Technique Introduction

Recent progress in photonics and nanotechnology has generated increased interest in THz research and its applications. Furthermore, THz spectroscopy offers several additional advantages. Most semiconductor materials exhibit carrier scattering rates in the range of 10^{11} to 10^{12} s^{-1} , which align with THz frequencies (**Figure 2.27**).^{95–98}

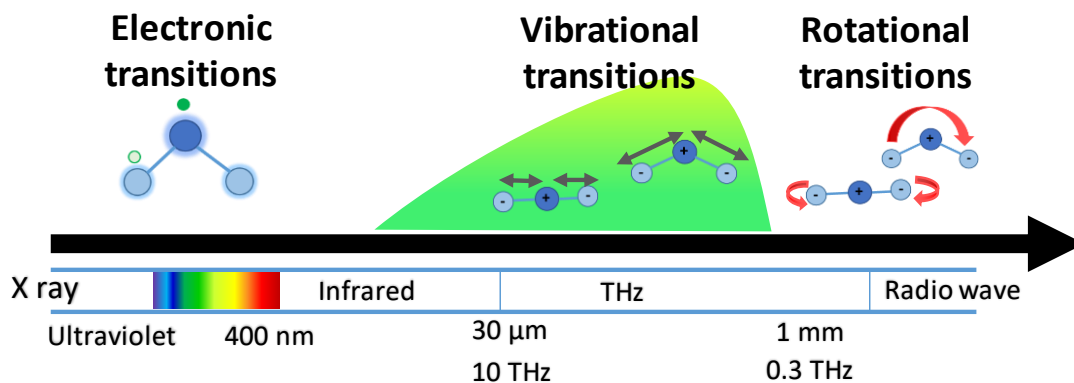


Figure 2.27 THz radiation is present in the region of the electromagnetic spectrum that comprises rotational, vibrational, and electronic transition frequencies.

This makes THz spectroscopy a valuable tool for accurately estimating carrier scattering rates and mobilities within such materials. Additionally, THz radiation provides a more precise and repeatable method for measuring photoconductivity when compared to traditional techniques like the Hall effect or four-probe methods. This is attributed to its non-invasive nature, which results in a superior model for determining photoconductivity. Another significant benefit of

THz spectroscopy lies in its capacity to detect the transient electric field, not just its intensity.⁹⁸ This assists in directly determining the amplitude as well as phase of each spectrum component through Fourier transformation. Consequently, researchers can establish crucial parameters such as the real and imaginary refractive index (n), mobility, photoconductivity, and absorption coefficient of the sample. Importantly, this complex-valued permittivity can be determined without relying on a Kramers-Kronig analysis. The determination of carrier mobilities in a given material can yield significantly divergent results when employing different techniques. This variation arises primarily from the inherent challenges associated with establishing connections between micro-sized wires and nano-sized particles, which are intrinsic to certain measurement methods. In contrast, TRTS which is a noninvasive method, distinguishes itself by avoiding the need for such electrical contacts, thus mitigating some of the aforementioned challenges and promoting consensus in the determination of carrier mobilities and diffusion lengths. Nevertheless, it is worth noting that the extraction of conductivity and subsequent data analysis in TRTS can be a non-trivial endeavor.^{96,99}

2.3.6.3. Time-Resolved Terahertz Spectroscopy (TRTS)

TRTS is a subgroup of the pump-probe technique (**Figure 2.28**) that offers unique insights not attainable through other spectroscopic methods. TRTS is a non-contact method capable of measuring transient photoconductivity with sub-picosecond temporal resolution. In a typical TRTS experiment, a pump pulse is used to excite the sample above its band gap, generating various charge carriers such as free carriers, excitons, and polarons. Subsequently, after photoexcitation, these charge carriers interact with the THz probe beam, and their response is reflected in the transient photoconductivity and mobility traces. The specific response to the THz probe depends on the nature of the photo-generated carriers. Furthermore, TRTS offers insights into scattering mechanisms that restrict charge carrier transport, including electron-phonon and impurity scattering. In this thesis, the TRTS study was conducted, where a single point on the THz waveform (often the peak point due to signal strength) is measured as a function of pump-probe delay.

this nonlinear interaction, electrons in the plasma are accelerated by the strong electric fields of the laser pulses.¹⁰¹⁻¹⁰⁴As a result, these accelerated electrons em

it radiation in the THz frequency range. This emission contains information about the plasma dynamics and can be detected as THz radiation.

2.3.6.3.2. Detection of THz

THz detection is a distinctive methodology prominently utilizing the electro-optic effect as shown in **Figure 2.30**. A fraction of the incident fundamental laser beam is judiciously partitioned and subjected to adjustable temporal delays, facilitating precise gating of the time-varying THz electric field. The gate beam is then directed to the balanced detector pair when no THz radiation is present; the detectors are in a balanced state, resulting in a nearly zero differential signal. However, the interaction of this THz electric field (after passing through a sample) with the gate pulse stimulates birefringence in the electro-optic crystal, which induces a change in the polarization of the gate pulse. This disturbance results in a signal that is observed due to the change in polarization due to the THz beam (which is detected after passing from the sample). Analogous the other ultrafast optical technique, phase-matching criteria is imperative for ensuring optimal coherence between the THz radiation and the gate beam. This necessity, in turn, imposes constraints upon the selection of gate wavelength and the choice of materials to be employed in the detection process.¹⁰¹

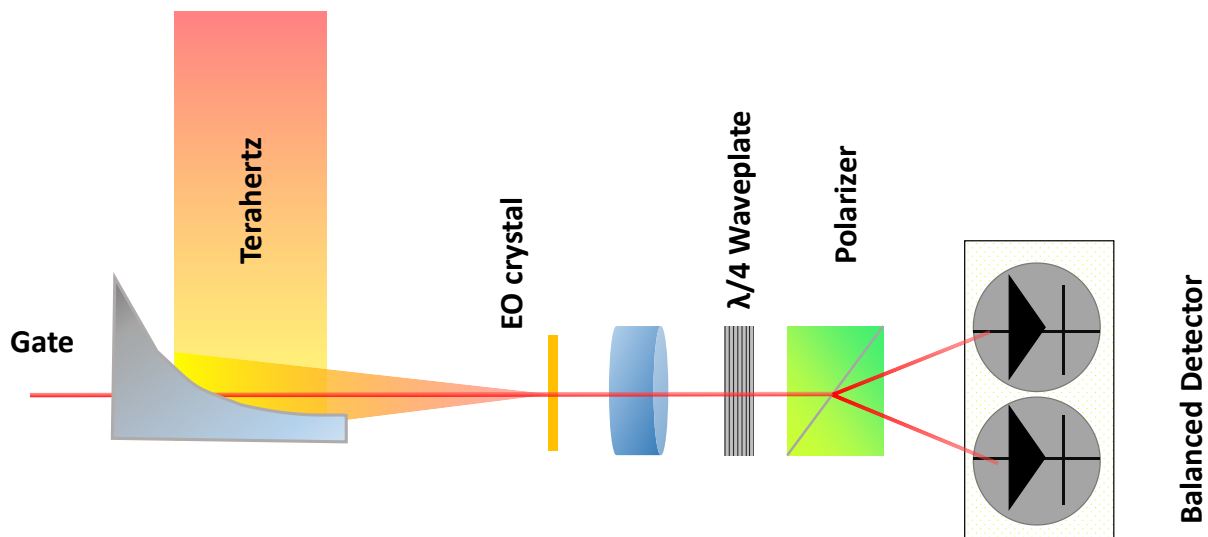


Figure 2.30 Electro optic detection setup in THz-TDS .

2.3.6.4. Experimental setup in our lab

In our lab we have employed the **Newport THz Time-domain Spectrometer (THz-TDS)** for performing the OPTP experiments in order to calculate the mobility and photoconductivity of various perovskite nanostructures which are under consideration. The complete layout is shown in **Figure 2.31**. The details of the instruments are discussed below:

- THz Generation Mechanism:** THz generation in this setup is based on a two-color laser-induced air plasma formation mechanism. This mechanism relies on either the asymmetric transient current model or the four-wave mixing method. The setup employs the transient current model, where the interaction of the second harmonic generation (SHG) and the fundamental laser beam results in alternating current and the generation of a strong plasma.

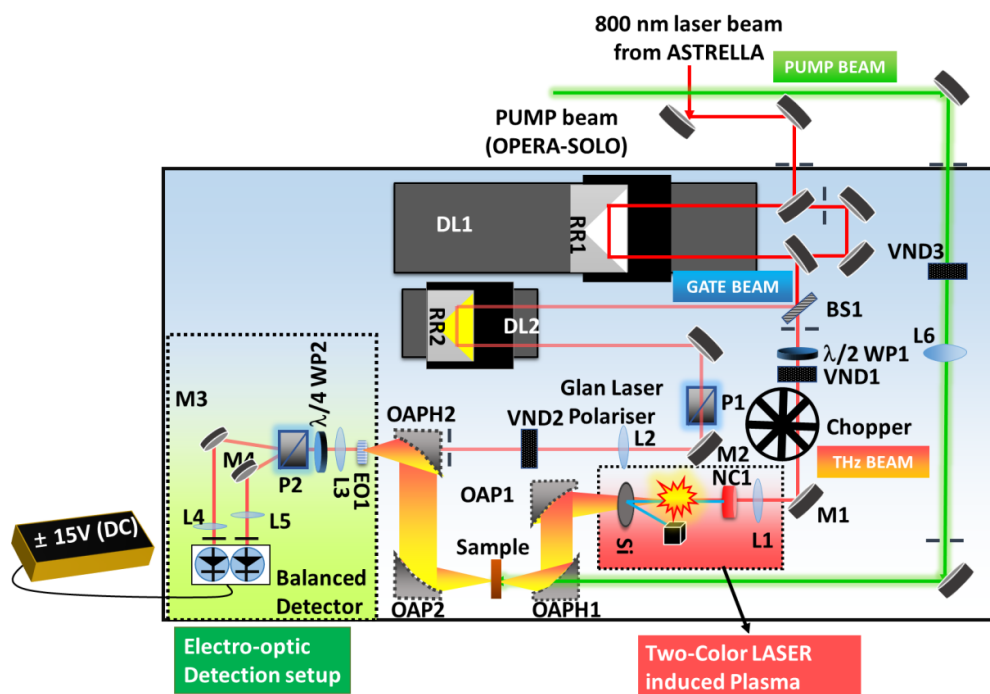


Figure 2.31 The schematic layout of Newport Terahertz Time Domain spectrometer.

- THz Detection:**

The system can acquire data in the standard THz detection range of 0.25 – 3 THz, with a best resolution of 1.25 GHz. Upgrading the system can extend the detection range to 4 THz with the best resolution of 0.23 GHz.

- **Optical Pump-THz Probe Delay:** The maximum delay range for the optical pump and THz probe is 4.3 ns, with a minimum step size of 1 fs. Upgraded versions can extend this range to 8.3 ns with a minimum step size of 0.13 fs.

2.3.6.4.1. Working of the Terahertz Time-domain Spectrometer (THz-TDS)

To operate as a TDS setup, the spectrometer only requires one input beam (p-polarized) from the Astrella system, centered at 800 nm with an energy of 1 mJ and 0.5 μ J for optimal electro-optic detection.

1. Beam Splitting:

- The incoming beam (800 nm) is divided into two parts using a beam splitter (BS1) placed near the spectrometer entrance, set at a 45° angle to the incoming beam.
- The transmitted portion carries most of the energy (~99%), while the reflected part contains less than 1% of the total power.
- This energy division is essential because the **transmitted beam** is used for generating THz radiation, while the **reflected beam** is needed for electro-optic measurements.

2. Optical Components:

- The **transmitted beam** undergoes polarization rotation of 180° with a $\lambda/2$ waveplate (WP1).
- Following WP1, a variable neutral density filter (VND1) is introduced to control the beam's intensity.
- The beam then passes through an optical chopper, synchronized with the laser output frequency, before being directed towards mirror M1.
- After reflecting off M1, the light is focused onto a nonlinear crystal (NLC NC1) made of Type-1 BBO, cut at 29.2° , and with a thickness of 0.2 mm. This results in the Second Harmonic Generation (SHG) at 400 nm from the fundamental beam at 800 nm.

- Both the fundamental and the second harmonic beams are jointly focused in air to create two-color laser-induced air plasma, emitting frequencies in the range of 0.2 - 3 THz.

3. THz Filtering:

- To isolate THz radiation from unwanted optical frequencies, a high-resistivity silicon (Si) wafer of sufficient thickness is inserted into the beam's path.

4. THz Beam Handling:

- The THz beam is focused and collimated onto the sample, which is positioned on a sample holder, using an off-axis parabolic mirror (OAP1) and an off-axis parabolic mirror with a hole (OAPH1).
- The beam is further manipulated by mirrors (OAP2 and OAPH2) after passing through the sample.
- Subsequently, the beam is focused onto the "EO1" NLC crystal using the parabolic mirror OPAH2.
- In this setup, ZnTe serves as the NLC medium, though GaAs and GaP can be used for higher detection bandwidths.

5. Electro-Optic Sampling:

- The reflected beam is used as the THz gate pulse for electro-optic sampling.
- To introduce a delay, the beam is redirected towards the retro-reflector RR2, which is securely mounted on the delay line DL2.
- Afterward, the beam passes through the GLAN Laser Polarizer P1, which sets the initial polarization for detection.
- The beam then travels through mirror M2 and lenses (L2, L3), as well as a central hole in OAPH2, before reaching the EO1 crystal.
- The incoming light's polarization state is transformed from linear to circular using a $\lambda/4$ waveplate (WP2), and a Wollaston prism (P2) separates perpendicular polarization components.

- This gate beam is then directed to the balanced detector pair (New FocusTM Nirvana). When no THz radiation is present, the detectors are in a balanced state, resulting in a nearly zero differential signal. However, in the presence of THz radiation after passing through a sample, birefringence is induced in the ZnTe <110> crystal (EO1), which induces a change in the polarization of the gate pulse. This disturbance results in a signal that is observed due to the change in polarization due to the THz beam (which is detected after passing from the sample).

6. Optical Pump THz Probe Spectroscopy (TRTS):

- The same experimental setup can be used for TRTS, also known as Optical OTP spectroscopy.
- An additional tunable pump beam, provided by OPERA SOLO (which is already detailed above) for sample photoexcitation, is incorporated into the setup.
- After passing through optical components for precise focusing (L6) and controlling pump beam intensity (VND3), the pump beam, which is collinear with the THz beam, is directed onto the sample through OAPH1.
- To ensure uniform excitation of the sample, the pump beam diameter is greater than the THz beam diameter.

2.3.6.4.2. Data acquisition and calculations involved

The Graphic User Interface (GUI) software of THz-TDS spectrometer generates an ASCII CSV output file, which can be easily imported into a variety of analysis programs for further processing. The pump-triggered Time-Resolved THz Spectroscopy (TRTS) scans can be conducted in two ways: frequency-averaged or frequency-resolved experiments.

Two categories of Time-Resolved THz Spectroscopy (TRTS) experiments are carried out, In the frequency-resolved TDS measurements, the entire THz waveform is recorded keeping the THz probe delay constant, while only the THz gate delay (DL2) is adjusted. This approach

provides comprehensive data that enables the determination of frequency-dependent conductivity information and a more detailed understanding of the material's response at different time delays. In the case of frequency-averaged experiments, a single point on the THz waveform is typically selected, often the peak point due to its signal strength. This chosen point is measured while varying the pump-probe delay. This offers an insight into the average material response over time. In this thesis to gain insights into the effect of excitation energy on the mobility of nanostructures or to gain the comparative insights of mobility or photoconductivity of different materials, we have opted for the frequency-averaged experiments to determine the peak THz photoconductivity and mobility in various perovskite nanostructures. Thus, the peak THz photoconductivity can be computed using the $\frac{-\Delta E(t_p)}{E_0(t_p)}$ traces obtained from the TRTS study.

The photoconductivity of the perovskite nanostructures has been computed using the following equation¹⁰⁵

$$\Delta\sigma(t_p) = \frac{d \varepsilon_0 (n_a + n_b)}{c} * \left(\frac{-\Delta E(t_p)}{E_0(t_p)} \right) \quad \text{Eq.2.23}$$

Here, d represents the sample thickness, n_a and n_b stands for the refractive indices of the media on either side of the sample, ε_0 stands for the permittivity of free space, c is the speed of light, ΔE represents the variation in THz field transmission after photoexcitation, while E_0 denotes the THz field that passes through the samples before any photoexcitation occurs. Following the photoconductivity determination, it can be utilized to estimate the effective mobility ($\varphi\mu$) of the carriers using the following equation

$$\varphi\mu = \frac{\Delta\sigma}{eN_0} \quad \text{Eq.2.24}$$

in the above equation the N_0 represents the total carrier density, e is the elementary charge and φ is the photon to free carrier conversion ratio. It's important to acknowledge that as the precise value of the photon-to-free carrier conversion ratio (φ) remains unknown, so this method yields an effective mobility ($\varphi\mu$) rather than absolute mobility (μ).

2.4. References

- (1) B. Murray, C.; J. Norris, D.; G. Bawendi, M. Synthesis and Characterization of Nearly Monodisperse CdE (E = Sulfur, Selenium, Tellurium) Semiconductor Nanocrystallites. *J. Am. Chem. Soc.* **2002**, *115* (19), 8706–8715.
- (2) Murray, C. B.; Kagan, C. R.; Bawendi, M. G. Synthesis and Characterization of Monodisperse Nanocrystals and Close-Packed Nanocrystal Assemblies. *Annu. Rev. Mater. Sci.* **2000**, *30* (1), 545–610.
- (3) K. LaMer, V.; H. Dinegar, R. Theory, Production and Mechanism of Formation of Monodispersed Hydrosols. *J. Am. Chem. Soc.* **2002**, *72* (11), 4847–4854.
- (4) MØLLER, C. H. R. K. N. Crystal Structure and Photoconductivity of Cæsium Plumbahalides. *Nature* **1958**, *182* (4647), 1436.
- (5) C. Schmidt, L.; Pertegás, A.; González-Carrero, S.; Malinkiewicz, O.; Agouram, S.; Mínguez Espallargas, G.; J. Bolink, H.; E. Galian, R.; Pérez-Prieto, J. Nontemplate Synthesis of CH₃NH₃PbBr₃ Perovskite Nanoparticles. *J. Am. Chem. Soc.* **2014**, *136* (3), 850–853.
- (6) Protesescu, L.; Yakunin, S.; I. Bodnarchuk, M.; Krieg, F.; Caputo, R.; H. Hendon, C.; Xi Yang, R.; Walsh, A.; V. Kovalenko, M. Nanocrystals of Cesium Lead Halide Perovskites (CsPbX₃, X = Cl, Br, and I): Novel Optoelectronic Materials Showing Bright Emission with Wide Color Gamut. *Nano Lett.* **2015**, *15* (6), 3692–3696.
- (7) Rosiles-Perez, C.; Serrano-Estrada, M. A.; Sidhik, S.; Alatorre-Ordaz, A.; Torres-Castro, A.; Vallejo, M. A.; Jiménez-González, A. E.; López-Luke, T. Synthesis of High Quality PbS Colloidal Quantum Dots by Ultrasonic Bath as Photosensitizers in a TiO₂ Solar Cell. *J. Solid State Chem.* **2020**, *292*, 121720.
- (8) Chang, J.; Waclawik, E. R. Colloidal Semiconductor Nanocrystals: Controlled Synthesis and Surface Chemistry in Organic Media. *RSC Adv.* **2014**, *4* (45), 23505–23527.
- (9) Lv, L.; Xu, Y.; Fang, H.; Luo, W.; Xu, F.; Liu, L. Generalized Colloidal Synthesis of High-Quality , Two-Dimensional Cesium Lead Halide Perovskite Nanosheets and Their Applications in Photodetectors. **2016**, 1–8.
- (10) Shekhirev, M.; Goza, J.; D. Teeter, J.; Lipatov, A.; Sinitiskii, A. Synthesis of Cesium Lead Halide Perovskite Quantum Dots. *J. Chem. Educ.* **2017**, *94* (8), 1150–1156.
- (11) Miyasaka, T. Perovskite Photovoltaics and Optoelectronics: From Fundamentals to Advanced Applications; John Wiley & Sons, **2021**.
- (12) Yang, S.; Qiu, Y. *Materials and Interfaces for Clean Energy*; CRC Press, **2021**.
- (13) Polavarapu, L.; Nickel, B.; Feldmann, J.; Urban, A. S. Advances in Quantum-Confined Perovskite Nanocrystals for Optoelectronics. *Adv. Energy Mater.* **2017**, *7* (16), 1700267.

- (14) Bera, S.; Kumar Behera, R.; Pradhan, N. α -Halo Ketone for Polyhedral Perovskite Nanocrystals: Evolutions, Shape Conversions, Ligand Chemistry, and Self-Assembly. *J. Am. Chem. Soc.* **2020**, *142* (49), 20865–20874.
- (15) Pan, G.; Bai, X.; Yang, D.; Chen, X.; Jing, P.; Qu, S.; Zhang, L.; Zhou, D.; Zhu, J.; Xu, W.; Dong, B.; Song, H. Doping Lanthanide into Perovskite Nanocrystals: Highly Improved and Expanded Optical Properties. *Nano Lett.* **2017**, *17* (12), 8005–8011.
- (16) Bragg, W. H.; Bragg, W. L. The Reflection of X-Rays by Crystals. *Proc. R. Soc. London. Ser. A, Contain. Pap. a Math. Phys. Character* **1997**, *88* (605), 428–438.
- (17) Stanjek, H. Basics of X-Ray Diffraction. **2004**, 107–119.
- (18) Le Pevelen, D. D. Small Molecule X-Ray Crystallography, Theory and Workflow; Lindon, J. C. B. T.-E. of S. and S. (Second E., Ed.; Academic Press: Oxford, **2010**, 2559–2576.
- (19) Patterson, A. L. The Scherrer Formula for X-Ray Particle Size Determination. *Phys. Rev.* **1939**, *56* (10), 978–982.
- (20) Bunaciu, A. A.; Udriștioiu, E. G.; Aboul-Enein, H. Y. X-Ray Diffraction: Instrumentation and Applications. *Crit. Rev. Anal. Chem.* **2015**, *45* (4), 289–299.
- (21) Lee, M. *X-Ray Diffraction for Materials Research: From Fundamentals to Applications*; CRC Press, 2017.
- (22) Tan, W. L.; McNeill, C. R. X-Ray Diffraction of Photovoltaic Perovskites: Principles and Applications. *Appl. Phys. Rev.* **2022**, *9* (2).
- (23) Braun, F. Über Ein Verfahren Zur Demonstration Und Zum Studium Des Zeitlichen Verlaufes Variabler Ströme. *Ann. Phys.* **1897**, *296* (3), 552–559.
- (24) Carter, D. B. W. C. B. Transmission Electron Microscopy A Textbook for Materials Science; springer publication, **2009**.
- (25) Freundlich, M. M. Origin of the Electron Microscope: The History of a Great Invention, and of a Misconception Concerning the Inventors, Is Reviewed. *Science.* **1963**, *142* (3589), 185–188.
- (26) Carter, C. B.; Williams, D. B. Transmission Electron Microscopy: Diffraction, Imaging, and Spectrometry; Springer, **2016**.
- (27) Shindo, D.; Oikawa, T. Analytical Electron Microscopy for Materials Science; Springer Science & Business Media, **2013**.
- (28) Winey, M.; Meehl, J. B.; O’Toole, E. T.; Giddings Jr, T. H. Conventional Transmission Electron Microscopy. *Mol. Biol. Cell* **2014**, *25* (3), 319–323.
- (29) Fultz, B.; Howe, J. M. Transmission Electron Microscopy and Diffractometry of Materials; Springer Science & Business Media, **2012**.
- (30) Shindo, D.; Oikawa, T.; Shindo, D.; Oikawa, T. Constitution and Basic Operation of Analytical Electron Microscopes. *Anal. Electron Microsc. Mater. Sci.* **2002**, 13-41.

- (31) Misra, P.; Dubinskii, M. A. *Ultraviolet Spectroscopy and UV Lasers*; CRC Press, 2002.
- (32) Thomas, M. J. K. *Ultraviolet and Visible Spectroscopy*; John Wiley & Sons: New York, **1996**.
- (33) Ball, D. W. *Modern Spectroscopy*, J. Michael Hollas. New York: John Wiley & Sons, Inc., 2004, 428, Paperback. ISBN 0-470-84416-7. Oxford University Press **2004**.
- (34) Mayerhöfer, T. G.; Pahlow, S.; Popp, J. The Bouguer-Beer-Lambert Law: Shining Light on the Obscure. *ChemPhysChem* **2020**, *21* (18), 2029–2046.
- (35) Pfeiffer, H. G.; Liebhafsky, H. A. The Origins of Beer's Law. *J. Chem. Educ.* **1951**, *28* (3), 123.
- (36) Beer. Bestimmung Der Absorption Des Rothen Lichts in Farbigen Flüssigkeiten. *Ann. Phys.* **1852**, *162* (5), 78–88.
- (37) Lambert, J. H. Photometry, or, on the Measure and Gradations of Light. *Color. Shade, Ed. by DL Di-Laura (Illum. Eng. Soc., 2001)* **1760**.
- (38) Skoog, D. A.; Holler, F. J.; Crouch, S. R. *Principles of Instrumental Analysis*; Cengage learning, 2017.
- (39) Tebyetekerwa, M.; Zhang, J.; Xu, Z.; N. Truong, T.; Yin, Z.; Lu, Y.; Ramakrishna, S.; Macdonald, D.; T. Nguyen, H. Mechanisms and Applications of Steady-State Photoluminescence Spectroscopy in Two-Dimensional Transition-Metal Dichalcogenides. *ACS Nano* **2020**, *14* (11), 14579–14604.
- (40) Yu, Y.; Fan, G.; Fermi, A.; Mazzaro, R.; Morandi, V.; Ceroni, P.; Smilgies, D.-M.; Korgel, B. A. Size-Dependent Photoluminescence Efficiency of Silicon Nanocrystal Quantum Dots. *J. Phys. Chem. C* **2017**, *121* (41), 23240–23248.
- (41) Albani, J. R. *Principles and Applications of Fluorescence Spectroscopy*; John Wiley & Sons, **2008**.
- (42) Hayes, G. R.; Deveaud, B. Is Luminescence from Quantum Wells Due to Excitons? *Phys. status solidi* **2002**, *190* (3), 637–640.
- (43) Wang, Z.; Zeng, H.; Sun, L. Graphene Quantum Dots: Versatile Photoluminescence for Energy, Biomedical, and Environmental Applications. *J. Mater. Chem. C* **2015**, *3* (6), 1157–1165.
- (44) Braslavsky, S. E. Glossary of Terms Used in Photochemistry, (IUPAC Recommendations 2006). *Pure Appl. Chem.* **2007**, *79* (3), 293–465.
- (45) Lakowicz, J. R. *Principles of Fluorescence Spectroscopy*; Springer, 2006.
- (46) Burda, C.; El-Sayed, M. A. High-Density Femtosecond Transient Absorption Spectroscopy of Semiconductor Nanoparticles. A Tool to Investigate Surface Quality. *Pure Appl. Chem.* **2000**, *72* (1–2), 165–177.

- (47) Buschmann, V.; Hempel, H.; Knigge, A.; Kraft, C.; Roczen, M.; Weyers, M.; Siebert, T.; Koberling, F. Characterization of Semiconductor Devices and Wafer Materials via Sub-Nanosecond Time-Correlated Single-Photon Counting. *J. Appl. Spectrosc.* **2013**, *80*, 449–457.
- (48) Rouzafzay, F.; Shidpour, R.; Abou-Zied, O. K.; Bagheri, K.; Al-Abri, M. Z. M. Lifetime and Dynamics of Charge Carriers in Carbon-Incorporated ZnO Nanostructures for Water Treatment under Visible Light: Femtosecond Transient Absorption and Photoluminescence Study. *J. Environ. Chem. Eng.* **2020**, *8* (5), 104097.
- (49) Phillips, D.; Drake, R. C.; O'Connor, D. V.; Christensen, R. L. Time Correlated Single-Photon Counting (TCSPC) Using Laser Excitation. **1985**.
- (50) Hirvonen, L. M.; Suhling, K. Fast Timing Techniques in FLIM Applications. *Front. Phys.* **2020**, *8*, 161.
- (51) Becker, W. Building Blocks of Advanced TCSPC Devices. *Adv. Time-Correlated Single Phot. Count. Tech.* **2005**, 47–60.
- (52) Dorow, C. An Introduction to the Technique and Applications of Pump-Probe Spectroscopy. *Phys. (College Park Md)* **2014**, 1–7.
- (53) Maiuri, M.; Garavelli, M.; Cerullo, G. Ultrafast Spectroscopy: State of the Art and Open Challenges. *J. Am. Chem. Soc.* **2019**, *142* (1), 3–15.
- (54) Porter, G. Flash Photolysis and Some of Its Applications. *Science* **1968**, *160* (3834), 1299–1307.
- (55) Edgerton, H. E.; Killian, J. R. Moments of Vision: The Stroboscopic Revolution in Photography. **1981**. *Leonardo* *14*, 3, 258-258.
- (56) Abraham, H.; Lemoine, J. Disparition Instantanée Du Phénomène de Kerr. *CR Acad. Sci. Hebd Seances Acad. Sci. D* **1899**, *129*, 206–208.
- (57) Zewail, A. H. Femtochemistry: Atomic-Scale Dynamics of the Chemical Bond. *J. Phys. Chem. A* **2000**, *104* (24), 5660–5694.
- (58) Shah, J. *Ultrafast Spectroscopy of Semiconductors and Semiconductor Nanostructures*; Springer Science & Business Media, **2013**; Vol. 115.
- (59) Kraabel, B.; McBranch, D.; Sariciftci, N. S.; Moses, D.; Heeger, A. J. Ultrafast Spectroscopic Studies of Photoinduced Electron Transfer from Semiconducting Polymers to C₆₀. *Phys. Rev. B* **1994**, *50* (24), 18543–18552.
- (60) Awschalom, D. D.; Freeman, M. R.; Samarth, N.; Luo, H.; Furdyna, J. K. Observation of Polaron Dynamics in Magnetic Quantum Wells. *Phys. Rev. Lett.* **1991**, *66* (9), 1212–1215.
- (61) Göbel, E. O. Ultrafast Spectroscopy of Semiconductors. In *Festkörperprobleme 30: Plenary*

Lectures of the Divisions Semiconductor Physics Thin Films Dynamics and Statistical Physics Magnetism Metal Physics Surface Physics Low Temperature Physics Molecular Physics of the German Physical Society (DPG), Regensburg, ; Rössler, U., Ed.; Springer Berlin Heidelberg: Berlin, Heidelberg, 1990; pp 269–294.

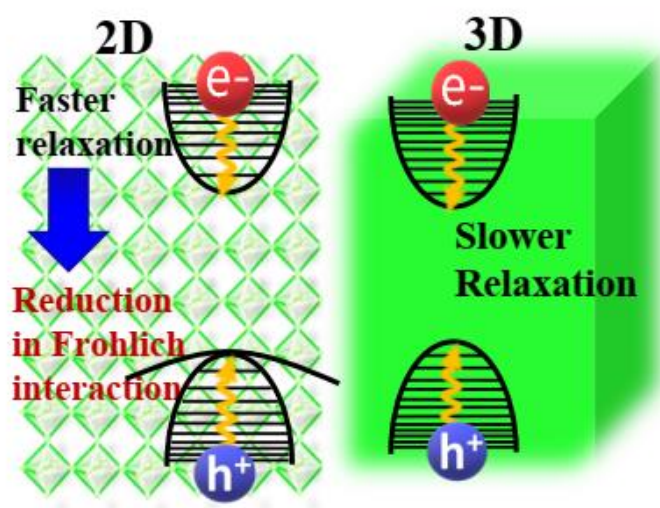
- (62) Nüsse, S.; Haring Bolivar, P.; Kurz, H.; Klimov, V.; Levy, F. Carrier Cooling and Exciton Formation in GaSe. *Phys. Rev. B* **1997**, *56* (8), 4578–4583.
- (63) Silfvast WT (**1996**) Laser fundamentals, Cambridge University Press. ISBN 0-521-55617-1
- (64) Wang, L.; Pyle, J. R.; Cimatu, K. L. A.; Chen, J. Ultrafast Transient Absorption Spectra of Photoexcited YOYO-1 Molecules Call for Additional Investigations of Their Fluorescence Quenching Mechanism. *J. Photochem. Photobiol. A Chem.* **2018**, *367*, 411–419.
- (65) Zewail, A. H. Femtochemistry: Atomic-scale Dynamics of the Chemical Bond Using Ultrafast Lasers (Nobel Lecture). *Angew. Chemie Int. Ed.* **2000**, *39* (15), 2586–2631.
- (66) Taylor, N. *LASER: The Inventor, the Nobel Laureate, and the Thirty-Year Patent War*; Simon and Schuster, 2002.
- (67) DeMaria, A. J.; Stetser, D. A.; Glenn Jr, W. H. Ultrashort Light Pulses. *Science* (80-.). **1967**, *156* (3782), 1557–1568.
- (68) McClung, F. J.; Hellwarth, R. W. Giant Optical Pulsations from Ruby. *Appl. Opt.* **1962**, *1* (101), 103–105.
- (69) Mocker, H. W.; Collins, R. J. Mode Competition and Self-locking Effects in Aq-switched Ruby Laser. *Appl. Phys. Lett.* **1965**, *7* (10), 270–273.
- (70) Wagner, W. G.; Lengyel, B. A. Evolution of the Giant Pulse in a Laser. *J. Appl. Phys.* **1963**, *34* (7), 2040–2046.
- (71) DeMaria, A. J.; Stetser, D. A.; Heynau, H. Self Mode-locking of Lasers with Saturable Absorbers. *Appl. Phys. Lett.* **1966**, *8* (7), 174–176.
- (72) Hönninger, C.; Paschotta, R.; Morier-Genoud, F.; Moser, M.; Keller, U. Q-Switching Stability Limits of Continuous-Wave Passive Mode Locking. *JOSA B* **1999**, *16* (1), 46–56.
- (73) Weiner, A. Principles of Mode-Locking. **2009**.
- (74) Laser, W. D. *Laser Spectroscopy: Vol. 1 Basic Principles*; Springer-Verlag, 2008.
- (75) Ducasse, A.; Rullière, C.; Couillaud, B. Methods for the Generation of Ultrashort Laser Pulses: Mode-Locking. *Femtosecond laser pulses Princ. Exp.* **2005**, 57–87.
- (76) Haus, H. A. Mode-Locking of Lasers. *IEEE J. Sel. Top. Quantum Electron.* **2000**, *6* (6), 1173–1185.
- (77) Brabec, T.; Spielmann, C.; Curley, P. F.; Krausz, F. Kerr Lens Mode Locking. *Opt. Lett.* **1992**, *17* (18), 1292–1294.

- (78) Nurhuda, M.; Suda, A.; Midorikawa, K. Generalization of the Kerr Effect for High Intensity, Ultrashort Laser Pulses. *New J. Phys.* **2008**, *10* (5), 53006.
- (79) Paufler, P. Introduction to Nonlinear Optics. Cambridge: University Press, **2011**, ISBN-9780521877015. International Union of Crystallography **2012**.
- (80) Ippen, E. P.; Haus, H. A.; Liu, L. Y. Additive Pulse Mode Locking. *JOSA B* **1989**, *6* (9), 1736–1745.
- (81) Ippen, E. P. Principles of Passive Mode Locking. *Appl. Phys. B* **1994**, *58*, 159–170.
- (82) Giordmaine, J. A.; Miller, R. C. Tunable Coherent Parametric Oscillation in LiNbO₃ at Optical Frequencies. *Phys. Rev. Lett.* **1965**, *14* (24), 973–976.
- (83) Jefferson Flórez Gutiérrez. Optical Parametric Amplification : From Nonlinear Interferometry to Black Holes. **2022**.
- (84) Giese, E.; Fickler, R.; Zhang, W.; Chen, L.; Boyd, R. W. Influence of Pump Coherence on the Quantum Properties of Spontaneous Parametric Down-Conversion. *Phys. Scr.* **2018**, *93* (8), 84001.
- (85) Brodeur, A.; Chin, S. L. Ultrafast White-Light Continuum Generation and Self-Focusing in Transparent Condensed Media. *JOSA B* **1999**, *16* (4), 637–650.
- (86) Fork, R. L.; Shank, C. V; Hirlimann, C.; Yen, R.; Tomlinson, W. J. Femtosecond White-Light Continuum Pulses. *Opt. Lett.* **1983**, *8* (1), 1–3.
- (87) Marburger, J. H. Self-Focusing: Theory. *Prog. quantum Electron.* **1975**, *4*, 35–110.
- (88) Shimizu, F. Frequency Broadening in Liquids by a Short Light Pulse. *Phys. Rev. Lett.* **1967**, *19* (19), 1097.
- (89) Ashcroft, C. M.; Cole, J. M. *Molecular Engineering of Organic and Organometallic Second-Order Nonlinear Optical Materials*, 2nd ed.; Elsevier Ltd., 2018.
- (90) Brochard-Wyart, F.; Gennes, P. G.; Lkger, L.; Marciano, Y.; Raphael, E. Feature Article. *P.G. Gennes' Impact Sci. Soft Matter Biophys.* **2009**, *2*, 121–126.
- (91) Huang, S.; Deng, H.; Wei, X.; Zhang, J. Progress in Application of Terahertz Time-Domain Spectroscopy for Pharmaceutical Analyses. *Front. Bioeng. Biotechnol.* **2023**, *11*.
- (92) Nichols, E. F.; Tear, J. D. Joining the Infra-Red and Electric Wave Spectra. *Astrophys. Journal*, *vol. 61, p. 17* **1925**, *61*, 17.
- (93) Huang, S.; Deng, H.; Wei, X.; Zhang, J. Progress in Application of Terahertz Time-Domain Spectroscopy for Pharmaceutical Analyses. *Front. Bioeng. Biotechnol.* **2023**, *11* (July), 1–29.
- (94) Kumar, P.; Pratyush, S.; Mishra, R.; Behera, S. An Introduction to Terahertz Technology, Its History, Properties and Application. *Int. Conf. Comput. Commun.* **2015**, No. February, 1–5.

- (95) Strait, J. H.; Wang, H.; Shivaraman, S.; Shields, V.; Spencer, M.; Rana, F. Very Slow Cooling Dynamics of Photoexcited Carriers in Graphene Observed by Optical-Pump Terahertz-Probe Spectroscopy. *Nano Lett.* **2011**, *11* (11), 4902–4906.
- (96) Milot, R. L.; Eperon, G. E.; Snaith, H. J.; Johnston, M. B.; Herz, L. M. Temperature-dependent Charge-carrier Dynamics in CH₃NH₃PbI₃ Perovskite Thin Films. *Adv. Funct. Mater.* **2015**, *25* (39), 6218–6227.
- (97) Goyal, R.; Tiwari, A. Terahertz Conductivity of Nanoscale Materials and Systems. *Terahertz Technol.* **2022**, 185.
- (98) Dexheimer, S. L. *Terahertz Spectroscopy: Principles and Applications*; CRC press, 2017.
- (99) George, P. A.; Strait, J.; Dawlaty, J.; Shivaraman, S.; Chandrashekar, M.; Rana, F.; Spencer, M. G. Ultrafast Optical-Pump Terahertz-Probe Spectroscopy of the Carrier Relaxation and Recombination Dynamics in Epitaxial Graphene. *Nano Lett.* **2008**, *8* (12), 4248–4251.
- (100) Zhuldybina, M.; Ropagnol, X.; Trudeau, C.; Bolduc, M.; Zednik, R. J.; Blanchard, F. Contactless in Situ Electrical Characterization Method of Printed Electronic Devices with Terahertz Spectroscopy. *Sensors* **2019**, *19* (3), 444.
- (101) Gallot, G.; Grischkowsky, D. Electro-Optic Detection of Terahertz Radiation. *J. Opt. Soc. Am. B* **1999**, *16* (8), 1204–1212.
- (102) Sun, W.; Wang, X.; Zhang, Y. Terahertz Generation from Laser-Induced Plasma. *Opto-Electronic Sci.* **2022**, *1* (8), 220003–220027.
- (103) Andreeva, V. A.; Kosareva, O. G.; Panov, N. A.; Shipilo, D. E.; Solyankin, P. M.; Esaulkov, M. N.; de Alaiza Martinez, P.; Shkurinov, A. P.; Makarov, V. A.; Bergé, L.; Chin, S. L. Ultrabroad Terahertz Spectrum Generation from an Air-Based Filament Plasma. *Phys. Rev. Lett.* **2016**, *116* (6), 63902.
- (104) You, Y. S.; Oh, T. I.; Kim, K. Y. Off-Axis Phase-Matched Terahertz Emission from Two-Color Laser-Induced Plasma Filaments. *Phys. Rev. Lett.* **2012**, *109* (18), 183902.
- (105) Yettapu, G. R.; Talukdar, D.; Sarkar, S.; Swarnkar, A.; Nag, A.; Ghosh, P.; Mandal, P. Terahertz Conductivity within Colloidal CsPbBr₃ Perovskite Nanocrystals: Remarkably High Carrier Mobilities and Large Diffusion Lengths. *Nano Lett.* **2016**, *16* (8), 4838–4848.

Chapter 3

Effect of Confinement on the Exciton and Bi-exciton Dynamics in Perovskite 2D-Nanosheets and 3D-Nanocrystals



The performance of the high-end optoelectronic devices is essentially influenced by the intrinsic relaxation mechanisms pursued by the hot carriers. Therefore, the key towards achieving progression in such fields lies in developing a complete understanding of the involved carrier cooling dynamics. In this work, an endeavour has been made to highlight the difference in the cooling mechanisms in 2D CsPbBr₃ nanosheets (NSs) and their 3D counterpart nanocrystals (NCs) with the aid of femto-second broadband pump-probe spectroscopy, varying the excitation energies. The exciton and bi-exciton dynamics in both the systems are found to be retarded upon increasing the excitation energy. However, in contrast to 3D NCs, carrier cooling is found to be faster in 2D system, regardless of the excitation energy used, attributing this to less efficient charge screening by Fröhlich interaction in low-dielectric medium. Similar trend replicates in the biexciton formation rate since the formation is also found to be faster in NSs compared to NCs.

3.1 Introduction

Research on all inorganic lead halide perovskite (LHP) materials has witnessed tremendous interest in the scientific community due to their remarkable performance in optoelectronic devices such as solar cells,¹⁻³ light-emitting diodes (LEDs),^{4,5} photodetector,⁶ lasers.^{7,8} The impressive combination of optical properties such as tunable bandgap⁹, strong absorption coefficient,¹⁰ high photoluminescence (PL),¹¹ high carrier mobility,¹² and defect tolerant nature¹³ accompanied by low cost and easier processability has evidently made the perovskites to emerge as one of the potential candidates for the above applications. Research on LHPs are widely investigated not only with bulk material but also in different quantum confined structures which include quantum dots (0D),¹⁴ nanorods (1D),¹⁵ nanoplatelets¹⁶ and nanosheets (2D)¹⁷ and NCs (3D)⁹. Two-dimensional (2D) LHPs have already established themselves as magnificent material for optoelectronic devices with certain added advantages over 3D counterparts such as their higher absorption coefficient, larger transition oscillator strength with strongly bound excitons (higher binding energy) and faster radiative lifetime¹⁸, faster charge transport properties, unique planar geometry, and reduced charge hopping barriers.¹⁹⁻²¹

Moreover, the drastic difference upon altering the dimensionality of the LHPs, with the stoichiometric ratios left unchanged can manifest itself as different charge carrier cooling rates. This is an indirect outcome of the variation in the strength of the Fröhlich interaction which results from altering the number of confinement dimensions. So, in order to design and develop any kind of optoelectronic devices employing such LHP materials, understanding of the underlying charge carrier dynamics taking place on ultrafast time scale is essentially important. For example in solar cell applications, a knowledge of charge separation and the carrier cooling processes in the photo-excited LHPs is extremely useful.²² Previous reports suggest that slower hot-carrier relaxation indeed helps in increasing the carrier diffusion length which eventually increases the efficiency of the solar cell.²³ On the contrary for LEDs and lasing applications, faster hot-carrier dynamics is expected due to competition between hot-carrier relaxation and charge-trapping dynamics. The aforementioned properties make the 2D materials more promising candidates than their bulk counterparts for light-emitting diodes (LEDs) and lasing applications.^{24,25} Recently Lv and co-workers²⁰ reported synthesis of high-quality 2D LHP NSs and their applications in photodetectors, where they have focussed mainly on device performance while ultrafast carrier dynamics is not explored. However, it is well documented in the literature that clear insights of ultrafast carrier dynamics which includes hot carrier

cooling, exciton and bi-exciton dynamics is extremely important to improve the device performance.²⁵

In the present studies, we have synthesized 2D CsPbBr₃NSs and its 3D counterpart NCs to investigate the effect of quantum confinement on charge carrier relaxation dynamics by exciting the samples near-band edge and far band edge excitation. A strong dependency on hot carrier cooling and bi-exciton dynamics was observed by changing both dimensionality (2D to 3D) and excitation (pump) energy. Hot carrier relaxation process is found to be slowed down with excess photo-excitation energy which can be related to increase in the intra band relaxation time for carriers to reach the band edge position. In 2D NSs, faster hot carrier relaxation has been attributed due to less efficient screening of charge carriers by Fröhlich interaction in the layered structure which has higher surface to volume ratio. Ultrafast carrier dynamics of these materials can have immense implications in design and development 2D nano-structured devices.

3.2 Results and Discussion

3.2.1 Structural Analysis

In the present study, our main aim is to investigate the quantum confinement effects on the exciton and biexciton dynamics in CsPbBr₃ NCs and nanosheets (NSs) with the aid of Femto-second broad band pump-probe spectroscopy.

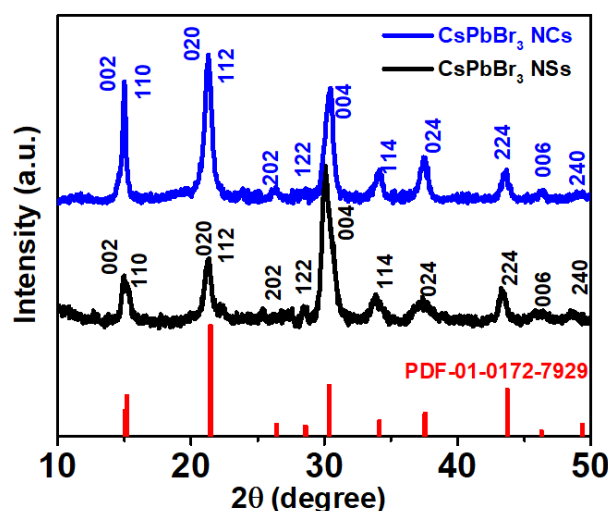


Figure 3.1 XRD patterns of CsPbBr₃ NCs and NSs.

Both NCs and NSs were synthesized after following reported literature with minor modifications by changing reaction time and temperature. The synthesis details for the same have been provided in the Chapter 2. The XRD patterns of as synthesized CsPbBr₃ NCs and NSs are depicted in **Figure 3.1**. The XRD peaks are well defined and are in good agreement with the reported JCPDS Values (PDF-01-0172-7929). The XRD studies reveal that both in the case of CsPbBr₃ NCs and NSs the orthorhombic phase of the CsPbBr₃ is maintained.

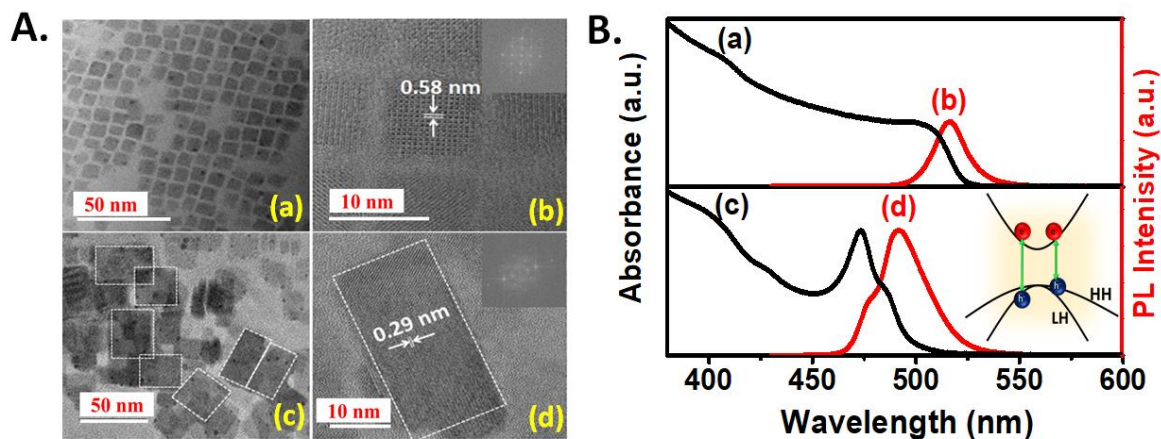


Figure 3.2 (A) HR-TEM images of (a, b) CsPbBr₃ NCs and (c, d) NSs (Inset: corresponding FFT patterns). (B) Optical absorbance and PL studies for (a,b) CsPbBr₃ NCs and (c, d) CsPbBr₃ NSs. (Inset: Schematic representation of the splitting in the VB due to increased spin-orbit coupling in NSs)

Figure 3.2 A shows the HR-TEM image of as synthesized CsPbBr₃ NCs (a, b) and NSs (c, d). The NCs are seen to have an edge length of 14 nm whereas the NSs have average length 32 nm and width 15nm. **Figure 3.2 B** (upper panel) shows the first excitonic absorption peak at 504 nm and corresponding PL peak at 516 nm (FWHM =16 nm) for CsPbBr₃ NCs. However, for the corresponding NSs the effect of enhanced quantum confinement is clearly manifested in the steady state optical absorption data which shows the absorption onset to commence at comparatively higher energy (blue shift by 90meV), along with this there is a noticeable appearance of three distinctive absorption peaks. The two energetically close features peaking at 487 nm and 473 nm are observed as an outcome of the VB splitting into the heavy hole (HH) and light hole (LH) band due to spin orbit coupling. A similar observation was observed in CsPbBr₃ NSs by Lv and group.²⁰ The explicit thickness of the as synthesised NSs can be

estimated to be ~3 nm from the steady state optical absorption spectral data as corresponding to 3 perovskite layers, equivalent to a width of 3 nm.²⁰ Concurrently, in addition to these low energy features, another upper excitonic peak at 400 nm is also noticeable. The two observed absorption features at 473 nm and 487 nm can be attributed to the electron- light hole and electron-heavy hole transitions respectively.^{20,26} In contrast, the PL spectra seems as a mirror reflected image of the optical absorption spectra. The detailed investigations of the optical properties in very strongly confined CsPbBr₃ QDs (particle size = 5.5 nm i.e. lesser than the exciton Bohr radius for CsPbBr₃) have also come across with similar observations.²⁶ Such effect of confinement in these highly confined CsPbBr₃ QDs has manifested itself as two energetically separated peaks, an outcome of two distinct transition as observed in the steady state absorption data and the similar effect is also reflected in PL data (**Figure 3.2 B**) also.²⁶ It exhibits a hump at 476 nm with the main peak centered at 490 nm (FWHM=30nm) in photoluminescence data. The PL peak at 476 nm (higher energy) and 490 nm (lower energy), which is ascribed to the LH to electron and HH to electron transitions respectively. Interestingly, the PL peak intensity at 490 nm is much higher as compared to that of 476 nm, which can be associated to the de-population of the carriers from LH band moving towards the HH band. Owing to the increment in the PL intensity at 490 nm it implies to the enhanced population of the carriers in the HH state following the de-population from the LH state augmenting the recombination of the carriers in the HH state. The so far established TRPL measurements cannot provide clear picture of the overall dynamics. Thus, in order to monitor such ultrafast processes in both CsPbBr₃ NCs and NSs, Femto-second TA studies have been carried out and are discussed in next section.

3.2.2 Ultrafast Transient absorption studies

The present studies are primarily aimed to probe the effect of quantum confinement on charge carrier dynamics with intense focus laid on understanding the carrier cooling and bi-exciton dynamics. To carry on such investigations, femto-second pump-probe TA spectroscopy fits as a suitable technique owing to its sensitivity at such time scales. We have employed specifically two different excitation energies for monitoring the carrier dynamics for both the investigated systems, one far above bandgap (4.13eV) i.e., 300 nm and another near band-edge (2.9eV) i.e. 420 nm in order to explore the change in carrier relaxation pathways depending upon initial photoexcitation energies, specifically biexciton and exciton transient dynamics. It is observed

that due to the divergence in the underlying carrier-phonon, carrier- carrier scattering processes which ultimately help in the attainment of the thermal equilibrium, the carrier dynamics are seen to differ greatly in the two systems (NCs and NSs) under such extreme excitations. It has also been ensured that all the experimental data have been collected under the same incident laser fluence ($\sim 50 \text{ uJ/cm}^2$) and similar sample optical density to ascertain the same experimental conditions.

3.2.2.1 3D CsPbBr₃ NCs

Figures 3.3 A and 3.3 B show the differential absorption spectra of CsPbBr₃ NCs at different pump-probe time delays for both 420 nm and 300 nm pump excitation respectively. The TA spectra for both the excitations is mainly dominated by state filling which results in analogous ground state bleach (GSB) peaking at 510 nm (excitonic absorption) with positive absorption bands on both side of the GSB, one on the higher energy side and another towards the lower energy side of the spectra.^{27,28} These positive bands have been discussed elaborately in the later sections. It is found that in case of just above bandgap (420 nm) excitation, the bleach appears to be narrower (475-525 nm, FWHM = 50 nm) (**Figure 3.3 A**) than that observed upon far band-gap excitation (300 nm) where the transient bleach expands over much larger spectral extent (445-525 nm, FWHM = 80 nm) (**Figure 3.3 B**). This observation clearly suggests that 420 nm excitation populates only the near band edge states, while in case of 300 nm excitation the broadening of the bleach band can be attributed due to excitation into the upper electronic states of the CB (**Figure 3.3 D**). We have monitored the bleach growth and recovery kinetics at 510 nm after exciting at both 420 nm and 300 nm for CsPbBr₃ NCs as shown in **Figure 3.3 C**. The transient kinetics for both the excitation wavelengths can be fitted multi-exponentially as shown in **Table 3.1**. The bleach growth can be fitted bi-exponentially with time constants $\tau_1^g = < 100 \text{ fs}$ (35%) and $\tau_2^g = 460 \text{ fs}$ (65%) for 420 nm excitation, and $\tau_1^g = 190 \text{ fs}$ (54%) and $\tau_2^g = 1.18 \text{ ps}$ (46%) for 300 nm excitation. These growth time constants monitored at the excitonic bleach position can be attributed to the time taken by the carriers to cool down to the band edge subsequent to photo-excitation. These constants thus provide a clear evidence that the carrier cooling time for 300 nm excitation is much slower as compared to that at 420 nm excitation, which implies that longer time is required by the carriers to relax to the band edge.²⁹

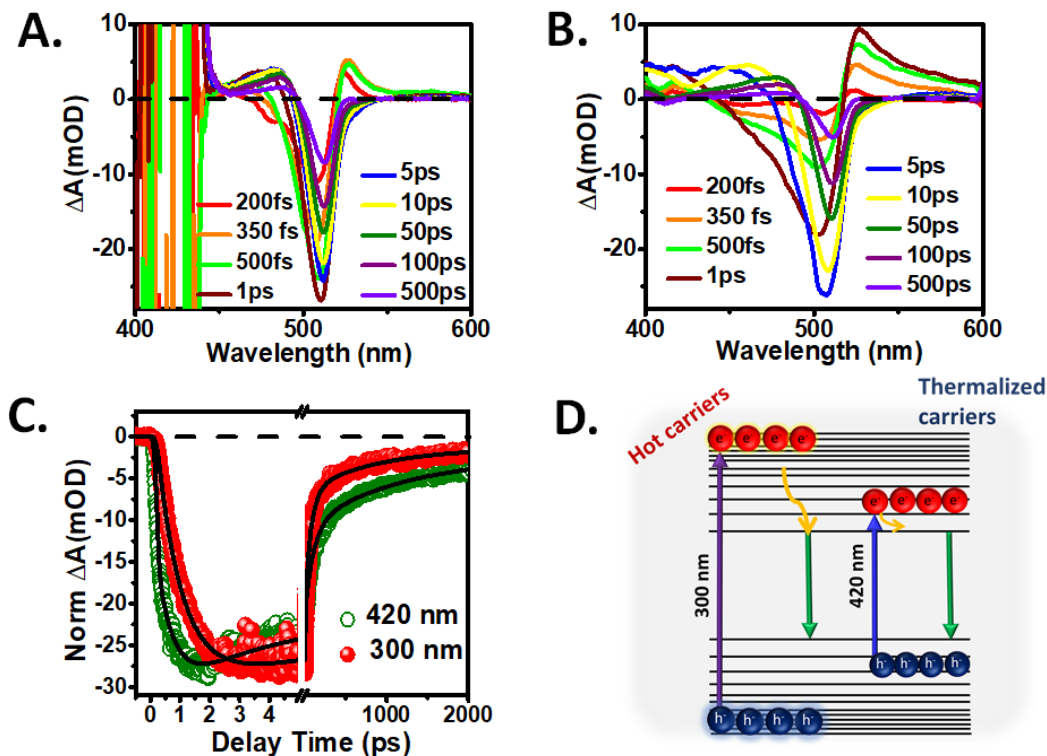


Figure 3.3 (A, B) TA spectra of CsPbBr₃ NCs at different time delays after exciting the samples at 420 nm and 300 nm laser light respectively. **(C)** Bleach recovery kinetics monitored at 510 nm for both the 420 nm (green: open circles) and 300 nm excitation (red: closed circles), **(D)** Schematic representation of the photoexcited charge carrier cooling involved after the pump excitation.

A schematic representation explaining the increase in carrier cooling time for far bandgap excitation in the early time scale is depicted in **Figure 3.3 D**. Initial bleach recovery kinetics is found to be faster for 420 nm ($\tau_1 = 8$ ps (-32.68%), $\tau_2 = 42$ ps (-31.5%)) excitation as compared to 300 nm excitation ($\tau_1 = 4.42$ ps (-28%), $\tau_2 = 25.25$ ps (-44%)). This is quite expected due to quicker filling of the band-edge states by the charge carriers as a result of their depopulation from the excited states in lesser time and thereby accelerating their relaxation to the ground state at lower excitation energies. (**Figure 3.3 C, Table 3.1**).

Table 3.1 Kinetics Fitting Parameters for CsPbBr₃ NCs Dispersed in n-hexane after exciting the Samples at 420 nm and 300 nm.

	λ_{pump} (nm)	λ_{probe} (nm)	τ_{growth}	τ_1	τ_2	τ_3	τ_4
CsPbBr ₃ NCs	420	510	$\tau_1^g = < 100$ fs (35%) $\tau_2^g = 460$ fs (65%)	8ps (-32.68%)	42ps (-31.5%)	211ps (-22.62%)	>1ns (-13.2%)
	300	510	$\tau_1^g = 190$ fs (54%) $\tau_2^g = 1.18$ ps (46%)	4.42ps (-28%)	25.25ps (-44%)	162ps (-20%)	>1ns (-8%)

3.2.2.2 2D CsPbBr₃ NSs

In order to comprehend the effect of confinement on the exciton and biexciton dynamics transient absorption studies were conducted for both near band edge and far band edge excitation for CsPbBr₃ NSs.

3.2.2.2.1 Near bandgap excitation (420 nm)

It is seen that the TA response of the NSs displays quite interesting features as shown in Figure 3.3A. Two negative absorption bands in the region around 450-490 nm with minima at 474 nm and 487 nm are discerned accompanied by two positive bands, one on the higher energy side (around 450 nm) and the other towards the lower energy side at 498 nm. It is interesting to see that in contrast to the 3D NCs (**Figure 3.2 A**), the bleach intensity of 2D counterparts (**Figure 3.4 A**) is much higher, even after maintenance of similar experimental conditions. This can be attributed to the higher physical confinement of the carriers in one direction resulting in the increase in overlap of electron and hole wave-functions allowing them to stay in close proximity. It consequently increases the coulomb binding of these charge carriers and results in formation of strongly bound excitons with larger oscillator strength, leading to higher extinction coefficient observed in 2D as compared to 3D counterparts.^{30,31}

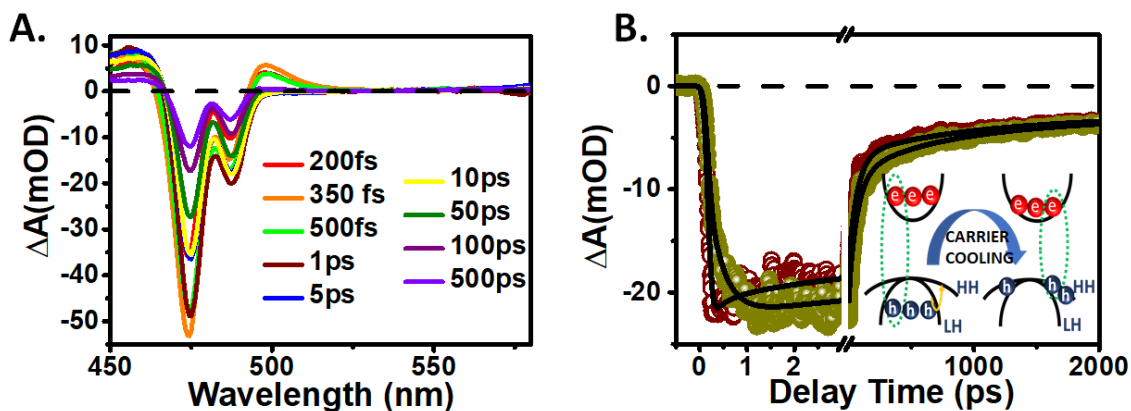


Figure 3.4 (A) TA Spectra for 2D CsPbBr₃ NSs under 420 nm pump excitation (B) Comparative kinetic traces for system probed at probe wavelength $\lambda = 474$ nm and 487 nm; Inset: schematic representation of carrier cooling process in 2D CsPbBr₃ NSs.

Successively, the higher magnitude of extinction coefficient (α) augments the injected carrier density (n_0) in case of NSs in contrast to that expected for NCs even under the condition of the same laser fluence (J) ($n_0 = J\alpha$).³² The higher energy positive band can be simply attributed to photoinduced absorption (PIA) of the charge carriers. Interestingly, the positive signal on the lower energy side of the bleach band is visible only at the early time scales, later replaced by the strong bleaching and can be attributed to the biexciton signal.²⁷

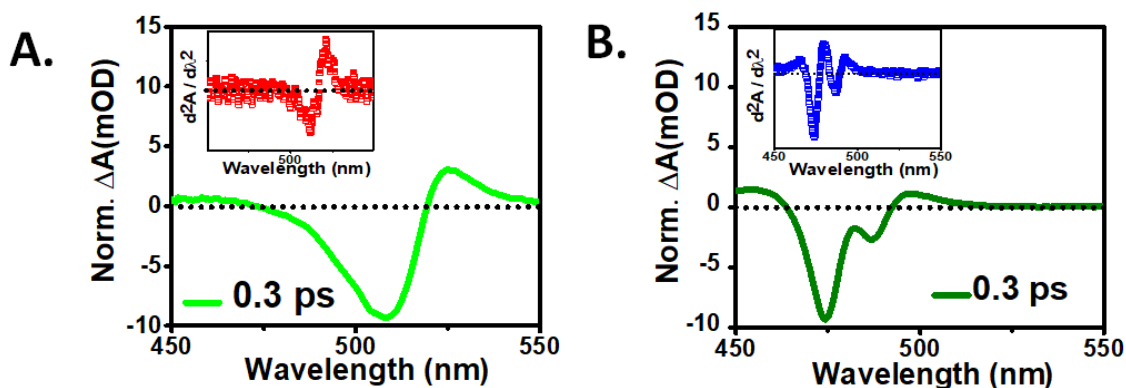


Figure 3.5 Early time (0.3 ps) TA spectra of (A) CsPbBr₃ NC and (B) CsPbBr₃ NSs matches with the second derivative of steady-state absorption for CsPbBr₃ (inset), which clearly signifies the biexciton-induced Stark effect in the TA spectra

Briefly, this conclusive remark regarding the biexciton signal can be drawn since the TA spectra of NSs at early time scale is analogous to the second derivative of the absorption spectrum (**Figure 3.5A**) which is in coherence with the bi-excitonic Stark effect as in the case of NCs. In this section we aim to limit the discussion details to the exciton dynamics while the bi-exciton dynamics will be explained in the latter section of the paper (**Figure 3.7 B**). To figure out charge carrier and recombination dynamics transient kinetics at both 474 nm and 487 nm bleach positions have been monitored and shown in **Figure 3.4 B**. Bleach kinetics at both the excitonic positions are fitted multi-exponentially and shown in **Table 3.2**. Apparently, on comparing the transient kinetics it is clearly seen that the bleach at 474 nm grows as well as decays faster as compared to that at 487 nm. The bleach growth kinetics at 474 nm can be fitted mono-exponentially with time constant $\tau_g = <100$ fs (pulse-width limited), while at 487 nm it can still be fitted mono-exponentially but with relatively slower time constant $\tau_g = 330$ fs (**Table 3.2**).

Table 3.2. Kinetics fitting parameters for CsPbBr₃ NSs at different wavelengths dispersed in n-hexane after exciting the samples at 420 nm.

	Probe	Bleach growth	Recovery				
			τ_1	τ_2	τ_3	τ_4	τ_5
CsPbBr ₃ NSs	474nm	$\tau_1^g < 100$ fs (100%)	310 fs (-7.3%)	2.21ps (-24.2%)	66.3ps (-45.75%)	150ps (-11.2%)	>1ns (-11.55%)
	487nm	$\tau_1^g = 330$ fs (100%)	3.37ps (-28.1%)	78ps (-47%)	161ps (-12.1%)	>1ns (-12.8%)	

Interestingly, the bleach growth time at 487 nm matches with first decay component of 474 nm bleach. This observation can be briefed as subsequent to photo-excitation, the electrons are generated in the upper excitonic states of CB and then with the increase in the probe delay times ultimately relax to the CB edge. Also, simultaneously the holes created in the upper VB states while relaxing back towards the VB edge, initially relax to the lower VB band (LH) during the early probe delays. While at a later time, these holes thermalize towards the HH

band resulting in the formation of 487 nm bleach band which explains the time delay in the bleach growth monitored at the position of the 487 nm in contrast to that observed for 474nm. Thus, we can assign this time scale as the “carrier” cooling time in 2D CsPbBr₃ NSs after 420 nm excitation. The inset inside **Figure 3.4 B** shows the schematic diagram illustrating this carrier cooling process. Our earlier investigation also demonstrates such cooling dynamics observed in 2D MoS₂.³³

To understand the effect of confinement we have compared the carrier cooling dynamics in 2D CsPbBr₃ NSs with that of 3D NCs. As we have observed that carrier cooling time for 2D NSs is 330 fs while for 3D NCs it is bi-exponential with time constants as $\tau_1 = < 100$ fs (35%) and $\tau_2 = 460$ fs (65%), it clearly suggests slower dynamics in 3D NCs. This observation can be understood as a resultant of the low dielectric constant of the NSs, which results in less efficiently screened Fröhlich interaction due to large surface-to-volume ratio of the 2D NSs.³⁴ The resultant is the increase in the rate of the phonon emission and quick dissipation of the excessive energy via this phonon system to the adjacent environment, as is clearly reflected in the fast cooling rate monitored for the 2D NSs.

3.2.2.2 Far Band gap excitation (300 nm)

Exciting with 300 nm pump (excitation energy = 4.1eV), which is much higher than the energy band gap provides a great opportunity to investigate the hot carrier cooling dynamics in NSs, due to the involvement of upper excitonic states which are not invoked when the sample is excited with energies quite close to the energy band gap.

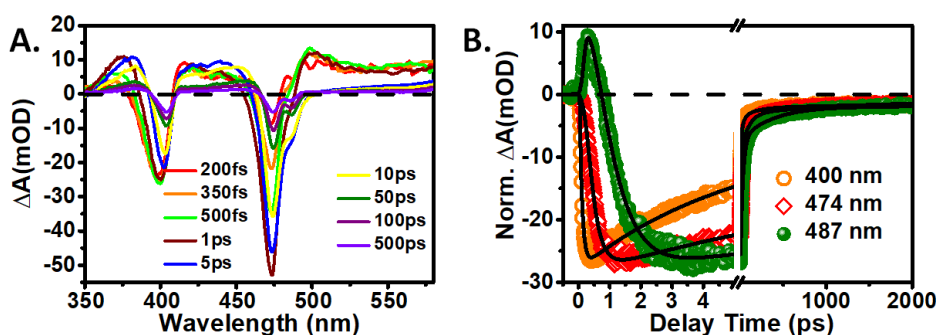


Figure 3.6 (A) TA spectra for CsPbBr₃ NSs at different time delays after exciting at 300 nm laser light. (B) Comparative kinetic traces at different probe wavelength i.e., 400 nm, 474nm and 487 nm.

The TA spectra of CsPbBr₃ NSs when excited with 300 nm pump (**Figure 3.6 A**) reveals quite similar bleach as well positive absorption features as that observed upon 420 nm pump excitation. However, in addition to the two bleach (negative absorption) bands at 487nm and 474 nm exciton, an additional prominent high energy excitonic bleach at 400 nm is discernible. A worth noting observation is that upon 300 nm excitation, bleach due to upper excitonic band was not observed for CsPbBr₃ NCs. Presence of higher excitonic bleach at 400 nm for CsPbBr₃ NSs can be attributed to the stronger confinement in 2D NSs as compared to that in 3D NCs.³⁵ The enhancement of this feature in absorption makes the bleach prominently observable in the transient absorption data for the NSs whereas the same remains absent for the transient absorption data of NCs. To understand charge carrier cooling dynamics between different excitonic states, transient kinetics were monitored at 400 nm, 474 nm and 487 nm respectively as shown in **Figure 3.6 B**.

Table 3.3 Kinetics fitting parameters for CsPbBr₃ NSs dispersed in n-hexane after exciting the samples at 300 nm.

	Probe wavelength	Growth (positive signal)	Bleach growth	Recovery		
				τ_1	τ_2	τ_3
CsPbBr ₃ NSs	400 nm		$\tau_1^g=100\text{fs}$ (100%)	7.2ps (-81.3%)	45ps (-16.2%)	>1ns (-2.5%)
	474 nm		$\tau_2^g=320\text{fs}$ (100%)	15.5 ps (75.2%)	440ps (21.4%)	>1ns (-3.4%)
	487 nm	$\tau_{g1} < 100 \text{ fs}$ (-25.6%) $\tau_{d1}=158 \text{ fs}$ (32%)	$\tau_1^g=835\text{fs}$ (68%)	38.75ps (-58.5%)	465 ps (-11.7%)	>1ns (-4.2%)

The transient kinetics have been fitted multi-exponentially and shown in **Table 3.3**. The kinetics at 400 nm can be fitted with pulse-width limited (<100 fs) growth and multi-exponential recovery with time constants as ($\tau_1 = 7.2\text{ps}$ (-81.3%), $\tau_2= 45\text{ps}$ (-16.2%) and

$\tau_3 = > 1$ ns (-2.5%)), while the kinetics at 474 nm can be best fitted with single growth component 320 fs followed by multi-exponential recovery with time constants ($\tau_1 = 15.5$ ps (-75.2%), $\tau_2 = 440$ ps (-21.4%) and $\tau_3 = > 1$ ns (-3.4%)) (**Table 3.3**). Further, with the recovery of bleach band at 474 nm, the bleach band at 487 nm starts coming into picture with much slower growth time 835 fs which can be attributed to cooling time of initially photo-excited carriers from the upper excitonic state to form the subsequent exciton. Another observation made upon such far band gap excitation is the complicated kinetics obtained at the position of the 487 nm. The acquired kinetics probed at this excitonic position for this high excitation energy differs from that observed at low energy pump. The kinetics plotted here reveals itself as an initial positive absorption with pulse-width limited (< 100 fs) growth followed by bi-exponential transient decay with time constants of (158 fs (32%) and 835 fs(68%)) and finally followed by a multi-exponential bleach recovery with time constants of $\tau_1 = 38.75$ ps (-58.5%), $\tau_2 = 465$ ps (-11.7%) and $\tau_3 = > 1$ ns (-4.2%) (**Table 3.3**). The positive signal observed in the bleach band can be due to the higher biexcitonic signal which is impacting the bleach band position also. The bleach recovery components can be attributed to charge carrier recombination which includes both radiative and non-radiative components.

3.2.2.3 Hot carrier Cooling Dynamics

The overall cooling process undergone by the charge carriers is an outcome of multiple underlying processes which include the carrier-carrier (which take place sub-100 fs time scale), carrier-phonon, and phonon-phonon scatterings that are entirely a function of the material's intrinsic band structure.³⁶ Herein the hot carrier cooling takes place mainly through carrier-phonon coupling which plays a major role in the carrier cooling rate determination.³⁷ At high energy excitation by pump pulse, highly non-thermal electrons and holes are generated. This non-equilibrium carrier distribution created after photoexcitation undergoes thermalization by subsequent energetic distribution of electrons and holes into a quasi-equilibrium state following Fermi-Dirac (FD) distribution functions.³⁸ These quasi-equilibrated charge carriers, namely the hot charge carriers eventually reach thermal equilibrium with the crystal lattice through phonon emission. Herein the initial cooling process takes place within few sub-picoseconds due Coulomb-mediated scattering with optical phonons termed as Fröhlich interaction. For the estimation of the carrier temperature in the 2D

NSs, the fitting has been conducted along the high energy tail of the TA spectra normalized above the continuum onset which provides an idea of the initial carrier cooling that occurs in the continuum states just subsequent to photoexcitation.^{39,40} The Fermi Dirac distribution of two dimensional methylammonium lead iodide (MAPI) nanoplatelets has also been reported by Hintermayr and co-workers.³⁴

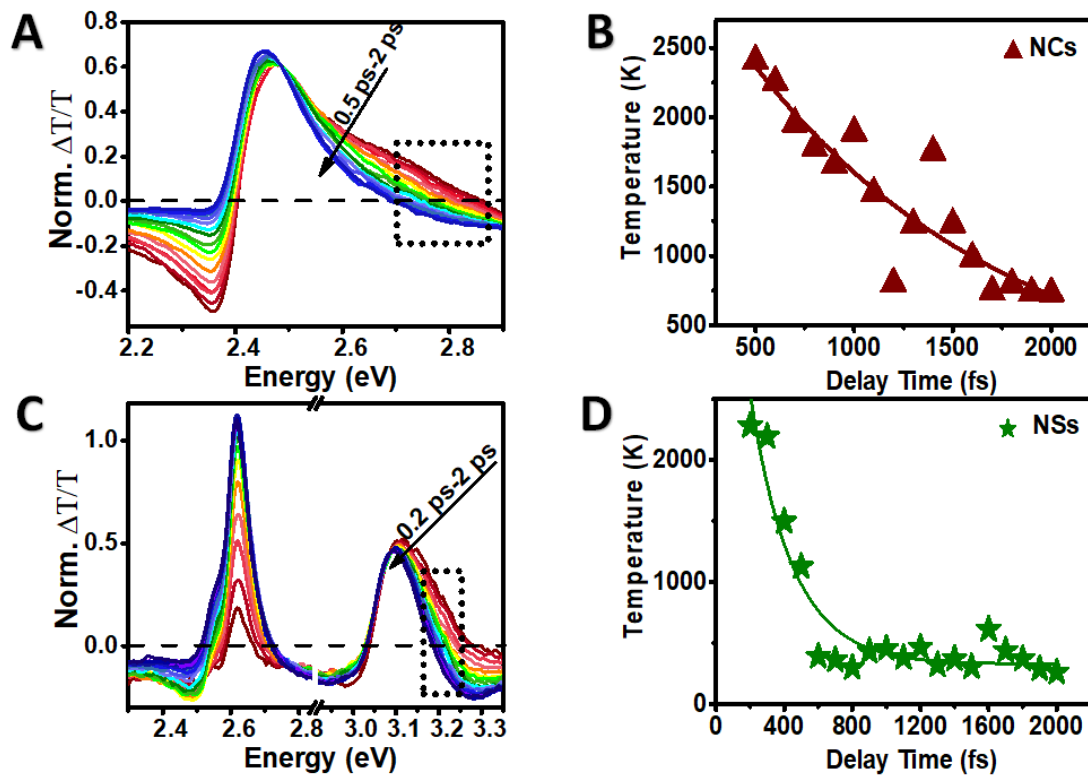


Figure 3.7 (A, C) Normalized TA spectra under pump excitation (300 nm) for probe delays (from 500fs to 2 ps for NCs and 300fs to 2 ps for NSs); the dashed boxes drawn to show the high-energy tail region on which MB fitting has been done. (B,D) Change in carrier temperature T_c with time for NCs and NSs respectively.

To follow initial T_c in both and systems in the present studies, change in transmission (ΔT) was monitored in the early time from 500fs to 2 ps for 3D CsPbBr₃ NCs in the high energy side of the 1st excitonic transient bleach, while for 2D CsPbBr₃ NSs it was monitored from 200fs to 2 ps in the high energy side of the 3rd excitonic transient bleach as shown in **Figure 3.7 A and 7 C** respectively in order to consider the initial cooling of hot carriers following Fermi Dirac distribution. The hot T_c (**Figure 3.7 B, 7 D**) can be estimated from the MB (Maxwell Boltzman) fitting of the high-energy tail of the normalized TA data (because the FD

distribution can be approximated as a MB type of distribution for the energies far above the Fermi energy), which can be quantitatively represented as^{37,41}

$$\Delta T(\hbar\omega) = -T_0(\hbar\omega)\exp\left(-\frac{\hbar\omega}{k_B T_c}\right) \quad \text{Eq. 3.1}$$

Here, ΔT stands for the bleach amplitude at a particular probe wavelength, and k_B is the Boltzmann constant. Thereby, we have constructed the transient cooling curves for T_c for both 3D NCs and 2D NSs as depicted in **Figure 3.7 B** and **Figure 3.7 D** respectively. Both the systems depict that the initial charge carrier temperatures are well above 2000 K. The cooling of the photoexcited charge carriers in both the systems occur due to emission of optical phonon, which can be modeled by assuming an exponential decay. It is interesting to see that carrier temperature (T_c) decreases drastically in early time scale for 2D NSs as compared to that 3D NCs. Ideally, due to reduction in dimensionality from 3D to 2D, there will be comparative reduction in the number of phonon modes and the density of states (DOS) in CsPbBr₃ NSs. So, it should be expected that it can result in the observation of the phonon bottleneck effect in NSs that should have ideally decelerated the cooling.^{34,42,43} Conversely, in the present studies faster carrier cooling was observed in 2D NSs, which can be attributed to direct consequence of the reduced screening of the Coulomb-mediated carrier-LO-phonon scattering (interaction) in the low-dielectric surrounding.³⁴

The excitons are strongly confined in the 2D NSs in comparison to the 3D counterparts, owing to the reduction in dielectric screening of Coulombic exchanges.⁴⁴ Here in the creation of hot phonons is hindered due to the increased ratio of surface-to-volume in 2D materials, leads to higher scattering rates of optical phonon, which is governed by the Fröhlich interaction.³⁴ While in 3D NCs due to pronounced screening of charge carriers, slower cooling process of carriers has been observed.⁴⁴

3.2.2.4 Bi-exciton Dynamics

In addition to the pronounced bleach apparent due to the state filling, many body interactions induced Stark effect also plays a vital role in the TA response in these systems. The band observed towards the lower energy i.e. peaked at 525 nm for NCs and at 498 nm for NSs can be attributed to be a typical bi-exciton signal²⁷ and the other towards the higher energy originates due to the PIA of the charge carriers.

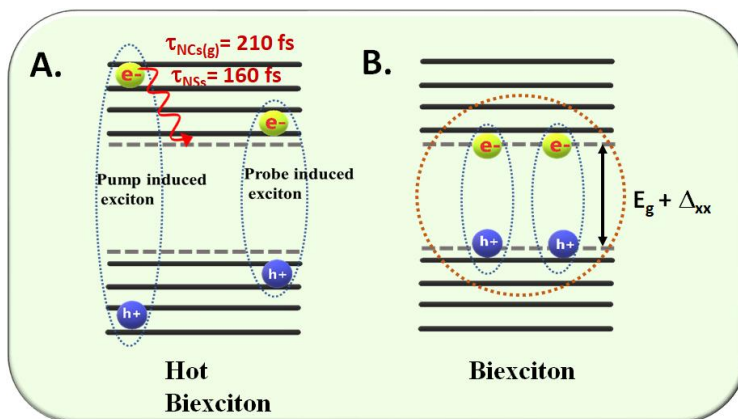


Figure 3.8 Schematic representation illustrating (A) the hot biexciton formation by the coulombic interaction between pump induced hot exciton and probe induced exciton. (B) biexciton (thermalized pump induced exciton and probe induced exciton) formed as the band gap is renormalized due to the bi-excitonic induced stark effect.

The bi-exciton signal observed here is the probe induced bi-exciton that is a resultant of the Coulombic interaction between the hot exciton generated by pump pulse and the band edge exciton generated by the probe beam (**Figure 3.8**) similar to the one observed by Kambhampati and co-workers in their work⁴⁵ where they detected such a bi-excitonic feature for CdSe QD on the red side of the bleach maxima, under the low pump fluence ($\langle N \rangle < 1$). This exciton-exciton interaction leads to a red shift in the band edge excitonic peak at initial time delays due to the attractive nature of $-\Delta_{xx}$ (having negative value), recognized as bi-exciton binding energy.⁴⁶ The overall TA spectrum is an average of the signal due to the excitonic bleach band ($-ve$ signal at E_g) and photo induced absorption ($+ve$ signal at $E_g + \Delta_{xx}$). It is seen that soon after the photo induced absorption signal in the red-region of the spectra (an early time effect of the bi-exciton formation) vanishes following the hot carrier relaxation, the TA spectra is dominated by the bleach band at later times.

Here in this present study, we attempt to understand the differences encountered in hot bi-exciton dynamics for the differently quantum confined systems *i.e.* 3D NCs and 2D NSs with the variation in pump excitation energy. **Figure 3.5 B** depicts the origin of derivative-like feature in the TA data at the early time scale forthright the excitation which are attributed to the bi-exciton effect.³⁷ **Figure 3.9 A, B** clearly indicate the biexciton formation to be much enhanced in case of higher excitation (300 nm) as the intensity of the positive signal is much higher.

Table 3.4 Kinetics fitting parameters for CsPbBr₃ NCs and NSs dispersed in n-hexane after exciting the samples at 300 nm and 420 nm respectively.

	Pump λ_{nm}	Probe λ_{nm}	Biexciton		Single Exciton			
			Growth τ_{g_b}	Decay τ_{d_b}	growth	recovery		
						τ_1	τ_2	τ_3
CsPbBr ₃ NCs	420	527	< 100 fs (62.68%)	150 fs (-62.8%)	0.485 ps (-37.2)	2.4 ps (17.7%)	51ps (15.42%)	>1ns (4.2%)
	300	527	210 fs (78.6%)	550 fs (-78%)	2.4 ps (-22%)	30ps (16.8%)	>1ns (4.6%)	
CsPbBr ₃ NSs	420	498	< 100 fs (70.3%)	160 fs (-71%)	0.460 ps (-29%)	2.3 ps (11.4%)	35 ps (15.2%)	>1ns (3.1%)
	300	498	160 fs (89.45%)	0.730ps (-90.4%)	1.89 ps (-9.6%)	25.5ps (7.43%)	>1ns (3.12%)	

This observation is in accordance with the fact that the contribution from the PIA (positive signal) to the overall bi-exciton signal enhances upon raising the excitation energy.⁴⁶ Similar observation has been made by Yumoto and group in CSPbI₃.⁴⁶ The TA kinetics monitored at the bi-excitonic position represents complicated dynamics, which includes an initial fast positive growth signal followed by fast decay which can be attributed to bi-exciton formation and decay respectively.^{47,48} Following this bi-exciton decay, the transient signal shows bleach growth followed by its recovery which can be attributed to carrier cooling and recombination processes respectively.⁴⁷⁻⁴⁹ **Table 3.4** shows the time components for both the positive signals with single-exponential growth and multi-exponential recovery. We also found that keeping all experimental conditions same the bi-exciton signal intensity is still higher in the NSs due to the increase in absorption coefficient which enhanced the bleach signal also and similar trend here. The growth component is $\tau_1 = <100$ fs (63%) in case of 420 nm excitation in NCs and $\tau_1 = 210$ fs (77.9%) for 300 nm excitation.

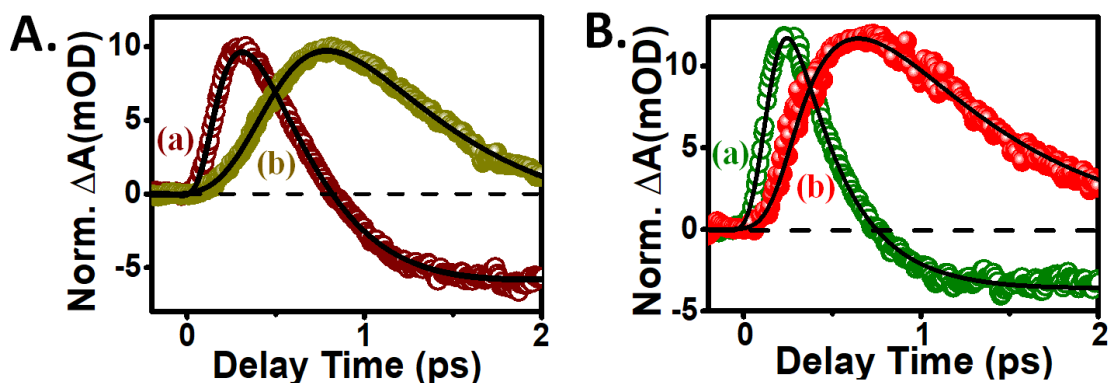


Figure 3.9 (A) Normalized kinetic traces for CsPbBr_3 NCs probed at probe wavelength $\lambda = 525$ nm at (a) 420 nm and (b) 300 nm pump excitation, (B) Normalized kinetic traces for CsPbBr_3 NSs probed at probe wavelength $\lambda = 498$ nm (positive band) for both (a) 420 nm and (b) 300 nm pump excitation.

Whereas in the case of NSs the best fitted growth component is $\tau_1 = <100$ fs (70%) for 420 nm excitation and $\tau_1 = 160$ fs for 300 nm excitation. We find the bi-exciton growth and decay dynamics to be slower with 300 nm laser pulse as compared to that for 420 nm for both the systems (**Table 3.4**). The initial growth time of the bi-exciton signal which essentially arises due to the intra band carrier relaxation followed by the hot carriers from upper excitonic state to the band-edge state suggests the formation of the hot bi-exciton. Additional factor that slows the positive growth for 300 nm excitation further comes from the shifting of the intrinsic band gap towards lower energies, thus providing larger surplus of pump energy (bi-exciton binding energy (Δ_{xx}) enhances with the increase in the pump energy). This estimation of the binding energy can come from the asymmetry in energy between the hot exciton (pump induced) and the band-edge exciton (probe induced).⁴⁶ As far band edge excitation creates much greater imbalance in energy between pump exciton and probe induced exciton, so it results in an increased Δ_{xx} . Also, the bi-exciton decay is found to be slower at 300 nm than at 420 nm since the carriers populate the band edges for 420 nm excitation at faster rates, resulting in faster band edge bi-exciton formation. Therefore, sooner the carriers constituting the band edge bi-excitons undergo recombination to yield a single exciton, faster is the bi-exciton decay. Further, following this decay of the bi-exciton into a single exciton, the emitted excessive energy results in the re-excitation of the band edge single exciton, with the rest of the dynamics

to follow a similar trend analogous to that followed by the single exciton at the respective excitation wavelengths.

3.3 Conclusion

In summary, with the help of TA spectroscopy, a comparison of the ultrafast charge carrier dynamics in the 2D CsPbBr₃ NSs and 3D CsPbBr₃ NCs has been made to see the effect of confinement by exciting the samples at different wavelengths. Steady state absorption and luminescence studies indicate that due to quantum confinement splitting of VB in 2D NSs leads to discrete optical absorption bands. Charge carrier dynamics which includes both exciton and bi-exciton dynamics are found to be slower at high energy excitation in both 2D and 3D systems which is because carriers are pumped into much higher states and take time to relax onto the band edge position. Further, the studies are clearly suggestive that the hot carrier cooling rate is faster in 2D NSs as compared to 3D NCs, which has been attributed to reduction in the Fröhlich interaction in the 2D system due to its higher surface-volume ratio and lower dielectric constant hence providing an easy dissipation of the energy to the surrounding medium. Our investigation gives a fundamental understanding on the effect of dimensionality in LHP carrier relaxation dynamics by changing excitation energies. The knowledge of the faster hot carrier relaxation observed in 2D perovskite system in this finding can assist in the development of technologically high-end optoelectronic devices based on these materials.

3.4 References

- (1) Li, Z.; Wang, R.; Xue, J.; Xing, X.; Yu, C.; Huang, T.; Chu, J.; Wang, K. L.; Dong, C.; uWei, Z.; Zhao, Y.; Wang, Z. K.; Yang, Y. Core-Shell ZnO@SnO₂ Nanoparticles for Efficient Inorganic Perovskite Solar Cells. *J. Am. Chem. Soc.* **2019**, *141* (44), 17610–17616.
- (2) Liang, J.; Wang, C.; Wang, Y.; Xu, Z.; Lu, Z.; Ma, Y.; Zhu, H.; Hu, Y.; Xiao, C.; Yi, X.; Zhu, G.; Lv, H.; Ma, L.; Chen, T.; Tie, Z.; Jin, Z.; Liu, J. All-Inorganic Perovskite Solar Cells. *J. Am. Chem. Soc.* **2016**, *138* (49), 15829–15832.
- (3) Zhu, W.; Zhang, Z.; Chai, W.; Chen, D.; Xi, H.; Chang, J.; Zhang, J.; Zhang, C.; Hao, Y. Benign Pinholes in CsPbIBr₂ Absorber Film Enable Efficient Carbon-Based, All-Inorganic Perovskite Solar Cells. *ACS Appl. Energy Mater.* **2019**, *2* (7), 5254–5262.
- (4) Yoon, H. C.; Do, Y. R. Stable and Efficient Green Perovskite Nanocrystal-Polysilazane Films for White LEDs Using an Electrospray Deposition Process. *ACS Appl. Mater. Interfaces* **2019**, *11*, 22510–22520.

- (5) Shi, Z.; Li, S.; Li, Y.; Ji, H.; Li, X.; Wu, D.; Xu, T.; Chen, Y.; Tian, Y.; Zhang, Y.; Shan, C.; Du, G. Strategy of Solution-Processed All-Inorganic Heterostructure for Humidity/Temperature-Stable Perovskite Quantum Dot Light-Emitting Diodes. *ACS Nano* **2018**, *12* (2), 1462–1472.
- (6) Yang, T.; Zheng, Y.; Du, Z.; Liu, W.; Yang, Z.; Gao, F.; Wang, L.; Chou, K. C.; Hou, X.; Yang, W. Superior Photodetectors Based on All-Inorganic Perovskite CsPbI₃ Nanorods with Ultrafast Response and High Stability. *ACS Nano* **2018**, *12* (2), 1611–1617.
- (7) Liu, P.; He, X.; Ren, J.; Liao, Q.; Yao, J.; Fu, H. Organic-Inorganic Hybrid Perovskite Nanowire Laser Arrays. *ACS Nano* **2017**, *11* (6), 5766–5773.
- (8) Huang, C. Y.; Zou, C.; Mao, C.; Corp, K. L.; Yao, Y. C.; Lee, Y. J.; Schlenker, C. W.; Jen, A. K. Y.; Lin, L. Y. CsPbBr₃ Perovskite Quantum Dot Vertical Cavity Lasers with Low Threshold and High Stability. *ACS Photonics* **2017**, *4* (9), 2281–2289.
- (9) Protesescu, L.; Yakunin, S.; Bodnarchuk, M. I.; Krieg, F.; Caputo, R.; Hendon, C. H.; Yang, R. X.; Walsh, A.; Kovalenko, M. V. Nanocrystals of Cesium Lead Halide Perovskites (CsPbX₃, X = Cl, Br, and I): Novel Optoelectronic Materials Showing Bright Emission with Wide Color Gamut. *Nano Lett.* **2015**, *15* (6), 3692–3696.
- (10) Yang, W. S.; Noh, J. H.; Jeon, N. J.; Kim, Y. C.; Ryu, S.; Seo, J.; Seok, S. II. High-Performance Photovoltaic Perovskite Layers Fabricated through Intramolecular Exchange. *Science* **2015**, *348* (6240), 1234–1237.
- (11) Zhang, L.; Yang, X.; Jiang, Q.; Wang, P.; Yin, Z.; Zhang, X.; Tan, H.; Yang, Y. M.; Wei, M.; Sutherland, B. R.; Sargent, E. H.; You, J. Ultra-Bright and Highly Efficient Inorganic Based Perovskite Light-Emitting Diodes. *Nat. Commun.* **2017**, *8*, 1–8.
- (12) Yettapu, G. R.; Talukdar, D.; Sarkar, S.; Swarnkar, A.; Nag, A.; Ghosh, P.; Mandal, P. Terahertz Conductivity within Colloidal CsPbBr₃ Perovskite Nanocrystals: Remarkably High Carrier Mobilities and Large Diffusion Lengths. *Nano Lett.* **2016**, *16* (8), 4838–4848.
- (13) Bartel, C. J.; Sutton, C.; Goldsmith, B. R.; Ouyang, R.; Musgrave, C. B.; Ghiringhelli, L. M.; Scheffler, M. New Tolerance Factor to Predict the Stability of Perovskite Oxides and Halides. *Sci. Adv.* **2019**, *5* (2), 1–10.
- (14) Zheng, C.; Bi, C.; Huang, F.; Binks, D.; Tian, J. Stable and Strong Emission CsPbBr₃ Quantum Dots by Surface Engineering for High-Performance Optoelectronic Films. *ACS Appl. Mater. Interfaces* **2019**, *11* (28), 25410–25416.
- (15) Yang, D.; Li, P.; Zou, Y.; Cao, M.; Hu, H.; Zhong, Q.; Hu, J.; Sun, B.; Duhm, S.; Xu, Y.; Zhang, Q. Interfacial Synthesis of Monodisperse CsPbBr₃ Nanorods with Tunable Aspect Ratio and Clean Surface for Efficient Light-Emitting Diode Applications. *Chem. Mater.* **2019**, *31* (5), 1575–1583.

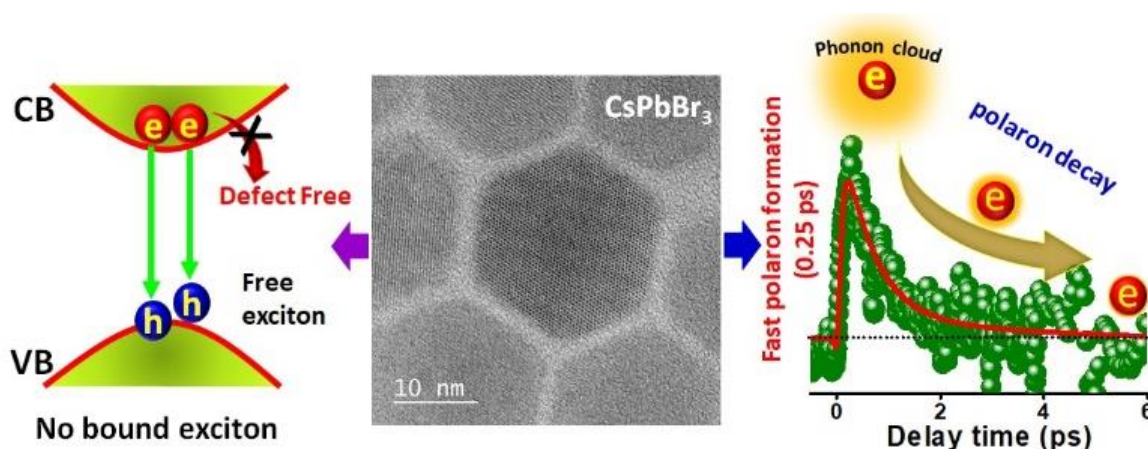
- (16) Akkerman, Q. A.; Motti, S. G.; Srimath Kandada, A. R.; Mosconi, E.; D’Innocenzo, V.; Bertoni, G.; Marras, S.; Kamino, B. A.; Miranda, L.; De Angelis, F.; Petrozza, A.; Prato, M.; Manna, L. Solution Synthesis Approach to Colloidal Cesium Lead Halide Perovskite Nanoplatelets with Monolayer-Level Thickness Control. *J. Am. Chem. Soc.* **2016**, *138* (3), 1010–1016.
- (17) Shamsi, J.; Dang, Z.; Bianchini, P.; Canale, C.; Stasio, F. Di; Brescia, R.; Prato, M.; Manna, L. Colloidal Synthesis of Quantum Confined Single Crystal CsPbBr₃ Nanosheets with Lateral Size Control up to the Micrometer Range. *J. Am. Chem. Soc.* **2016**, *138* (23), 7240–7243.
- (18) Li, Q.; Lian, T. Ultrafast Charge Separation in Two-Dimensional CsPbBr₃ Perovskite Nanoplatelets. *J. Phys. Chem. Lett.* **2019**, *10* (3), 566–573.
- (19) Yang, Z.; Wang, M.; Qiu, H.; Yao, X.; Lao, X.; Xu, S.; Lin, Z.; Sun, L.; Shao, J. Engineering the Exciton Dissociation in Quantum-Confined 2D CsPbBr₃ Nanosheet Films. *Adv. Funct. Mater.* **2018**, *28* (14), 1–10.
- (20) Lv, L.; Xu, Y.; Fang, H.; Luo, W.; Xu, F.; Liu, L.; Wang, B.; Zhang, X.; Yang, D.; Hu, W.; Dong, A. Generalized Colloidal Synthesis of High-Quality, Two-Dimensional Cesium Lead Halide Perovskite Nanosheets and Their Applications in Photodetectors. *Nanoscale* **2016**, *8* (28), 13589–13596.
- (21) Wang, Q. H.; Kalantar-Zadeh, K.; Kis, A.; Coleman, J. N.; Strano, M. S. Electronics and Optoelectronics of Two-Dimensional Transition Metal Dichalcogenides. *Nat. Nanotechnol.* **2012**, *7* (11), 699–712.
- (22) Kirchartz, T.; Bisquert, J.; Mora-Sero, I.; Garcia-Belmonte, G. Classification of Solar Cells According to Mechanisms of Charge Separation and Charge Collection. *Phys. Chem. Chem. Phys.* **2015**, *17* (6), 4007–4014.
- (23) Queisser, S.; Kahmann, S.; Loi, M. A. Hot Carrier Solar Cells and the Potential of Perovskites for Breaking The Shockley–Queisser limit Simon. *J. Mater. Chem. C* **2019**, *7*, 2471–2486.
- (24) Li, J.; Luo, L.; Huang, H.; Ma, C.; Ye, Z.; Zeng, J.; He, H. 2D Behaviors of Excitons in Cesium Lead Halide Perovskite Nanoplatelets. *J. Phys. Chem. Lett.* **2017**, *8* (6), 1161–1168.
- (25) Vale, B. R. C.; Socie, E.; Burgos-Caminal, A.; Bettini, J.; Schiavon, M. A.; Moser, J. E. Exciton, Biexciton, and Hot Exciton Dynamics in CsPbBr₃ Colloidal Nanoplatelets. *J. Phys. Chem. Lett.* **2020**, *11* (2), 387–394.
- (26) Shinde, A.; Gahlaut, R.; Mahamuni, S. Low-Temperature Photoluminescence Studies of CsPbBr₃ Quantum Dots. *J. Phys. Chem. C* **2017**, *121* (27), 14872–14878.
- (27) Aneesh, J.; Swarnkar, A.; Kumar Ravi, V.; Sharma, R.; Nag, A.; Adarsh, K. V. Ultrafast Exciton Dynamics in Colloidal CsPbBr₃ Perovskite Nanocrystals: Biexciton Effect and Auger Recombination. *J. Phys. Chem. C* **2017**, *121* (8), 4734–4739.

- (28) Dana, J.; Maity, P.; Jana, B.; Maiti, S.; Ghosh, H. N. Concurrent Ultrafast Electron- and Hole-Transfer Dynamics in CsPbBr₃ Perovskite and Quantum Dots. *ACS Omega* **2018**, *3* (3), 2706–2714.
- (29) Chen, J.; Messing, M. E.; Zheng, K.; Pullerits, T. Cation-Dependent Hot Carrier Cooling in Halide Perovskite Nanocrystals. *J. Am. Chem. Soc.* **2019**, *141* (8), 3532–3540.
- (30) Marongiu, D.; Saba, M.; Quochi, F.; Mura, A.; Bongiovanni, G. The Role of Excitons in 3D and 2D Lead Halide Perovskites. *J. Mater. Chem. C* **2019**, *7* (39), 12006–12018.
- (31) Telfah, H.; Jamhawi, A.; Teunis, M. B.; Sardar, R.; Liu, J. Ultrafast Exciton Dynamics in Shape-Controlled Methylammonium Lead Bromide Perovskite Nanostructures: Effect of Quantum Confinement on Charge Carrier Recombination. *J. Phys. Chem. C* **2017**, *121* (51), 28556–28565.
- (32) Saba, M.; Cadelano, M.; Marongiu, D.; Chen, F.; Sarritzu, V.; Sestu, N.; Figus, C.; Aresti, M.; Piras, R.; Geddo Lehmann, A.; Cannas, C.; Musinu, A.; Quochi, F.; Mura, A.; Bongiovanni, G. Correlated Electron–Hole Plasma in Organometal Perovskites. *Nat. Commun.* **2014**, *5* (1), 5049.
- (33) Goswami, T.; Rani, R.; Hazra, K. S.; Ghosh, H. N. Ultrafast Carrier Dynamics of the Exciton and Trion in MoS₂ Monolayers Followed by Dissociation Dynamics in Au@MoS₂ 2D Heterointerfaces. *J. Phys. Chem. Lett.* **2019**, *10*, 3057–3063.
- (34) Hintermayr, V. A.; Polavarapu, L.; Urban, A. S.; Feldmann, J. Accelerated Carrier Relaxation Through Reduced Coulomb Screening in Two- Dimensional Halide Perovskite Nanoplatelets. *ACS Nano* **2018**, *12*, 10151–10158.
- (35) Paul, S.; Bladt, E.; Richter, A. F.; Döblinger, M.; Tong, Y.; Huang, H.; Dey, A.; Bals, S.; Debnath, T.; Polavarapu, L.; Feldmann, J. Manganese-Doping-Induced Quantum Confinement within Host Perovskite Nanocrystals through Ruddlesden–Popper Defects. *Angew. Chemie - Int. Ed.* **2020**, *59* (17), 6794–6799.
- (36) Li, M.; Fu, J.; Xu, Q.; Sum, T. C. Slow Hot-Carrier Cooling in Halide Perovskites: Prospects for Hot-Carrier Solar Cells. *Adv. Mater.* **2019**, *31* (47), 1–17.
- (37) Kaur, G.; Justice Babu, K.; Ghorai, N.; Goswami, T.; Maiti, S.; Ghosh, H. N. Polaron-Mediated Slow Carrier Cooling in a Type-1 3D/0D CsPbBr₃@Cs₄PbBr₆ Core-Shell Perovskite System. *J. Phys. Chem. Lett.* **2019**, *10* (18), 5302–5311.
- (38) Richter, J. M.; Branchi, F.; Valduga De Almeida Camargo, F.; Zhao, B.; Friend, R. H.; Cerullo, G.; Deschler, F. Ultrafast Carrier Thermalization in Lead Iodide Perovskite Probed with Two-Dimensional Electronic Spectroscopy. *Nat. Commun.* **2017**, *8* (1), 1–7.
- (39) Pelton, M.; Ithurria, S.; Schaller, R. D.; Dolzhenkov, D. S.; Talapin, D. V. Carrier Cooling in Colloidal Quantum Wells. *Nano Lett.* **2012**, *12* (12), 6158–6163.

- (40) Snoke, D. W.; Rhle, W. W.; Lu, Y. C.; Bauser, E. Evolution of a Nonthermal Electron Energy Distribution in GaAs. *Phys. Rev. B* **1992**, *45* (19), 10979–10989.
- (41) Fu, J.; Xu, Q.; Han, G.; Wu, B.; Huan, C. H. A.; Leek, M. L.; Sum, T. C. Hot Carrier Cooling Mechanisms in Halide Perovskites. *Nat. Commun.* **2017**, *8* (1), 1300.
- (42) Klimov, V. I.; McBranch, D. W. Femtosecond 1P-to-1S Electron Relaxation in Strongly Confined Semiconductor Nanocrystals. *Phys. Rev. Lett.* **1998**, *80* (18), 4028–4031.
- (43) Pandey, A.; Guyot-Sionnest, P. Slow Electron Cooling in Colloidal Quantum Dots. *Science* **2008**, *322* (5903), 929–932.
- (44) Wang, Q.; Liu, X.-D.; Qiu, Y.-H.; Chen, K.; Zhou, L.; Wang, Q.-Q. Quantum Confinement Effect and Exciton Binding Energy of Layered Perovskite Nanoplatelets. *AIP Adv.* **2018**, *8* (2), 25108.
- (45) Sewall, S. L.; Cooney, R. R.; Anderson, K. E. H.; Dias, E. A.; Sagar, D. M.; Kambhampati, P. State-Resolved Studies of Biexcitons and Surface Trapping Dynamics in Semiconductor Quantum Dots. *J. Chem. Phys.* **2008**, *129* (8), 84701..
- (46) Yumoto, G.; Tahara, H.; Kawawaki, T.; Saruyama, M.; Sato, R.; Teranishi, T.; Kanemitsu, Y. Hot Biexciton Effect on Optical Gain in CsPbI₃ Perovskite Nanocrystals. *J. Phys. Chem. Lett.* **2018**, *9* (9), 2222–2228.
- (47) Debnath, T.; Maiti, S.; Maity, P.; Ghosh, H. N. Subpicosecond Exciton Dynamics and Biexcitonic Feature in Colloidal CuInS₂ Nanocrystals: Role of In-Cu Antisite Defects. *J. Phys. Chem. Lett.* **2015**, *6* (17), 3458–3465.
- (48) Dana, J.; Debnath, T.; Ghosh, H. N. Involvement of Sub-Bandgap States in Subpicosecond Exciton and Biexciton Dynamics of Ternary AgInS₂ Nanocrystals. *J. Phys. Chem. Lett.* **2016**, *7* (16), 3206–3214.
- (49) Debnath, T.; Ghosh, H. N. Ternary Metal Chalcogenides: into the Exciton and Bi-exciton Dynamics. *J. Phys. Chem. Lett. (Perspective)* **2019**, *10* (20), 6227–6238.

Chapter 4

Fast Polaron Formation and Low Carrier Mobility in Defect Free Polyhedral CsPbBr₃ Perovskite Nanocrystals



Albeit enormous achievement has already been made in photovoltaic and optoelectronic field with perovskites, yet further advancement is needed to address the key challenges encountered in these systems. Here, we synthesized polyhedral dodecahedron cesium lead bromide (dodecahedron-CsPbBr₃) perovskite, which offers new polar facets on the surface, longer carrier life time and high photoluminescence PLQY. PL investigation conducted at cryogenic temperature for dodecahedron-CsPbBr₃ is clearly indicative of the absence of bound excitons originating from the shallow traps which otherwise are prevalent in the conventional CsPbBr₃ nanocubes (cube). Furthermore, temperature dependent TA studies illustrate accelerated carrier cooling as lattice temperature is lowered upto 5 K, which is related to incapability of the lattice to support polarons. Terahertz (THz) spectroscopic measurements reflect lower carrier mobility in dodecahedron-CsPbBr₃ than cube-CsPbBr₃, which validate the claim of slower carrier cooling as demonstrated by TA studies. These findings make dodecahedron-CsPbBr₃ a potential contender for advanced next generation efficient optoelectronic devices.

4.1. Introduction

Architecture of highly luminescent NCs with extremely stable, low cost and scalable preparation methods have been encountered as long-standing challenges in optoelectronic applications.¹⁻² Over the past few years, all inorganic metal halide (CsPbX_3 , $\text{X}=\text{Cl}$, Br and I) perovskite NCs have shown as promising materials with exclusive properties including narrow emission, near unity quantum yield, broad tunable photoluminescence (400-700 nm).³⁻⁵ These aforementioned properties are chiefly significant assets for display devices, light-emitting diodes, lasers, photodetectors and solar cells etc.,⁶⁻¹⁰ However, still there are plenty of complications associated with the device performance including defects stemming from Br and Pb vacancies, detachment of ligands from CsPbBr_3 surface leads to decrement in PLQY and changing the morphology with time.¹¹⁻¹⁷ Recently, Manna and co-workers reported truncated octahedron shape of CsPbBr_3 with high photoluminescence yield using alkylphosphonate ligand and they found that new facets are exposed on the surface albeit it having poor thermal stability.¹⁸ Importantly, Pradhan and co-workers synthesized uncommon non-cube morphology including rhombic dodecahedrons and rhombicuboctahedrons of CsPbBr_3 by changing the reaction conditions.¹⁹ Remarkably, the rhombic dodecahedrons exhibit high colloidal stability and near unity PLQY. Interestingly, in-situ formed tertiary ammonium ions opened the new facet including ($\{200\}$ and $\{112\}$) on the surface stabilized the polyhedral morphology and concurrently reduced the defects states.^{19,20}

A profound understanding of incomparable photophysical properties of polyhedron CsPbBr_3 remains unknown towards the application prospects. Architecture of high-efficiency solar cells primarily depends on slow hot carrier (HC) cooling, which can stem from phonon bottleneck, Auger heating, surface passivation, acoustical–optical phonon up-conversion or large polaron screening effect.²¹⁻²⁸ So far, the explored photophysical properties remain confined to nanocubes while the photo physics for these new polyhedral NCs are still unknown. In our previous work, we have demonstrated the interplay of polaron formation and HC cooling in CsPbBr_3 up to 5K. The low temperature study gives clear insight of mechanistic processes involved within the lattice.²⁹⁻³¹ Herein, we are interested to explore how HC cooling, polaron and biexciton formation is affected upon opening the new facets in dodecahedron - CsPbBr_3 while varying the lattice temperature from 300 to 5K. Quite fascinatingly, the TA investigations demonstrate 20-30 % further enhancement in terms of biexciton formation and

huge retardation in the carrier cooling rate in the dodecahedron-CsPbBr₃ in contrast to that observed for cube-CsPbBr₃. In addition to that, we utilized time-resolved THz spectroscopy to corroborate the conclusions drawn from the TA investigations, which altogether anticipate superior behaviour of these dodecahedron -CsPbBr₃ in the photovoltaic devices.

4.2. Result and Discussion

The nanocube and dodecahedron -CsPbBr₃ samples were prepared using hot injection method after following reported literature with minor modification as detailed in Chapter 2.^{3,20} High-resolution transmission electron microscope (HR-TEM) images of dodecahedron-CsPbBr₃ exhibit hexagonal morphology with an average edge length of 22 nm (**Figure 4.1 a and 4.2 a**). **Figure 4.2 a** clearly suggests that dodecahedron-CsPbBr₃ display highly crystalline structure with d-spacing of 0.41 nm, which corroborates to the (020)/(112) planes of an orthorhombic CsPbBr₃ (**inset: Figure 4.2 a**). Interestingly, in the present synthesis *in situ* formation of tertiary ammonium ions opened up new facets by changing the morphology from nanocubes to rhombic dodecahedrons, efficiently stabilized by twelve (200), (020) and (122) facets (**right panel of Figure 4.1 a**).^{18,19}

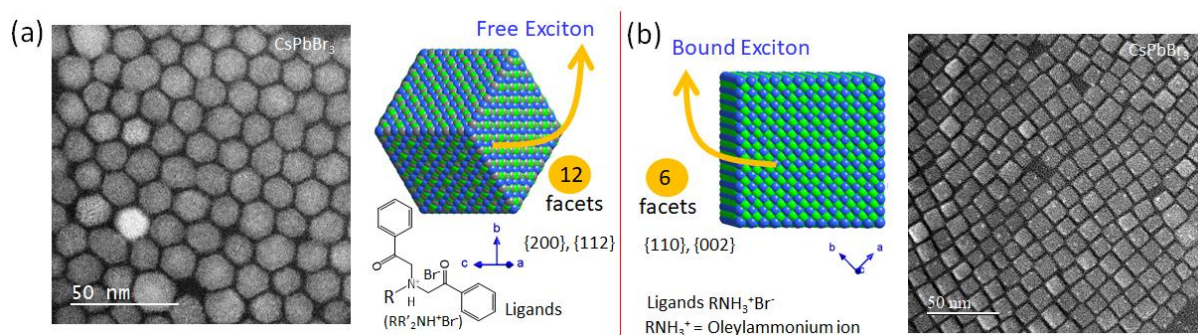


Figure 4.1 (a, b) HR-TEM images of dodecahedron and cube-CsPbBr₃ atomic model showing orthorhombic phase of dodecahedron-CsPbBr₃ having (200), (112) facets (right panel of Figure 4.1a), and cube- CsPbBr₃ having (110), (002) facets (left panel of Figure 4.1b); (Diamond software version 4.5.3 with ICSD 97851 for CsPbBr₃ was used for the formation atomic models), the models and ligands were designed as per the previous reported literature.¹⁹

The cube -CsPbBr₃ exhibits cubic shape with an edge length of approximately 14 nm (**Figure 4.1 b, 4.2 b**). It possesses interplanar distances of 0.58 nm, which corresponds to the (110)

plane (**Figure 4.2 b**). Interestingly, the oleylammonium ions stabilized the six (100) and (002) facets in the cube-CsPbBr₃, which formed the cubic morphology (**left panel of Figure 4.1 b**).

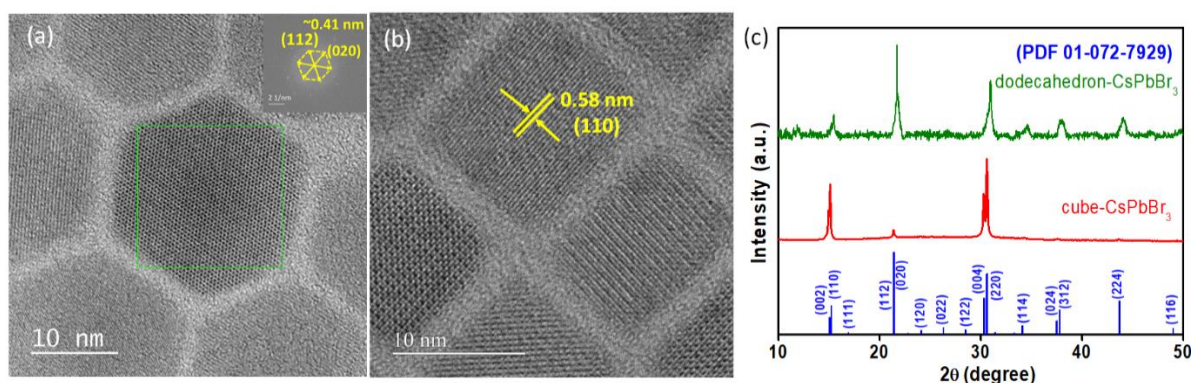


Figure 4.2 HR-TEM images of (a) dodecahedron-CsPbBr₃ (Inset: generated FFT pattern from green rectangle), (b) cube-CsPbBr₃, (c) XRD pattern of cube and dodecahedron-CsPbBr₃ along with orthorhombic CsPbBr₃ PDF line are also shown in the bottom (PDF: 01-072-7929).

Further, the structure of prepared samples has been simulated from HR-TEM images and the corresponding shape was confirmed. XRD patterns for cube and dodecahedron-CsPbBr₃ exhibit an orthorhombic phase with space group *Pbnm* (62) and are matched with the standard value (PDF-01-0172-7929). The peaks corresponding to (112) and (020) planes in dodecahedron -CsPbBr₃ are most intense as compared to that of (002) and (110) plane (**Figure 4.2 c**). These observations clearly demonstrate that the dodecahedron-CsPbBr₃ maintained the polyhedron morphology and it exactly matches with earlier report.¹⁹

4.2.1. Optical Studies

Optical absorption and steady state PL spectra ($\lambda_{\text{ex}} = 420 \text{ nm}$) of dodecahedron and cube-CsPbBr₃ are presented in **Figure 4.3 a, b**. It is clearly seen that dodecahedron-CsPbBr₃ exhibit the first excitonic absorption peak at 511 nm and the corresponding PL emission peak at 518 nm with the full width at half maximum (FWHM) of 23 nm (**Figure 4.3 a**). The prepared cube-CsPbBr₃ has band edge absorption peak at 501 nm and a narrow PL emission band peaking at 505 nm with FWHM of 15 nm (**Figure 4.3 b**). The PLQY of dodecahedron-CsPbBr₃ was found to be ~92 %, which is ~22 % higher than that of cube- CsPbBr₃ (**Table 4.1**). Since the obtained dimensions of dodecahedron-CsPbBr₃ outsize the Bohr diameter (7 nm)³¹ in a greater manner

as compared to cube-CsPbBr₃, it clearly suggests that there is relatively weak confinement in the dodecahedron -CsPbBr₃.

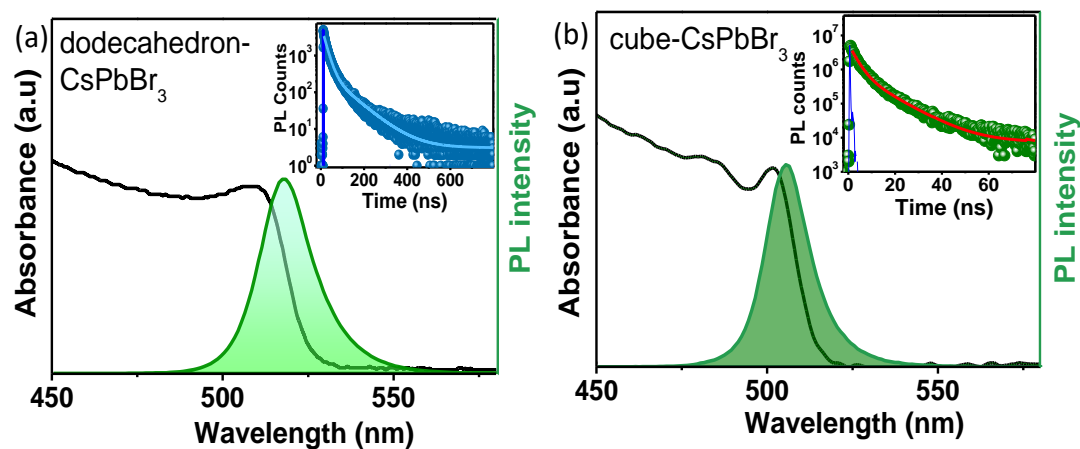


Figure 4.3 Steady state absorption and corresponding PL spectra ($\lambda_{ex} = 420$ nm) of (a) dodecahedron- CsPbBr₃ and (b) cube-CsPbBr₃ (inset: Time-correlated single photon counting (TCSPC) study of dodecahedron and cube-CsPbBr₃ after exciting the sample at 402 nm and monitoring at emission peak position, and laser pulse (IRF) blue line).

Time resolved PL (TRPL) decay trace is fitted bi- exponentially with average life time of 25 ns (**Figure 4.3 a inset**). It is intriguing to see that PL lifetime of dodecahedron-CsPbBr₃ is four times longer as compared to that of cube-CsPbBr₃, ($\tau_{PL}^{cube} = \sim 6$ ns, **Figure 4.3 b inset**, **Table 4.2**). Moreover, dodecahedron -CsPbBr₃ has ~ 2 -fold larger size as compared to that of cube -CsPbBr₃. This might be a consequence of the increased reaction temperature and similar observation has also been established in earlier reports.^{19,20}

Table 4. 1 PL quantum yield calculation

Sample	Sample (area)	Reference (area)	OD sample (450 nm)	OD reference (450 nm)	PLQY (%)
dodecahedron-CsPbBr ₃	22950000	19040000	0.048	0.039	92
cube-CsPbBr ₃	19600000	19040000	0.055	0.039	70

Table 4.2 Details of PL-decay fitting parameters of prepared samples.

System	τ_1 (ns)	A_1 (%)	τ_2 (ns)	A_2 (%)	τ_3 (ns)	A_3 (%)	τ_{avg} (ns)	χ^2
dodecahedron- CsPbBr ₃	18.42	64.63	86.11	35.37			25.5	1.07
cube-CsPbBr ₃	3.28	32.66	8.0	53.81	24.69	13.53	6.01	1.01

The PL life time and PLQY for dodecahedron -CsPbBr₃ are found to be much longer as compared to that of cube-CsPbBr₃ owing to the defect passivation or trap removal, stemming from Br and Pb vacancies and strong binding affinity of dodecahedron-CsPbBr₃ by tertiary ammonium ions.^{19,32-34}

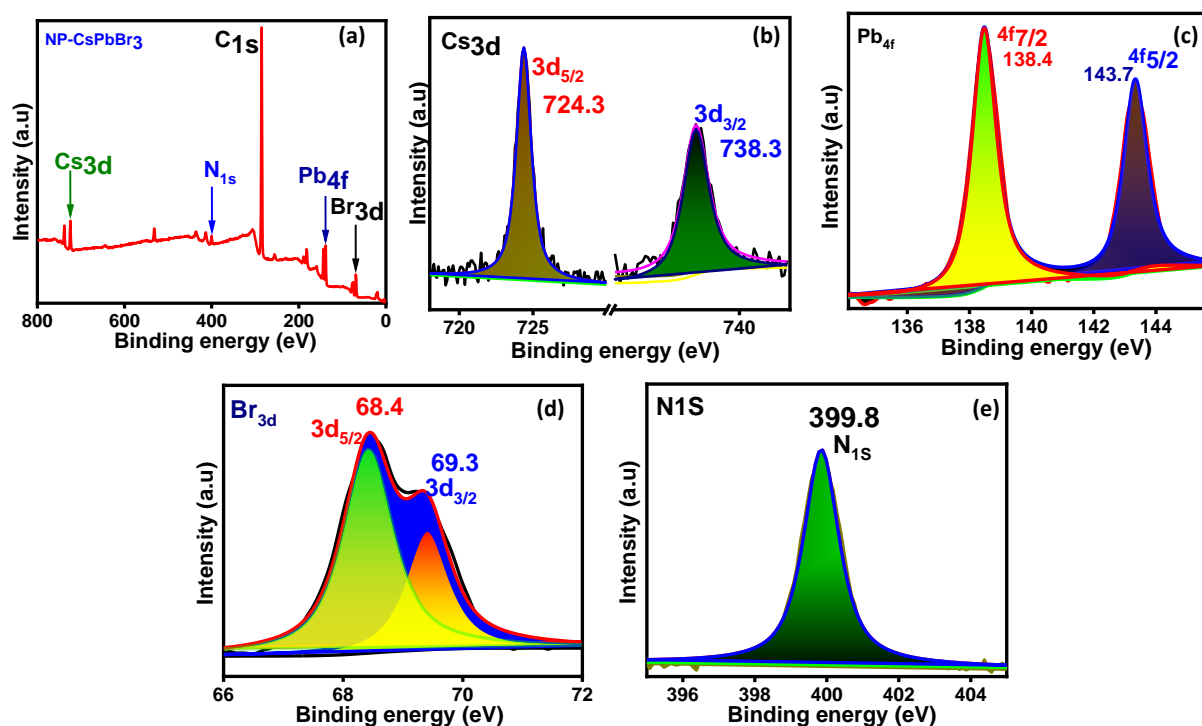


Figure 4.4 XPS spectra of dodecahedron- CsPbBr₃ (a) survey scan; and high-resolution scans of (b) Cs_{3d}, (c) Pb_{4f}, (d) Br_{3d} and (e) N_{1s}.

We further evaluated the surface composition and chemical states of the elements in dodecahedron-CsPbBr₃ by XPS. XPS wide-angle survey reports confirm the peak

corresponding to the binding energy of Cs, Pb, Br, C, and N elements present in the dodecahedron-CsPbBr₃ material (**Figure 4.4 a**). The element ratio of Cs, Pb, and Br are found to be 0.59:0.74:3.1, which is close to the ideal stoichiometry of CsPbBr₃. The binding energy of Pb 4f_{5/2} and Pb 4f_{7/2} were noticed at 143.7 and 138.4 eV, respectively (**Figure 4.4 c**). The binding energy at 738.3 and 724.3 eV can be ascribed to Cs 3d_{3/2} and Cs 3d_{5/2} respectively (**Figure 4.4 b**). Similarly, the peak located at 69.3 and 68.4 eV can be attributed to the spin-orbit splitting of Br 3d_{3/2} and Br 3d_{5/2}, respectively (**Figure 4.4 d**), which matches with previously reported literature.^{35,36} Importantly, the N1s spectrum shows the peak at 399.8 eV related to tertiary nitrogen, which clearly proved the *insitu* formation tertiary ammonium ions from the nucleophilic substitution reaction of oleylamine and 2-bromoacetophenone (**Figure 4.4 e**).^{20,37} From the above, it is obvious that the tertiary ammonium ions formed in the solution that act as the ligand for the assembly of polyhedral morphology.

4.2.2. Transient Absorption Studies

The TRPL measurements are not adequate enough to probe the deeper photophysical aspects of dodecahedron-CsPbBr₃, so we have carried out femtosecond TA studies after exciting the samples at 350 nm laser light. In order to make a comparative analysis of carrier dynamics in both dodecahedron and cube-CsPbBr₃, we have ensured similar experimental conditions. **Figure 4.5 a,c** shows the TA spectra of dodecahedron and cube-CsPbBr₃ sample subsequent to the far band edge excitation (350 nm). Analogous features have been observed in both the cases with a transient ground state bleach (GSB) peaking at 506 and 510 nm for cube-CsPbBr₃ and dodecahedron-CsPbBr₃ corresponding to the formation of band edge exciton respectively. Further, photo-induced absorption (PIA) originated in either side of GSB located near 480 nm i.e. above band gap (blue side) or 526 nm lying below band gap (red side) respectively for dodecahedron-CsPbBr₃.

The PIA signal observed towards the higher energy region is mainly due to the excited state absorption. The positive signal representing the PIA on the high energy side of the bleach mainly stems from the probe induced absorption undergone by the charge carriers already placed in the electronic states above the band gap subsequent to photoexcitation.^{38,39} The PIA feature below the band gap lying towards lower energy side i.e. 526 nm has been ascribed to the carrier induced bi-excitonic stark effect and this PIA signal is observed to be shifted with respect to GSB which might be the exciton-exciton interaction.^{31,35,40-42} The initial delay time

spectra is comparable to the asymmetric double derivative of absorption spectra are provided in **Figure 4.6 (a-d)** for both the systems.⁴³ The biexciton feature discerned in this case is the probe induced biexciton which is an outcome of the Coulombic interaction among the pump generated hot exciton and the band-edge exciton generated by the probe beam which is analogous to the one discerned by Kambhampati in their work where they noticed such biexcitonic signal in the case of CdSe QD.⁴⁴

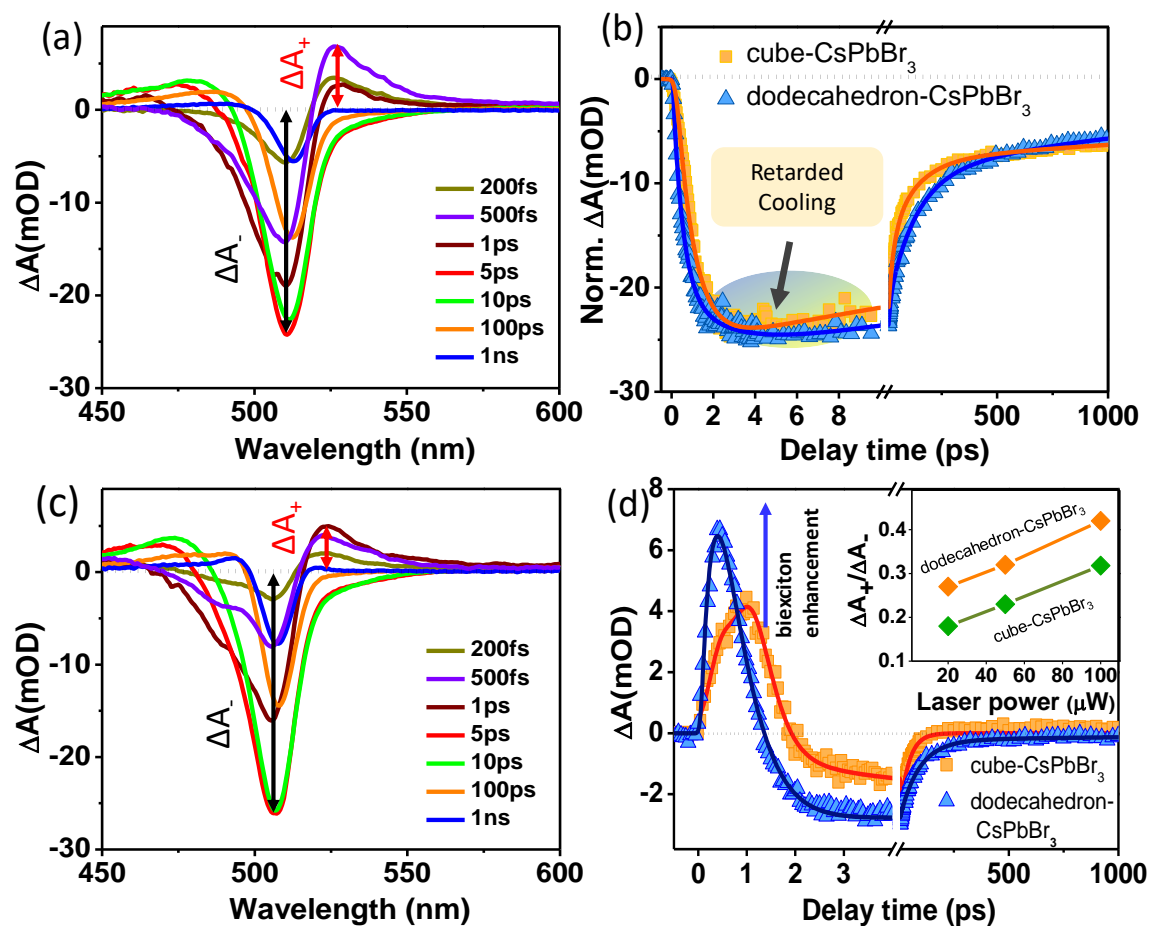


Figure 4.5 TA spectra of (a) dodecahedron- CsPbBr_3 and (c) cube- CsPbBr_3 at different time delays in hexane after exciting the samples at 350 nm, (b) Comparison of bleach kinetics monitored at 510 and 506 nm for dodecahedron - CsPbBr_3 and cube- CsPbBr_3 respectively, (d) Comparison of bi-exciton kinetics monitored at 528 and 524 nm for dodecahedron - CsPbBr_3 and cube- CsPbBr_3 respectively. Inset: change in ratio of bi-exciton signal and excitonic bleach intensity with laser power for both dodecahedron- CsPbBr_3 and cube- CsPbBr_3 .

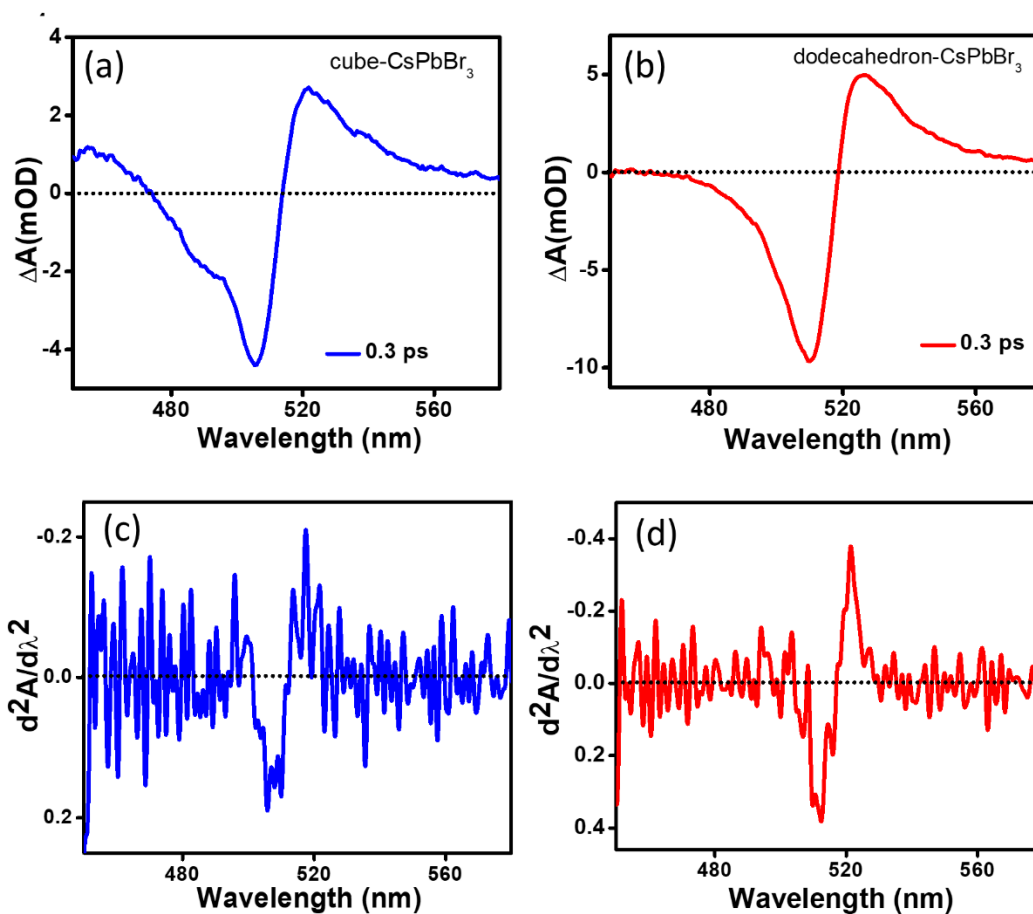


Figure 4.6 (a,b) Early time TA spectra (0.3 ps) of cube-CsPbBr₃ and dodecahedron-CsPbBr₃ which matches with the second derivative of steady-state absorption for **(c)** cube and **(d)** dodecahedron-CsPbBr₃, which clearly indicate the biexciton-induced stark effect in the TA spectra.

There is a significant red shift in the band edge bleach at early time scale due to the exciton-exciton interaction because of the attractive nature of biexciton binding energy ($-\Delta_{xx}$, having negative value). This coulombic interaction leads to a reduction in the electronic bandgap which is generally termed as band gap renormalization. The overall TA spectra is average of the signal due to band edge bleach and photoinduced absorption i.e., the positive signal observed due to biexciton ($E_g + \Delta_{xx}$) at early time scales and later the TA spectra is dominated by the bleach band.⁴⁴ In spite of both of the TA spectra (**Figure 4.5 (a,c)**) having similar features, there are certain prominent differences in the bleach profile and biexciton signal. To understand

the carrier relaxation dynamics of cube-CsPbBr₃ and dodecahedron-CsPbBr₃ the transient kinetics were compared at bleach maxima and biexciton position as shown in **Figure 4.5 b** and **Figure 4.5 d** respectively.

Table 4.3 Kinetics of fitting parameters at bleach position after exciting the samples at 350 nm laser pulse.

System	λ (nm)	τ_{g1}	τ_{g2}	τ_1	τ_2	τ_3	τ_4
cube-CsPbBr ₃	506	<150fs (72%)	0.98ps (28%)	5.8ps (-16%)	43.7ps (-45%)	250ps (-19%)	>1ns (-20%)
dodecahedron-CsPbBr ₃	510	290fs (69%)	1.60ps (31%)	7.2ps (-13%)	58.2ps (-39%)	210ps (-36%)	>1ns (-12%)

The cube-CsPbBr₃ bleach growth kinetics is fitted bi-exponentially with time constants of $\tau_{g1} = <150$ fs and $\tau_{g2} = 0.98$ ps while that for dodecahedron-CsPbBr₃ is also fitted bi-exponentially but with longer time constants of $\tau_{g1} = <290$ fs and $\tau_{g2} = 1.6$ ps (**Table 4.3**).^{31,35,40-42} Thus, the bleach growth profile of the dodecahedron-CsPbBr₃ is slower than cube-CsPbBr₃ (**Table 4. 3**). However, TEM suggests that the particle size is relatively higher for dodecahedron-CsPbBr₃, so carrier dynamics is expected to be faster due to moderately weaker confinement. Such confinement strength rules out the possibility of hot phonon bottleneck effect which is generally liable for slow cooling to prevail in this system. Furthermore, it has been observed that the electronic structure of dodecahedron-CsPbBr₃ is unaffected despite the restructuring of crystals.¹⁸ This slower cooling observed here for dodecahedron-CsPbBr₃ is therefore an unconventional observation, the grounds of which are provided in the later section. **Figure 4.5 d** shows the kinetics profile probed at the respective bi-excitonic maxima for both dodecahedron-CsPbBr₃ (528 nm) and cube-CsPbBr₃ (524 nm). The biexciton kinetics^{31,35,43} for cube-CsPbBr₃ can be fitted multi-exponentially where bi-exciton growth and decay time were determined to be 220 fs and 380 fs respectively, while for dodecahedron-CsPbBr₃ system bi-exciton growth and decay time were determined to be 150 fs and 310 fs respectively (**Table 4. 4**). Interestingly both growth and decay time of bi-exciton is faster for dodecahedron-CsPbBr₃ system. The intensity of bi-exciton absorption maxima (ΔA^+) to excitonic bleach minima (ΔA^-)

for both the systems as a function of laser fluency (20, 50 and 100 μW) are depicted in **Figure 4.5 d inset**.

Table 4.4 Kinetics fitting parameters bi-excitonic peak position of cube-CsPbBr₃ and dodecahedron-CsPbBr₃ after exciting the samples at 350 nm laser pulse.

System	λ nm	(bi-exciton)		single exciton			
		Growth τ_{g1}	Decay τ_{d1}	Growth	Recovery		
cube-CsPbBr ₃	524	220 fs (68.1%)	380 fs (-74.6%)	3.2 ps (-25.4%)	19.8 ps (24.5%)	102 ps (6.45%)	>1ns (1.05%)
dodecahedron-CsPbBr ₃	528	< 150 fs (72.2 %)	310 fs (-71.3%)	1.8 ps (-28.7%)	25.2 ps (15.5%)	125 ps (10.5%)	>1ns (1.8%)

It is clearly evident that the biexciton yield is comparatively much higher (20-30%) in the dodecahedron-CsPbBr₃ system as compared to that of cube-CsPbBr₃. This higher biexciton yield is justified by the scarcity of bound exciton due to lesser number of close to band gap defects which otherwise provide an extra channel for the depopulation of the carriers in dodecahedron-CsPbBr₃. As there is no depopulation of carriers to the defects level, the carriers do not have any other channel available but can only directly populate the biexciton state thus the biexciton formation is much faster and also higher in dodecahedron-CsPbBr₃. The increased bi-exciton magnitude in dodecahedron-CsPbBr₃ suggests that a greater number of excited charge carriers are present in the closely confined region in these -CsPbBr₃ as compared to cube-CsPbBr₃. Formation of biexciton is a kind of multiple exciton generation (MEG). When a solar cell absorbs a photon with far greater energy than the bandgap, the photon creates an energetic electron hole pair. In a bulk- semiconductor cell, the electron and hole quickly relax to the edges of the CB and VB, losing much of their energy to heat. In NC-based solar cells, on the other hand, the conduction-band electronic states are more widely spaced, so phonon-mediated cooling is slowed, and the electron has time to excite a second electron. A single energetic photon can excite more than one electron in a NCs. Gathering those electrons may

be a route to higher solar cell efficiencies. Thus, will lead to increase in the external quantum efficiency (EQE) of a solar cell as it is the ratio of collected charge-carrier pairs to incident photons and MEG leads to increase in the charge carrier pairs per photon. Accordingly, the increase in biexciton formation will increase the power conversion efficiency of solar cell.⁴⁵⁻⁴⁸ The room temperature TA spectroscopy data is unable to answer the reason behind slow carrier cooling and faster formation of biexciton in dodecahedron-CsPbBr₃. So, to gain the clear insights we performed low temperature PL and TA study to unravel these veiled mechanisms.

4.2.3. Low temperature photoluminescence

To investigate the temperature dependent emission properties of dodecahedron-CsPbBr₃, we explored the PL emission measured from 300 to 5 K after exciting at 350 nm (λ_{ex}) (**Figure 4.7 a**). Temperature dependent PL studies from 5 to 300 K show symmetric PL emission with blue shifted peak ranges from 523 to 519 nm, signifying an increasing bandgap (**Figure 4.7 b**). The reason responsible for this observation as found in the literature is: the band edges are constituted by the hybridization between the 6s orbital of Pb and the 4p orbital of Br; upon increasing the temperature, the lattice expands and the hybridization between the two orbitals is reduced which concurrently increases the band gap.^{49,50} In addition, all the recorded PL emission with wide range of temperature can be fitted well with single-Gaussian function which can ascribed to recombination of free excitons. Importantly, there is no signature of any auxiliary peak stemming from bound exciton (**Figure 4.7 a,e**) perceptible unlike that noticeable for cube-CsPbBr₃ even at cryogenic temperatures (**Figure 4.7 c**).²⁹ In our earlier report, at low temperature asymmetric PL spectra of the cube-CsPbBr₃ was detected, which mainly originated from the contribution of band edge emission related to free exciton and bound exciton are pictorially represented in **Figure 4.7 f, g**.^{29,51-55} On the other hand, **Figure 4.7 d, e** pictorially demonstrates the defect free PL emission for dodecahedron-CsPbBr₃ which appears only from free exciton.²⁹ The tertiary ammonium ions in the Polyhedral CsPbBr₃ opened the new facets concurrently reduced the defects stemming from Br⁻ (**Figure 4.7 e**).¹⁹ Temperature dependent PL studies clearly suggest that dodecahedron-CsPbBr₃ is a defect free all-inorganic perovskite with high PL lifetime and PLQY. Unlike the case of conventional cube-CsPbBr₃, there is not much variation in the PL peak maxima with temperature which suggests temperature has not much influence on the orbital hybridization (**Figure 4.7 a, c**).

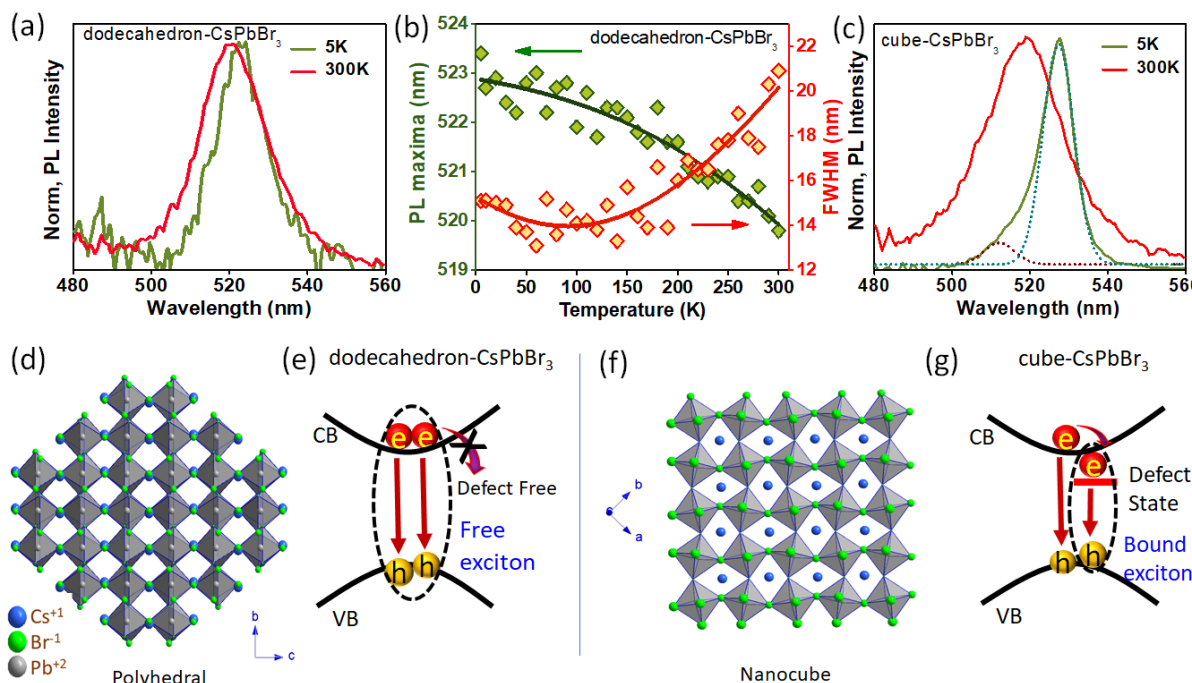


Figure 4.7. (a) Normalized temperature-dependent PL plots for dodecahedron- CsPbBr_3 film. (b) Representative shift in the PL peak position maxima and the FWHM line monitored as a function of temperature (300 – 5K), (c) PL spectra of cube- CsPbBr_3 at 300 and 5 K under 350 nm excitation (the contribution of bound (blue) and free exciton (violet) at 527 and 510 nm respectively in the PL spectrum were deconvoluted with non-Lorentzian fit in the cube- CsPbBr_3 at 5 K also plotted), (d,f) Orthorhombic crystal structure of dodecahedron and cube- CsPbBr_3 and (e,g) corresponding schematic representation of bound exciton and free exciton formation in dodecahedron and cube- CsPbBr_3 respectively.

4.2.4. Low Temperature Transient Absorption Study

Upon execution of temperature dependent TA measurements of dodecahedron- CsPbBr_3 , spectral features illustrate obvious distinction in behaviour in contrast to cube- CsPbBr_3 (Figure 4.8 a, d).²⁹ Interestingly, there is no extra lower energy bleach (due to bound exciton) noticed in the spectra. This goes in synchronization with low temperature PL investigations where there is no asymmetry observed in the obtained PL spectra even at low temperatures (Figure 4.7 a).²⁹ Reduced number of Br⁻ vacancies in these materials accounts for lower density of shallow defect states which can explain the absence of bound excitons in these structures.^{29,56}

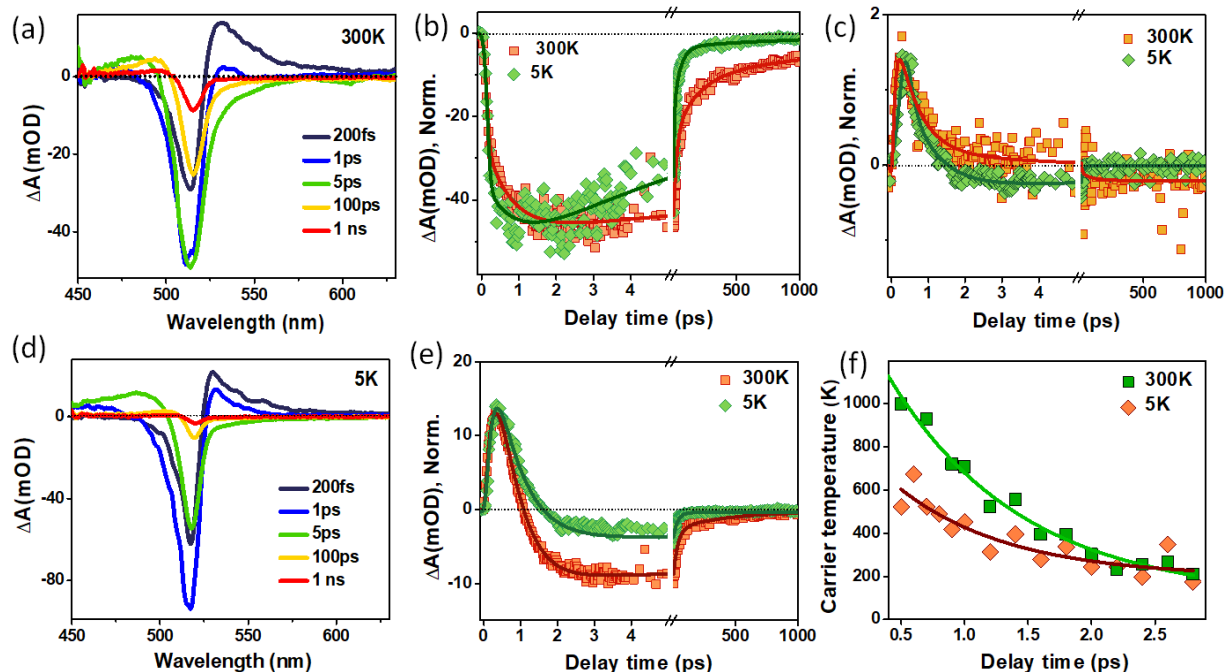


Figure 4. 8 (a, d) TA spectra of dodecahedron- CsPbBr_3 with the temperature of 300 and 5 K under 350 nm pump excitation; (b, c, e) Bleach, polaron and bi-exciton kinetics at different temperature for dodecahedron- CsPbBr_3 monitored at 514, 530 and 620 nm probe wavelength respectively; and (f) Carrier temperature at 300 and 5 K as a function of time delay obtained by Maxwell-Boltzmann fitting of the high energy region of the TA spectra.

The temperature dependent carrier cooling dynamics monitored at the position of the bleach maxima reveal interesting aspects as shown in **Figure 4.8 b**. At temperature close to 5 K, *i.e.* when the lattice is nearly frozen, the hot carriers quickly relax down to the band edges since there is no effective exciton–LO phonon coupling that can result in formation of Fröhlich interaction mediated polaron. This leads to faster cooling of carriers at 5 K (**Figure 4.8 f**) but biexciton formation and decay is intact (**Figure 4.8 e**). However, this cooling observed at 5 K (**Figure 4.8 b**) for the dodecahedron- CsPbBr_3 tends to be retarded (0.2 ps) (**Table 4.5**) in contrast to that observed at 5 K for cube- CsPbBr_3 (0.12 ps).^{29,30} The ground for such behaviour can be related to the absence of a supplementary channel *viz.* bound exciton which otherwise provides an additional pathway for the carriers to relax besides the conventional band edge relaxation. With the elevation of lattice temperature, the bleach growth dynamics of dodecahedron- CsPbBr_3 tend to retard drastically.

Table 4.5 Kinetic fitting parameters at excitonic bleach position for *dodecahedron*-CsPbBr₃ deposited over a glass substrate at different temperature under 350 nm pump excitation.

Lattice Temp (K)	τ_{g1}	τ_{g2}	τ_1	τ_2	τ_3	τ_4
300	<100fs (78%)	0.82 ps (22%)	12 ps (-23.8%)	25.6ps (-42%)	210ps (-20%)	>1ns (-14.2%)
5	<100fs (96%)	0.2ps (4%)	4.5 ps (-68.5%)	28 ps (-27.1%)	139 ps (4.4%)	

Moreover, at 5K bleach growth dynamics of *dodecahedron*-CsPbBr₃ can be fitted single exponentially with time component of 0.2 ps. While, the bleach growth dynamics at 300 K is fitted bi-exponentially with time constants of < 100 fs and 0.82 ps. Further, as for the case of 5K, the data is best fitted using only a single exponential component that is due to the acoustic phonon mode mediated carrier cooling process. But for 300 K bi-exponential fitting goes best for the bleach growth since an additional late time component comes into play due to the process of polaron formation besides the process of carrier cooling. CsPbBr₃ is capable of sustaining large polaron owing to the soft lattice and this *dodecahedron*-CsPbBr₃ are expected to have higher polarity as a consequence of new facets. The significant decelerated cooling observed in *dodecahedron*-CsPbBr₃ can be associated with the difference in the polaron formation time. The kinetics probed at 620 nm is absolute evidence of the fact that in the later system, the process of polaron formation completes at an earlier time scale (polaron formation time, $\tau_{\text{form}}^{\text{dodecahedron}} = 0.25$ ps) than that for *cube*-CsPbBr₃ ($\tau_{\text{form}}^{\text{cube}} = 0.55$ ps)²⁹ (**Figure 4.8 c**). Not only this, the polaron decay also illustrates distinction in the time scale. For the case of *cube*-CsPbBr₃,²⁹ the polaron decay completes roughly 3.5 ps, which is the estimated prototypical duration over which the LO phonons decay into acoustic ones (lower energy phonons). However, it can be proposed that the time over which the LO phonons persist before annihilating into acoustic phonons differs considerably in context of *cube*-CsPbBr₃. They seem to persist around the crystal lattice for relatively higher time before decaying into acoustic ones. This early formation of polaron reflects itself in the observed decelerated hot carrier cooling.

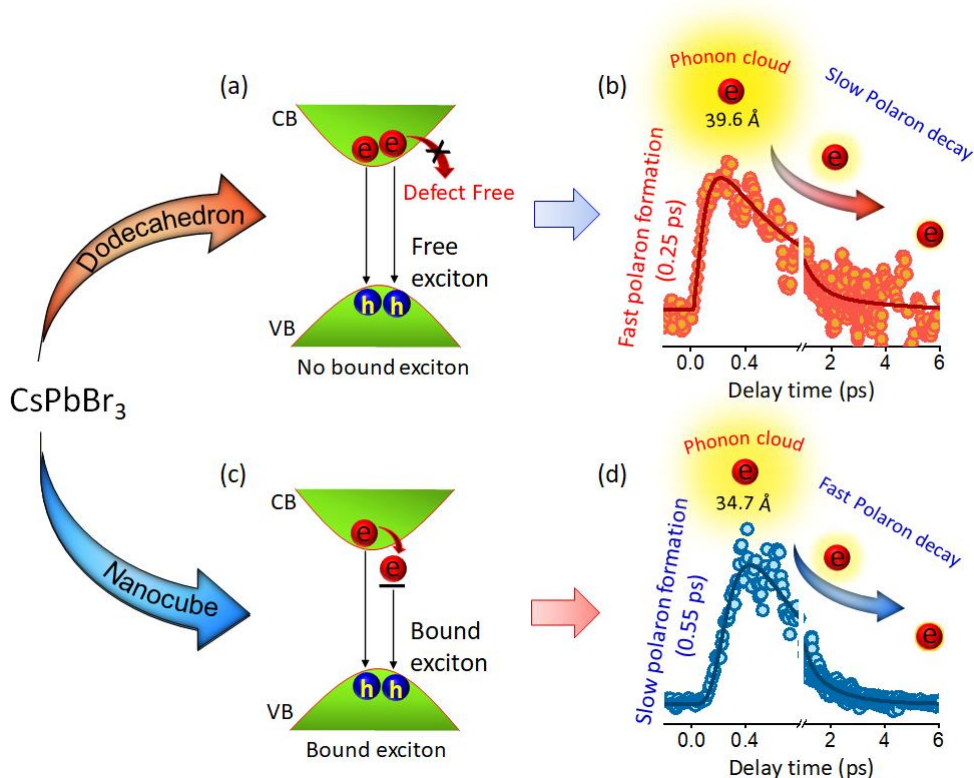


Figure 4. 9 Schematic representation portraying (a,c) the defect free nature of dodecahedron CsPbBr₃ and the traditional CsPbBr₃ nanocubes accounting for the absence of bound exciton in the former system; (b,d) reveal the contrasting polaron dynamics of dodecahedron and traditional cube-CsPbBr₃ illustrating the relatively fast polaron formation in dodecahedron (0.25 ps) than nanocubes (0.55 ps). These two factors together are liable for the retarded carrier cooling dynamics observed for dodecahedron CsPbBr₃.

The charge carrier dressed all around by the LO phonon cloud, forming a polaron has much higher effective mass than the bare charge carriers.^{57,58} Owing to the subsequently lower mobility, the carriers undergo drastically slower cooling due to their heavier masses and sturdy Fröhlich interaction with the lattice. The effect of long lasting LO phonons and their delayed decay into acoustic phonons is manifested in the slowed down cooling rate of the hot carriers and the decelerated recovery dynamics of the bleach.^{21,29,30,59-64} The polaron size in the case of dodecahedron-CsPbBr₃⁶³ is larger ($L_{\text{dodecahedron}}^{\text{polaron}} = 39.6 \text{ \AA}$) than that of cube-CsPbBr₃ ($L_{\text{cube}}^{\text{polaron}} = 34.7 \text{ \AA}$),²⁹ resulting in probably larger neighbour phonon mode overlapping and correspondingly slower phonon dissipation (**Figure 4.9**).

4.2.4.1. Calculation of number of charge carriers (N) and polaron radius

The calculation of number of charge carrier N can be written as

$$N = \frac{A(\lambda) \times I}{t \times E} \quad \text{Eq.4.1}$$

Here $A(\lambda)$ implies the absorption intensity at the energy of the incident pump ($A(\lambda) = 1.1$ in the present case).

I stand for the incident laser intensity (here, power of the incident laser pump energy ($E = 3.54 \text{ eV}$) = $25 \mu\text{W}$)

Therefore, equivalent energy flux I, corresponding to a pump beam diameter of $250 \mu\text{m} = 50 \mu\text{J}/\text{cm}^2$.

t = deposited sample thickness (Here $t = 1 \text{ micron}$ as found from the FESEM measurements as shown in **Figure 4.10**).

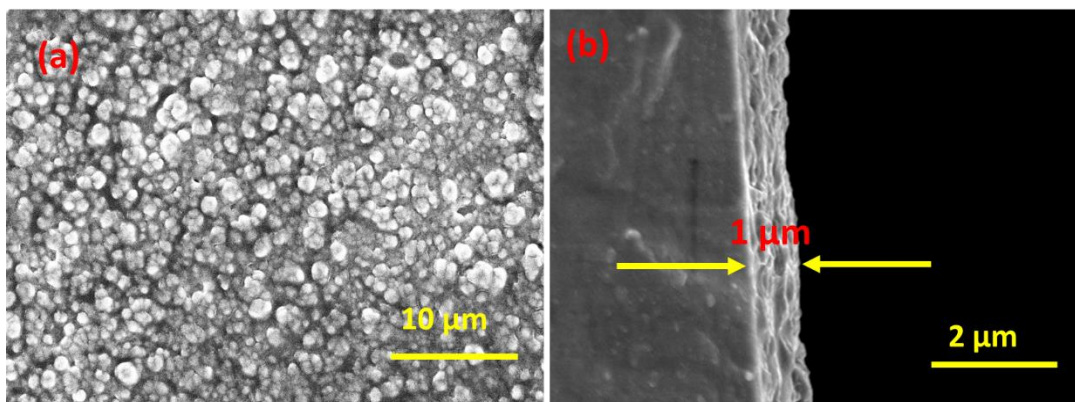


Figure 4.10 (a) FE-SEM images of the as-deposited dodecahedron- CsPbBr_3 over the glass substrate and (b) corresponding the thickness of the sample.

Consequently, the number of charge carriers (N) can be estimated to be $\sim 9.9 \times 10^{17} \text{ cm}^{-3}$.

The Fröhlich polaron radius (r_F) can be calculated using the number of injected charge carriers (N) through the relation connecting both these parameters, $N = (2(2r_F)^3)^{-1}$. The polaron radius for dodecahedron- CsPbBr_3 under the employed carrier density found to be 39.6 \AA . This value is roughly 7.3 times larger than the CsPbBr_3 lattice parameter (5.47 \AA), implying that the Fröhlich polaron in this instance spans over about 7-unit cells of the lattice.

To further validate the conclusions drawn regarding polaron from the low temperature-based TA studies, we performed contactless, non-invasive photoconductivity and mobility measurements for both the samples under investigation employing time dependent Terahertz

spectroscopy (THz-TDS). The comparative THz-TDS analysis is found to further strengthen the claims of slower carrier cooling in the dodecahedron-CsPbBr₃ system. THz temporal waveforms transmitted through the polystyrene substrate and samples spin-coated over the substrate (cube-CsPbBr₃ and dodecahedron-CsPbBr₃) are depicted in **Figure 4.11 a**. The inset of the **Figure 4.11 a** demonstrates the shift in the main peak feature observed for the THz pulse in the samples in contrast to that observed for bare substrate (both in amplitude and delay time due to the extra optical path transversed). The main THz peak amplitude is noticed to be reduced by a factor of 7.8 % and 7% for cube-CsPbBr₃ and dodecahedron-CsPbBr₃ respectively relative to hexane. This reduction can be directly correlated with the THz beam absorption that takes place as it transverses through the samples. Interestingly, there are no additional shape anomalies observed in the temporal THz spectrum for the spin-coated CsPbBr₃ samples. This is probably due to the fact that the main feature due to phonon absorption in CsPbBr₃ which is expected at 3.4 THz (115 cm⁻¹)⁶⁵ falls beyond the detection capability of our TDS photoreceiver.

4.2.5. Carrier Mobility calculations

To probe the carrier transport characteristics, particularly the frequency averaged mobility of both the samples, time resolved Terahertz studies (TRTS) were undertaken employing 480 nm pump. This choice of pump ensures excitation of the charge carriers across the band gap of both cube-CsPbBr₃ and dodecahedron-CsPbBr₃. THz TDS and time resolved THz spectra of cube CsPbBr₃ and dodecahedron-CsPbBr₃ were recorded in the frequency range of 0.1 – 3 THz, at room temperature. The transmitted THz waves were detected at specific pump-probe time delays following the excitation of the CsPbBr₃ samples using 480 nm pump wavelength (Pump power = 200μW). For THz-TDS and TRTS measurements, samples were deposited on Polystyrene substrate of thickness ~1 μm. The data was acquired using THz-TDS software, which was later used to extract the mobility and conductivity. Subsequent to initial photo-excitation, the pump induced changes in THz transmission ($-\Delta E(t_p)/E_0(t_p)$, where E_0 is the electric field maximum transmitted through the unexcited samples) at certain pump probe time delays (t_p) were then monitored (**Figure 4.11 b**).

The induced changes in the electric field are directly proportional to the instantaneous photoconductivity ($\Delta\sigma(t_p)$) as is obvious from the equation.⁶⁵⁻⁶⁷

$$\Delta\sigma(t_p) = \frac{\epsilon_0 c}{d} (n_a + n_b) \left[\frac{-\Delta(E(t_p))}{(E_0(t_p))} \right] \quad \text{Eq.4.2}$$

where ϵ is Permittivity of free space, c is the speed of light, d stands for the thickness of photoexcited samples, n_a is refractive index of air, n_b is refractive indices of polystyrene and ΔE is the Fourier transform of recorded photoinduced change in THz waveform and reference THz waveform.

Photoconductivity is also itself directly related to effective mobility ($\varphi\mu$) which can be calculated using the relation:

$$\varphi\mu = \frac{\Delta\sigma}{N_0 q} \quad \text{Eq.4.3}$$

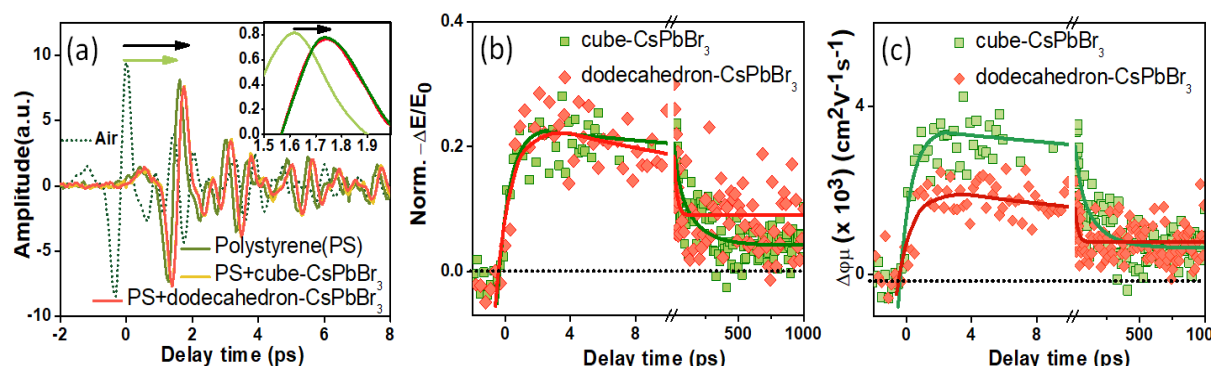


Figure 4.11 (a) THz-TDS waveforms transmitted through the air, polystyrene, cube-CsPbBr₃ and dodecahedron-CsPbBr₃ over polystyrene, (b) Normalized comparative photoinduced THz transmissions versus pump–probe delay for 480 nm pump and (c) Calculated time dependent effective mobility for both cube-CsPbBr₃ and dodecahedron-CsPbBr₃.

where $\Delta\sigma$ is the photoconductivity, N_0 is carrier density, q is the elementary charge and φ is photon to free carrier conversion ratio.

Thus, using the derived photoconductivity, effective mobility can also be deduced. However, the mobility obtained here is not actual but is an effective one since every absorbed incident photon is not expected to yield an electron-hole pair. Only in the most ideal case when each photon results into an electron-hole pair, φ can be equal to one, thus providing us only the low

limit of mobility *i.e.* effective mobility. Upon comparing the initial effective carrier mobilities in both CsPbBr₃ systems just immediate after photoexcitation, it is noticeable that the carrier mobility at very early time scales (few ps) in dodecahedron-CsPbBr₃ system is roughly two times lower than that in cube-CsPbBr₃ system (**Figure 4.11 c**). This lower magnitude of mobility in dodecahedron-CsPbBr₃ is in accordance with both faster and larger polaron formation in dodecahedron system (0.25 ps, 39.6 Å for dodecahedron-CsPbBr₃) than in cube-CsPbBr₃ (0.55 ps, 34.7 Å for cube-CsPbBr₃) which result in heavier effective carrier masses in the former system. Further, the long scale transient decay traces for effective mobility suggest that the recombination processes are retarded in dodecahedron-CsPbBr₃ than cube-CsPbBr₃ due to the reduced carrier wavefunction overlap (because of larger size of polaron) which prevents the recombination of the electron and hole.^{65,68,69}

4.3. Conclusion

In retrospect, dodecahedron-CsPbBr₃ has been prepared with new facets exposed on surface. The TA study clearly reveals that the dodecahedron-CsPbBr₃ exhibit prolonged carrier cooling and 20-30% enhanced bi-exciton yield as compared to cube-CsPbBr₃. The slow carrier cooling is ascribed to the complete absence of supplementary channel involving the bound exciton due to absence of defect/traps states. The claim for the absence of these states is further strengthened by the low temperature PL studies where no auxiliary PL emission found at cryogenic temperatures. Temperature dependent TA studies reveal that the fast polaron formation of 0.25 ps and polaron size enhancement have been observed in dodecahedron-CsPbBr₃. The increase in polaron size from 34.7 Å (cube-CsPbBr₃) to 39.6 Å (dodecahedron-CsPbBr₃) may be the root cause for the slower bleach growth and decay as compared to cube-CsPbBr₃. Furthermore, comparative THz-TDS clearly demonstrate that the carrier mobility at very early time scales (few ps) in dodecahedron-CsPbBr₃ system is roughly two times lower than that in cube-CsPbBr₃ system, which further supports our claim of slower carrier cooling in the dodecahedron-CsPbBr₃. Our results obtained in this work offer a fundamental understanding to establish the exciting possibility to take merits of the dodecahedron-CsPbBr₃ in the highly efficient device applications. We strongly believe that the established polyhedral

dodecahedron CsPbBr₃ architecture with open facets and new ligands can be employed in energy harvesting and optoelectronic field.

4.4. References

- (1) Kovalenko, M. V.; Protesescu, L.; Bodnarchuk, M. I. Properties and potential optoelectronic applications of lead halide perovskite nanocrystals. *Science* **2017**, *358*, 745–750.
- (2) Akkerman, Q. A.; Raino, G.; Kovalenko, M. V.; Manna, L. Genesis, challenges and opportunities for colloidal lead halide perovskite nanocrystals. *Nat. Mater.* **2018**, *17*, 394–405.
- (3) Protesescu, L.; Yakunin, S.; Bodnarchuk, M. I.; Krieg, F.; Caputo, R.; Hendon, C. H.; Yang, R. X.; Walsh, A.; Kovalenko, M. V. Nanocrystals of cesium lead halide perovskites (CsPbX₃, X = Cl, Br, and I): novel optoelectronic materials showing bright emission with wide color gamut. *Nano Lett.* **2015**, *15*, 3692–3696.
- (4) Pan, J.; Shang, Y.; Yin, J.; De Bastiani, M.; Peng, W.; Dursun, I.; Sinatra, L.; El-Zohry, A. M.; Hedhili, M. N.; Emwas, A. H.; Mohammed, O. F. Bidentate ligand-passivated CsPbI₃ perovskite nanocrystals for stable near-unity photoluminescence quantum yield and efficient red light-emitting diodes. *J. Am. Chem. Soc.* **2017**, *140* (2), 562-565.
- (5) Bekenstein, Y.; Koscher, B. A.; Eaton, S. W.; Yang, P.; Alivisatos, A. P. Highly luminescent colloidal nanoplates of perovskite cesium lead halide and their oriented assemblies. *J. Am. Chem. Soc.* **2015**, *137*, 16008–16011.
- (6) Swarnkar, A.; Chulliyil, R.; Ravi, V. K.; Irfanullah, M.; Chowdhury, A.; Nag, A. Colloidal CsPbBr₃ Perovskite nanocrystals: luminescence beyond traditional quantum dots. *Angew. Chem., Int. Ed.* **2015**, *54* (51), 15424-15428.
- (7) Li, X.; Wu, Y.; Zhang, S.; Cai, B.; Gu, Y.; Song, J.; Zeng, H. Quantum dots: CsPbX₃ quantum dots for lighting and displays: room-temperature synthesis, photoluminescence superiorities, underlying origins and white light-emitting diodes. *Adv. Funct. Mater.* **2016**, *26* (15), 2584.
- (8) Yakunin, S.; Protesescu, L.; Krieg, F.; Bodnarchuk, M. I.; Nedelcu, G.; Humer, M.; De Luca, G.; Fiebig, M.; Heiss, W.; Kovalenko, M. V. Low-threshold amplified spontaneous emission and lasing from colloidal nanocrystals of caesium lead halide perovskites. *Nature Commun.* **2015**, *6* (1), 1-9.
- (9) Ramasamy, P.; Lim, D. H.; Kim, B.; Lee, S. H.; Lee, M. S.; Lee, J. S. All-inorganic cesium lead halide perovskite nanocrystals for photodetector applications. *Chem. Commun.* **2016**, *52*, 2067-2070.
- (10) Swarnkar, A.; Marshall, A. R.; Sanhira, E. M.; Chernomordik, B. D.; Moore, D. T.; Christians, J. A.; Chakrabarti, T.; Luther, J. M. Quantum dot-induced phase stabilization of α -CsPbI₃ perovskite for high-efficiency photovoltaics. *Science* **2016**, *354*, 92-95.

- (11) Sun, S.; Yuan, D.; Xu, Y.; Wang, A.; Deng, Z. Ligand-mediated synthesis of shape-controlled cesium lead halide perovskite nanocrystals via reprecipitation process at room temperature. *ACS nano* **2016**, *10* (3), 3648-3657.
- (12) Yang, H.; Zhang, Y.; Pan, J.; Yin, J.; Bakr, O. M.; Mohammed, O. F. Room-temperature engineering of all-inorganic perovskite nanocrystals with different dimensionalities. *Chem. Mater.* **2017**, *29* (21), 8978-8982.
- (13) Krieg, F.; Ochsenbein, S. T.; Yakunin, S.; Ten Brinck, S.; Aellen, P.; Süess, A.; Clerc, B.; Guggisberg, D.; Nazarenko, O.; Shynkarenko, Y.; Kumar, S.; Colloidal CsPbX₃ (X= Cl, Br, I) nanocrystals 2.0: Zwitterionic capping ligands for improved durability and stability. *ACS energy Lett.* **2018**, *3* (3), 641-646.
- (14) Manser, J. S.; Christians, J. A.; Kamat, P. V. Intriguing optoelectronic properties of metal halide perovskites. *Chem. Rev.* **2016**, *116* (21), 12956-13008.
- (15) Pan, J.; Shang, Y.; Yin, J.; De Bastiani, M.; Peng, W.; Dursun, I.; Sinatra, L.; El-Zohry, A. M.; Hedhili, M. N.; Emwas, A.-H.; Mohammed, O. F.; Ning, Z.; Bakr, O. M. Bidentate ligand-passivated CsPbI₃ perovskite nanocrystals for stable near-unity photoluminescence quantum yield and efficient red light-emitting diodes. *J. Am. Chem. Soc.* **2018**, *140*, 562-565.
- (16) Dang, Z.; Dhanabalan, B.; Castelli, A.; Dhall, R.; Bustillo, K. C.; Marchelli, D.; Spirito, D.; Petralanda, U.; Shamsi, J.; Manna, L.; Krahn, R.; Temperature-driven transformation of CsPbBr₃ nanoplatelets into mosaic nanotiles in solution through self-assembly. *Nano Lett.* **2020**, *20* (3), 1808-1818.
- (17) Zhang, B.; Goldoni, L.; Lambruschini, C.; Moni, L.; Imran, M.; Pianetti, A.; Pinchetti, V.; Brovelli, S.; De Trizio, L.; Manna, L. Stable and size tunable CsPbBr₃ nanocrystals synthesized with oleylphosphonic acid. *Nano Lett.* **2020**, *20* (12), 8847-8853.
- (18) Zhang, B.; Goldoni, L.; Zito, J.; Dang, Z.; Almeida, G.; Zaccaria, F.; de Wit, J.; Infante, I.; De Trizio, L.; Manna, L. Alkyl phosphonic acids deliver CsPbBr₃ nanocrystals with high photoluminescence quantum yield and truncated octahedron shape. *Chem. Mater.* **2019**, *31*, 9140-9147.
- (19) Pradhan, N. Alkylammonium halides for facet reconstruction and shape modulation in lead halide perovskite nanocrystals. *Acc. Chem. Res.* **2021**, *54* (5), 1200-1208.
- (20) Bera, S.; Behera, R. K.; Pradhan, N. α -Halo ketone for polyhedral perovskite nanocrystals: evolutions, shape conversions, ligand chemistry, and self-assembly. *J. Am. Chem. Soc.* **2020**, *142* (49), 20865-20874.
- (21) Joshi, P. P.; Maehrlein, S. F.; Zhu, X. Dynamic screening and slow cooling of hot carriers in lead halide perovskites. *Adv. Mater.* **2019**, *31* (47), 1803054.

- (22) Yang, Y.; Ostrowski, D. P.; France, R. M.; Zhu, K.; Van De Lagemaat, J.; Luther, J. M.; Beard, M. C. Observation of a Hot Phonon Bottleneck in Lead-Iodide Perovskites. *Nat. Photonics* 2016, 10, 53-59.
- (23) Achermann, M.; Bartko, A. P.; Hollingsworth, J. A.; Klimov, V. I. The effect of auger heating on intraband carrier relaxation in semiconductor quantum rods. *Nat. Phys.* 2006, 2, 557-561.
- (24) Boehme, S. C.; Brinck, S. T.; Maes, J.; Yazdani, N.; Zapata, F.; Chen, K.; Wood, V.; Hodgkiss, J. M.; Hens, Z.; Geiregat, P.; Ifante, I. Phonon-mediated and weakly size-dependent electron and hole cooling in CsPbBr₃ nanocrystals revealed by atomistic simulations and ultrafast spectroscopy. *Nano Lett.* **2020**, 20 (3), 1819-1829.
- (25) Fu, J.; Xu, Q.; Han, G.; Wu, B.; Huan, C. H. A.; Leek, M. L.; Sum, T. C. Hot carrier cooling mechanisms in halide perovskites. *Nature Commun.* **2017**, 8 (1), 1-9.
- (26) Nah, S.; Spokoyny, B. M.; Soe, C. M. M.; Stoumpos, C. C.; Kanatzidis, M. G.; Harel, E. Ultrafast imaging of carrier cooling in metal halide perovskite thin films. *Nano Lett.* 2018, 18, 1044-1048.
- (27) Yang, J.; Wen, X.; Xia, H.; Sheng, R.; Ma, Q.; Kim, J.; Tapping, P.; Harada, T.; Kee, T. W.; Huang, F. Acoustic-optical phonon upconversion and hot-phonon bottleneck in lead-halide perovskites. *Nat. Commun.* 2017, 8, 1.
- (28) Xing, G.; Mathews, N.; Sun, S.; Lim, S. S.; Lam, Y. M.; Grätzel, M.; Mhaisalkar, S.; Sum, T. C. Long-range balanced electron-and hole-transport lengths in organic-inorganic CH₃NH₃PbI₃. *Science* **2013**, 342 (6156), 344-347.
- (29) Kaur, G.; Justice Babu, K.; Ghosh, H. N. Temperature- dependent interplay of polaron formation and hot carrier cooling dynamics in CsPbBr₃ nanocrystals: role of carrier-phonon coupling strength. *J. Phys. Chem. Lett.* **2020**, 11, 6206-6213.
- (30) Kaur, G.; Ghosh, H. N. Hot carrier relaxation in CsPbBr₃-based perovskites: a polaron perspective. *J. Phys. Chem. Lett.* 2020, 11, 8765-8776.
- (31) Kaur, G.; Justice Babu, K.; Ghorai, N.; Goswami, T.; Maiti, S.; Ghosh, H. N. polaron-mediated slow carrier cooling in a type-1 3D/0D CsPbBr₃@Cs₄PbBr₆ core-shell perovskite system. *J. Phys. Chem. Lett.* 2019, 10, 5302-5311.
- (32) Zhang, X.; Gao, X.; Pang, G.; He, T.; Xing, G.; Chen, R. Effects of material dimensionality on the optical properties of CsPbBr₃ nanomaterials. *J. Phys. Chem. C* **2019**, 123, 28893–28897.
- (33) Bohn, B. J.; Tong, Y.; Gramlich, M.; Lai, M. L.; Döblinger, M.; Wang, K.; Hoye, R. L.; Müller-Buschbaum, P.; Stranks, S. D.; Urban, A. S.; Polavarapu, L.; Feldmann, J. Boosting tunable blue luminescence of halide perovskite nanoplatelets through post-synthetic surface trap repair. *Nano Lett.* **2018**, 18, 5231-5238.

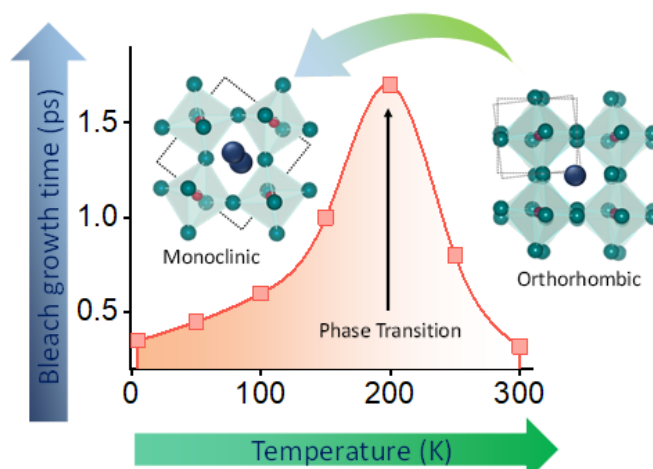
- (34) Justice Babu, K.; Kaur, G.; Shukla, A.; Kaur, A.; Goswami, T.; Ghorai, N.; Ghosh, H. N. Concurrent energy-and electron-transfer dynamics in photoexcited Mn-Doped CsPbBr₃ perovskite nanoplatelet architecture. *J. Phys. Chem. Lett.* **2020**, *12*, 302-309.
- (35) Justice Babu, K.; Kaur, G.; Biswal, L.; De, G.; Ghosh, H. N. Ultrafast charge delocalization dynamics of ambient stable CsPbBr₃ nanocrystals encapsulated in polystyrene fiber. *Chem. Eur. J.* **2021**, *27*, 683–691.
- (36) Cho, H.; Jeong, S. H.; Park, M. H.; Kim, Y. H.; Wolf, C.; Lee, C. L.; Heo, J. H. Sadhanala, A.; Myoung, N.; Yoo, S.; Im, S. H. Overcoming the electroluminescence efficiency limitations of perovskite light-emitting diodes. *Science* **2015**, *350* (6265), 1222-1225.
- (37) Ge, L.; Han, C. Synthesis of MWNTs/g-C₃N₄ composite photocatalysts with efficient visible light photocatalytic hydrogen evolution activity. *Appl. Catal. B. Environ.* **2012**, *117*, 268-274.
- (38) Kumar, V.; Nagal, V.; Kumar, R.; Srivastava, S.; Gupta, B. K.; Kumar, M.; Hafiz, A. K.; Singh, K. Influence of the rate of radiation energy on the charge-carrier kinetics application of all-inorganic CsPbBr₃ perovskite nanocrystals. *RSC Adv.* **2020**, *10*(57), 34651-34657.
- (39) Han, Q.; Wu, W.; Liu, W.; Yang, Y. The peak shift and evolution of upconversion luminescence from CsPbBr₃ nanocrystals under femtosecond laser excitation. *RSC adv.* **2017**, *7*(57), 35757-35764.
- (40) Wu, K.; Liang, G.; Shang, Q.; Ren, Y.; Kong, D.; Lian, T. Ultrafast interfacial electron and hole transfer from CsPbBr₃ perovskite quantum dots. *J. Am. Chem. Soc.* **2015**, *137* (40), 12792-12795.
- (41) Maity, P.; Dana, J.; Ghosh, H. N. Multiple charge transfer dynamics in colloidal CsPbBr₃ perovskite quantum dots sensitized molecular adsorbate. *J. Phys. Chem. C* **2016**, *120*, 18348-18354.
- (42) Dana, J.; Maity, P.; Jana, B.; Maiti, S.; Ghosh, H. N. concurrent ultrafast electron- and hole-transfer dynamics in CsPbBr₃ perovskite and quantum dots. *ACS Omega* **2018**, *3*, 2706-2714.
- (43) Shukla, A.; Kaur, G.; Babu, K. J.; Ghorai, N.; Goswami, T.; Kaur, A.; Ghosh, H. N. effect of confinement on the exciton and biexciton dynamics in perovskite 2D-nanosheets and 3D-nanocrystals. *J. Phys. Chem. Lett.* **2020**, *11*, 6344-6352.
- (44) Sewall, S. L.; Franceschetti, A.; Cooney, R. R.; Zunger, A.; Kambhampati, P. Direct observation of the structure of band-edge biexcitons in colloidal semiconductor CdSe quantum dots. *Phys. Rev. B: Condens. Matter Mater. Phys.* 2009, *80*, 81310.
- (45) De Weerd, C.; Gomez, L.; Capretti, A.; Lebrun, D. M.; Matsubara, E.; Lin, J.; Ashida, M.; Spoor, F. C.; Siebbeles, L. D.; Houtepen, A. J.; Suenaga, K. Efficient carrier multiplication in CsPbI₃ perovskite nanocrystals. *Nature commun.* **2018**, *9*(1), 1-9.
- (46) Miller, J. L. Multiple Exciton Generation Enhances A Working Solar Cell. *Phys. Today*, **2012**, *65*(2), 17.

- (47) Cong, M.; Yang, B.; Chen, J.; Hong, F.; Yang, S.; Deng, W.; Han, K. Carrier multiplication and hot-carrier cooling dynamics in quantum-confined CsPbI₃ Perovskite nanocrystals. *J. Phys. Chem. Lett.* **2020**, *11*(5), 1921-1926.
- (48) Debnath, T.; Maiti, S.; Maity, P.; Ghosh, H. N. Subpicosecond exciton dynamics and diexcitonic feature in colloidal CuInS₂ nanocrystals: role of In–Cu antisite defects. *J. Phys. Chem. Lett.* **2015**, *6*(17), 3458-3465.
- (49) Diroll, B. T.; Zhou, H.; Schaller, R. D. Low-temperature absorption, photoluminescence, and lifetime of CsPbX₃ (X = Cl, Br, I) nanocrystals. *Adv. Funct. Mater.* **2018**, *28*, 1800945.
- (50) Liu, Z.; Shang, Q.; Li, C.; Zhao, L.; Gao, Y.; Li, Q.; Chen, J.; Zhang, S.; Liu, X.; Fu, Y.; Zhang, Q. Temperature-dependent photoluminescence and lasing properties of CsPbBr₃ nanowires. *Appl. Phys. Lett.* **2019**, *114* (10), 101902.
- (51) Ryu, H.; Byun, H. R.; McCall, K. M.; Park, D. Y.; Kim, T. J.; Jeong, M. S.; Kanatzidis, M. G.; Jang, J. I. Role of the A-site cation in low-temperature optical behaviors of APbBr₃ (A = Cs, CH₃NH₃). *J. Am. Chem. Soc.* **2021**, *143* (5), 2340-2347.
- (52) Crane, M. J.; Jacoby, L. M.; Cohen, T. A.; Huang, Y.; Luscombe, C. K.; Gamelin, D. R. Coherent spin precession and lifetime-limited spin dephasing in CsPbBr₃ perovskite nanocrystals. *Nano Lett.* **2020**, *20* (12), 8626-8633.
- (53) Dey, A.; Rathod, P.; Kabra, D. Role of localized states in photoluminescence dynamics of high optical gain CsPbBr₃ nanocrystals. *Adv. Opt. Mater.* **2018**, *6* (11), 1800109.
- (54) Iaru, C. M.; Geuchies, J. J.; Koenraad, P. M.; Vanmaekelbergh, D.; Silov, A. Y. Strong carrier-phonon coupling in lead halide perovskite nanocrystals. *ACS Nano* **2017**, *11*, 11024–11030.
- (55) Lee, S. M.; Moon, C. J.; Lim, H.; Lee, Y.; Choi, M. Y.; Bang, J. Temperature-dependent photoluminescence of cesium lead halide perovskite quantum dots: splitting of the photoluminescence peaks of CsPbBr₃ and CsPb(Br/I)₃ quantum dots at low temperature. *J. Phys. Chem. C* **2017**, *121*, 26054-26062.
- (56) Diroll, B.T.; Nedelcu, G.; Kovalenko, M. V.; Schaller, R. D. High-temperature photoluminescence of CsPbX₃ (X = Cl, Br, I) nanocrystals. *Adv. Func. Mater.* **2017**, *27* (21), 1606750.
- (57) Dey, A.; Ye, J.; De, A.; Debroye, E.; Ha, S. K.; Bladt, E.; Kshirsagar, A. S.; Wang, Z.; Yin, J.; Wang, Y.; Quan, L.N. et al. State of the Art and Prospects for Halide Perovskite Nanocrystals. *ACS Nano*. **2021**, *15*, 7, 10775–10981.
- (58) Landau, L. D.; Pekar, S. I. Effective Mass of a Polaron. *Zh. Eksp. Teor. Fiz.*, **1948**, *18*(5), 419-423.
- (59) Evans, T. J.; Miyata, K.; Joshi, P. P.; Maehrlein, S.; Liu, F.; Zhu, X. Y. Competition between hot-electron cooling and large polaron screening in CsPbBr₃ perovskite single crystals. *J. Phys. Chem. C* **2018**, *122* (25), 13724-13730.

- (60) Bretschneider, S. A.; Ivanov, I.; Wang, H. I.; Miyata, K.; Zhu, X.; Bonn, M. Quantifying polaron formation and charge carrier cooling in lead-iodide perovskites. *Adv. Mater.* **2018**, *30*, 1707312.
- (61) Zheng, F.; Wang, L. Large polaron formation and its effect on electron transport in hybrid perovskites. *Energy Environ. Sci.* **2019**, *12*, 1219-1230.
- (62) Meggiolaro, D.; Ambrosio, F.; Mosconi, E.; Mahata, A.; De Angelis, F. Polarons in metal halide perovskites. *Adv. Energy Mater.* **2020**, *10* (13), 1902748.
- (63) Frost, J. M.; Whalley, L. D.; Walsh, A. Slow cooling of hot polarons in halide perovskite solar cells. *ACS energy Lett.* **2017**, *2* (12), 2647-2652.
- (64) Sonnichsen, C. D.; Strandell, D. P.; Brosseau, P. J.; Kambhampati, P. Polaronic quantum confinement in bulk CsPbBr₃ perovskite crystals revealed by state-resolved pump/probe spectroscopy. *Phys. Rev. Res.* **2021**, *3* (2), 023147.
- (65) Yettapu, G. R.; Talukdar, D.; Sarkar, S.; Swarnkar, A.; Nag, A.; Ghosh, P.; Mandal, P. Terahertz conductivity within colloidal CsPbBr₃ perovskite nanocrystals: remarkably high carrier mobilities and large diffusion lengths. *Nano Lett.* **2016**, *16*, 4838–4848.
- (66) Buizza, L. R.; Wright, A. D.; Longo, G.; Sansom, H. C.; Xia, C. Q.; Rosseinsky, M. J.; Johnston, M. B.; Snaith, H. J.; Herz, L. M. Charge-carrier mobility and localization in semiconducting Cu₂AgBiI₆ for photovoltaic applications. *ACS Energy Lett.* **2021**, *6*(5), 1729-1739.
- (67) Zhang, H.; Debroye, E.; Steele, J. A.; Roeffaers, M. B.; Hofkens, J.; Wang, H. I.; Bonn, M. Highly mobile large polarons in black phase CsPbI₃. *ACS Energy Lett.* **2021**, *6*(2), 568-573.
- (68) Buizza, L. R.; Wright, A. D.; Longo, G.; Sansom, H. C.; Xia, C. Q.; Rosseinsky, M. J.; Johnston, M. B.; Snaith, H. J.; Herz, L. M. Charge-carrier mobility and localization in semiconducting Cu₂AgBiI₆ for photovoltaic applications. *ACS Energy Lett.* **2021**, *6*(5), 1729-1739.
- (69) Zhang, H.; Debroye, E.; Steele, J. A.; Roeffaers, M. B.; Hofkens, J.; Wang, H. I.; Bonn, M. Highly mobile large polarons in black Phase CsPbI₃. *ACS Energy Lett.* **2021**, *6*(2), 568-573.

Chapter 5

Spectroscopic Investigation of Structural Perturbations in CsPbCl₃ Perovskite Nanocrystals: Temperature and Excitation Energy Dependent Study



Inorganic lead halide perovskites are at the frontier of photovoltaic research due to their groundbreaking performance as an absorbing layer in solar cells. Cesium lead chloride (CsPbCl₃) known to be a competent material for its blue emission, undergoes subsequent temperature-dependent phase transitions. The photophysical aspects reliant on temperature as well as the phase exhibited by the material are still unknown. Herein, we have studied the temperature and excitation energy-dependent underlying photophysics in CsPbCl₃ nanocrystals (NCs) employing ultrafast transient absorption (TA) and terahertz (THz) spectroscopy. The direct dependence of carrier relaxation, carrier temperature, and energy loss on the phase transition has been established. Also, to comprehend the outcome of excitation energy, photoconductivity, and mobility were determined with the help of OPTP spectroscopy, and it is established that as the excitation energy is reduced, mobility decay is found to be slow due to diminishing auger recombination and augmented penetration depth.

5.1 Introduction

Inorganic lead halide perovskites have been under continuous demand so far due to their fascinating optical behavior, including higher absorption coefficient, long carrier diffusion length, high PLQY, sharp excitonic emission, and also better stability than their organic counterparts.¹⁻⁴ Moreover, in a short span of time, halide perovskites have established themselves with their breakthrough performance in the field of photovoltaics and the maximum 31.2% PCE achieved in perovskite solar cells.^{5,6} Further, the wide band gap perovskite semiconductors are of particular importance to the field of optoelectronics as they have a great potential for minimalizing thermalization losses simply by stacking up the wideband gap and narrow band gap absorber layers together to prevail over the Shockley-Queisser efficiency limit $\sim 33.7\%$.^{7,8} Recently, Zhang and co-workers designed a nickel oxide-based CsPbCl₃/silicon tandem solar cell that could successfully deliver a final efficiency of 27.2%.⁹ Besides, CsPbCl₃ with a band gap of approximately 3 eV has been under continuous attention for its ability to emit blue light and has the potential to be doped or stacked with another complementary material to emit white light.^{10,11} Apart from this CsPbCl₃ is a promising contender in several applications counting light-emitting diodes, photodetectors, and photovoltaics.^{12,13} Also, to commercialize a material as a working layer in photovoltaic devices during operation it is exposed to extreme temperature ranges, so understanding of temperature dependent material properties is vital.^{14,15} Nonetheless, various reports have pointed out that CsPbCl₃ exhibits a successive temperature assisted phase transition.^{16,17} Earlier Schaller et al. reported a temperature-dependent deep analysis of the photoluminescence (PL) properties of CsPbX₃ NCs (X=Cl, Br, and I).¹⁸ Further, Hoshino et al. studied successive phase transitions exhibited by the CsPbCl₃ due to softening of phonons.¹⁹ Several research is focused on unravelling the charge carrier dynamics of CsPbCl₃ NCs but is limited to room temperature (RT) study only.²⁰ Samanta and co-workers have studied charge carrier dynamics of CsPbCl₃ NCs upon varying lead precursor ratio as well as doping the lattice with impurity ions but have been limited to RT studies.²⁰⁻²² The behavior of charge carriers could not be fully understood at RT due to hindrance of thermal vibrations thus a detailed understanding of carriers at low temperature is of great importance. Till date, so far no report has been studied comprising the effect of phase transition exhibited by CsPbCl₃ NCs on the carrier dynamics, lattice temperature, and energy losses. Thus, temperature-dependent studies provide a unique

opportunity to probe the fundamental properties at low temperatures that remain completely unknown at RT. Such information is of great importance in order to further enhance the optoelectronic devices based on the CsPbCl₃ NCs.

Herein, we have extensively studied the PL, exciton as well as biexciton dynamics of CsPbCl₃ NCs as a function of temperature. The PL investigations suggest an increment in PL intensity and the presence of multiple PL peaks at low temperatures. Further, the TA studies depict a clear dependence of the carrier relaxation process, T_c, as well as the energy loss mechanism over the phase transition. Additionally, to comprehend the effect of excitation energy, we have also calculated the photoconductivity and carrier mobility of CsPbCl₃ NCs with the help of time-resolved terahertz spectroscopy, to figure out its wider applicability in the field of photovoltaics.

5.2 Result and Discussion

In the present investigation, CsPbCl₃ NCs were prepared using the hot injection method²³ and spin coated over quartz substrate for further characterizations. The synthesis procedure has been detailed in Chapter 2.

5.2.1. Crystallographic studies and Morphological investigations

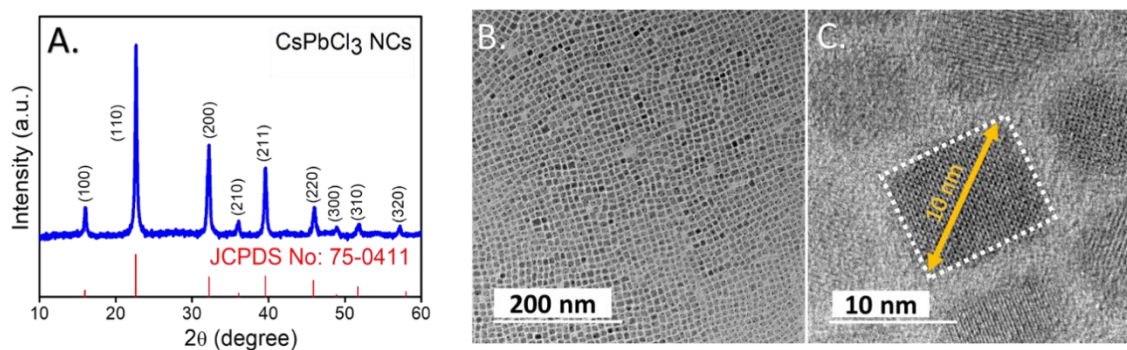


Figure 5.1 (A) XRD pattern of as-prepared CsPbCl₃ NCs film. The standard JCPDS data of cubic CsPbCl₃ is also shown as lines at the bottom, (B) TEM and (C) HR-TEM images of CsPbCl₃ NCs.

XRD, TEM and HRTEM images are provided in **Figure 5.1**. In general, bulk CsPbCl₃ crystallizes in orthorhombic phase at room temperature and it undergoes successive phase transition under narrow temperature range from 310 to 320 K.³ In our present study, at room

temperature all the diffraction peaks (**Figure 5.1 A**) of CsPbCl₃ NCs exactly matched with the cubic phase of CsPbCl₃. The TEM and HR-TEM images of CsPbCl₃ NCs (**Figure 5.1 B,C**) affirm that average length of NCs is ~10 nm. Recent reports clearly mentioned that at room temperature CsPbCl₃ NCs is found to crystallize in the cubic phase⁴⁻⁶ The temperature dependent studies have witnessed that the cubic phase at room temperature of CsPbCl₃ NCs gradually converts to the orthorhombic phase at around ~ 300 K.^{3,7}

5.2.2. Steady State Optical Properties

The optical absorbance spectrum of as prepared film of CsPbCl₃ NCs, is depicted in **Figure 5.2 A**. As the primary determination of this study is to have a profound understanding of the carrier dynamics as a function of temperature. Therefore, in the same intent, a PL study of CsPbCl₃ NCs has been conducted in a wide range of temperatures (300K to 5K) (**Figure 5.2 B and 5.3**). The temperature-dependent PL shows that as we lower the temperature to 5K (**Figure 5.2 B, 5.3 A**) certain new features appear which were indistinguishable at 300K (**Figure 5.3 A**). Another striking reflection is that at 300 K, only one peak is apparent, nevertheless, upon deconvolution of the PL spectra it could be deconvoluted into five features peaking at 3.03, 3.00, 2.97, 2.93, and 2.89 eV (**Figure 5.3 B**) respectively. But as the temperature drops, certain new features appear and dominate the overall PL spectra. At 5K, the apparent features are placed at 2.89, 2.91, 2.92, 2.95, 2.98, and 3.01 eV (**Figure 5.2 B**). The features at 2.98 and 3.01 eV are ascribed to the bound exciton (BE) and free exciton (FE), respectively (**Figure 5.2 D**). The BE holds its contribution from the shallow trap states stemming from the halide vacancies, Cl⁻ in the present case.^{4,24} In the halide perovskites, the BE is a result of electrons that get trapped in the Cl⁻ vacancy defect state created just below the CB which form a bound exciton with free holes in the VB.²⁵⁻²⁷ The energy difference among FE and BE is about 30 meV, which is in close approximation with the earlier reported energy difference, thus rationalizes the origin of the two peaks.⁴ Furthermore, the peak at 2.95 eV at 5K is expected to be the biexcitonic luminescence and the energy difference with the FE is around 60 meV, which is twice the energy difference between FE and BE. Furthermore, Mahamuni and co-workers have found that the sharp PL feature at 2.97 eV observed at low temperatures in CsPbCl₃ NCs is due to stimulated biexciton emission.⁴

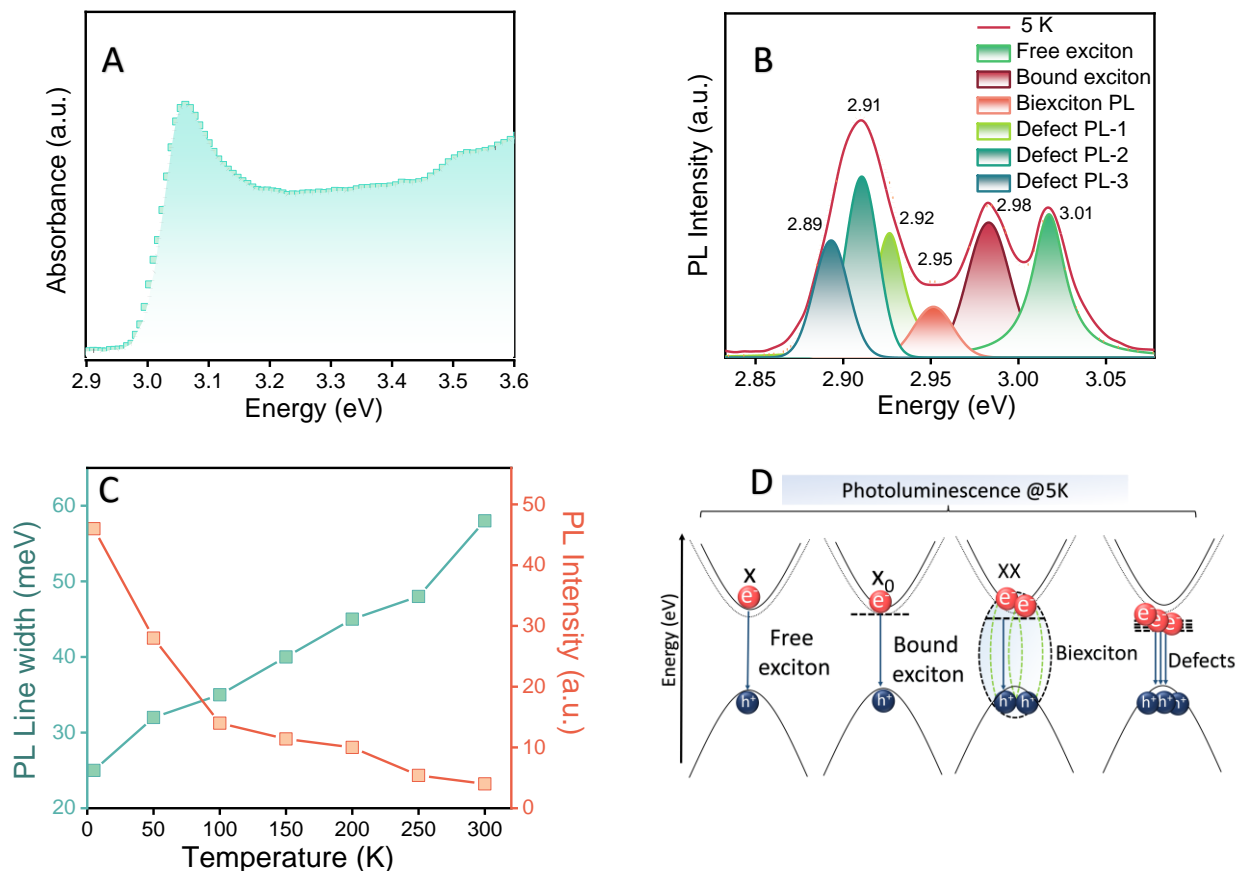


Figure 5.2 (A) The absorption spectra of CsPbCl₃ NCs, (B) Deconvoluted PL spectrum of CsPbCl₃ NCs at 5K, (C) The band-edge PL peak intensity and PL line width plotted against the temperature, and (D) Schematic representation of various PL transitions taking place at 5K.

Moreover, the other features are ascribed to the PL transitions allied to the structural defects and halogen vacancies.⁴ Previously, such defect PL was observed as sharp peaks in CsPbCl₃ NCs perovskites at low temperature, due to shallow defect states created in the lattice.^{4,25,27} These defects in CsPbCl₃ NCs are found to be sharp and are perceivable only at low temperatures.^{4,27} Also, such sharp defect induced PL peaks are observed even in perovskites of another family (oxides) such as LaAlO₃ and SrTiO₃.²⁸ Another captivating observation is that as temperature is lowered the PL intensity shows the first spike at 200 K and displays a steady increase upon further lowering temperature up to 5 K, which is a consequence of fading phonon perturbation (**Figure 5.2 C**).⁴

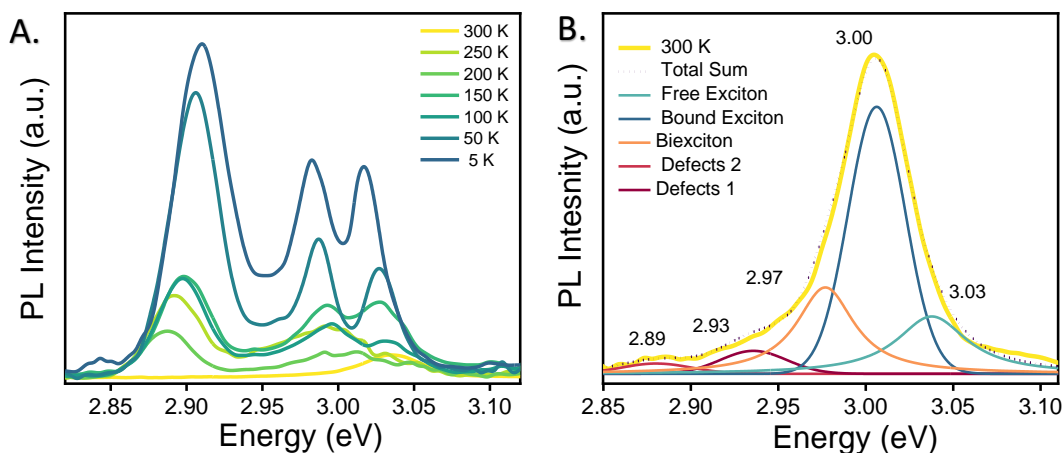


Figure 5.3 (A) The PL spectrum of CsPbCl₃ NCs in the temperature range of 300 to 5 K, (B) deconvoluted PL spectrum of CsPbCl₃ NCs at 300 K.

The term fading perturbation generally means diminishing of phonons at low temperatures. This could be attributed to the fact that when the temperature is reduced, the lattice emits phonons with lower energy. Thus, the phonon contribution will be marginally reduced, which decreases the non-radiative pathway and thus, increase in PL intensity is pragmatic at low temperatures.⁴ Additionally, the elevated temperature triggers the non-radiative pathways leading to the continuous decrease in intensity, stimulated via thermal effects.^{29,30}

5.2.3. Transient Absorption Study

Although PL gives brief analogy about the temperature-assisted phase transition and Frohlich interaction processes but the underlying carrier relaxation mechanism is still unclear. So, to introspect the deeper aspects of the temperature-assisted carrier-phonon coupling the charge carrier dynamics of CsPbCl₃ NCs has been scrutinized. **Figure 5.4 A-D**, depicts TA spectra of CsPbCl₃ NCs in the temperature range of 300 to 5 K upon 4.42 eV pump excitation and 40 $\mu\text{J}/\text{cm}^2$ pump fluence.

5.2.3.1. Temperature Dependent Carrier Cooling

The TA spectrum of CsPbCl₃ NCs displays three distinct features counting, a ground state bleach peaking at 3.07 eV originating due to reduction of the exciton absorption through phase space-filling, a positive signal towards the lower photon energies than the bandgap at early time delay due to biexciton stark shift and photoinduced absorption (PIA) towards the high

energy region.^{31,32} The worth asserting point is that as temperature is lowered a new bleach is noticeable towards the lower energy regime (2.96 eV). As already proclaimed by the low-temperature PL study, the PL at 2.96 eV is due to biexciton driven stimulated emission with energy difference of about 60 meV from the free exciton. Such biexciton-driven stimulated emission is manifested as a negative signal (bleach) in TA spectra.

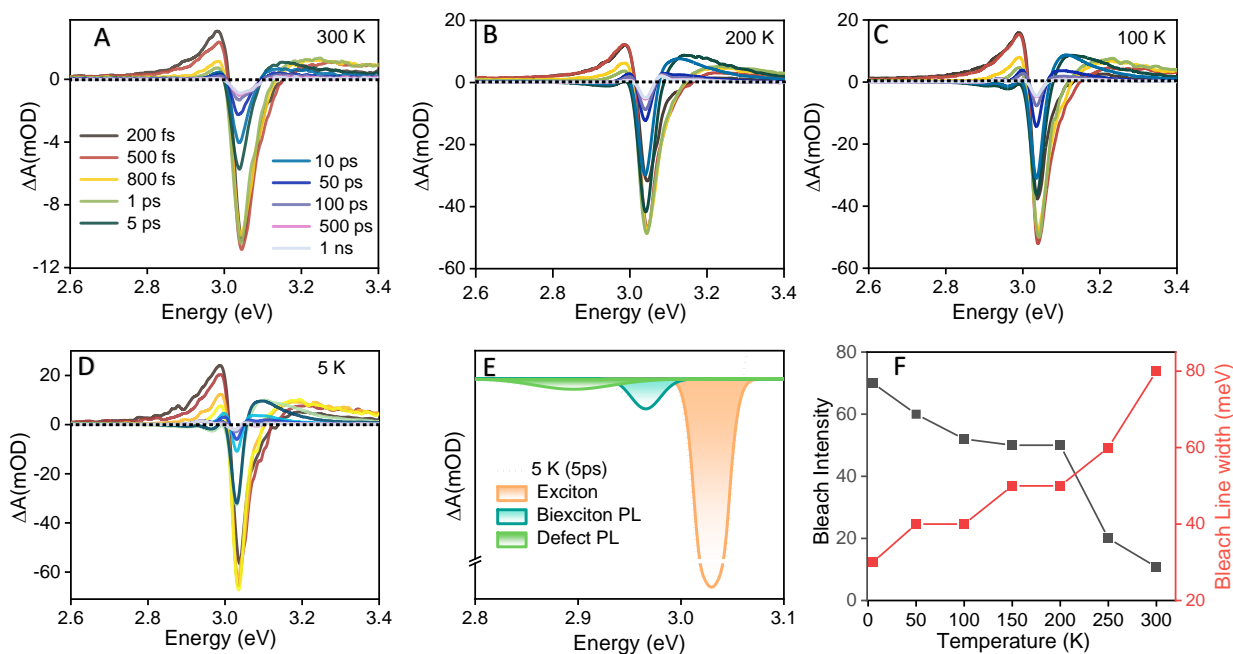


Figure 5.4 (A-D) TA spectra of CsPbCl₃ NCs spreading over the temperature range 300K to 5K under 3.54 eV pump excitation, (E) The deconvoluted transient spectra at 5 ps corresponding to 5K depicting exciton, biexciton stimulated and defect emission, (F) The Plot of bleach maximum intensity and FWHM as a function of Temperature (T).

But, upon further stepping down the temperature at 5 K two distinct negative features start to appear one of which at 2.96 eV is due to biexciton stimulated emission while the other one (2.90 eV) is due to defects. As temperature is lowered the non-radiative processes are reduced, and it leads to splitting of peaks into biexciton and defect mediated stimulated emission (**Figure 5.4 E**) which are in good match with the PL data.²⁴ Furthermore, it is also evident that as we lower the temperature the FWHM of the bleach (**Figure 5.4 F**) also decreases with which is a indicative of the reduced interplay LO phonons at lower temperatures.^{15,33} The increase in bleach intensity with reducing temperature evidently portrays the first spike at around 200 K

due to the second-order transition experienced by the CsPbCl₃ NCs, as it gets deviated from its centrosymmetric structure due condensation of vibrational modes above 193 K and phase of CsPbCl₃ NCs changes from orthorhombic to monoclinic.^{16,17} The phase transitions in a temperature span above 200 K are first-order transitions due to condensation of rotational modes PbCl₆ octahedra.^{4,16,30,34} Further, Gao et al. performed low temperature PL studies of CsPbCl₃ NCs and correlated the PL lifetime with the phase transitions exhibited by CsPbCl₃ NCs.³⁰ Moreover, it has been found that confined quantum dots didn't exhibit the phase transition at 200 K due to strong quantum confinement conditions.¹⁸ However, our TEM and HR-TEM images of the CsPbCl₃ NCs (**Figure 5.1 B,C**) confirm that particle sizes are ~10 nm, which comes under a weakly confined system thus the crystals exhibit phase transition at 200 K.^{4,30} However, at 200 K the CsPbCl₃ NCs displays a second-order phase transition as shown in **Figure 5.4 F** due to the participation of elastic soft mode.^{16,35} The Raman studies have witnessed phonon softening of lower lying modes ($\nu < 50\text{cm}^{-1}$) at 200 K.^{17,19,35}

5.2.3.2. Temperature Dependent Exciton and Biexciton Transient Kinetics

To further, probe into the temperature dependent relaxation processes transient kinetics at excitonic (**Figure 5.5 A, B**) and biexciton position (**Figure 5.5 C**) has been plotted for all the temperatures. The temperature-dependent bleach growth profile of CsPbCl₃ NCs seems to be apparently divided in two distinct regimes (**Figure 5.5 D**). To start with, as the temperature is lowered from 300 to 200 K the bleach growth time increases, but further letting down the temperature from 200 to 5 K it shows a reduction in the bleach growth time. However, as the bleach growth process is governed by an inevitable factor i.e., the Frohlich interaction that is a consequence of coupling amid carriers and LO phonons. Two processes could perhaps affect the entire scenario, first one is the behavior of carriers as free carriers at elevated temperatures and the excitonic behavior at lower temperatures. However, this could be entirely ruled out in this case as the exciton binding energy of CsPbCl₃ NCs is (75 meV) which unavoidably portrays that even at RT the carriers will behave as exciton only as the thermal energy (~26 meV) is insufficient to disrupt up the exciton into free carriers.^{23,36} Another vital factor is that carrier relaxation is influenced through phonon emission and at RT the lattice is capable of producing the high energy LO phonons (~26 meV).⁴ However, as we lower the temperature from 300 to 200 K (Regime -I) the lattice becomes incapable of producing the high energy LO phonons, and in turn, emits lower energy acoustic phonons (< 2 meV)³⁸

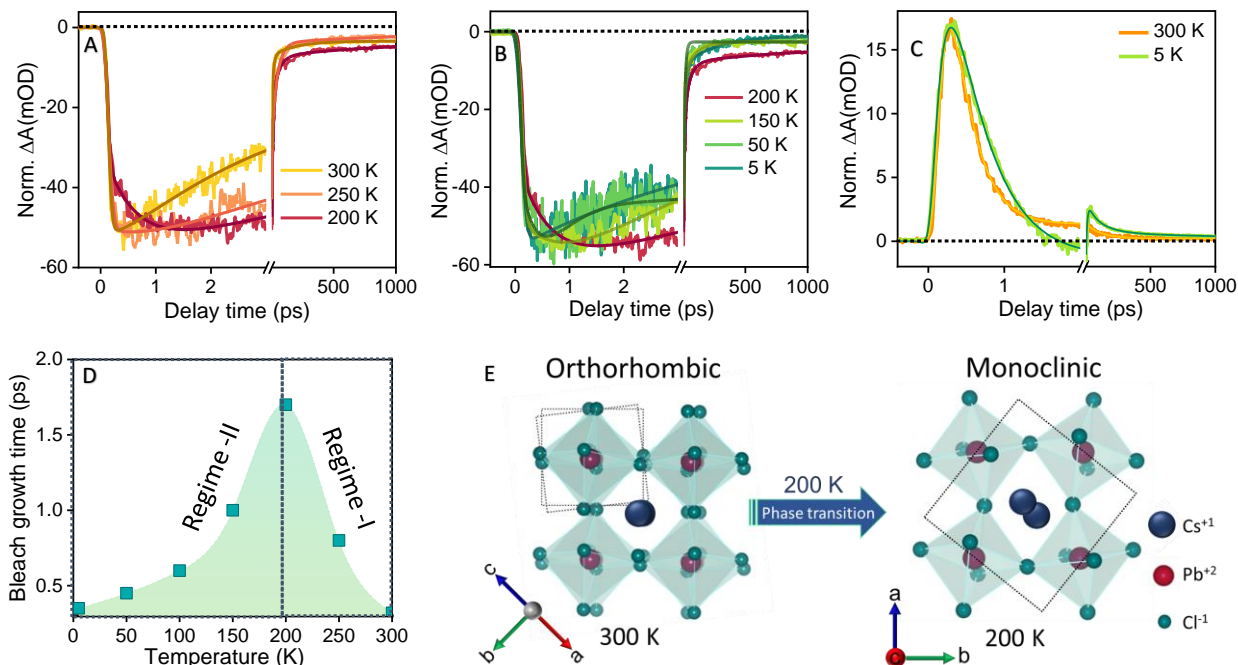


Figure 5.5 Comparative ground state excitonic bleach kinetic traces of CsPbCl_3 NCs film monitored for the energy corresponding to bleach maximum in the temperature range of (A) 300 K to 200 K, (B) 200 K to 5 K (C) The normalized kinetics at the position of biexciton maxima at two extreme temperature ends (300K and 5K), (D) The bleach growth time is plotted as a function of the temperature, and (E) Schematic representation of phase transition experienced by CsPbCl_3 NCs (The crystal structure of orthorhombic and monoclinic CsPbCl_3 models were designed using Vesta software from CIF file with ICSD code of 243734).³⁷

which dominates the picture thus, increases the relaxation time of carriers.³⁸⁻⁴¹ But the trend is opposite in Regime II where a monotonic reduction in carrier cooling lifetime is observed (fitting parameters provided in **Table 5.1**). Another vital factor is that carrier relaxation is influenced through phonon emission and at RT the lattice is capable of producing the high energy LO phonons (~ 26 meV).⁴ However, as we lower the temperature from 300 to 200 K (Regime -I) the lattice becomes incapable of producing the high energy LO phonons, and in turn, emits lower energy acoustic phonons (< 2 meV)³⁸ which dominates the picture thus,

Table 5.1 Kinetic fitting parameters upon fitting the band edge bleach for CsPbCl₃ NCs for different lattice temperature under 4.41 eV pump excitation.

Lattice Temperature (K)	Growth	Recovery			
	τ_g	τ_1	τ_2	τ_3	τ_4
300	<150 fs (100%)	2.5 ps (-74%)	20 ps (-12.6%)	280 ps (- 8%)	>1 ns (- 5.4%)
250	290 fs (100%)	5.3 ps (-59 %)	35 ps (-14.2%)	320 ps (- 21%)	>1 ns (- 5.8%)
200	680 fs (100%)	8.2 ps (-53.6%)	42 ps (- 17.5%)	380 ps (- 20.4%)	>1 ns (- 8.5%)
150	320 fs (100%)	5.1 ps (- 68%)	35 ps (- 9.5%)	310 ps (- 17.3%)	>1 ns (- 5.2%)
50	<150 fs (100%)	6.2 ps (- 65%)	33 ps (- 8.9%)	315 ps (- 21%)	>1 ns (- 5.1%)
5	< 150 fs (100%)	5.8 ps (- 62%)	36 ps (- 9.1%)	314 ps (- 23.6%)	>1 ns (- 5.3%)

increases the relaxation time of carriers.³⁸⁻⁴¹ But the trend is opposite in Regime II where a monotonic reduction in carrier cooling lifetime is observed (fitting parameters provided in **Table 5.1**. This is contradictory to what was anticipated as upon further lowering down the temperature the generation of LO phonons would be reduced, so the cooling was expected to deaccelerate. The faster cooling has been anticipated as a consequence of the phase transition exhibited by CsPbCl₃ NCs as depicted in **Figure 5.5 E**. Apart from the excitonic processes, we have also explored the biexciton transient characteristics. As already mentioned, that the biexciton driven stimulated emission becomes prominent at low temperatures. Apart from this, even though the excitation rate is quite low (the average number of excites generated per pulse is $\langle N \rangle \sim 0.05$) biexciton signal can be perceived, as it is a probe-induced biexciton. Here, we have kept the pump fluence low to ensure per pump photon not more than one exciton is

generated. Nonetheless, the biexciton formed in these perovskite systems is a probe-induced biexciton.^{11,20,32,42} A probe-induced biexciton is a product of the coulombic interaction between the hot photogenerated exciton (created by the pump pulse) as it cools to the band edges and the exciton created by the probe pulse.^{11,20} Previously, numerous reports have found a concurrent increase in biexciton PL at low temperatures.^{43,44} However, the reason for the increase in biexciton PL at low temperatures remains unclear, but our combined analysis of PL and TA gives an analogy of this temperature-dependent process taking place in CsPbCl₃ NCs.

Table 5.2 Biexciton formation and decay components obtained upon fitting the Biexciton maxima for CsPbCl₃ NCs for different lattice temperature under 4.42 eV pump excitation.

Lattice Temperature (K)	Biexciton	
	τ_{g1} (Formation time)	τ_{d1} (Decay time)
300	<150 fs	280 fs
250	<150 fs	290 fs
200	<150 fs	320 fs
150	<150 fs	355 fs
50	<150 fs	360 fs
5	<150 fs	365 fs

So, in order to disentangle this insight, we have compared the biexciton dynamics of CsPbCl₃ NCs as a function of temperature. On comparing the transient kinetics (**Figure 5.5 C**) corresponding to 300 and 5 K, we found that although the formation time (**Table 5.2**) remains same (<150 fs) irrespective of the lattice temperature. Nonetheless, the decay time displays a gradual increase with decreasing lattice temperature. The foremost interruption in the biexciton PL is rapid auger recombination and small biexciton binding energy. As it is well known that thermal energy is higher at RT in comparison to the low temperatures (at 5K the thermal energy is merely ~ 0.43 meV) which is almost negligible to thermally dissociate the biexcitonic states which could have been easily dissociated at RT. This is the reason that there is no significant separate peak from stimulated emission by biexciton at RT, but it becomes prominent at low temperatures. Further, the PL observed here is an outcome of thermal dissociation, as the decrease of biexciton emission at higher temperature is possible only if the formation rate of biexciton remains constant while the dissociation rate is thermally activated.⁴⁴ So, the best plausible explanation from the collective scrutinization of PL as well as TA studies is that since the thermal energy is inadequate to thermally dissociate the biexciton driven states and thus makes biexciton transition separable from the excitonic states.⁴³ Such behavior could only be explained with a model in which the formation rate remains the same irrespective of temperature while the decay rate is dependent upon temperature, which is clearly observed from our transient study (**Table 5.2**).^{45,46} Further, the decay rate of the biexciton population is quantified in form of given equation mentioned below:^{44,45}

$$\gamma(T) = \tau_{xx}^{-1} + K_0 \exp\left(\frac{E_a}{K_B T}\right) \quad \text{Eq. 5.1}$$

Here, τ_{xx} is termed as biexciton lifetime, E_a is known as the dissociation energy, and k_0 is a constant. Also, it is an identified fact that the biexciton intensity is inversely proportional to decay rate of the biexciton ($\gamma(T)$) thus at low temperatures PL intensity increases and a negative bleach is observed in the transient data.⁴³

5.2.3.3. Effect of Phase Transition on Carrier Temperature and Energy Loss

To further emphasize our results, we have calculated the T_c (**Figure 5.6 A-C**) for CsPbCl₃ NCs for all the temperatures under consideration. In order to calculate the T_c , the high energy tail of the normalized TA bleach is fitted using the Maxwell Boltzmann (MB) approximation.^{47–49} However, after being stimulated by an ultrashort pulse, both holes and electrons populate the higher energy levels rapidly and thermalize within sub picoseconds.^{47,48,50} They eventually relax to the band edge via carrier-carrier scattering, carrier-phonon scattering, and phonon-phonon scattering.⁵⁰ Diroll conducted a study to describe the temperature-dependent relaxation process in perovskite NCs, and observed the phase transitions from the high-temperature cubic phases to low-temperature orthorhombic phases in MAPbI₃.¹⁵

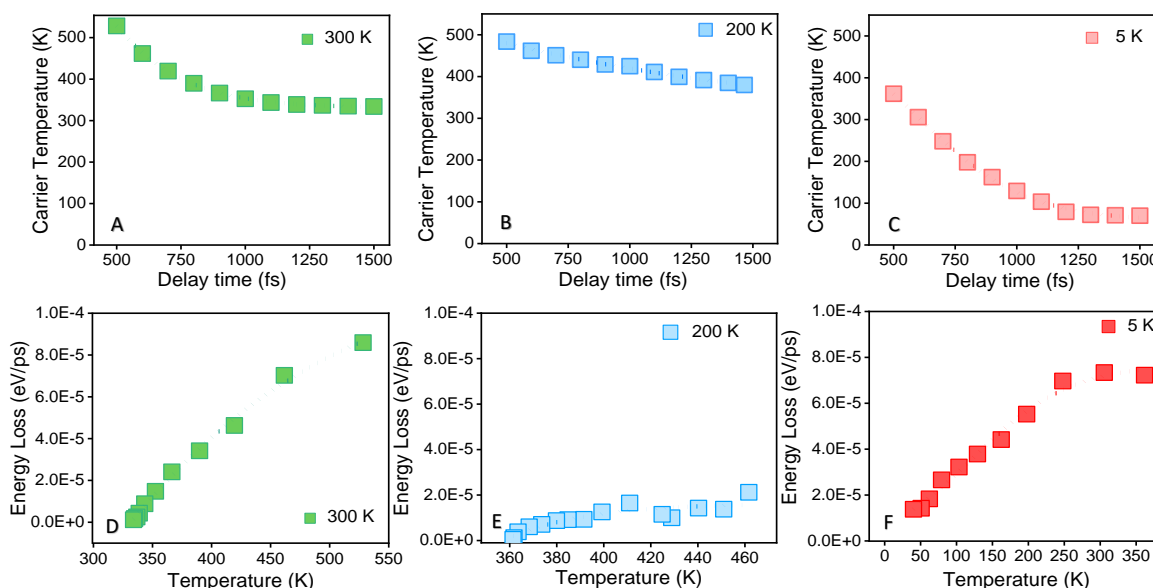


Figure 5.6 The plots for carrier temperature were calculated for (A) 300 K, (B) 200 K, and (C) 5K. The energy loss is calculated as a function of T_c corresponding to the different lattice temperatures i.e., (D) 300 K, (E) 200 K, and (F) 5K.

The relative plots for T_c for 300, 200 and 5K (**Figure 5. 7A**) shows that the carrier cooling is slowed down from 300 to 200 K. But interestingly, at 5K extreme endpoint, the T_c displays a fast decay in comparison to the 200 K and the slope of T_c becomes again steeper. The cooling of hot carriers apparently slows down from 300 to 200 K and such manifestation is due to phonon interplay which occurs when a major portion of carrier distribution is below the LO

phonon energy and the carriers cooling ultimately opt for acoustic phonon-mediated carrier decay.⁵¹ As per the previous reports, the Fröhlich interaction in lead halide perovskites is mainly affected by coupling of phonons and charge carriers which oversees the cooling processes at the primary stage.^{15,24,32,52} Additionally, above Debye temperatures the relaxation time of electrons is found to be inversely proportional to the corresponding lattice temperature.³⁰ Thus, the relaxation time increases upon decreasing the temperature till 200 K. At this point, the preliminary speedy cooling is ascribed to the coupling established among carrier and LO phonons, which creates a thermal steadiness amid the population of LO-phonons and the photogenerated hot carriers. But, after 200 K the lattice experiences a phase transition from orthorhombic to monoclinic as a clear consequence of phonon softening and inclusion of elastic soft mode along with that the fact that temperatures further taken under consideration are lower than the Debye temperature.^{18,53}

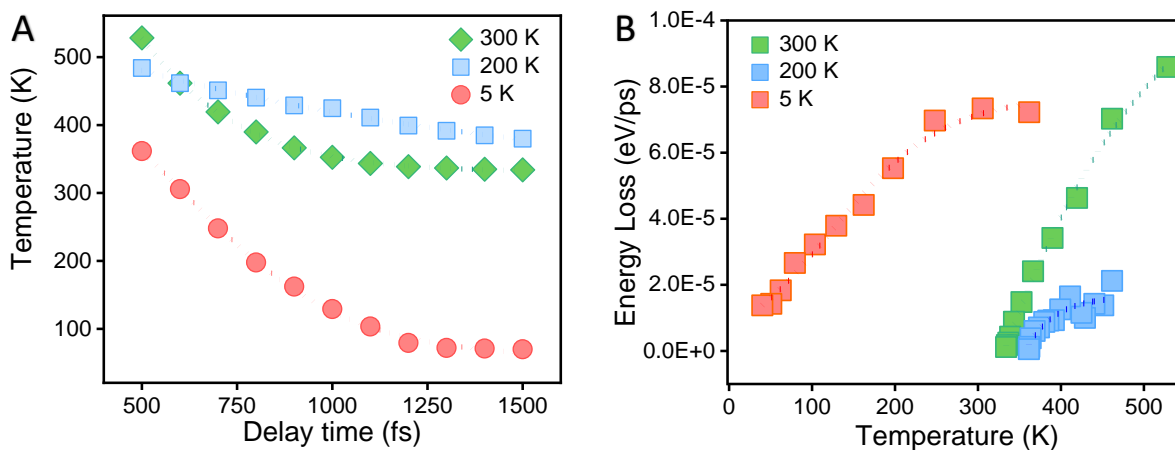


Figure 5.7 (A) The relative carrier temperature plots, (B) The comparative energy loss vs carrier temperature plots of $CsPbCl_3$ NCs for the various lattice temperatures.

The carrier relaxation processes are fundamentally reliant on quite a few factors counting the excitation energy, the initial carrier concentration, and also the rate at which energy is lost at a definite T_c . However, such implication can be emphasized strongly after calculating the energy loss rate w.r.t. temperature. So, in the same inference, we have calculated the energy loss at different lattice temperatures (**Figure 5.6 D-F**) to understand the dependence of energy loss on the lattice temperature using the following equation.⁵⁴

$$Jr = - 3/2K_b (dT_c/dt) \quad \text{Eq.5.2}$$

Where J_r is the energy loss rate per carrier, K_b is the Boltzmann constant and (dT_c/dt) is the derivative of carrier temperature w.r.t. time. The initial value of J_r at 200 K lattice temperature is almost 1.5 times lower than that of 300 K (**Figure 5.7 B**). Another captivating observation is that the rate of energy loss is found to be relatively slower at 200 K in contrast to that of 300 K. Thus, this reduction in the energy loss rate at 200 K ascertain the possibility of cooling mediated *via* acoustic phonons thus obstructing the quicker loss of energy. Further, stepping down the temperature to 5 K we evidently observe that the energy loss rate displays a quicker dissipation and such a transition is again ascribed to the phonon diminution at cryogenic temperatures.^{4,15,24} Thus, we have certainly observed a direct effect of phase transition on the carrier dynamics, T_c , as well as the rate of energy loss. This combined analysis of low temperature PL and TA study demonstrates that the carrier relaxation lifetime is inextricably associated to the structural phase transitions exhibited by the lattice. Such a correlation of phase transition with carrier relaxation has not been observed in other materials of the perovskite family such as, CsPbBr₃ and CsPbI₃.³⁰

5.2.3.4. Excitation Energy Dependent Photoconductivity and Carrier Mobility

After getting a comprehensive analogy of the phonon-mediated phase transition (Phonon-mediated phase transition is the transition exhibited by the lattice due to the softening of phonons) processes occurring in CsPbCl₃ NCs we further determined to check it from the application point of view and study the effect of excitation energy on mobility, we performed OPTP measurements. As of now, so far no study emphasizing the photoconductivity and mobility of CsPbCl₃ NCs.

THz Time-Domain Spectroscopy (THz-TDS) and time-resolved THz spectra for CsPbCl₃ were conducted within the frequency range of 0.1-3 THz at room temperature. The transmitted THz waves were detected at specific pump-probe time delays. In both THz-TDS and Time-Resolved THz Spectroscopy (TRTS) measurements, samples were deposited on a Polystyrene substrate with a thickness of approximately 1.3 μm . The OPTP measurements give us a unique prospect of quantifying the photoconductivity *via* the contactless method engaging time-dependent terahertz spectroscopy (THz-TDS). The THz temporal waveforms transmitted via air (N₂), bare polystyrene substrate, and CsPbCl₃ NCs (spin-coated over polystyrene substrate) are depicted in **Figure 5.8 A**. The THz temporal waveforms (**Figure 5.8 A**) demonstrate the shift in the

main peak feature observed for the THz pulse in the samples, in contrast to that observed for the bare substrate.⁵⁵ Similar experimental conditions are maintained for all the three excitation pump energies with carrier density $\sim 10^{18}$ photons/cm².

The photoconductivity ($\Delta\sigma(t_p)$) is directly proportionate to the transient deviation in electric field as derived from the equation:⁵⁶

$$\Delta\sigma(t_p) = \frac{\epsilon_0 c}{d} (n_a + n_b) \left[\frac{-\Delta(E(t_p))}{E_0(t_p)} \right] \quad \text{Eq.5.3}$$

Here, ΔE is the Fourier transform of photoinduced change in THz waveform and reference THz waveform, ϵ_0 is free space permittivity, c stands for the speed of light, d is the thickness of photoexcited samples, n_a and n_b are refractive indices of air and polystyrene respectively. Also, photoconductivity is proportionally associated to the effective mobility ($\varphi\mu$) as defined by the following equation:⁵⁷

$$\varphi = \frac{\Delta\sigma}{N_0 q} \quad \text{Eq.5.4}$$

Here, $\Delta\sigma$ is the change in photoconductivity, N_0 is the carrier density, q is the elementary charge and φ is conversion ratio of photon to free carrier. The obtained transient THz decay curves show that the amplitude of $\Delta E/E$ increases gradually upon increasing the pump energy **(Figure 5.8 B)**.

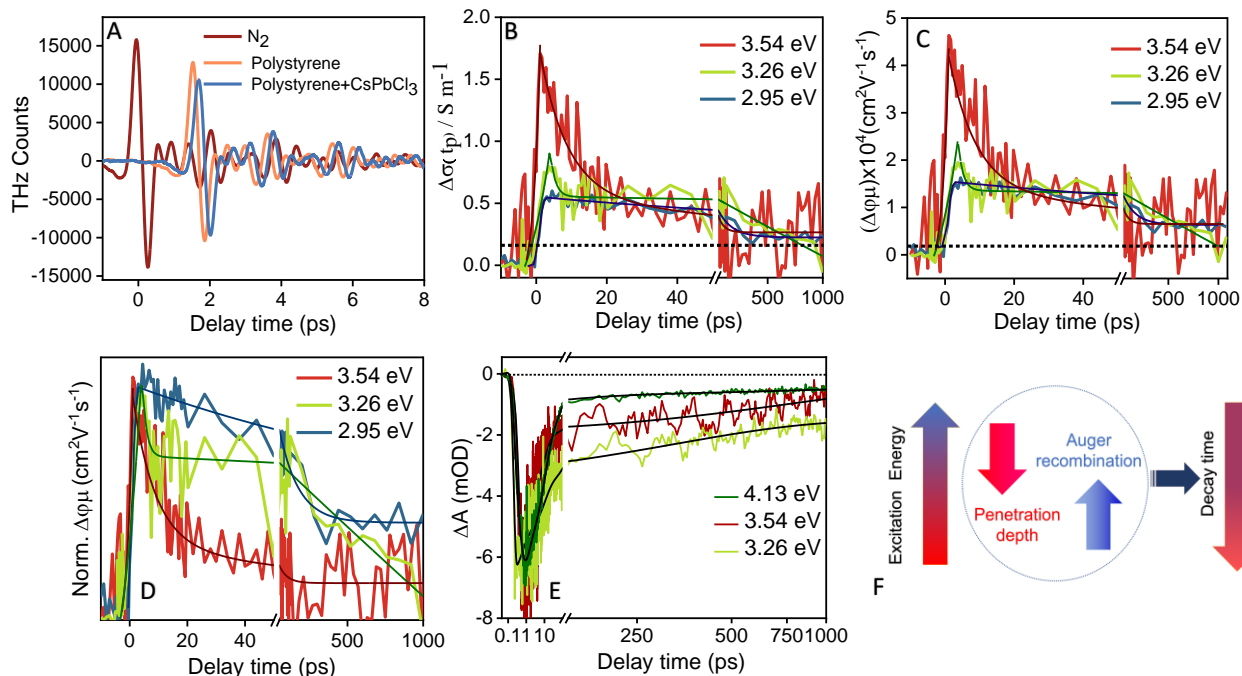


Figure 5.8 (A) The THz-TDS waveforms transmitted through the N₂, polystyrene (PS), and polystyrene CsPbCl₃ NCs (PS+ CsPbCl₃ NCs), (B) The THz transients of CsPbCl₃ NCs at 2.95, 3.26 and 3.54 eV pump excitation, (C) The time-dependent photoconductivity trace of CsPbCl₃ NCs at 2.95, 3.26 and 3.54 eV pump excitation, (D) Comparative normalized mobility trace versus pump-probe delay, (E) The transient excitonic bleach of CsPbCl₃ NCs at 3.26, 3.54, and 4.13 eV pump excitation, and (F) Schematic representation of the excitation energy dependent photophysical processes taking place in CsPbCl₃ NCs.

Furthermore, it is evident that the higher pump excitation energy leads to an increased amplitude of photoconductivity as well as mobility as both the parameters are directly proportional to $\Delta E/E$. The pump energy-dependent studies directly implicate the dependence of excitation energy with the mobility of carriers, which suggests that the carrier mobility increases with the increase in the excitation energy (**Figure 5.8 C**). The hot carriers are more mobile in contrast to the cold carriers, as the carriers are excited adjacent to band edge in case of 2.95 eV pump excitation. The excitation-dependent photoconductivity decay traces (**Figure 5.8 D**) are fitted exponentially (**Table 5.3**). The excitation dependent decay traces of photoconductivity (**Figure 5.8 D**) are fitted exponentially (**Table 5.3**). The decay traces (Figure 5.5D) are fitted exponentially using the following equation:⁵⁸

$$-\frac{\Delta E(t)}{E(t)} = A_1 \exp\left[-\frac{t}{\tau_1}\right] + A_2 \exp\left[-\frac{t}{\tau_2}\right] + A_3 \exp\left[-\frac{t}{\tau_3}\right] \quad \text{Eq.5.5}$$

The point worth asserting here is that the amplitude of fast component (τ_1) (**Table 5.3**) is found to be reduced as we decrease the excitation energy but the fast component remains almost same in both the 3.54 and 3.26 eV pump excitation. The amplitude of fast component reduces from -22% to merely -4% upon 3.54 eV and 2.95 eV pump excitation, respectively (**Table 5.3**), which clearly advocates that certain process is missing upon near band edge excitation. The fast component τ_1 is ascribed to the auger recombination process while the τ_2 and τ_3 are attributed to the carrier recombination processes.^{58,59}

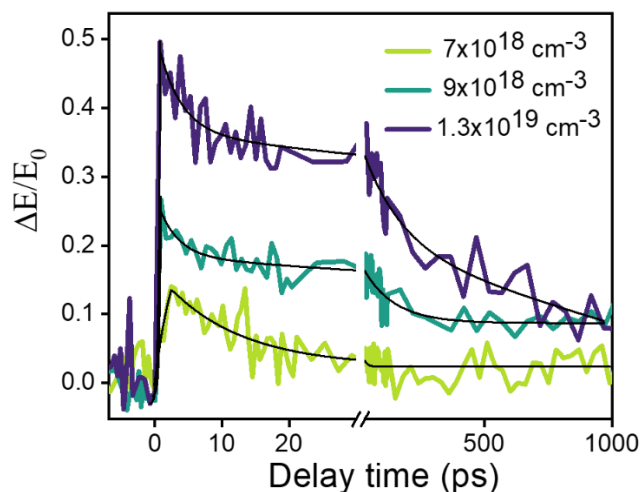


Figure 5.9 The temporal evolution of transient THz spectra at different carrier densities of CsPbCl_3 NCs.

Moreover, the slow component does not experience a dramatic variance with different pump excitation and exhibits almost constant behavior. The slower components (τ_2, τ_3) have the significant contribution of transfer process that takes place from the exciton to the nearby trap states.²⁴ Moreover, formerly slow rise in photoconductivity as well as mobility (**Figure 5. 8 C,D**) has been witnessed in perovskite structures upon near band edge excitation as the fast auger recombination process (τ_1) is completely missing out.^{24,60} Another plausible reason for the faster decay observed upon far band gap excitation could be the longer penetration depth of lower excitation energy than that of higher excitation energy.

Table 5.3 Kinetic fitting parameters upon fitting THz transient kinetics for CsPbCl₃ NCs for different pump excitation energy.

Excitation Energy (eV)	Growth	Recovery		
	τ_g	τ_1	τ_2	τ_3
3.54	655 fs	1.35 ps	58 ps	>1 ns
	(100 %)	(-22%)	(-54.9%)	(-20%)
3.26	820 fs	1.28 ps	51 ps	>1 ns
	(100 %)	(-18%)	(-66.3%)	(-15.7 %)
2.95	880 fs	1.85 ps	50 ps	>1 ns
	(100 %)	(-4.6%)	(-54.9%)	(-40.5%)

As the effective penetration depth can be estimated as $\lambda/4\pi n$ (n is refractive index), thus penetration depth is directly proportional to the excitation wavelength.^{61,62} Thus, the higher excitation pump pulse with shorter penetration depth led to a faster decay channel, thus advocating faster decay in the higher excitation energy.⁶³ To ascertain this, we conducted the TA measurements for 3.54 eV and 3.26 eV (**Figure 5.8 E**) and in the same trend we found that the bleach decay kinetics is faster in 3.54 eV in comparison to that of the excitation pump 3.26 eV. In order to lay more emphasis on the Auger process, intensity dependent THz OPTP measurements (**Figure 5.9**) have been performed. The fast time component assigned to auger recombination (**Table 5.4**) is reduced, while the amplitude of the fast component increases as the pump fluence increases. Cinquanta et al. also observed a fast component in a similar THz TDS of CsPbBr₃ NCs and attributed it to auger recombination processes in their earlier work.⁶⁴ Similar behavior in perovskites has been observed employing OPTP spectroscopy, and these investigations observed a faster response component (auger recombination) with increased pump fluences.^{49,64,65} Thus, it's fair to ascertain that the both absence of auger recombination process as well as higher penetration depth upon lower pump excitation governs the slower decay of mobility and photoconductivity upon near band gap excitation (**Figure 5.8 F**).

Table 5.4 Kinetic fitting parameters upon fitting THz transient kinetics for CsPbCl₃ NCs for different carrier density (fluence).

Carrier density	Growth	Recovery		
	τ_g	τ_1	τ_2	τ_3
1.3x10¹⁹ cm⁻³	190 fs	1.05 ps	80 ps	>1 ns
	(100 %)	(-26%)	(-56%)	(-18%)
9x10¹⁸ cm⁻³	210 fs	1.20 ps	79 ps	>1 ns
	(100 %)	(-25.5%)	(-36.3%)	(-38.2%)
7x10¹⁸ cm⁻³	655 fs	1.35 ps	58 ps	>1 ns
	(100 %)	(-22%)	(-54.9%)	(-23.1%)

5.3. Conclusion

In summary, we have successfully introspected the optical properties of CsPbCl₃ NCs with the help of low-temperature ultrafast TA and OPTP spectroscopy. The detailed analysis of low-temperature PL evidently advocates the presence of multiple peaks upon lowering the lattice temperature. Apart from this, the PL intensity was found to increase at low temperature due to diminishing thermal perturbations. Furthermore, carrier relaxation, carrier temperature, and energy loss show a direct dependence on phase transition. The excitation energy-dependent THz -OPTP measurements show that the initial mobility decay slows down as the excitation energy decreases and is attributed to the radical decrease in the Auger recombination and increased penetration depth. The spectroscopic investigation enables us to understand the temperature dependent behavior of carriers across the orthorhombic to monoclinic phase transition, as during the operation of photovoltaic devices in the field they have to undergo through various temperatures. These excitation energy and temperature dependent relaxation processes would give important direction for high-end optoelectronic devices based on CsPbCl₃ NCs perovskite. These excitation energy and temperature dependent relaxation processes would can provide an important direction for developing high-end optoelectronic devices based on CsPbCl₃ perovskite NCs.

5.4. References

- (1) Li, J.; Luo, L.; Huang, H.; Ma, C.; Ye, Z.; Zeng, J.; He, H. 2D Behaviors of Excitons in Cesium Lead Halide Perovskite Nanoplatelets. *J. Phys. Chem. Lett.* **2017**, *8* (6), 1161–1168.
- (2) He, T.; Li, J.; Qiu, X.; Xiao, S.; Yin, C.; Lin, X. Highly Enhanced Normalized-Volume Multiphoton Absorption in CsPbBr₃ 2D Nanoplates. *Adv. Opt. Mater.* **2018**, *6* (21), 2–8.
- (3) Li, Q.; Liu, Y.; Chen, P.; Hou, J.; Sun, Y.; Zhao, G.; Zhang, N.; Zou, J.; Xu, J.; Fang, Y.; Dai, N. Excitonic Luminescence Engineering in Tervalent-Europium-Doped Cesium Lead Halide Perovskite Nanocrystals and Their Temperature-Dependent Energy Transfer Emission Properties. *J. Phys. Chem. C* **2018**, *122* (50), 29044–29050.
- (4) Lohar, A. A.; Shinde, A.; Gahlaut, R.; Sagdeo, A.; Mahamuni, S. Enhanced Photoluminescence and Stimulated Emission in CsPbCl₃ Nanocrystals at Low Temperature. *J. Phys. Chem. C* **2018**, *122* (43), 25014–25020.
- (5) George, J.; Joseph, A. P.; Balachandran, M. Perovskites: Emergence of Highly Efficient Third-Generation Solar Cells. *Int. J. Energy Res.* **2022**, *46* (15), 21856–21883.
- (6) National Renewable Energy Laboratory, <https://www.nrel.gov/pv/assets/pdfs/best-research-cell-efficiencies-rev220630.pdf>. 2020.
- (7) Zhang, Z.; Li, Z.; Meng, L.; Lien, S.-Y.; Gao, P. Perovskite-Based Tandem Solar Cells: Get the Most Out of the Sun. *Adv. Funct. Mater.* **2020**, *30* (38), 2001904.
- (8) Kim, M.; Jeong, J.; Lu, H.; Lee, T. K.; Eickemeyer, F. T.; Liu, Y.; Choi, I. W.; Choi, S. J.; Jo, Y.; Kim, H.-B.; Mo, S.-I.; Kim, Y.-K.; Lee, H.; An, N. G.; Cho, S.; Tress, W. R.; Zakeeruddin, S. M.; Hagfeldt, A.; Kim, J. Y.; Grätzel, M.; Kim, D. S. Conformal Quantum Dot-SnO₂ Layers as Electron Transporters for Efficient Perovskite Solar Cells. *Science* **2022**, *375* (6578), 302–306.
- (9) Li, R.; Chen, B.; Ren, N.; Wang, P.; Shi, B.; Xu, Q.; Zhao, H.; Han, W.; Zhu, Z.; Liu, J.; Huang, Q.; Zhang, D.; Zhao, Y.; Zhang, X. CsPbCl₃-Cluster-Widened Bandgap and Inhibited Phase Segregation in a Wide-Bandgap Perovskite and Its Application to NiOx -Based Perovskite/Silicon Tandem Solar Cells. *Adv. Mater.* **2022**, *34* (27), e2201451.
- (10) Cheng, Y.; Shen, C.; Shen, L.; Xiang, W.; Liang, X. Tb³⁺, Eu³⁺ Co-Doped CsPbBr₃ QDs Glass with Highly Stable and Luminous Adjustable for White LEDs. *ACS Appl. Mater. Interfaces* **2018**, *10* (25), 21434–21444.
- (11) Shukla, A.; Kaur, G.; Babu, K. J.; Kaur, A.; Yadav, D. K.; Ghosh, H. N. Defect-Interceded Cascading Energy Transfer and Underlying Charge Transfer in Europium-Doped CsPbCl₃ Nanocrystals. *J. Phys. Chem. Lett.* **2022**, *13* (1), 83–90.
- (12) Zhang, C.; Wan, Q.; Ono, L. K.; Liu, Y.; Zheng, W.; Zhang, Q.; Liu, M.; Kong, L.; Li, L.; Qi,

- Y. Narrow-Band Violet-Light-Emitting Diodes Based on Stable Cesium Lead Chloride Perovskite Nanocrystals. *ACS Energy Lett.* **2021**, *6* (10), 3545–3554.
- (13) Gong, M.; Sakidja, R.; Goul, R.; Ewing, D.; Casper, M.; Stramel, A.; Elliot, A.; Wu, J. Z. High-Performance All-Inorganic CsPbCl₃ Perovskite Nanocrystal Photodetectors with Superior Stability. *ACS Nano* **2019**, *13* (2), 1772–1783.
- (14) Yu, C.; Chen, Z.; J. Wang, J.; Pfenninger, W.; Vockic, N.; Kenney, J. T.; Shum, K. Temperature Dependence of the Band Gap of Perovskite Semiconductor Compound CsSnI₃. *J. Appl. Phys.* **2011**, *110* (6), 63526.
- (15) Diroll, B. T. Temperature-Dependent Intraband Relaxation of Hybrid Perovskites. *J. Phys. Chem. Lett.* **2019**, *10* (18), 5623–5628.
- (16) Cohen, M. I.; Young, K. F.; Chang, T.; Brower, W. S. Phase Transitions in CsPbCl₃. *J. Appl. Phys.* **1971**, *42* (13), 5267–5272.
- (17) Hirotsu, S. Experimental Studies of Structural Phase Transitions in CsPbCl₃. *J. Phys. Soc. Japan* **1971**, *31* (2), 552–560.
- (18) Diroll, B. T.; Zhou, H.; Schaller, R. D. Low-Temperature Absorption, Photoluminescence, and Lifetime of CsPbX₃ (X = Cl, Br, I) Nanocrystals. *Adv. Funct. Mater.* **2018**, *28* (30), 1–7.
- (19) Fujii, Y.; Hoshino, S.; Yamada, Y.; Shirane, G. Neutron-Scattering Study on Phase Transitions of CsPbCl₃. *Phys. Rev. B* **1974**, *9* (10), 4549–4559.
- (20) Ahumada-Lazo, R.; Alanis, J. A.; Parkinson, P.; Binks, D. J.; Hardman, S. J. O.; Griffiths, J. T.; Wisnivesky Rocca Rivarola, F.; Humphrey, C. J.; Ducati, C.; Davis, N. J. L. K. Emission Properties and Ultrafast Carrier Dynamics of CsPbCl₃ Perovskite Nanocrystals. *J. Phys. Chem. C* **2019**, *123* (4), 2651–2657.
- (21) De, A.; Mondal, N.; Samanta, A. Luminescence Tuning and Exciton Dynamics of Mn-Doped CsPbCl₃ Nanocrystals. *Nanoscale* **2017**, *9* (43), 16722–16727.
- (22) Paul, S.; Ahmed, T.; Das, S.; Samanta, A. Effect of Lead:Halide Precursor Ratio on the Photoluminescence and Carrier Dynamics of Violet- and Blue-Emitting Lead Halide Perovskite Nanocrystals. *J. Phys. Chem. C* **2021**, *125* (42), 23539–23547.
- (23) Protesescu, L.; Yakunin, S.; Bodnarchuk, M. I.; Krieg, F.; Caputo, R.; Hendon, C. H.; Yang, R. X.; Walsh, A.; Kovalenko, M. V. Nanocrystals of Cesium Lead Halide Perovskites (CsPbX₃, X = Cl, Br, and I): Novel Optoelectronic Materials Showing Bright Emission with Wide Color Gamut. *Nano Lett.* **2015**, *15* (6), 3692–3696.
- (24) Kaur, G.; Babu, K. J.; Ghosh, H. N. Temperature-Dependent Interplay of Polaron Formation and Hot Carrier Cooling Dynamics in CsPbBr₃ Nanocrystals: Role of Carrier–Phonon Coupling Strength. *J. Phys. Chem. Lett.* **2020**, *11* (15), 6206–6213.

- (25) Sebastian, M.; Peters, J. A.; Stoumpos, C. C.; Im, J.; Kostina, S. S.; Liu, Z.; Kanatzidis, M. G.; Freeman, A. J.; Wessels, B. W. Excitonic Emissions and Above-Band-Gap Luminescence in the Single-Crystal Perovskite Semiconductors CsPbBr₃ and CsPbCl₃. *Phys. Rev. B - Condens. Matter Mater. Phys.* **2015**, *92* (23), 1–9.
- (26) Ahmed, G. H.; Yin, J.; Bakr, O. M.; Mohammed, O. F. Near-Unity Photoluminescence Quantum Yield in Inorganic Perovskite Nanocrystals by Metal-Ion Doping. *J. Chem. Phys.* **2020**, *152* (2), 20902.
- (27) Peters, J. A.; Liu, Z.; De Siena, M. C.; Kanatzidis, M. G.; Wessels, B. W. Photoluminescence Spectroscopy of Excitonic Emission in CsPbCl₃ Perovskite Single Crystals. *J. Lumin.* **2022**, *243*, 118661.
- (28) Sarkar, S.; Saha, S.; Motapothula, M. R.; Patra, A.; Cao, B.-C.; Prakash, S.; Cong, C. X.; Mathew, S.; Ghosh, S.; Yu, T.; Venkatesan, T. Magneto-Optical Study of Defect Induced Sharp Photoluminescence in LaAlO₃ and SrTiO₃. *Sci. Rep.* **2016**, *6* (1), 33145.
- (29) Liu, Y.; Lu, H.; Niu, J.; Zhang, H.; Lou, S.; Gao, C.; Zhan, Y.; Zhang, X.; Jin, Q.; Zheng, L. Temperature-Dependent Photoluminescence Spectra and Decay Dynamics of MAPbBr₃ and MAPbI₃ Thin Films. *AIP Adv.* **2018**, *8* (9), 95108.
- (30) Yi, J.; Ge, X.; Liu, E.; Cai, T.; Zhao, C.; Wen, S.; Sanabria, H.; Chen, O.; Rao, A. M.; Gao, J. The Correlation between Phase Transition and Photoluminescence Properties of CsPbX₃ (X = Cl, Br, I) Perovskite Nanocrystals. *Nanoscale Adv.* **2020**, *2* (10), 4390–4394.
- (31) Justice Babu, K.; Kaur, G.; Shukla, A.; Saha, R.; Kaur, A.; Sachdeva, M.; Yadav, D. K.; Ghosh, H. N. Fast Polaron Formation and Low Carrier Mobility in Defect-Free Polyhedral CsPbBr₃ Perovskite Nanocrystals. *ACS Photonics* **2022**, *9*(3), 969-978.
- (32) Shukla, A.; Kaur, G.; Justice Babu, K.; Ghorai, N.; Goswami, T.; Kaur, A.; N. Ghosh, H. Effect of Confinement on the Exciton and Biexciton Dynamics in Perovskite 2D-Nanosheets and 3D-Nanocrystals. *J. Phys. Chem. Lett.* **2020**, *11* (15), 6344–6352.
- (33) D’Innocenzo, V.; Grancini, G.; Alcocer, M. J. P.; Kandada, A. R. S.; Stranks, S. D.; Lee, M. M.; Lanzani, G.; Snaith, H. J.; Petrozza, A. Excitons versus Free Charges in Organo-Lead Tri-Halide Perovskites. *Nat. Commun.* **2014**, *5* (1), 3586
- (34) Carabatos-Nédelec, C.; Oussaïd, M.; Nitsch, K. Raman Scattering Investigation of Cesium Plumbochloride, CsPbCl₃, Phase Transitions. *J. Raman Spectrosc.* **2003**, *34* (5), 388–393.
- (35) Hidaka, M.; Okamoto, Y.; Zikumaru, Y. Structural Phase Transition of CsPbCl₃ below Room Temperature. *Phys. status solidi* **1983**, *79* (1), 263–269.
- (36) Strait, J. H.; Wang, H.; Shivaraman, S.; Shields, V.; Spencer, M.; Rana, F. Very Slow Cooling Dynamics of Photoexcited Carriers in Graphene Observed by Optical-Pump Terahertz-Probe

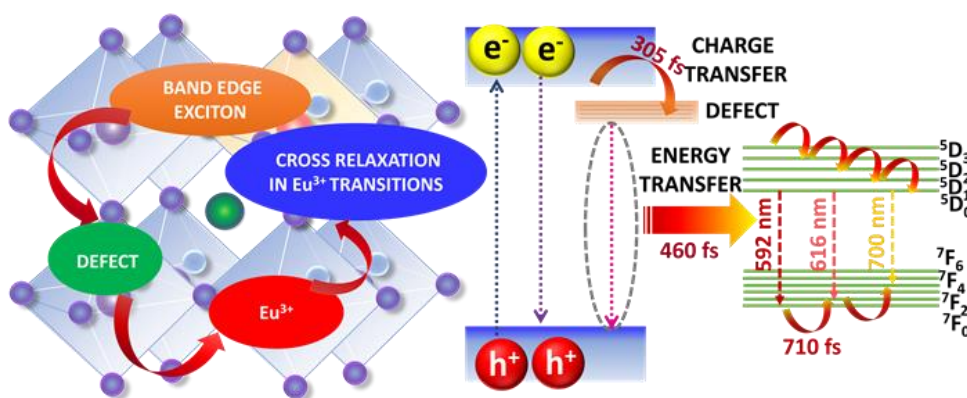
- Spectroscopy. *Nano Lett.* **2011**, *11* (11), 4902–4906.
- (37) Pinchetti, V.; Anand, A.; Akkerman, Q. A.; Sciacca, D.; Lorenzon, M.; Meinardi, F.; Fanciulli, M.; Manna, L.; Brovelli, S. Trap-Mediated Two-Step Sensitization of Manganese Dopants in Perovskite Nanocrystals. *ACS Energy Lett.* **2019**, *4* (1), 85–93.
- (38) Even, J.; Carignano, M.; Katan, C. Molecular Disorder and Translation/Rotation Coupling in the Plastic Crystal Phase of Hybrid Perovskites. *Nanoscale* **2016**, *8* (12), 6222–6236.
- (39) Songvilay, M.; Bari, M.; Ye, Z. G.; Xu, G.; Gehring, P. M.; Ratcliff, W. D.; Schmalzl, K.; Bourdarot, F.; Roessli, B.; Stock, C. Lifetime-Shortened Acoustic Phonons and Static Order at the Brillouin Zone Boundary in the Organic-Inorganic Perovskite $\text{CH}_3\text{NH}_3\text{PbCl}_3$. *Phys. Rev. Mater.* **2018**, *2* (12), 1–8.
- (40) Sadhukhan, P.; Pradhan, A.; Mukherjee, S.; Sengupta, P.; Roy, A.; Bhunia, S.; Das, S. Low Temperature Excitonic Spectroscopy Study of Mechano-Synthesized Hybrid Perovskite. *Appl. Phys. Lett.* **2019**, *114* (13).
- (41) Fu, M.; Tamarat, P.; Trebbia, J. B.; Bodnarchuk, M. I.; Kovalenko, M. V.; Even, J.; Lounis, B. Unraveling Exciton–Phonon Coupling in Individual FAPbI_3 Nanocrystals Emitting near-Infrared Single Photons. *Nat. Commun.* **2018**, *9* (1), 3318.
- (42) Yumoto, G.; Tahara, H.; Kawawaki, T.; Saruyama, M.; Sato, R.; Teranishi, T.; Kanemitsu, Y. Hot Biexciton Effect on Optical Gain in CsPbI_3 Perovskite Nanocrystals. *J. Phys. Chem. Lett.* **2018**, *9* (9), 2222–2228.
- (43) Yu, J.; Sharma, M.; Li, M.; Hernández-Martínez, P. L.; Delikanli, S.; Sharma, A.; Altintas, Y.; Hettiarachchi, C.; Sum, T.; Demir, H. V.; Dang, C. Sustained Biexciton Emission in Colloidal Quantum Wells Assisted by Dopant-Host Interaction. *arXiv* **2019**, 1–11.
- (44) Upadhyay, B.; Thakur, D.; Pramanick, B.; Bhandari, S.; Balakrishnan, V.; Pal, S. K. Anomalous Emission Behavior of Excitons at Low Temperature in Monolayer WS_2 . *J. Phys. D: Appl. Phys.* **2022**, *55* (23), 235105.
- (45) You, Y.; Zhang, X.-X.; Berkelbach, T. C.; Hybertsen, M. S.; Reichman, D. R.; Heinz, T. F. Observation of Biexcitons in Monolayer WSe_2 . *Nat. Phys.* **2015**, *11* (6), 477–481.
- (46) He, Z.; Xu, W.; Zhou, Y.; Wang, X.; Sheng, Y.; Rong, Y.; Guo, S.; Zhang, J.; Smith, J. M.; Warner, J. H. Biexciton Formation in Bilayer Tungsten Disulfide. *ACS Nano* **2016**, *10* (2), 2176–2183.
- (47) Wang, T.; Jin, L.; Hidalgo, J.; Chu, W.; Snaider, J. M.; Deng, S.; Zhu, T.; Lai, B.; Prezhdo, O.; Correa-Baena, J.-P.; Huang, L. Protecting Hot Carriers by Tuning Hybrid Perovskite Structures with Alkali Cations. *Sci. Adv.* **2023**, *6* (43), eabb1336.
- (48) Li, M.; Fu, J.; Xu, Q.; Sum, T. C. Slow Hot-Carrier Cooling in Halide Perovskites: Prospects

- for Hot-Carrier Solar Cells. *Adv. Mater.* **2019**, *31* (47), 1802486.
- (49) Li, Z. H.; He, J. X.; Lv, X. H.; Chi, L. F.; Egbo, K. O.; Li, M.-D.; Tanaka, T.; Guo, Q. X.; Yu, K. M.; Liu, C. P. Optoelectronic Properties and Ultrafast Carrier Dynamics of Copper Iodide Thin Films. *Nat. Commun.* **2022**, *13* (1), 6346.
- (50) Fu, J.; Xu, Q.; Han, G.; Wu, B.; Huan, C. H. A.; Leek, M. L.; Sum, T. C. Hot Carrier Cooling Mechanisms in Halide Perovskites. *Nat. Commun.* **2017**, *8* (1), 1300.
- (51) Kaur, G.; Ghosh, H. N. Hot Carrier Relaxation in CsPbBr₃-Based Perovskites: A Polaron Perspective. *J. Phys. Chem. Lett.* **2020**, *11* (20), 8765–8776.
- (52) Němec, P.; Malý, P. Temperature Dependence of Coherent Phonon Dephasing in CsPbCl₃Nanocrystals. *Phys. Rev. B - Condens. Matter Mater. Phys.* **2005**, *72* (23), 1–6.
- (53) Ghebouli, M. A.; Ghebouli, B.; Fatmi, M. First-Principles Calculations on Structural, Elastic, Electronic, Optical and Thermal Properties of CsPbCl₃ Perovskite. *Phys. B Condens. Matter* **2011**, *406* (9), 1837–1843.
- (54) Wei, Q.; Yin, J.; Bakr, O. M.; Wang, Z.; Wang, C.; Mohammed, O. F.; Li, M.; Xing, G. Effect of Zinc-Doping on the Reduction of the Hot-Carrier Cooling Rate in Halide Perovskites. *Angew. Chem. Int. Ed.* **2021**, *60* (19), 10957–10963.
- (55) Yang, D.; Cheng, X.; Liu, Y.; Shen, C.; Xu, Z.; Zheng, X.; Jiang, T. Dielectric Properties of a CsPbBr₃ Quantum Dot Solution in the Terahertz Region. *Appl. Opt.* **2017**, *56* (10), 2878–2885.
- (56) Sarkar, S.; Ravi, V. K.; Banerjee, S.; Yettapu, G. R.; Markad, G. B.; Nag, A.; Mandal, P. Terahertz Spectroscopic Probe of Hot Electron and Hole Transfer from Colloidal CsPbBr₃ Perovskite Nanocrystals. *Nano Lett.* **2017**, *17* (9), 5402–5407.
- (57) Yettapu, G. R.; Talukdar, D.; Sarkar, S.; Swarnkar, A.; Nag, A.; Ghosh, P.; Mandal, P. Terahertz Conductivity within Colloidal CsPbBr₃ Perovskite Nanocrystals: Remarkably High Carrier Mobilities and Large Diffusion Lengths. *Nano Lett.* **2016**, *16* (8), 4838–4848.
- (58) Qin, Z.; Zhang, C.; Chen, L.; Wang, X.; Xiao, M. Charge Carrier Dynamics in Sn-Doped Two-Dimensional Lead Halide Perovskites Studied by Terahertz Spectroscopy. *Front. Energy Res.* **2021**, *9*, 658270.
- (59) Okochi, H.; Katsuki, H.; Tsubouchi, M.; Itakura, R.; Yanagi, H. Photon Energy-Dependent Ultrafast Photoinduced Terahertz Response in a Microcrystalline Film of CH₃NH₃PbBr₃. *J. Phys. Chem. Lett.* **2020**, *11* (15), 6068–6076.
- (60) Zhang, H.; Debroye, E.; Zheng, W.; Fu, S.; Virgilio, L. D.; Kumar, P.; Bonn, M.; Wang, H. I. Highly Mobile Hot Holes in Cs₂AgBiBr₆ Double Perovskite. *Sci. Adv.* **2021**, *7* (52), eabj9066.
- (61) Yang, Y.; Yan, Y.; Yang, M.; Choi, S.; Zhu, K.; Luther, J. M.; Beard, M. C. Low Surface Recombination Velocity in Solution-Grown CH₃NH₃PbBr₃ Perovskite Single Crystal. *Nat.*

- Commun.* **2015**, 6 (1), 7961.
- (62) Sabbah, A. J.; Riffe, D. M. Femtosecond Pump-Probe Reflectivity Study of Silicon Carrier Dynamics. *Phys. Rev. B* **2002**, 66 (16), 165217.
- (63) Yan, H.; An, B.; Fan, Z.; Zhu, X.; Lin, X.; Jin, Z.; Ma, G. Ultrafast Terahertz Probe of Photoexcited Free Charge Carriers in Organometal $\text{CH}_3\text{NH}_3\text{PbBr}_3$ Perovskite Thin Film. *Appl. Phys. A* **2016**, 122 (4), 414.
- (64) Cinquanta, E.; Meggiolaro, D.; Motti, S. G.; Gandini, M.; Alcocer, M. J. P.; Akkerman, Q. A.; Vozzi, C.; Manna, L.; De Angelis, F.; Petrozza, A.; Stagira, S. Ultrafast THz Probe of Photoinduced Polarons in Lead-Halide Perovskites. *Phys. Rev. Lett.* **2019**, 122 (16), 166601.
- (65) Piatkowski, P.; Cohen, B.; Kazim, S.; Ahmad, S.; Douhal, A. How Photon Pump Fluence Changes the Charge Carrier Relaxation Mechanism in an Organic-Inorganic Hybrid Lead Triiodide Perovskite. *Phys. Chem. Chem. Phys.* **2016**, 18 (39), 27090–27101.

Chapter 6

Defect interceded Cascading Energy Transfer and Underlying Charge Transfer in Europium Doped CsPbCl₃ Nanocrystals



Rare earth ion (RE^{3+}) doping in cesium lead chloride ($CsPbCl_3$) has unlocked novel prospects to explore changes in optical, magnetic, and charge carrier transport properties. This leads to huge advancement in optoelectronic applications yet deep understanding of photo physics governing the energy transfer processes is lacking and demands vital attention. Herein, we probe into the mechanistic transfer processes from the band edge of host ($CsPbCl_3$) to dopant Europium ion (Eu^{3+}) with the aid of femtosecond fluorescence upconversion and transient absorption (TA) spectroscopy. The upconversion measurement portrays defect mediated cascading energy transfer from $CsPbCl_3$ to Eu^{3+} and further cross-relaxation among Eu^{3+} states. Moreover, TA studies reveal that there is charge transfer from the band edge of $CsPbCl_3$ to doping induced shallow defect state. Furthermore, two photon absorption (TPA) study establishes no compromise in the transfer mechanism even upon bandgap excitation. This work validates that $Eu-CsPbCl_3$ is an apt entrant for optoelectronic applications.

6.1. Introduction

Semiconductor NCs doped with transition metal ions have engrossed great consideration for their unique optical, electronic, and magnetic properties.¹⁻⁶ Commonly, lanthanide ions act as optically active centers with energy levels within the host bandgap, thus resulting in increased Photoluminescence (PL) transitions at relatively lower energies than the host.^{1,7-9} It is significantly observed that doping of RE³⁺ in conventional hosts such as Gallium Nitride (GaN) have stabilization issues associated with mismatch of the ionic size of RE³⁺ with ions to be substituted i.e., Ga, Al, Y creating strain in the lattice.^{2,10} Conversely, perovskites prove to be excellent hosts for RE doping since the ionic radii of Pb²⁺ (lead ion) and Eu³⁺ (Europium ion) match closely creating relatively less strain in the perovskite lattice.^{11,12} The Eu³⁺ transitions lead to new relaxation pathways, millisecond PL lifetime due to their spin forbidden nature, and higher stoke shift reduces the reabsorption losses which help in improvising the optoelectronic device performance.¹³⁻¹⁵

Plentiful reports have pointed out that doping NCs with Manganese (Mn), Eu and Ytterbium (Yb) gives broader PL thus, leading to better performance of the optoelectronic devices.^{3,16-19} Previously, Wang and coworkers successfully observed white light emission as a result of coupling among self-trapped exciton, free excitons as well as Mn²⁺ emission (⁴T₁-⁶A₁ transition).²⁰ Also, the impurity ion doping in the crystal has given new avenues to the field of perovskite as it enables to tune the emission color and PLQY upon varying the doping concentration.^{21,22} As a consequence of energy transfer from the exciton to the dopant, spin-polarized ⁵D₀-⁷F_J emissions of Eu³⁺ were noticeable.^{14,23-25} Moreover, doping impurity ions often leads to incorporation of defects as a consequence of non-compensation of charges (replacing Pb²⁺ by Eu³⁺) creating charge imbalance in the system.^{26,27} Recent reports have come up with trap mediated exciton to dopant energy transfer in doped perovskites.^{18,28-30} Nevertheless, still the energy transfer mechanism from host (CsPbCl₃) to dopant (Eu³⁺) is open for discussion as there is no comprehensive report with a detailed mechanistic illustration of such defect mediated energy transfer from CsPbCl₃ to Eu³⁺ and further transfer process occurring within the Eu³⁺ levels. Additionally, it is well-accepted fact that the profound insights of carrier cooling, energy/charge transfer, exciton/biexciton dynamics are vital to enhance the photovoltaic performance.³¹⁻³⁵

In this report, we have primarily focused to unravel the underlying transfer mechanisms affecting the charge carrier dynamics after doping of Eu^{3+} in CsPbCl_3 through the fluorescence upconversion and femtosecond TA spectroscopy. To further extend the understanding of energy transfer upon exciting the samples with energy lower than the bandgap TPA studies are explored. It is concluded that the energy transfer is not at all negotiated even at very low excitation energy. TPA provides a unique opportunity to utilize the greater portion of the solar spectrum which remains unused otherwise. Through combined spectroscopic analysis, the transfer mechanism of the observed Eu^{3+} emission has been proposed, which indicates that the energy transfer process from CsPbCl_3 to Eu^{3+} levels is stepwise, mediated through defect states, and has been discussed in detail.

6.2. Results and discussion

6.2.1. Structural and morphological studies of CsPbCl_3 and Eu-CsPbCl_3

The synthesis of both CsPbCl_3 and Eu-CsPbCl_3 NCs was conducted following the reported literature with minor modifications and is detailed in Chapter 2.¹ Structural and morphological characterizations (**Figure 6.1**) suggest that the properties of CsPbCl_3 NCs have been successfully engineered after introduction of Eu^{3+} within CsPbCl_3 lattice.

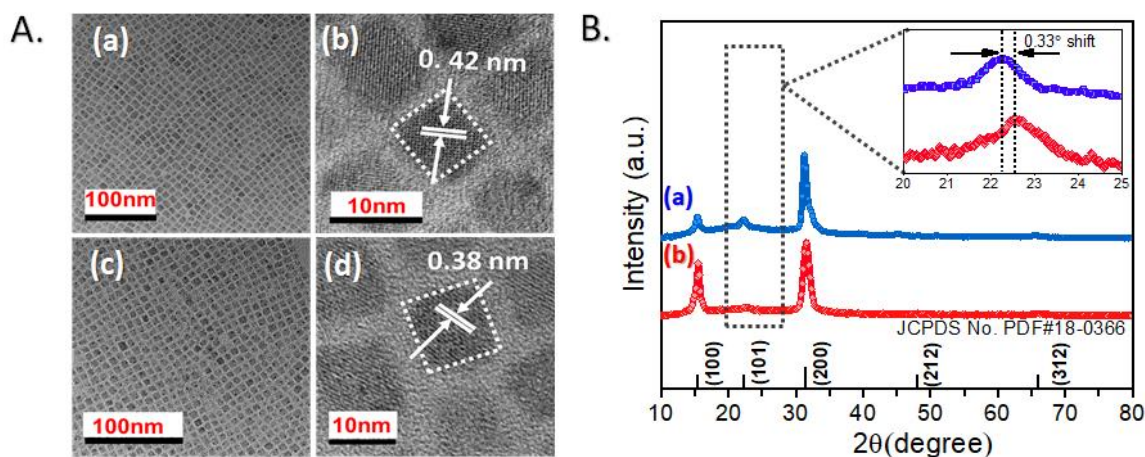


Figure 6.1 (A) TEM and HR-TEM images of (a, b) CsPbCl_3 NCs, (c, d) Eu-CsPbCl_3 NCs; (B) XRD pattern of (a) CsPbCl_3 NCs, and (b) Eu-CsPbCl_3 NCs; **Inset:** shows the enlarged comparative XRD pattern of (101) plane.

Figure 6.1 A illustrates the transmission electron microscopy TEM and HR-TEM images of CsPbCl₃ NCs and Eu-CsPbCl₃ NCs (Eu³⁺ doped). The TEM images clearly depict the uniformity of as prepared CsPbCl₃ and Eu-CsPbCl₃ NCs and also illustrates that the cubic structure of the NCs is maintained even after doping. The calculated interplanar distance (spacing) of CsPbCl₃ and Eu-CsPbCl₃ is found to be 0.42 and 0.38 nm, respectively. **Figure 6.1 B** shows the X-ray diffraction (XRD) pattern of CsPbCl₃ and Eu-CsPbCl₃. Both the XRD patterns maintained cubic phase and the planes were exactly matched with the standard JCPDS No. PDF#18-0366. Remarkably, the diffraction angle i.e., two theta values corresponding to the (101) plane of Eu-CsPbCl₃ NCs shifts 0.33° towards the higher angle in comparison to the pristine CsPbCl₃ as a consequence of the lattice contraction.^{1,5} This shift is because of the ionic radius of Eu³⁺ (0.95 Å) which is smaller in comparison to the ionic radius of Pb²⁺ (six-coordinate effective radii of 1.33 Å) results in the shrinking of the NC lattice.^{6,7} From the combined analysis of HR-TEM and XRD, it can thus be certified that Eu³⁺ is successfully doped in the CsPbCl₃ lattice.

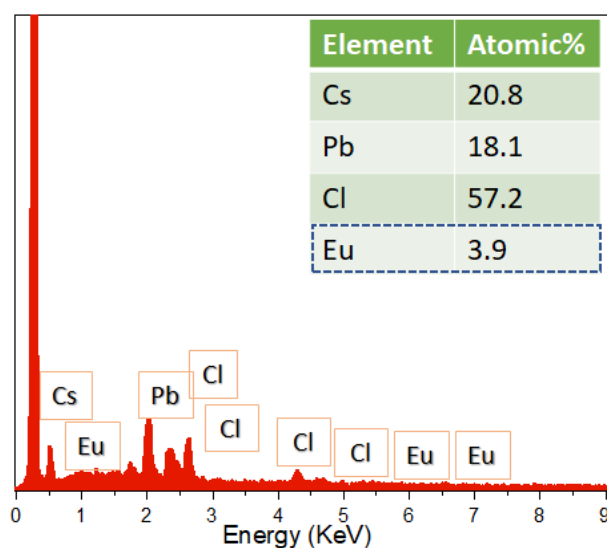


Figure 6.2 The Energy dispersive spectra for Eu-CsPbCl₃ NCs; inset table shows different atomic percent of elements.

The Elemental analysis verifies the presence of Eu in as synthesized Eu-CsPbCl₃ NCs with the 3.9% atomic percentage (**Figure 6.2**). This atomic percentage is with reference to all elements present within the NC. However, the percentage of Eu replaced with respect to Pb is 17.7 %

by EDS measurement. The EDS analysis verifies 3.9 % atomic percentage of Eu in as synthesized Eu-CsPbCl₃ NCs (**Figure 6.2**).

6.2.2. Optical Studies of CsPbCl₃ and Eu-CsPbCl₃

The band-edge absorption of CsPbCl₃ appears at 398 nm (**Figure 6.3 A**) while the peak of Eu-CsPbCl₃ appears at 401 nm.

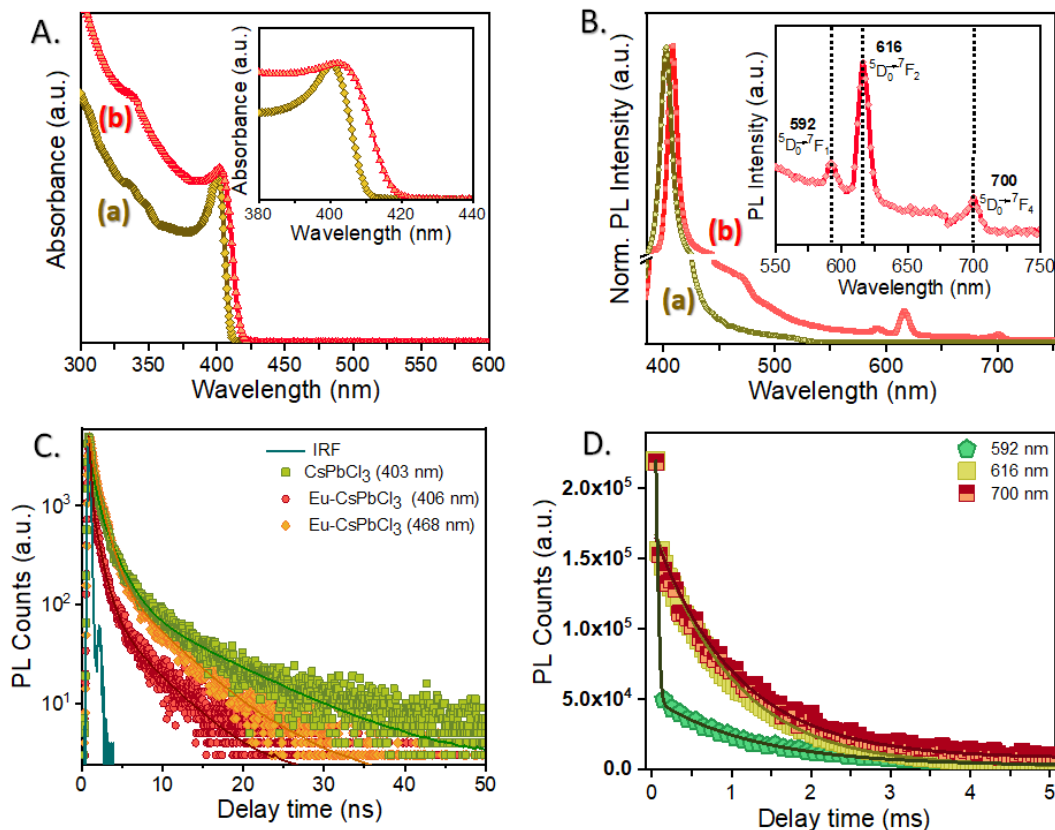


Figure 6.3 (A) The comparative absorption spectra for both (a) CsPbCl₃ and (b) Eu-CsPbCl₃ NCs; Inset: shows the enlarged absorbance near band edge; (B) The comparative PL spectra of both (a) CsPbCl₃ and (b) Eu-CsPbCl₃ NCs; Inset: illustrates the PL transitions of Eu³⁺. (C) TRPL decay traces of CsPbCl₃ (403 nm), Eu-CsPbCl₃ (406 nm), and Eu-CsPbCl₃ (468 nm) after exciting at 375 nm and (D) PL decay traces of Eu-CsPbCl₃ NCs monitoring Eu³⁺ D-F emissions at 592 nm (⁵D₀-⁷F₁), 616 nm (⁵D₀-⁷F₂) and 700 nm (⁵D₀-⁷F₄) after exciting the sample at 375 nm. Interestingly, PL lifetime of Eu transition peaking at 592 nm which is MD transition is much lower in comparison to the 616 and 700 nm (both are ED transitions).

Here, the slight red shifting in the excitonic band edge observed in Eu-CsPbCl₃ in contrast to CsPbCl₃ is due to the mild alteration of the electronic structure of CsPbCl₃ upon doping.³⁶ Moreover, the additional broad absorption in the Eu-CsPbCl₃ towards the higher wavelength region (shown in the inset of **Figure 6.3 A**) can be attributed to the introduction of defects into the system which will be detailed in later section. The PL spectrum of CsPbCl₃ exhibits the band edge emission at 403 nm (**Figure 6.3 Ba**). The asymmetric PL in CsPbCl₃ has been attributed to the bound excitons due to higher lying defects in CsPbCl₃ as compared to CsPbBr₃ which are prominently observable at low temperatures.³⁷ However, in case of Eu-CsPbCl₃ NCs, apart from band edge emission peaking at 406 nm a broad hump appears at 468 nm (**Figure 6.3 Bb**) with few additional peaks at 592, 616, and 700 nm. Moreover, the PLQY shows two-fold increment (~23 %) in the case of Eu-CsPbCl₃ NCs in contrast to that of the pristine CsPbCl₃ NCs (~12 %). These peaks are attributed to the ⁵D₀-⁷F_J transitions of Eu³⁺. Although there are a total of seven possible (⁵D₀-⁷F₀₋₆) transitions in Eu³⁺, yet only three transitions corresponding to ⁵D₀-⁷F₁(592 nm), ⁵D₀-⁷F₂ (616 nm), ⁵D₀-⁷F₄ (700 nm) are discernible in the emission spectra.^{23,38} This is due to non-compliance of the other transitions with angular momentum based selection rule. The selection rules allow observation of only those transitions for which $|\Delta J| = 0, \pm 1$ for magnetic dipole (MD) transition (592 nm) and $|\Delta J| = \text{even}$ for electric dipole (ED) transition (616 nm, 700 nm). The broad PL band observed in the region (415-500 nm) for Eu-CsPbCl₃ NCs can be ascribed to the defect state emission.³⁹ Herein, the nature of the three dopant emission peaks (592, 616, and 700 nm) is distinctly different from each other. The primary peaks for the emission of Eu³⁺, located at 616 and 700 nm are derived from the simultaneously existing inverse parity ED transition while the peak at 592 nm is derived from the MD transition.^{40,41} Moreover, the additional broad absorption in the Eu-CsPbCl₃ towards the higher wavelength region (shown in the inset of **Figure 6.3 A**) can be attributed to the introduction of defects into the system which will be detailed in later section. The PL spectrum of CsPbCl₃ exhibits the band edge emission at 403 nm (**Figure 6.3 Ba**). The asymmetric PL in CsPbCl₃ has been attributed to the bound excitons due to higher lying defects in CsPbCl₃ as compared to CsPbBr₃ which are prominently observable at low temperatures.³⁷ However, in case of Eu-CsPbCl₃ NCs, apart from band edge emission peaking at 406 nm a broad hump appears at 468 nm (**Figure 6.3 Bb**) with few additional peaks at 592, 616, and 700 nm.

Moreover, the PLQY shows two-fold increment ($\sim 23\%$) in the case of Eu-CsPbCl₃ NCs in contrast to that of the pristine CsPbCl₃ NCs ($\sim 12\%$).

Table 6.1 Fitting parameters of PL decay of both CsPbCl₃ and Eu-CsPbCl₃ after exciting samples at 375 nm.

Sample	Emission Wavelength (nm)	Decay (ns)		
		τ_1	τ_2	τ_{ave}
CsPbCl ₃	403	2.01 (86 %)	13 (14 %)	2.90
Eu-CsPbCl ₃	406	1.04 (88%)	6 (12%)	1.35
Eu-CsPbCl ₃	468	1.65 (85 %)	10 (15 %)	1.80

Table 6.2 Fitting parameters of PL decay of Eu- CsPbCl₃ after exciting samples at 375 nm and monitoring the Eu³⁺ transitions.

Sample	Emission Wavelength (nm)	Decay		
		τ_1	τ_2	τ_{ave}
Eu-CsPbCl ₃	592	70ns (69%)	0.75ms (31%)	0.25ms
Eu-CsPbCl ₃	616	1.03ms (100%)		1.03ms
Eu-CsPbCl ₃	700	1.06ms (100%)		1.06ms

These peaks are attributed to the ⁵D₀-⁷F_J transitions of Eu³⁺. Although there are a total of seven possible (⁵D₀-⁷F₀₋₆) transitions in Eu³⁺, yet only three transitions corresponding to ⁵D₀-⁷F₁ (592 nm), ⁵D₀-⁷F₂ (616 nm), ⁵D₀-⁷F₄ (700 nm) are discernible in the emission spectra.^{23,38} This is due to non-compliance of the other transitions with angular momentum based selection rule. The selection rules allow observation of only those transitions for which $|\Delta J| = 0, \pm 1$ for magnetic dipole (MD) transition (592 nm) and $|\Delta J| = \text{even}$ for electric dipole (ED) transition

(616 nm, 700 nm). The broad PL band observed in the region (415-500 nm) for Eu-CsPbCl₃ NCs can be ascribed to the defect state emission.³⁹ Herein, the nature of the three dopant emission peaks (592, 616, and 700 nm) is distinctly different from each other. The primary peaks for the emission of Eu³⁺, located at 616 and 700 nm are derived from the simultaneously existing inverse parity ED transition while the peak at 592 nm is derived from the MD transition.^{40,41} TRPL decay traces for the both samples were monitored and the average PL lifetime was found to be 2.90 and 1.35 ns (**Table 6.1**) for CsPbCl₃ and Eu-CsPbCl₃, respectively (**Figure 6.3 C**). The decrement in band edge PL lifetime in Eu-CsPbCl₃ can be attributed to the energy transfer from CsPbCl₃ to Eu³⁺ states.³ Further, we monitored the defect PL (468 nm) and PL lifetime is 1.80 ns which is higher than the band edge PL lifetime in Eu-CsPbCl₃ NCs (**Table 6.1**). This observation proposes that the carriers relaxing from the band edge are later populating defect states. To investigate the energy transfer mechanism among different Eu³⁺ states in Eu-CsPbCl₃, lifetime analysis has been carried out after monitoring 592, 616, and 700 nm (**Figure 6.3 D**). PL lifetime at 592 nm, 616 nm, and 700 nm was found to be 0.25, 1.03, and 1.06ms, respectively (**Table 6.2**).

6.2.3. Florescence Upconversion Studies of CsPbCl₃ and Eu-CsPbCl₃

Also, it has been observed that there is a sharp difference in PL lifetime of MD and ED transitions suggesting energy transfer plays a key role within Eu³⁺ states. Moreover, PL lifetime at 592 nm is dominated by fast component (70 ns) so, it is obvious that the transfer processes are occurring at very short time scales, which cannot be concluded only with TRPL. To get a profound understanding of involved energy-transfer processes at early time scale (sub picoseconds) we have carried out femtosecond fluorescence upconversion.

For this purpose, the samples were excited at 390 nm and due to unavoidable scattering effects, we were unable to monitor the band edge PL of CsPbCl₃ (403 nm). So, we monitored the closest possible wavelength to compare the temporal kinetics near band edge position i.e., 440 nm. It has also been observed that RE³⁺ doping often leads to the incorporation of defects leading broad PL peaking at 468 nm.³ Such states lead to a sequential process where after excitation, carriers relax from band edge to defect level (468 nm) and further relax to the Eu³⁺ (5D₀ state).

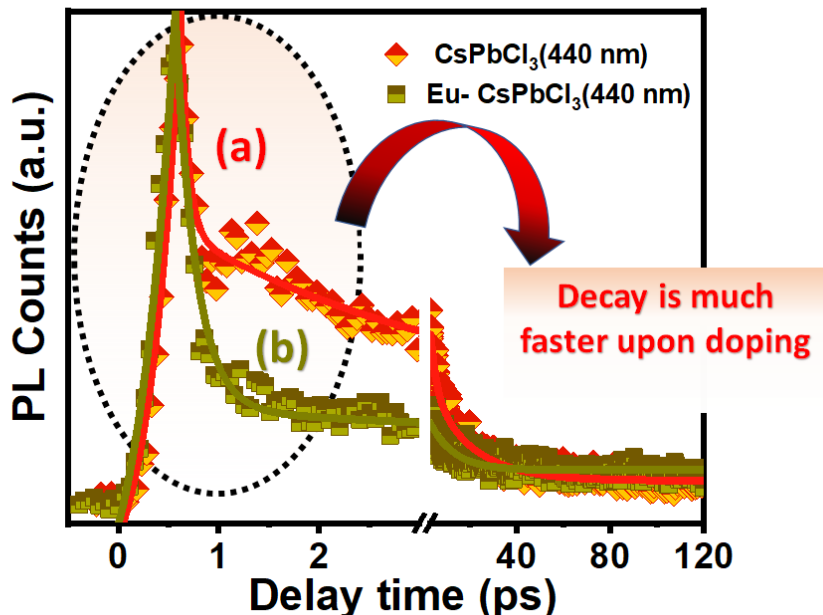


Figure 6.4 PL upconversion decay comparative kinetic traces of both (a) CsPbCl_3 and (b) Eu-CsPbCl_3 dispersed in toluene upon probing 440 nm after exciting both the samples at 390 nm.

The upconversion data for both the systems probed at 440 nm (nearest band edge position) show a drastic difference (**Figure 6.4**). The growth time for both the samples is IRF limited and the decay time of Eu-CsPbCl_3 NCs is much faster than the CsPbCl_3 NCs (**Figure 6.4**). This observation directly indicates that the carriers relax through a supplementary channel which facilitates a much faster decay. The temporal evolution of the corresponding emissions was monitored at 440, 468, 592, and 616 nm for Eu-CsPbCl_3 (**Figure 6.5 A**).

The obtained time constants after monitoring consecutive wavelengths suggest the cascading energy transfer from one state to another since the decay component of one state holds a good match with the growth constant of the subsequently populated state (**Table 6.3**). For instance, the observation worth noting is that the first decay component of 440 nm matches closely with the growth component of 468 nm in the time range of 305-315 fs (**Table 6.3**). Again, the first decay component (0.460ps) of defect state (468 nm) in Eu-CsPbCl_3 closely matched with the growth time (0.490ps) of Eu transition ($^5\text{D}_0$ - $^7\text{F}_1$) at 592 nm (**Table 6.3**).

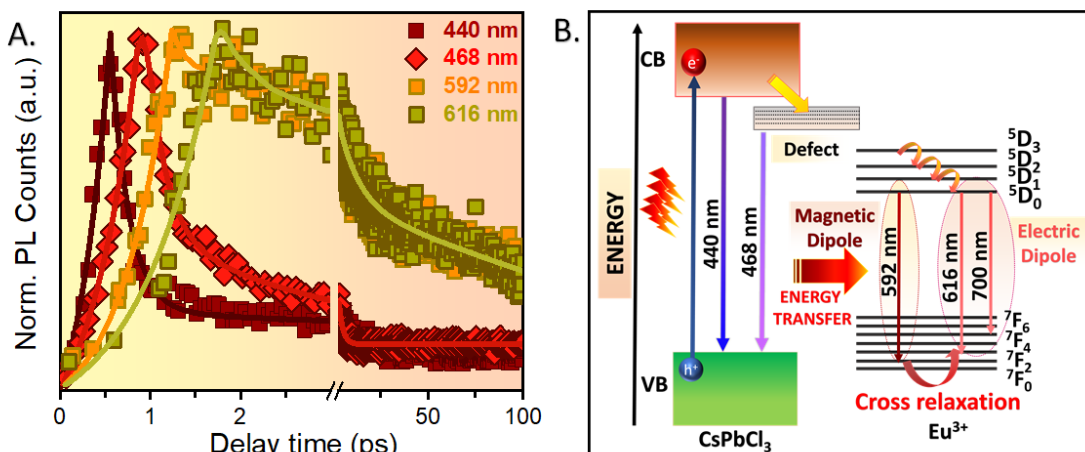


Figure 6.5 (A) PL upconversion decay traces of Eu-CsPbCl_3 dispersed in toluene after monitoring at (a) 440 nm, (b) 468 nm, (c) 592 nm, and (d) 616 nm after exciting at 390 nm and (B) Schematic representation of the cascading energy transfer processes in photo-excited Eu-CsPbCl_3 manifested by the PL decay traces where the recovery component of one transition is in good agreement with the growth of succeeding transition portraying the defect mediated transfer from CsPbCl_3 to Eu^{3+} and further transfer mechanism taking place among Eu^{3+} transition states.

This observation is a reflection of the energy transfer occurring from the defect states to Eu^{3+} .⁴⁰ The consequence of the difference in the characteristic of the transitions (MD or ED) is manifested in their probability of occurrence. It is conventionally known that the MD transitions are parity allowed but the ED transitions are parity forbidden.⁴¹ Therefore, out of all the transitions, the $^5\text{D}_0$ - $^7\text{F}_1$ is the most probable as it is parity allowed which makes the corresponding signal growth quicker (**Table 6.3**). Furthermore, the different transitions will have different resonances with the host emission. The transition corresponding to 592 nm being an MD transition, which is parity allowed that makes its growth faster and the energy emitted is utilized by the successive transition at 616 nm which results in delayed signal growth at 616 nm.⁴¹ This anticipation is noticeable in the upconversion measurements where the signal growth time monitored at 592 nm ($^5\text{D}_0$ - $^7\text{F}_1$) is faster than that of 616 nm ($^5\text{D}_0$ - $^7\text{F}_2$). This longer signal growth time for the 616 nm transition can be attributed to the cross-relaxation time taken by carriers to move from the state responsible for 592 nm transition to the one responsible for 616 nm transition. In Eu-CsPbCl_3 NCs due to the existence of intermediate energy level (defect

state), the energy transfer takes place from defect state to the upper excited energy states of Eu^{3+} later relaxing to the $^5\text{D}_0$ state, further energy transfer process is observed within the Eu^{3+} states (592 and 616 nm). Thus, with the aid of fluorescence upconversion, we directly probe the cascading energy transfer from CsPbCl_3 to Eu^{3+} states, and the schematic representation is shown in **Figure 6.5 B**.

Table 6.3 Fitting parameters of fluorescence upconversion study for both CsPbCl_3 and Eu-CsPbCl_3 after exciting samples at 390 nm.

Sample	Probe Wavelength (nm)	Growth (τ_{g1})	Decay			
			τ_1	τ_2	τ_3	τ_4
CsPbCl₃	440	< 150 fs (-100%)	0.750 ps (62%)	2.65 ps (10%)	11.80 ps (15%)	>100 ps (13%)
Eu-CsPbCl₃	440	< 150 fs (-100%)	0.310 ps (76 %)	8.15 ps (11%)	>100 ps (13%)	
Eu-CsPbCl₃	468	0.315 ps (-100%)	0.460 ps (62%)	9.55 ps (24%)	>100 ps (14%)	
Eu-CsPbCl₃	592	0.490 ps (-100%)	0.750 ps (20%)	17 ps (59%)	>100 ps (21%)	
Eu-CsPbCl₃	616	0.710 ps (-100%)	1.05 ps (19%)	17.5 ps (58%)	>100 ps (23%)	

6.2.4. Transient Absorption Studies of CsPbCl_3 and Eu-CsPbCl_3

Through the inferences drawn from the upconversion studies, we have discerned defect mediated transfer from CsPbCl_3 to Eu^{3+} yet it is completely unclear that the transfer from the band edge to Eu^{3+} is energy or charge transfer. So, for a complete understanding, we have taken up TA studies for both systems. The TA spectra of undoped CsPbCl_3 (**Figure 6.6 A**) displays an excitonic bleach centered at 400 nm with FWHM of 13 nm and two positive bands. The transient peak in the higher energy region can be attributed to the photoinduced absorption (PA) and the signal in the lower energy region (410 nm) is a typical biexciton signal.⁴²⁻⁴⁵ For Eu-CsPbCl_3 (**Figure 6.6 B**), apart from consistent features of CsPbCl_3 including excitonic

bleach and two positive signals, we have discerned certain major changes counting with the reduced FWHM of the excitonic bleach from 13 nm in CsPbCl₃ to 8 nm (**Figure 6.7 A,B**) and also the substantial decrease in the biexciton intensity (**Figure 6.6 D**). These observations in Eu-CsPbCl₃ indicate decrement in the band edge carrier concentration regardless of keeping same experimental conditions in both the systems.

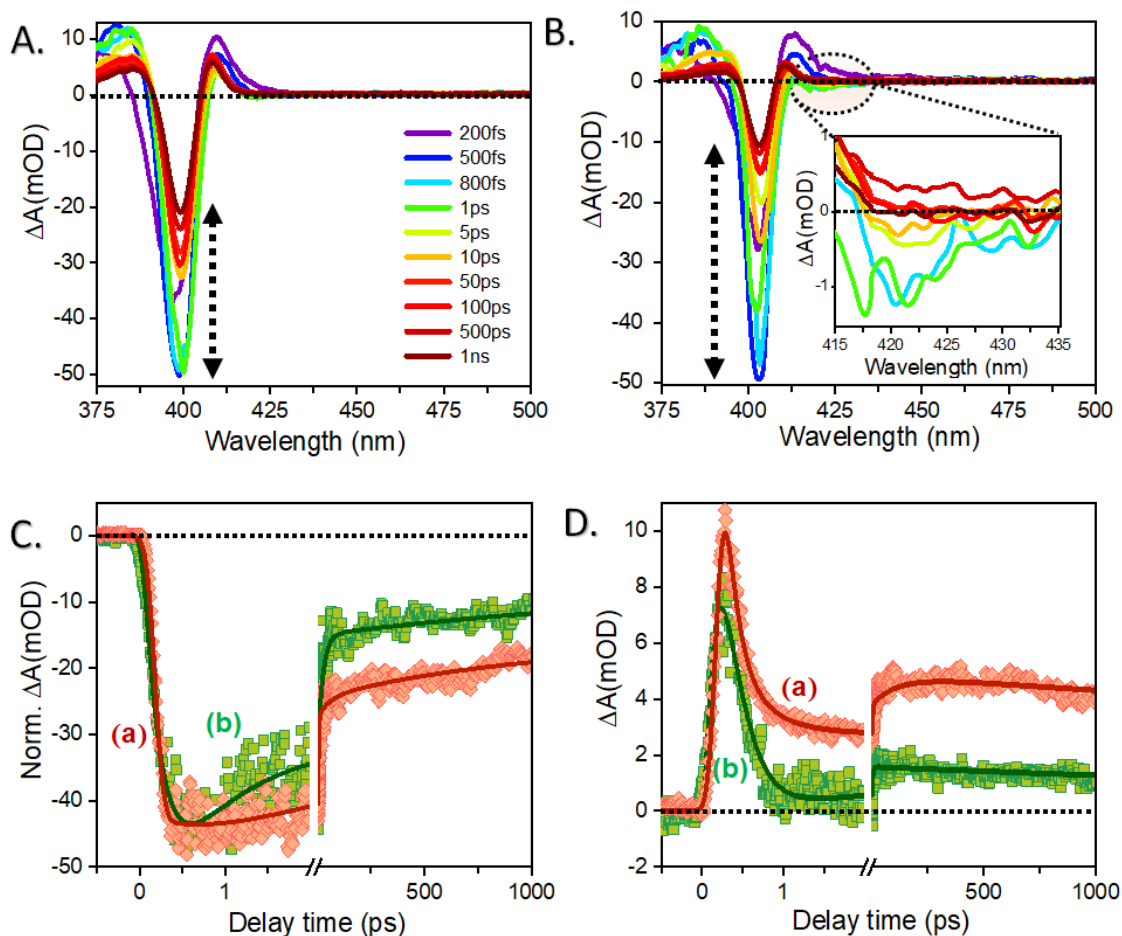


Figure 6.6 TA spectra of (A) CsPbCl₃ and (B) Eu-CsPbCl₃ NCs at different time delays, inset: The transient bleach observed due to the defect state; (C) Transient bleach kinetics and corresponding fitted data for (a) CsPbCl₃ and (b) Eu- CsPbCl₃ NCs probed at 400 nm and 403 nm, respectively with pump excitation of 350 nm and (D) Comparative transient biexciton signal for (a) CsPbCl₃ NCs, (b) Eu-CsPbCl₃ NCs probed at 410 and 413 nm, respectively.

Moreover, there is an onset of a new negative feature (bleach) in lower energy region around 412-430 nm for Eu-CsPbCl₃. Such bleach could be attributed to either formation of

intermediate charge transfer band or due to the presence of defect states.^{39,46} Moreover, unlike steady state optical absorption, in TA the two contributions, one from excitonic feature and one from defect states can be seen distinguishably. The dominant bleach is the one which is due to excitonic absorption while the bleach stemming from the defect states is seen separately towards the lower energy region. This decrement of the excitonic bleach FWHM in Eu-CsPbCl₃ indicates the decrement in the carrier concentration at excitonic position which signifies the depopulation of the charge carriers as occurrence of efficient charge transfer.⁴⁷

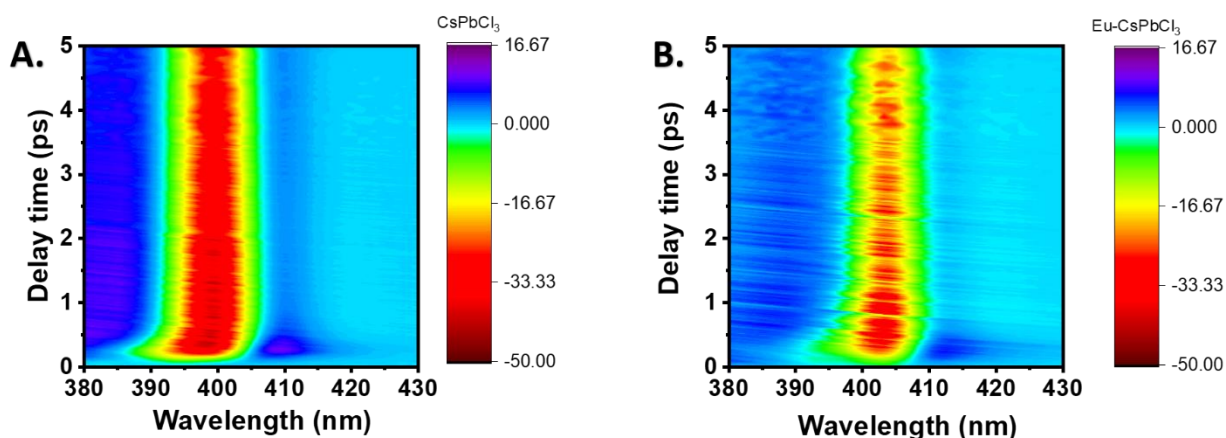


Figure 6.7 Pseudo contour plots of both (A) CsPbCl₃ and (B) Eu- CsPbCl₃ after exciting with 350 nm pump excitation.

However, no evidence of charge transfer state near 418 nm due to Eu³⁺ doping has been reported. To gain more clarity regarding this fact we have deconvoluted the absorption spectra of both systems (**Figure 6.8 A, B**). In CsPbCl₃ the absorption spectra refold into an excitonic peak at 3.05 eV and continuum band. However, for Eu-CsPbCl₃ there exists a supplementary feature continuum band attributable to absorption from shallow defect.⁴⁸ The introduction of dopant into the host lattice creates an open gateway for addition of defects into the system. Accordingly, such bleach is only visible if there is the transfer of charge carriers and not as a consequence of energy transfer. In the case of energy transfer, there would have been no such bleach coming into-picture. Thus, it can be concluded that the added bleach (**Figure 6.6 B**) is due to the transfer of carriers from the band edge to the defects. **Figure 6.6 C** shows the comparative analysis of bleach kinetic traces of for both systems. It is observed that the signal growth time (**Table 6.4**) is much faster in Eu-CsPbCl₃ in comparison to CsPbCl₃. The recovery components show an analogous trend and is approximately 20% faster in Eu-CsPbCl₃. The

new component $\tau_1 = 305$ fs in Eu-CsPbCl₃ NCs epitomizes exciton-defect charge transfer and its comparative amplitude is construed as the relative population of the carriers that experience charge transfer. Nevertheless, there may be an alternative pathway of energy transfer from band edge also that cannot be entirely neglected but the major contribution comes from the charge transfer.⁴⁹

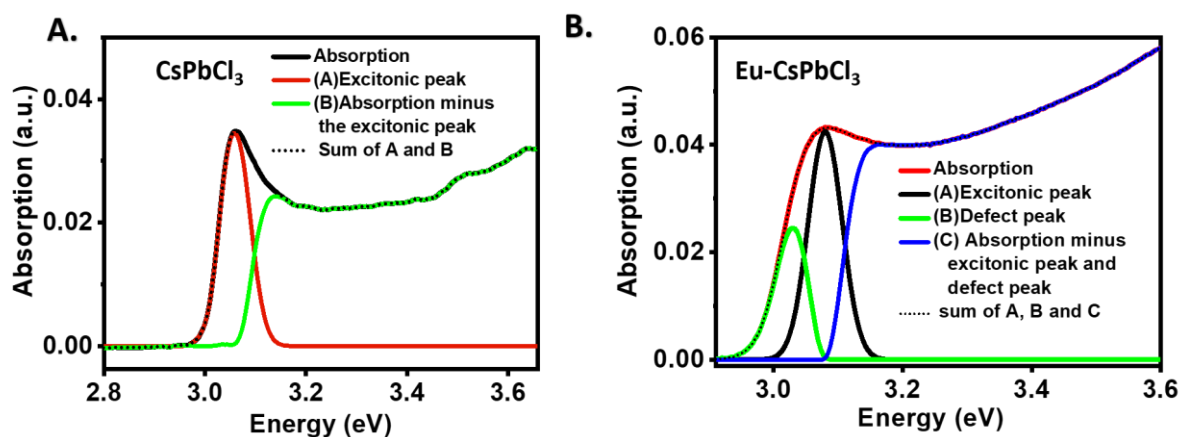


Figure 6.8 Deconvoluted absorption spectra of (A) CsPbCl₃ into the excitonic peak and the continuum peak and (B) Eu- CsPbCl₃ into the excitonic, absorption due to defect state and the continuum peak.

To gain a clear vision regarding the charge transfer time from band edge to defect states, we have probed the defect mediated bleach (418 nm) in both systems (**Figure 6.9**). The kinetics probed at 418 nm in Eu-CsPbCl₃ kinetics has a bleach growth component of 310 fs (**Figure 6.9, Table 6.5**). The most substantial implication drawn out upon comparing the transient kinetics is that the formation time of defect bleach is in close approximation with the first recovery component (305 fs) of the band edge bleach. So, the time constant of 310 fs can be attributed to the electron transfer time from the band edge of CsPbCl₃ to the defect state as it points out that transfer to Eu³⁺ will be defect mediated. The TA study provides a clear picture of charge transfer from band edge to defect states, displayed as a supplementary bleach in TA spectra and a thorough understanding of energy transfer processes is given by another complimentary technique of fluorescence upconversion. Accordingly, there could be two possible pathways opted by the photoexcited charge carriers in the doped system. The first mechanism involves direct energy transfer obtained from radiative recombination of carriers at the band edge of the host to the dopant states.

Table 6.4 Kinetics fitting parameters of transient absorption for both CsPbCl₃ and Eu-CsPbCl₃ after exciting samples at 350 nm.

Sample	Probe (nm)	Bleach Growth (τ_{g1})	Bleach recovery				
			τ_1	τ_2	τ_3	τ_4	τ_5
CsPbCl ₃	401	310fs (-100%)	6.25ps (36.6%)	50.5ps (9.5%)	250ps (15.9%)	>1ns (38%)	
Eu- CsPbCl ₃	405	<150fs (-100%)	305fs (6.9%)	3.5ps (11%)	20.8ps (31%)	104ps (32.1%)	>1ns (19%)
CsPbCl ₃	410	<150fs (-100%)	547fs (100%)	25ps (-100%)	180ps (12%)	>1ns (88%)	
Eu-CsPbCl ₃	413	< 150fs (-100%)	340fs (100%)	18ps (-100%)	165ps (40%)	>1ns (60%)	

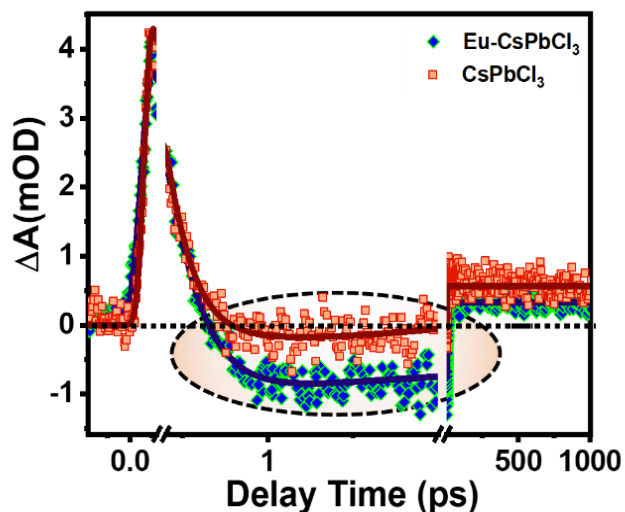


Figure 6.9 Normalized transient kinetics of both CsPbCl₃ and Eu- CsPbCl₃ monitored at 418 nm (defect) after exciting with 350 nm pump.

On the contrary, the second pathway involves depopulation of fraction of the initially photogenerated carriers from the excited states towards the band edge of CsPbCl₃ along with concurrent population of the remaining fraction of the carriers into the doping induced defect levels which finally make their way into the dopant states via energy transfer. However,

fluorescence upconversion and TA data suggest that the transfer is defect mediated thus minimalizing the probability of the first pathway.

Table 6.5 Kinetics fitting parameters of transient absorption data for both CsPbCl_3 and Eu-CsPbCl_3 after exciting samples at 350 nm monitoring the signal due to defect state.

Sample	Probe (nm)	Defect bleach					
		Growth (τ_{g1})	Recovery (τ_1)	Growth (τ_{g2})	Recovery		
					τ_1	τ_2	τ_3
CsPbCl_3	418	< 150 fs (-100%)	280fs (100%)	5.9 ps (-100%)	250 ps (40%)	>1ns (60%)	
Eu-CsPbCl_3	418	< 150 fs (-100%)	225fs (100%)	310 fs (-100%)	10 ps (60%)	180ps (10%)	>1ns (30%)

6.2.5. Two photon Absorption Studies in CsPbCl_3 and Eu-CsPbCl_3

The materials exhibiting TPA offer a unique prospect as they can be excited at two times lower energy as compared to the bandgap and a higher portion of the solar spectrum can be rehabilitated into usable energy.⁵⁰ The higher bandgap of CsPbCl_3 limits its application in high-performance optoelectronics. However, upon Eu^{3+} doping it gives broad PL extended up to visible range which was earlier constrained to UV region. Along with this if it displays TPA also it would be a potential material for both linear and nonlinear photovoltaics. Herein, we observed PL upon exciting the below band gap in both systems (**Figure 6.10 A**). This indicates that these systems are undergoing TPA. Manifestation of TPA in a system is mostly understood based on an intermediate state which could be a virtual state or a defect state. However, TPA in perovskites is occurring via virtual state not via defect state.⁵¹ Understanding the temporal behavior of the photo-excited charge carriers and the underlying energy transfer mechanisms in these doped systems under such below bandgap excitation is quite essential.⁵² So, to further probe the effect of TPA on transfer processes both samples were excited with 700 nm (1.77 eV), i.e., with energy much below the band gap of CsPbCl_3 (3.1 eV).

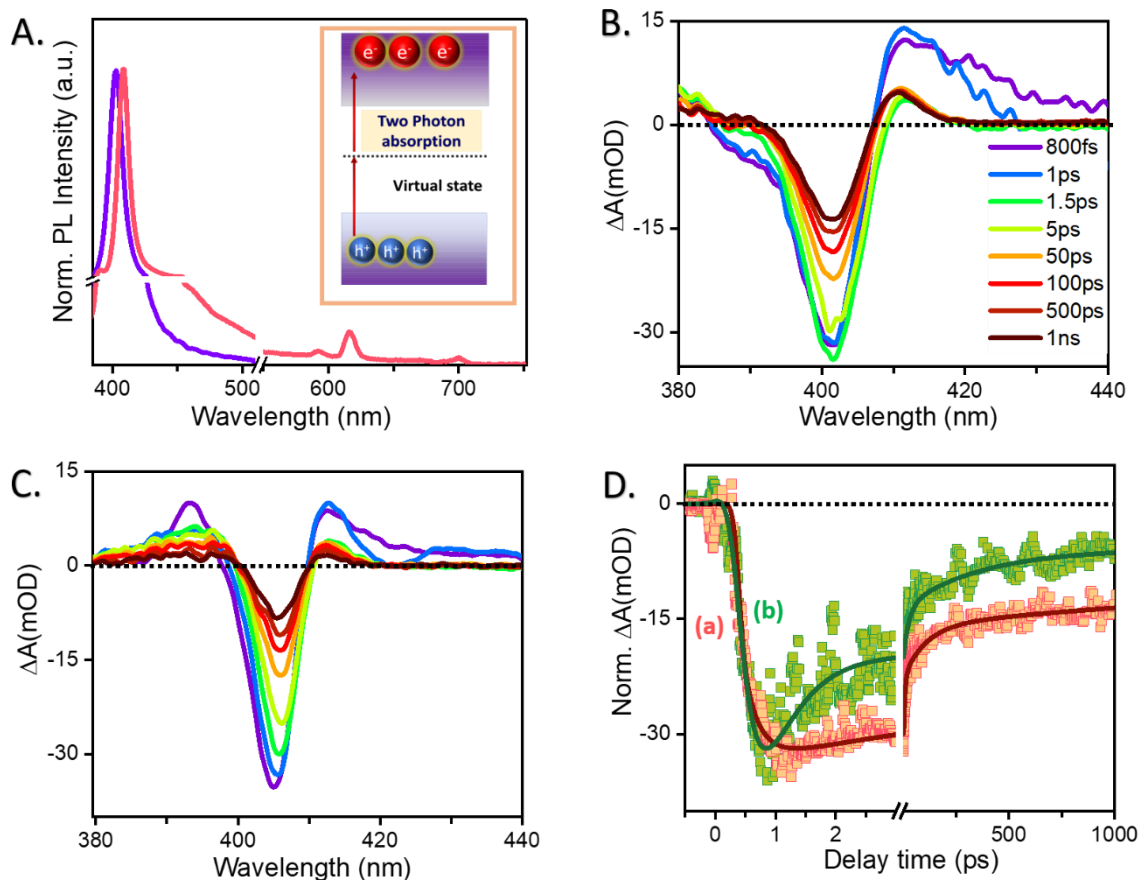


Figure 6.10 PL spectra for both CsPbCl₃ and Eu-CsPbCl₃ upon exciting at 750 nm (Inset: Schematic representation of the TPA in Eu-CsPbCl₃); TA spectra of (B) CsPbCl₃ and (C) Eu-CsPbCl₃ at different time delay after exciting at 700 nm laser light and (D) Comparative decay traces of bleach monitored for (a) CsPbCl₃ and (b) Eu- CsPbCl₃.

Figure 6.10 B,C show the temporal evolution of ΔA with delay time for both CsPbCl₃ and Eu-CsPbCl₃ systems. This below band-edge excitation ensures that no linear absorption would occur however, it will lead to interband transition from the VB to CB through TPA (**Figure 6.10 B,C**). It is also observed that the bleach growth and recovery is also found to be faster in Eu-CsPbCl₃ than CsPbCl₃. It has been observed that components obtained upon fitting the bleach profile (**Figure 6.10 D**) of both systems are in complete agreement with the components found on fitting the bleach profile with 3.54 eV excitation (**Table 6.6**). This ensures that such system not only provides the prospect of utilizing the below bandgap photon energy but also

at the same time does not negotiate with the underlying carrier relaxation pathways which is an added advantage.⁵³

Table 6.6. Kinetics fitting parameters of transient absorption data for both CsPbCl₃ and Eu-CsPbCl₃ after exciting samples at 700 nm.

Sample	Probe	Bleach Growth (τ_g)	Bleach recovery				
			τ_1	τ_2	τ_3	τ_4	τ_5
CsPbCl ₃	401	335 fs (-100%)	8.25ps (32%)	52.8ps (18%)	180ps (8%)	>1ns (42%)	
Eu-CsPbCl ₃	405	190 fs (-100%)	302fs (9.6%)	3.2ps (36.4%)	21.5ps (18%)	108ps (16%)	>1ns (20%)

6.3. Conclusion

In conclusion, we have successfully synthesized CsPbCl₃ and Eu-CsPbCl₃ NCs, and the effect of doping Eu³⁺ on the transfer processes is deeply studied. The two-step cascading competent energy transfer from CsPbCl₃ to Eu³⁺ is validated with fluorescence upconversion and TA studies. The spectroscopic investigations propose that Eu-CsPbCl₃ NCs exhibit charge transfer from the band edge to the shallow defect states and then fast energy transfer to Eu³⁺. Further, cross relaxation process is observed among Eu³⁺ states exhibiting two different kinds of characteristic traits out of which one has MD origin (592 nm) which grows faster and while the other one is of ED type (616 nm) which grows slower. Moreover, TPA is also explored upon exciting the samples below bandgap where it is successfully observed that transfer mechanism is not compromised at all. Thus, altogether our results offer a fundamental understanding of transfer processes even among Eu³⁺ levels which were not yet discussed. These captivating observations offer Eu-CsPbCl₃ NCs as a pertinent candidate for developing highly competent photonic applications.

6.4. References

- (1) Pan, G.; Bai, X.; Yang, D.; Chen, X.; Jing, P.; Qu, S.; Zhang, L.; Zhou, D.; Zhu, J.; Xu, W.; Dong, B.; Song, H. Doping Lanthanide into Perovskite Nanocrystals: Highly Improved and Expanded Optical Properties. *Nano Lett.* **2017**, *17*, 8005-8011.
- (2) Mir, W. J.; Sheikh, T.; Arfin, H.; Xia, Z.; Nag, A. Lanthanide Doping in Metal Halide Perovskite Nanocrystals: Spectral Shifting, Quantum Cutting and Optoelectronic Applications. *NPG Asia Mater.* **2020**, *12*, 9.
- (3) Zhou, L.; Liu, T.; Zheng, J.; Yu, K.; Yang, F.; Wang, N.; Zuo, Y.; Liu, Z.; Xue, C.; Li, C.; Cheng, B.; Wang, Q. Dual-Emission and Two Charge-Transfer States in Ytterbium-Doped Cesium Lead Halide Perovskite Solid Nanocrystals. *J. Phys. Chem. C* **2018**, *122*, 26825-26834.
- (4) Hu, Q.; Li, Z.; Tan, Z.; Song, H.; Ge, C.; Niu, G.; Han, J.; Tang, J. Rare Earth Ion-Doped CsPbBr₃ Nanocrystals. *Adv. Opt. Mater.* **2018**, *6*, 1-5.
- (5) Xing, K.; Yuan, X.; Wang, Y.; Li, J.; Wang, Y.; Fan, Y.; Yuan, L.; Li, K.; Wu, Z.; Li, H.; Zhao, J. Improved Doping and Emission Efficiencies of Mn-Doped CsPbCl₃ Perovskite Nanocrystals via Nickel Chloride. *J. Phys. Chem. Lett.* **2019**, *10*, 4177-4184.
- (6) Liu, H.; Wu, Z.; Shao, J.; Yao, D.; Gao, H.; Liu, Y.; Yu, W.; Zhang, H.; Yang, B. CsPb_xMn_{1-x}Cl₃ Perovskite Quantum Dots with High Mn Substitution Ratio. *ACS Nano* **2017**, *11*, 2239-2247.
- (7) Mir, W. J.; Mahor, Y.; Lohar, A.; Jagadeeswararao, M.; Das, S.; Mahamuni, S.; Nag, A. Postsynthesis Doping of Mn and Yb into CsPbX₃ (X = Cl, Br, or I) Perovskite Nanocrystals for Downconversion Emission. *Chem. Mater.* **2018**, *30*, 8170-8178.
- (8) Li, Z.; Wang, R.; Xue, J.; Xing, X.; Yu, C.; Huang, T.; Chu, J.; Wang, K. L.; Dong, C.; Wei, Z.; Zhao, Y.; Wang, Z. K.; Yang, Y. Core-Shell ZnO@SnO₂ Nanoparticles for Efficient Inorganic Perovskite Solar Cells. *J. Am. Chem. Soc.* **2019**, *141*, 17610-17616.
- (9) Wang, Y.; Zhu, Y.; Yang, G.; Yang, X.; Xu, X.; Huang, J.; Cui, S. Highly Efficient Silica-Coated Eu³⁺ and Mn²⁺ Doped CsPbCl₃ Perovskite Quantum Dots for Application in Light-Emitting Diodes. *Appl. Phys. Express* **2019**, *12*, 1-6.
- (10) Cheng, Y.; Shen, C.; Shen, L.; Xiang, W.; Liang, X. Tb³⁺, Eu³⁺ Co-Doped CsPbBr₃ QDs Glass with Highly Stable and Luminous Adjustable for White LEDs. *ACS Appl. Mater. Interfaces* **2018**, *10*, 21434-21444.

-
- (11) Bala, A.; Kumar, V. Stability of the Eu^{2+} Dopant in CsPbBr_3 Perovskites: A First-Principles Study. *J. Phys. Chem. C* **2019**, *123*, 6965-6969.
- (12) Wu, J.; Bai, H.; Qu, W.; Cao, G.; Zhang, Y.; Yu, J. Preparation of Eu^{3+} -Doped CsPbBr_3 Quantum-Dot Microcrystals and Their Luminescence Properties. *Opt. Mater. (Amst)*. **2019**, *97*, 109454.
- (13) Meinardi, F.; Akkerman, Q. A.; Bruni, F.; Park, S.; Mauri, M.; Dang, Z.; Manna, L.; Brovelli, S. Doped Halide Perovskite Nanocrystals for Reabsorption-Free Luminescent Solar Concentrators. *ACS Energy Lett.* **2017**, *2*, 2368-2377.
- (14) Liu, J.; Zhao, Y.; Li, X.; Wu, J.; Han, Y.; Zhang, X.; Xu, Y. Dual-Emissive CsPbBr_3 @Eu-BTC Composite for Self-Calibrating Temperature Sensing Application. *Cryst. Growth Des.* **2020**, *20*, 454-459.
- (15) Luo, X.; Ding, T.; Liu, X.; Liu, Y.; Wu, K. Quantum-Cutting Luminescent Solar Concentrators Using Ytterbium-Doped Perovskite Nanocrystals. *Nano Lett.* **2019**, *19*, 338-341.
- (16) Jena, A. K.; Kulkarni, A.; Sanehira, Y.; Ikegami, M.; Miyasaka, T. Stabilization of α - CsPbI_3 in Ambient Room Temperature Conditions by Incorporating Eu into CsPbI_3 . *Chem. Mater.* **2018**, *30*, 6668-6674.
- (17) Rossi, D.; Parobek, D.; Dong, Y.; Son, D. H. Dynamics of Exciton-Mn Energy Transfer in Mn-Doped CsPbCl_3 Perovskite Nanocrystals. *J. Phys. Chem. C* **2017**, *121*, 17143-17149.
- (18) Meng, J.; Lan, Z.; Abdellah, M.; Yang, B.; Mossin, S.; Liang, M.; Naumova, M.; Shi, Q.; Gutierrez Alvarez, S. L.; Liu, Y.; Lin, W.; Castelli, I. E.; Canton, S. E.; Pullerits, T.; Zheng, K. Modulating Charge-Carrier Dynamics in Mn-Doped All-Inorganic Halide Perovskite Quantum Dots through the Doping-Induced Deep Trap States. *J. Phys. Chem. Lett.* **2020**, *11*, 3705-3711.
- (19) Parobek, D.; Roman, B. J.; Dong, Y.; Jin, H.; Lee, E.; Sheldon, M.; Son, D. H. Exciton-to-Dopant Energy Transfer in Mn-Doped Cesium Lead Halide Perovskite Nanocrystals. *Nano Lett.* **2016**, *16*, 7376-7380.
- (20) Zhou, G.; Jiang, X.; Molokeev, M.; Lin, Z.; Zhao, J.; Wang, J.; Xia, Z. Optically Modulated Ultra-Broad-Band Warm White Emission in Mn^{2+} -Doped $(\text{C}_6\text{H}_{18}\text{N}_2\text{O}_2)\text{PbBr}_4$ Hybrid Metal Halide Phosphor. *Chem. Mater.* **2019**, *31*, 5788-5795.

- (21) Liu, Y.; Rong, X.; Li, M.; Molokeev, M. S.; Zhao, J.; Xia, Z. Incorporating Rare-Earth Terbium(III) Ions into Cs₂AgInCl₆:Bi Nanocrystals toward Tunable Photoluminescence. *Angew. Chemie - Int. Ed.* **2020**, *59*, 11634-11640.
- (22) Su, B.; Molokeev, M. S.; Xia, Z. Unveiling Mn²⁺ Dopant States in Two-Dimensional Halide Perovskite toward Highly Efficient Photoluminescence. *J. Phys. Chem. Lett.* **2020**, *11*, 2510-2517.
- (23) Li, Q.; Liu, Y.; Chen, P.; Hou, J.; Sun, Y.; Zhao, G.; Zhang, N.; Zou, J.; Xu, J.; Fang, Y.; Dai, N. Excitonic Luminescence Engineering in Tervalent-Europium-Doped Cesium Lead Halide Perovskite Nanocrystals and Their Temperature-Dependent Energy Transfer Emission Properties. *J. Phys. Chem. C* **2018**, *122*, 29044-29050.
- (24) Vu, T. H. Q.; Bondzior, B.; Stefańska, D.; Miniajluk, N.; Dereń, P. J. Synthesis, Structure, Morphology, and Luminescent Properties of Ba₂MgWO₆: Eu³⁺ Double Perovskite Obtained by a Novel Co-Precipitation Method. *Materials (Basel)*. **2020**, *13*, 1614.
- (25) Lin, C.Y.; Yang, S.H.; Lin, J.L.; Yang, C.F. Effects of the Concentration of Eu³⁺ Ions and Synthesizing Temperature on the Luminescence Properties of Sr_{2-x}Eu_xZnMoO₆ Phosphors. *Appl. Sci.* **2017**, *7*, 30.
- (26) Ma, J. P.; Chen, Y. M.; Zhang, L. M.; Guo, S. Q.; Liu, J. D.; Li, H.; Ye, B. J.; Li, Z. Y.; Zhou, Y.; Zhang, B. Bin; Bakr, O. M.; Zhang, J. Y.; Sun, H. T. Insights into the Local Structure of Dopants, Doping Efficiency, and Luminescence Properties of Lanthanide-Doped CsPbCl₃ Perovskite Nanocrystals. *J. Mater. Chem. C* **2019**, *7*, 3037-3048.
- (27) Alam, F.; Wegner, K. D.; Pouget, S.; Amidani, L.; Kvashnina, K.; Aldakov, D.; Reiss, P. Eu²⁺: A Suitable Substituent for Pb²⁺ in CsPbX₃ Perovskite Nanocrystals? *J. Chem. Phys.* **2019**, *151*, 231101.
- (28) Li, X.; Duan, S.; Liu, H.; Chen, G.; Luo, Y.; Ågren, H. Mechanism for the Extremely Efficient Sensitization of Yb³⁺ Luminescence in CsPbCl₃ Nanocrystals. *J. Phys. Chem. Lett.* **2019**, *10*, 487-492.
- (29) Abdi-Jalebi, M.; Pazoki, M.; Philippe, B.; Dar, M. I.; Alsari, M.; Sadhanala, A.; Divitini, G.; Imani, R.; Lilliu, S.; Kullgren, J.; Rensmo, H.; Grätzel, M.; Friend, R. H. Dedoping of Lead Halide Perovskites Incorporating Monovalent Cations. *ACS Nano* **2018**, *12*, 7301-7311.

-
- (30) Ågren, H.; Chen, G.; Li, D.; Li, X.; Zhao, T.; Liu, H.; Jiang, S.; Zhang, Q. Ultraefficient Singlet Oxygen Generation from Manganese-Doped Cesium Lead Chloride Perovskite Quantum Dots. *ACS Nano* **2020**, *14*, 12596-2604.
- (31) Szarko, J. M.; Rolczynski, B. S.; Lou, S. J.; Xu, T.; Strzalka, J.; Marks, T. J.; Yu, L.; Chen, L. X. Photovoltaic Function and Exciton/Charge Transfer Dynamics in a Highly Efficient Semiconducting Copolymer. *Adv. Funct. Mater.* **2014**, *24*, 10-26.
- (32) Cainelli, M.; Tanimura, Y. Exciton Transfer in Organic Photovoltaic Cells: A Role of Local and Nonlocal Electron–Phonon Interactions in a Donor Domain. *J. Chem. Phys.* **2021**, *154*, 34107.
- (33) Ricciarelli, D.; Mosconi, E.; Merabet, B.; Bizzarri, O.; De Angelis, F. Electronic Properties and Carrier Trapping in Bi and Mn Co-Doped CsPbCl₃ Perovskite. *J. Phys. Chem. Lett.* **2020**, *11*, 5482-5489
- (34) Long, R.; Prezhd, O. V. Dopants Control Electron À Hole Recombination at Perovskite À TiO₂. *ACS Nano* **2015**, *9*, 11143-11155.
- (35) Kaur, G.; Ghosh, H. N. Hot Carrier Relaxation in CsPbBr₃-Based Perovskites: A Polaron Perspective. *J. Phys. Chem. Lett.* **2020**, *11*, 8765-8776
- (36) Yong, Z. J.; Guo, S. Q.; Ma, J. P.; Zhang, J. Y.; Li, Z. Y.; Chen, Y. M.; Zhang, B. Bin; Zhou, Y.; Shu, J.; Gu, J. L.; Zheng, L. R.; Bakr, O. M.; Sun, H. T. Doping-Enhanced Short-Range Order of Perovskite Nanocrystals for Near-Unity Violet Luminescence Quantum Yield. *J. Am. Chem. Soc.* **2018**, *140*, 9942-9951.
- (37) Lohar, A. A.; Shinde, A.; Gahlaut, R.; Sagdeo, A.; Mahamuni, S. Enhanced Photoluminescence and Stimulated Emission in CsPbCl₃ Nanocrystals at Low Temperature. *J. Phys. Chem. C* **2018**, *122*, 25014-25020.
- (38) Liu, X.; Li, C.; Quan, Z.; Cheng, Z.; Lin, J. Tunable Luminescence Properties of CaIn₂O₄:Eu³⁺ Phosphors. *J. Phys. Chem. C* **2007**, *111*, 16601-16607.
- (39) Goswami, T.; Yadav, D. K.; Bhatt, H.; Kaur, G.; Shukla, A.; Babu, K. J.; Ghosh, H. N. Defect-Mediated Slow Carrier Recombination and Broad Photoluminescence in Non-Metal-Doped ZnIn₂S₄ Nanosheets for Enhanced Photocatalytic Activity. *J. Phys. Chem. Lett.* **2021**, *12*, 5000-5008.
- (40) Baur, F.; Jüstel, T. Eu³⁺ Activated Molybdates – Structure Property Relations. *Opt. Mater. X* **2019**, *1*, 1-10.

- (41) Binnemans, K. Interpretation of Europium(III) Spectra. *Coord. Chem. Rev.* **2015**, *295*, 1-45.
- (42) Ahumada-lazo, R.; Alanis, J. A.; Parkinson, P.; Binks, D. J.; Hardman, S. J. O.; Gri, J. T.; Wisnivesky, F.; Rivarola, R.; Humphrey, C. J.; Ducati, C.; Davis, N. J. L. K. Emission Properties and Ultrafast Carrier Dynamics of CsPbCl₃ Perovskite Nanocrystals. *J. Phys. Chem. C* **2019**, *123*, 2651-2657
- (43) Kaur, G.; Justice Babu, K.; Ghorai, N.; Goswami, T.; Maiti, S.; Ghosh, H. N. Polaron-Mediated Slow Carrier Cooling in a Type-1 3D/0D CsPbBr₃@Cs₄PbBr₆ Core-Shell Perovskite System. *J. Phys. Chem. Lett.* **2019**, *10*, 5302-5311.
- (44) Shukla, A.; Kaur, G.; Justice Babu, K.; Ghorai, N.; Goswami, T.; Kaur, A.; N. Ghosh, H. Effect of Confinement on the Exciton and Biexciton Dynamics in Perovskite 2D-Nanosheets and 3D-Nanocrystals. *J. Phys. Chem. Lett.* **2020**, *11*, 6344-6352.
- (45) Baars, T.; Braun, W.; Bayer, M.; Forchel, A. Biexcitons in Semiconductor Quantum Wires. *Phys. Rev. B* **1998**, *58*, R1750-R1753.
- (46) Justice Babu, K.; Kaur, G.; Shukla, A.; Kaur, A.; Goswami, T.; Ghorai, N.; Ghosh, H. N. Concurrent Energy- And Electron-Transfer Dynamics in Photoexcited Mn-Doped CsPbBr₃ Perovskite Nanoplatelet Architecture. *J. Phys. Chem. Lett.* **2021**, *12*, 302-309.
- (47) Wang, C.; Han, D.; Wang, J.; Yang, Y.; Liu, X.; Huang, S.; Zhang, X.; Chang, S.; Wu, K.; Zhong, H. Dimension Control of in Situ Fabricated CsPbClBr₂ Nanocrystal Films toward Efficient Blue Light-Emitting Diodes. *Nat. Commun.* **2020**, *11*, 2–9.
- (48) Milstein, T. J.; Kroupa, D. M.; Gamelin, D. R. Picosecond Quantum Cutting Generates Photoluminescence Quantum Yields Over 100% in Ytterbium-Doped CsPbCl₃ Nanocrystals. *Nano Lett.* **2018**, *18*, 3792-3799.
- (49) Kaur, G.; Saha, R.; Babu, K. J.; Shukla, A.; Ghosh, H. N. Unravelling the Underlying Hot Carrier Transfer and Relaxation Pathways in Type-1 CsPbBr₃-PbS System. *J. Phys. Chem. C* **2021**, *125*, 10516-10525.
- (50) He, T.; Li, J.; Ren, C.; Xiao, S.; Li, Y.; Chen, R.; Lin, X. Strong Two-Photon Absorption of Mn-Doped CsPbCl₃ Perovskite Nanocrystals. *Appl. Phys. Lett.* **2017**, *111*, 1-5.
- (51) Chen, J.; Židek, K.; Chábera, P.; Liu, D.; Cheng, P.; Nuuttila, L.; Al-Marri, M. J.; Lehtivuori, H.; Messing, M. E.; Han, K.; Zheng, K.; Pullerits, T. Size-And Wavelength-Dependent Two-Photon Absorption Cross-Section of CsPbBr₃ Perovskite Quantum

Dots. *J. Phys. Chem. Lett.* **2017**, *8*, 2316-2321.

- (52) He, T.; Li, J.; Qiu, X.; Xiao, S.; Yin, C.; Lin, X. Highly Enhanced Normalized-Volume Multiphoton Absorption in CsPbBr₃ 2D Nanoplates. *Adv. Opt. Mater.* **2018**, *6*, 2-8.
- (53) He, T.; Li, J.; Qiu, X.; Xiao, S.; Lin, X. Superior Multiphoton Absorption Properties in Nanoplatelets. *Photonics Res.* **2018**, *6*, 1021-1027.

Chapter 7

Retarded Hot Carrier Relaxation and Augmented Photoconductivity in Europium doped CsPbBr₃ Nanocrystals

Rapid hot carrier relaxation is the foremost obstacle for harnessing solar energy and reducing the hot carrier relaxation remains one of the most significant components for harvesting solar energy. Polaron formation is a significant factor influencing carrier cooling, also it is widely recognized that defects in perovskites have a substantial impact on carrier cooling. The introduction of rare-earth ions (RE^{3+}) perovskite lattice has opened up new possibilities for investigating alterations in optical, electronic, magnetic, and charge carrier transport properties. In this chapter, we have explored the spectroscopic aspects of both CsPbBr₃ and Eu-doped CsPbBr₃ (Eu-CsPbBr₃). The transient absorption studies show that the doped counterparts display much slower cooling, while the polaron formation and decay time remained intact. The low-temperature transient studies reveal that this is an outcome of absent bound exciton due to the passivation of Br⁻ vacancies. Further, optical pump THz probe studies reveal retarded carrier cooling also impacts carrier mobility and photoconductivity, where Eu-CsPbBr₃ displays higher photoconductivity and slow mobility. The implications drawn from our study inevitably show that the slower hot carrier cooling and slow transient carrier mobility in Eu-CsPbBr₃ make it a superior contender for photovoltaic applications.

7.1 Introduction

The rapid relaxation of hot carriers, occurring much faster than the time needed to transport the charge carriers in lead halide perovskites, leads to the dissipation of a significant amount of photon energy as heat. This phenomenon substantially diminishes the efficiency of these materials in hot carrier (HC) photovoltaics.¹⁻⁵ In the same context, researchers have been continuously trying to somehow increase the carrier cooling time in order to increase the hot carrier's extraction time. Hot carriers refer to electrons or holes having at least excess energy $>K_B T$, above the CB or VB. Almost 50% of the energy absorbed by solar cells is dissipated simply in the form of heat, so the principal focus of today's researchers is to utilize this energy of hot carriers by evolving hot carrier solar cell and breaking the Shockley-Queisser limit.⁶⁻⁸ The HC solar cell is so important as the predicted efficiency of HC solar cell is ~66 %, ⁵ and if the energy of hot carriers can be harnessed, it will ultimately assist in overcoming the Shockley-Queisser limit of ~33 %.^{9,10} The major challenges in the expansion of hot carrier solar cells are quicker carrier relaxation and slow extraction of the carriers.^{11,12-14} The strategies involved in increasing the carrier cooling time by providing a shell of a higher band gap and more polar material over the core material,¹⁵ tuning the dimensionality,¹⁶ doping,¹⁷ changing the ligand,¹⁸ altering the stoichiometric ratio of the A or B-site cation.¹⁹ Frohlich interaction is one of the key parameters which affects the carrier cooling, i.e., the interaction between electron and phonon cloud (which creates polaron).^{20,21}

The impurity ion doping acts as an additional lever, in order to modify the optical and electronic properties of host perovskite NCs without damaging its inherent properties.^{22,23} Doping of rare earth (RE) ions has been under continuous demand as they function as optically active centers with energy levels inside the host bandgap, leading to an increase in PL transitions at relatively lower energies than the host material. Among, the spin-forbidden nature of the Eu^{3+} transitions, results in millisecond PL lifetime and larger Stokes shift that decreases reabsorption losses. These properties add strength to the host perovskite material and help to improvise the device performance.²⁴⁻²⁵ Moreover, substituting the lead (Pb) with RE ions in perovskite lattice even in small amounts leads to the alteration of traps/defects, which eventually affects the hot carrier cooling. Thus, the comprehensive study of the hot carrier cooling in these doped counterparts is of utmost importance.

In this work, we have introspected the hot carrier cooling employing transient absorption spectroscopy in Eu-CsPbBr₃ and CsPbBr₃ NCs and found that the hot carrier cooling is drastically retarded in the doped counterparts. The low-temperature studies unravel that the retarded carrier cooling in Eu-CsPbBr₃ is due to the reduction of defects due to the passivation of Br⁻ vacancies although the polaron formation and decay time are similar in both the systems. Further, we have conducted OPTP spectroscopy to understand the effect of doping on transient photoconductivity and mobility. This ultimately leads to increase the photoconductivity and slow down the mobility in the Eu-CsPbBr₃ NCs. This approach of slowing down the hot carriers offers a thorough grasp of the mechanisms involved in hot carrier cooling and will create new opportunities for the development of perovskite hot carrier solar cells.

7.2 Results and discussion

The hot injection synthesis procedure was followed for the synthesis of CsPbBr₃ and Eu-CsPbBr₃ according to the previously reported literature with minor modifications (detailed in the chapter 2).²⁶

7.2.1 Structural and morphological studies

Size and morphology of CsPbBr₃ and Eu-CsPbBr₃ NCs were analyzed using TEM and HR-TEM. TEM and HR-TEM images of CsPbBr₃ (**Figure 7.1 a**) and Eu-CsPbBr₃ NCs (**Figure 7.1b**) display cubic morphology with an average size of 12 nm. Interestingly, even after doping with Eu³⁺ in the CsPbBr₃ lattice, the cubic structure, size and uniformity of the CsPbBr₃ NCs are maintained. However, the effect of doping is reflected in the calculated interplanar distance (d-spacing) of CsPbBr₃ and Eu-CsPbBr₃ calculated to be 0.58 and 0.55 nm, respectively of (002) plane of orthorhombic phase (**inset Figure 7.1 a,b**). The reduction in the interplanar spacing of Eu-CsPbBr₃ is due to the fact that the ionic radius of Eu³⁺ (0.95 Å) is smaller as compared to that of Pb²⁺ (six-coordinate effective radii of 1.33 Å), which outcomes the shrinkage of the NC lattice. Additionally, the XRD pattern of CsPbBr₃ and Eu-CsPbBr₃ NCs (**Figure 7.1 c**) show that both systems exhibit the orthorhombic phase of CsPbBr₃ and the planes were in good agreement with the standard JCPDF No. PDF-01-072-7929 with space group *Pbnm*(62). Interestingly, we observe a shift of 0.20° in the diffraction angle, i.e., two theta values corresponding to the (220) plane of Eu-CsPbBr₃ NCs, as a result of the lattice shrinkage.²⁷

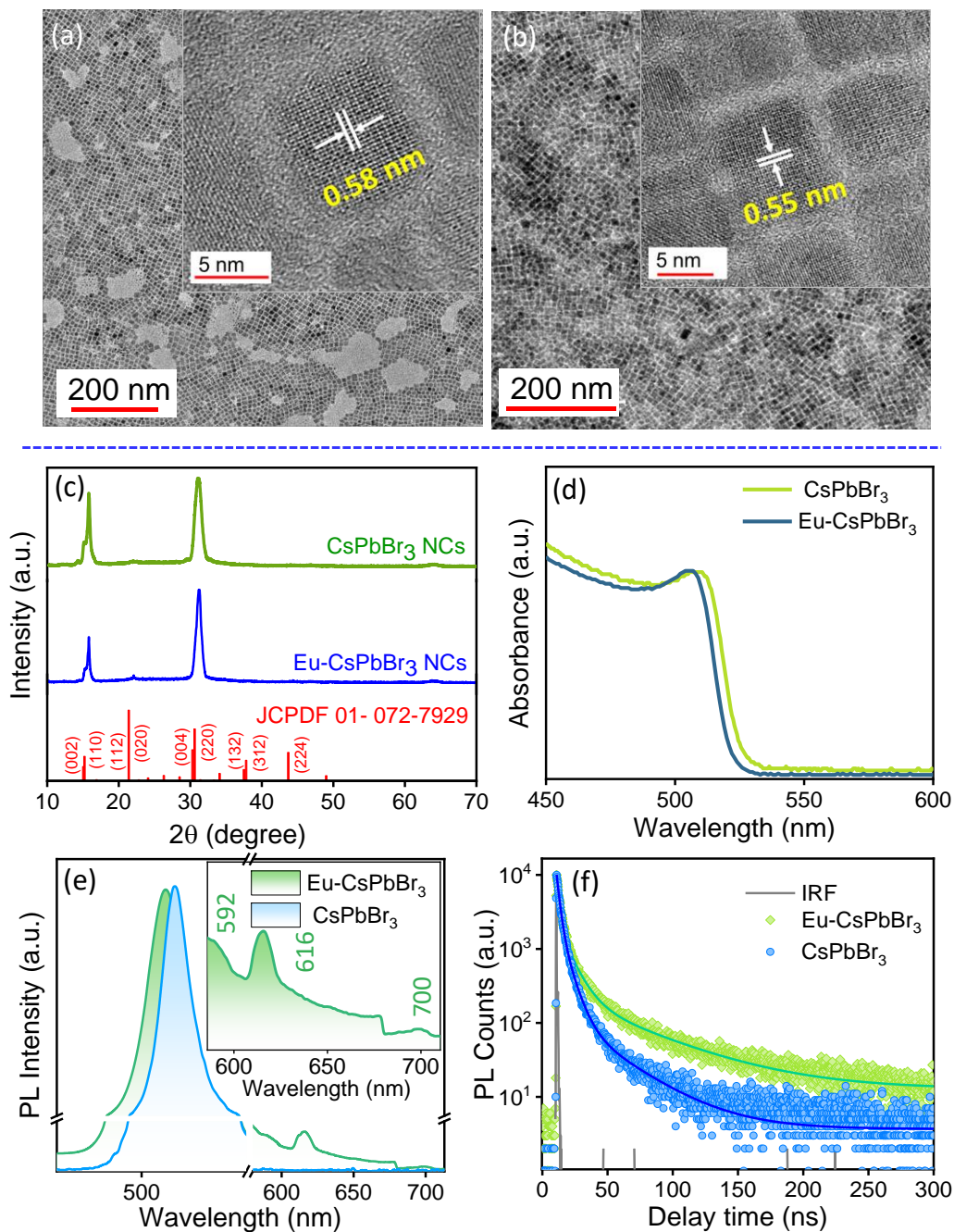


Figure 7.1 TEM and HR-TEM images of (a) CsPbBr₃ and (b) Eu-CsPbBr₃ NCs, (c) XRD pattern of CsPbBr₃ and Eu-CsPbBr₃ NCs, (d) optical absorbance of CsPbBr₃ and Eu-CsPbBr₃ (e) photoluminescence spectra of CsPbBr₃ and Eu-CsPbBr₃ NCs and (f) TCSPC study of CsPbBr₃ and Eu-CsPbBr₃ NCs after exciting at 3.08 eV and monitoring at the band edge emission.

7.2.2 Optical Studies of CsPbBr₃ and Eu-CsPbBr₃ NCs

Further, optical studies were conducted for both CsPbBr₃ and Eu-CsPbBr₃ NCs. The absorption spectra exhibit the band edge exciton peak at 2.45 and 2.43 eV for CsPbBr₃ and Eu-CsPbBr₃ NCs respectively (**Figure 7.1 d**). The PL spectra of CsPbBr₃ and Eu-CsPbBr₃ NCs was recorded and are depicted in **Figure 7.1 e**. The band edge PL of CsPbBr₃ NCs is observed at 510 nm while for Eu-CsPbBr₃ NCs apart from the band edge PL peaking at 508 nm certain additional peaks also appeared at 592, 616, and 700 nm. These peaks are attributed to the intra-configurational ⁵D₀-⁷F_J transitions of Eu³⁺.^{23,28-30} To further understand the transfer processes³¹ in doped counterparts, we have conducted the PL lifetime measurements and found that the band edge lifetime (average) of Eu-CsPbBr₃ NCs (**Figure 7.1 f**) is higher (8.1 ns) than that of CsPbBr₃ (5 ns). This observation was quite contrary to what we observed in the previous work in which we doped Eu³⁺ in lattice of CsPbCl₃.³² The PL lifetime of host CsPbCl₃ NCs was found to be faster due to involvement of charge and energy transfer processes.³² But the reason for this contrary result was not understood. Although a brief analogy could be drawn out from the steady state and PL lifetime measurements still the fact remains completely unclear how the PL lifetime of the doped system is increasing at the site of the band edge exciton.

7.2.3 Transient Absorption Study of CsPbBr₃ and Eu-CsPbBr₃ NCs

So, in order to understand the charge transfer processes and the underlying carrier dynamics, we have performed the transient absorption spectroscopy (**Figure 7.2 a**) of both CsPbBr₃ and Eu-CsPbBr₃ NCs as these processes occur at very short time scales and TRPL is not competent enough to resolve in such short time scales.

7.2.3.1 Near Resonant Excitation

To investigate the influence of Eu³⁺ doping in the lattice of CsPbBr₃ on charge carrier dynamics, we initiated the study by exciting both CsPbBr₃ and Eu-CsPbBr₃ NCs with near-resonant excitation energy, specifically at 2.54 eV. **Figure 7.2 b,c** shows the TA spectra of CsPbBr₃ and Eu-CsPbBr₃ NCs respectively. The TA spectra of CsPbBr₃ NCs comprise a negative excitonic bleach ($\Delta A < 0$) i.e., a photobleaching band that arises from the state filling effect, a positive signal ($\Delta A > 0$) towards a lower energy regime due to the probe-induced biexciton signal. Interestingly, the positive signal towards the lower energy regime is observable only at early time scales and later is replaced by a negative bleach.³¹

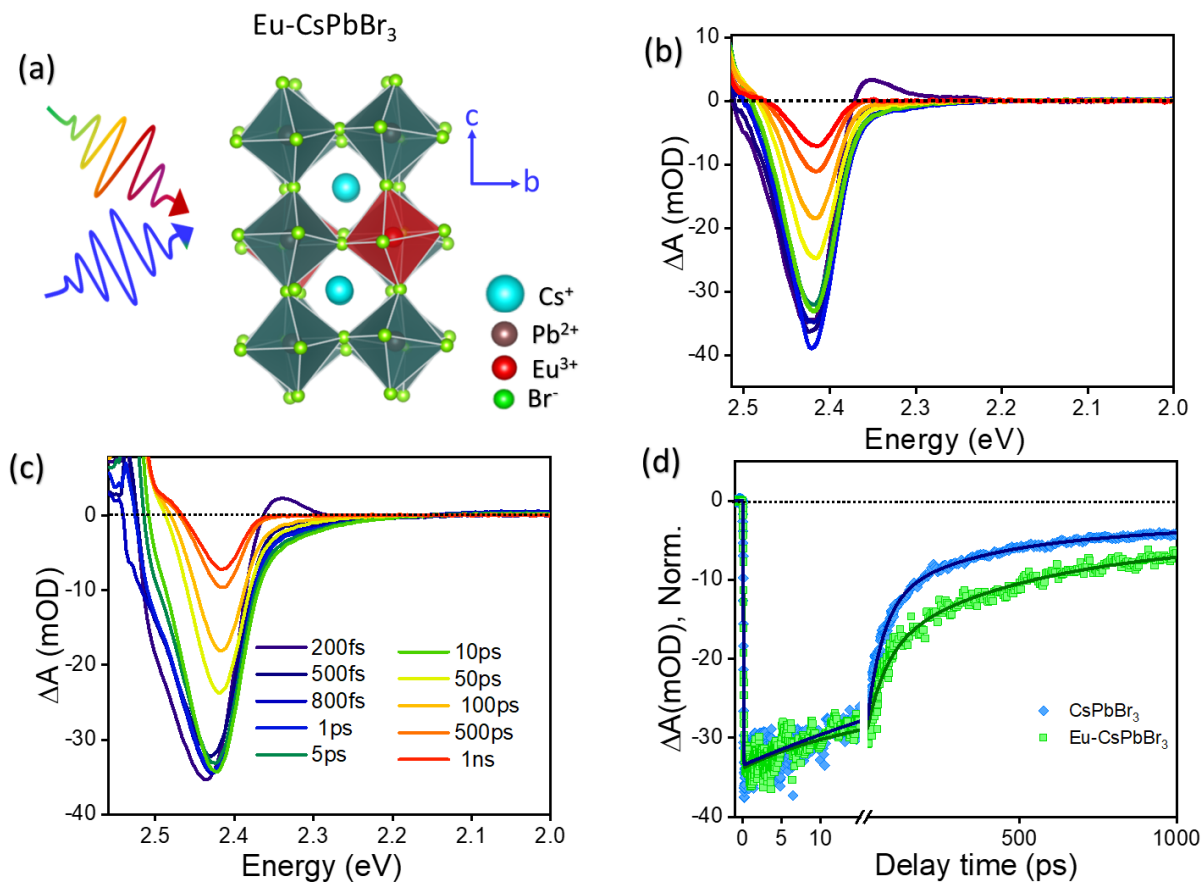


Figure 7.2 (a) The structure representation of the pump probe spectroscopy for Eu-CsPbBr₃ NCs; Transient absorption (TA) spectra of (b) CsPbBr₃, (c) Eu-CsPbBr₃, under 2.58 eV pump excitation and (d) comparative bleach decay kinetics of CsPbBr₃ and Eu-CsPbBr₃ probed at the bleach minima.

The TA spectra corresponding to Eu-CsPbBr₃ NCs also consist of the same spectral features as that of CsPbBr₃ NCs. But upon closely scrutinizing the transient bleach kinetics (**Figure 7.2 d**) we witness a strange observation, contrary to our expectations. The bleach growth is IRF limited (<150 fs) (**Table 7.1**) as the carriers are injected close to the band edge, so bleach growth is very fast. It was anticipated that the bleach dynamics should have been faster due to the underlying energy as well as charge transfer processes expected in the doped system. Although an additional channel is present in the Eu-CsPbBr₃ NCs as the energy transfer process is also expected from CsPbBr₃ to Eu³⁺ the recovery should have been faster as there is an additional pathway for carriers. However, we observe that the recombination is relatively

slower in the doped counterpart (**Table 7. 1**). Nonetheless, the reason behind this is completely unclear. To understand this in more detail the growth profile of the bleach should also be compared in both systems. As it is known that bleach growth is governed by multiple factors, including carrier-carrier scattering, carrier phonon scattering, polaron formation, charge and energy transfer rates.^{6,15,20,21} But in this case, carriers are energetically excited in much lower states (near resonant excitation), so the growth of the bleach is IRF limited (**Figure 7.2 d**). The carriers are excited into much lower energetic states in this case, and thus the carriers reach the band edge within <150 fs, and they prefer to recombine before the polaron could actually be formed (as the bleach growth time <150 fs is less than the polaron formation time). Thus, in this case we cannot compare the bleach growth in both the systems.¹⁸

Table 7.1 Kinetic fitting parameters at bleach position for CsPbBr₃ and Eu-CsPbBr₃ under 2.58 eV pump excitation.

Sample	Growth	Recovery			
	τ_g^1	τ_1	τ_2	τ_3	τ_4
CsPbBr ₃	<150fs	5.1 ps	45 ps	170 ps	>1 ns
	(100%)	(-21%)	(-52%)	(-15%)	(-12%)
Eu-CsPbBr ₃	<150fs	7.1 ps	60 ps	210 ps	>1 ns
	(100%)	(-24 %)	(-39 %)	(-16%)	(-21%)

7.2.3.2. Far Resonant Excitation

In order to explore the response of charge carriers when excited with higher energy, we conducted experiments where the samples were excited well above the band edge, specifically at 3.54 eV. So, to further understand and comprehend the effect of doping on the host carrier cooling rates we have tuned the excitation energy to 3.54 eV. The excitation of carriers far above the band gap leads to a concurrent population of electrons and holes in the energetically higher states of CB and VB respectively. The far band gap excitation gives a lap of surplus time such that carriers subsequent to photoexcitation take some time to thermalize to the band edges and thus there is adequate time for the formation of polaron. Upon far band gap excitation i.e., 3.54 eV the spectral features in the TA spectra of CsPbBr₃ and Eu-CsPbBr₃ NCs (**Figure 7.3 a,b**) comprises a negative excitonic bleach ($\Delta A < 0$), a positive signal ($\Delta A > 0$) towards lower

energy regime which is a typical biexciton signal, and another positive signal towards high energy regime due to photo-induced absorption.

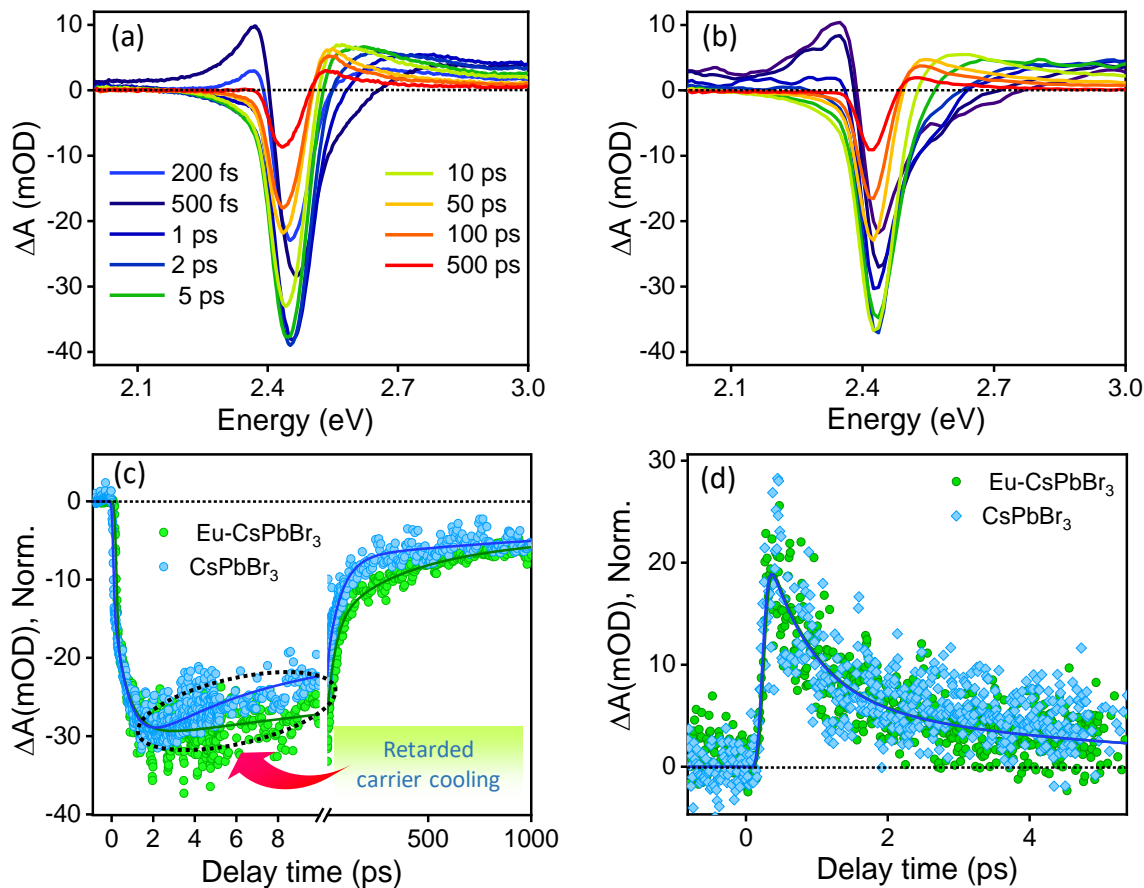


Figure 7.3 (a, b) Transient absorption spectra of CsPbBr₃ and Eu-doped CsPbBr₃ respectively after 3.54 eV pump excitation, (c) comparative transient bleach kinetics of CsPbBr₃ and Eu-doped CsPbBr₃ NCs and (d) comparative polaron kinetics probed at 2.0 eV.

Apart from this, we observe that the bleach growth (carrier cooling) is found to be retarded (**Figure 7.3 c**) along with the slower recovery in Eu-CsPbBr₃ system. Nevertheless, we observed a considerably much slower growth (**Table 7.2**) in the Eu-CsPbBr₃ NCs, which categorically suggests that the hot carrier cooling is retarded in the doped counterpart. The photoexcited carriers after the excitation are initially in non-equilibrium states and thermalized via carrier-carrier scattering within a few ps.^{32,33} As we are well aware of the fact that fast hot carrier cooling is one of the key parameter which needs to be judiciously dealt with. The growth

profile of bleach generally represents hot carrier cooling in the system. Hot carrier cooling in perovskites depends on carrier-carrier scattering, and carrier phonon scattering, which eventually leads to polaron formation.

Table 7.2 Kinetic fitting parameters at bleach position for CsPbBr₃ and Eu-CsPbBr₃ under 3.54 eV pump excitation.

Sample	Growth		Recovery			
	τ_g^1	τ_g^2	τ_1	τ_2	τ_3	τ_4
CsPbBr₃	<150fs (49 %)	850 fs (51 %)	6.2 ps (-43 %)	48 ps (-28%)	180 ps (-13%)	>1 ns (-16%)
Eu-CsPbBr₃	<150fs (53 %)	1.55 ps (47 %)	10 ps (- 41 %)	80 ps (-26 %)	250 ps (-15%)	>1 ns (-18%)

Polaron formation is one of the primary factors affecting hot carrier cooling, so, we suspected the role of polaron in this retarded hot carrier cooling in Eu-CsPbBr₃. Thus, with this, we probed the kinetics at 2 eV i.e., the signal corresponding to polaron formation as shown in **Figure 7.3 d**. It can be clearly seen that the polaron formation and the decay time is similar in both the doped and undoped system as seen in the transient kinetics. This clearly shows that the polaron formation is unaffected upon doping and is same in both the systems. Thus, in Eu-CsPbBr₃, we can rule out the involvement of polarons in the process of delayed cooling for charge carriers. This implies that the introduction of Eu³⁺ in the lattice of CsPbBr₃ does not affect the formation and decay of polarons. However, the excitation energy dependent TA study does not provide clear explanation for the sluggish cooling process in Eu-CsPbBr₃. Moreover, this is a known fact that at room temperature, we are unable to record the intrinsic properties of a material due to interference of thermal vibrations. Thus, the low-temperature transient absorption study was conducted from 200 K to 5 K, in order to investigate the temperature-dependent spectroscopic properties (**Figure 7.4 a-d**).

7.2.4 Low Temperature Transient Absorption Study

To explore how hot carriers, behave with varying temperatures in the doped counterpart, we conducted a temperature-dependent transient absorption study for both CsPbBr₃ and Eu-CsPbBr₃. We accomplished this by exciting both systems with a 3.54 eV pump pulse. The slow

hot carrier cooling is one of the most vital factors required to improve the perovskite-based solar cell efficiency.¹ The excitation energy-dependent TA study however fails to explain the reason behind the sluggish hot carrier cooling in Eu-CsPbBr₃. So, to understand this intriguing behavior of carriers, the temperature-dependent transient absorption study of Eu-CsPbBr₃ was conducted. The temperature-dependent TA spectral plots are shown in **Figure 7.4 (a-d)** in the temperature range from 200 K to 5 K. The transient plots evidently display that the spectral features of CsPbBr₃ NCs are intact (a bleach and two positive signals) irrespective of the lattice temperature. However, as it is well demonstrated in previous report that in CsPbBr₃ at 5 K, a supplementary bleach is observed due to the stimulated emission of bound exciton.³⁴ But in the Eu-CsPbBr₃ NCs no such bleach is observable. Basically, at low temperatures, an additional negative bleach signal was observed in CsPbBr₃ which is due to the stimulated emission of the defect-induced bound exciton. The origin of this bound exciton is attributable to the involvement of shallow trap states present near the CB edge due to Br⁻ vacancies (**Figure 7.4 f (left panel)**).^{18,31} The complete absence of such a feature in the TA plots even at 5K directly implies that there is no such bound exciton formation in this system. The fact that can't be ignored is that although this bound exciton is not pragmatic at room temperature, yet it's presence could not be resolved as it is overlapping with the band edge exciton. Nonetheless, as we lower the temperature the band edge exciton exhibits redshift and thus the bound exciton can be easily resolved at low temperatures.

The presence of bound exciton near the band edge inevitably creates an additional pathway (**Figure 7.4 f**) for the carriers and thus leads to faster growth and recovery. Summing up our entire studies this clears the confusion regarding contradiction of slow cooling in Eu-CsPbBr₃. As during the synthesis of Eu-CsPbBr₃ NCs, EuBr₃ was added as a precursor, so it reduces the Br⁻ vacancies in the doped system and similar observation identified in Mn-CsPbBr₃ nanoplatelets.³⁵ Even though the presence of Eu³⁺ introduces the potential for energy transfer in the system, but passivation of Br⁻ vacancies plays a crucial role in the doped system.

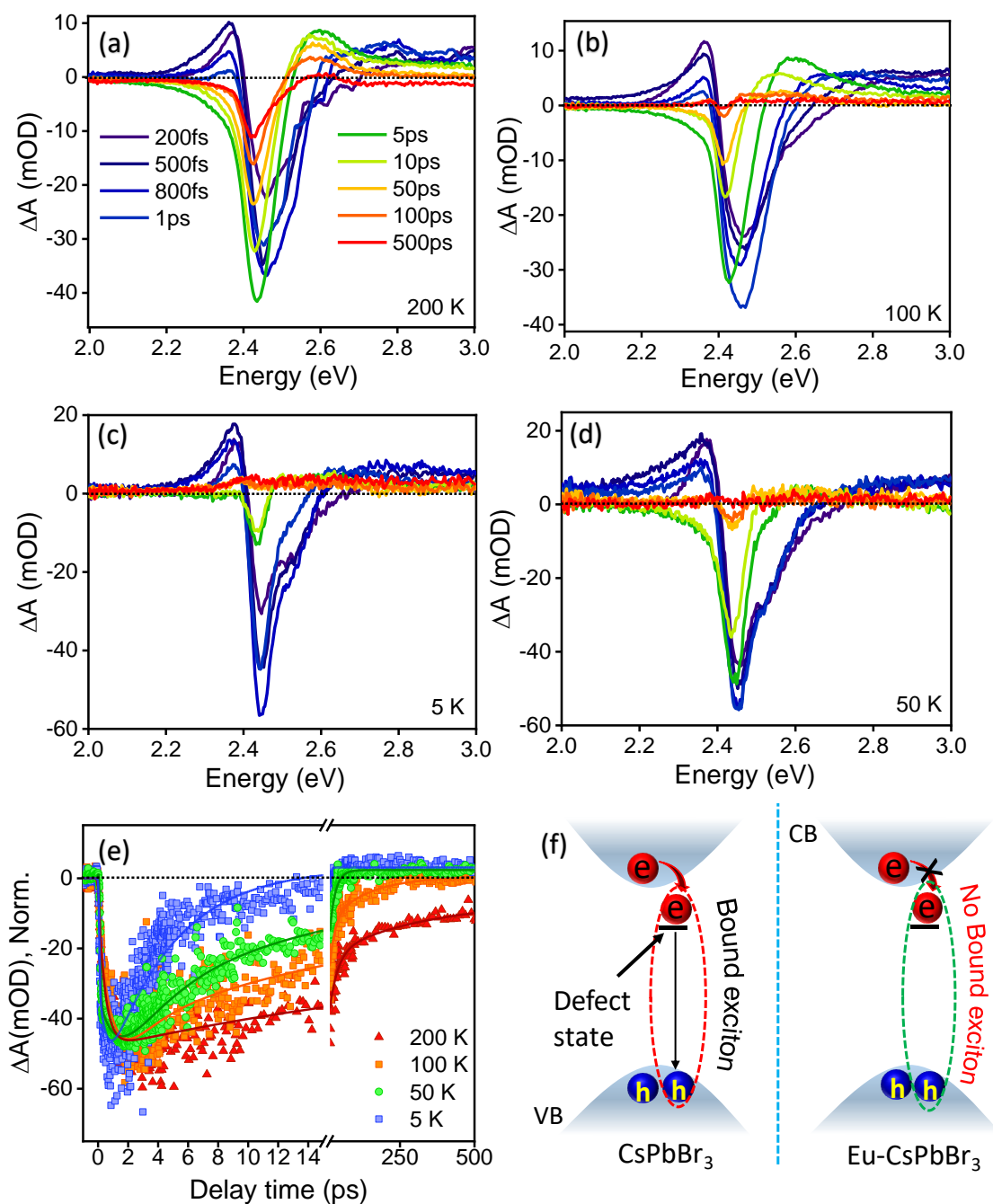


Figure 7.4 The transient absorption spectra of Eu-CsPbBr_3 in the temperature range of (a-d) 200 K-5K upon 3.54 eV pump excitation, (e) The normalized transient bleach recovery kinetics for all the temperatures under consideration, and (f) schematic representation of bound exciton formation in both systems

Table 7.3 Kinetic fitting parameters at bleach position for Eu-CsPbBr₃ at different temperature under 3.54 eV pump excitation.

Lattice temp. (K)	τ_g^1	τ_g^2	τ_1	τ_2	τ_3	τ_4
200	<150 fs (42%)	610 fs (58%)	8.5 ps (-39 %)	70 ps (-34%)	250 ps (-12%)	>1 ns (-15%)
100	<150 fs (44%)	470 fs (56%)	7.3 ps (-71 %)	41 ps (-22%)	150 ps (-7%)	
50	<150 fs (76%)	350 fs (20%)	5.6 ps (-76 %)	13.7 ps (-19.9%)	23.5 ps (4%)	>1 ns (-4.1%)
5	<150 fs (81%)	280 fs (12.8%)	4.5 ps (-93.5 %)	15.5 ps (6.2%)	>1ns (-6.5%)	

The absence of an alternative channel, i.e., bound excitons, which offer an additional route for carriers to relax, apart from the conventional band edge relaxation leads to the retarded carrier cooling. Thus, the reduction in the Br⁻ vacancies in the doped counterparts could be held accountable for a lesser density of shallow defect states, which eventually leads to the absence of bound exciton. Thus, this clears that the slow hot carrier cooling is definitely the outcome of the passivation of Br⁻ vacancies in the Eu-CsPbBr₃ NCs. Summing up all the previous annotations we can eventually draw a clear conclusion about the slow hot carrier cooling in Eu-CsPbBr₃ NCs it is due to the absence of bound exciton thus blocking the extra channel for the carriers to decay and henceforth the cooling time for carriers is increased. Previously, such observation has been perceived in case of dodecahedron CsPbBr₃ where due to passivation of Br⁻ vacancies sluggish carrier cooling is pragmatic.¹⁸ Further, the bleach decay kinetics is scrutinized for diverse temperatures and it can be observed that the bleach growth and decay are quicker (**Table 7.3**) as the temperature is reduced. This observation in perovskites is quite contrary to what is expected as upon lowering the temperature, the lattice is frozen, and accordingly, the carrier relaxation which was previously arbitrated via LO phonons at RT is later mediated via acoustic phonons thus the bleach growth time which implies the carrier relaxation should conventionally decelerate.³¹ As in the case of CsPbBr₃, the LO phonon energy is 16 meV, limiting the lattice's ability to create LO phonons at low temperatures, and thereby acoustic phonon-mediated carrier cooling is observed. However, contrary to that we witness a quicker growth and recovery at low temperatures in CsPbBr₃, (**Figure 7.4 e**) which

is attributed to absent of polaron formation at low temperatures. The interplay of charge carriers with energetically diverse phonon modes is one key determinant of carrier cooling rates. The TA spectral response shows that the carriers act quite differently at cryogenic and ambient temperatures. When we examine the bleach minima kinetics (**Figure 7.4 f**), we see that the carriers cool quickly at temperatures below 200 K, whereas they cool slowly at higher temperatures (>200 K). And it is well established that in CsPbBr₃ at RT polaron formation is feasible but at cryogenic temperatures, polaron formation is not viable because the lattice is not capable of generating high energy LO phonons (~16 meV) responsible for polaron formation. Thus, faster cooling is witnessed at cryogenic temperatures. The low temperature studies however give the answers to the retarded carrier cooling observed in Eu-CsPbBr₃, that is a clear indication of the absence of bound exciton (as no negative bleach is observed towards higher energy regime) which obstructs the additional relaxation pathway for the carriers and eventually decelerates the carrier cooling.

7.2.5 Photoconductivity and Mobility Calculations

Further, as we know there is a direct implication of carrier cooling over photoconductivity and carrier mobility, the optical pump THz probe spectroscopy was conducted which is a non-invasive spectroscopic method to determine the mobility and photoconductivity of semiconducting NCs. The conclusions drawn from excitation energy and low-temperature TA studies unquestionably explain that the carrier cooling is slow in Eu-CsPbBr₃ due to the absence of bound exciton. Also, it is a well-considered fact that the rate of carrier cooling has its direct implication over the mobility of the carriers. But these parameters could not be determined using TA study, so we took up a complementary technique i.e., OTP spectroscopy for CsPbBr₃ and Eu-CsPbBr₃ upon 2.58 eV pump excitation. The above-mentioned THz TDS approach, OTP spectroscopy, has been frequently employed in recent years to explore charge carrier dynamics in perovskite semiconductors spanning picosecond-to-nanosecond time scales.

Figure 7.5 a shows the THz temporal waveforms that were transmitted through the air, quartz substrate and samples that were spin-coated over the substrate (CsPbBr₃ and Eu-CsPbBr₃). The shift in the main peak feature of the THz pulse in the samples relative to the bare substrate (both in terms of amplitude and delay time due to the additional optical path traversed. The

dynamics of charge carriers are represented as photo-induced THz transmission variations ($\Delta E/E$) of the samples.

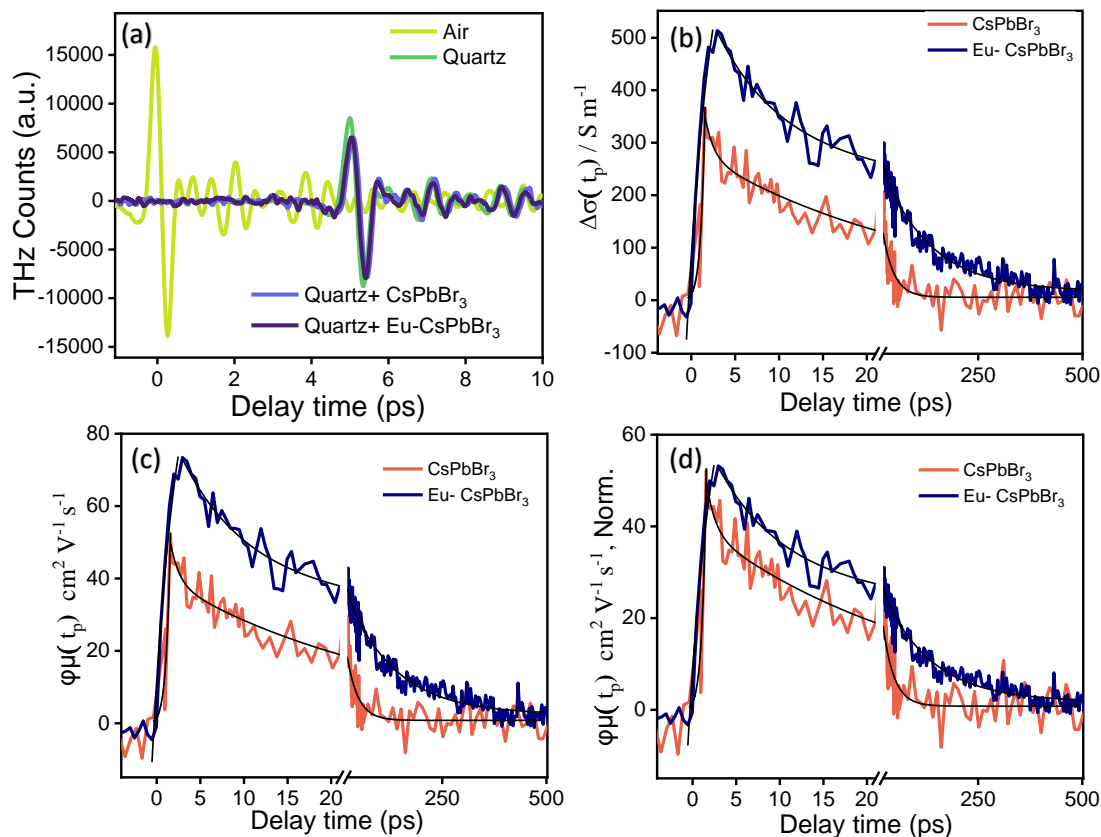


Figure 7.5 (a) THz waveforms transmitted through air, quartz, CsPbBr_3 , and Eu-CsPbBr_3 , the time-dependent traces of (b) THz conductivity, (c) effective mobility, and (d) Normalized effective mobility plot for CsPbBr_3 , and Eu-CsPbBr_3 upon 2.58 eV pump excitation.

Additionally, by assessing the THz response as with a time delay amid the optical pump and THz probe pulses, the transient decay kinetics of charge carriers could be acquired. Some previous investigations have unveiled a correlation between carrier mobility and the carrier cooling.³⁶⁻⁴⁰ OPTP spectroscopy is one of the principle methods that is frequently utilized to probe into the material's photoconductivity, mobility, and time evolution of charge carriers.⁴¹ The transient photoconductivity and mobility plots for both the samples have been provided in **Figure 7.5 (b-d)**.

According to the following equation, the photoconductivity ($\Delta\sigma$) is directly correlated to the transient variation of the electric field:⁴²

$$\Delta\sigma(t_p) = \frac{\epsilon_0 c}{d} (n_a + n_b) \left[\frac{-\Delta(E(t_p))}{(E_0(t_p))} \right] \quad \text{Eq.7.1}$$

Here, ΔE is the photo-induced change in the THz waveform. where n_a and n_b are the respective refractive indices of air and polystyrene, c stands for the speed of light, and d denotes the thickness of photo-excited samples.

Further, the effective mobility ($\varphi\mu$) is directly associated with the photoconductivity and is defined by the following equation:

$$\varphi\mu = \frac{\Delta\sigma}{N_0 q} \quad \text{Eq.7.2}$$

where $\Delta\sigma$ is the transient photoconductivity, N_0 defines the carrier density, q represents the elementary charge and φ denotes the conversion ratio of the incident photons to the free carriers.

The transient photoconductivity (**Figure 7.5 b**) shows that the value of photoconductivity is almost 1.5 times higher in the doped Eu-CsPbBr₃ in contrast to that of bare CsPbBr₃. Additionally, the slow cooling observed in the TA studies is a consequence of absence of bound exciton in the Eu-CsPbBr₃. This is a known fact that hot carrier cooling and polaron formation have an impact on mobility and photoconductivity. As witnessed by the transient absorption studies, carrier cooling is found to be much slower in the Eu-CsPbBr₃. In the same trend, it has also been observed that the value of photoconductivity is much higher (almost 1.5 times higher) in the doped counterpart which could be an outcome of the absent bound exciton. Additionally, slower growth in the transient mobility plot (**Figure 7.5 d**) at early time scales can also be witnessed. In our previous study we found the faster polaron formation in dodecahedron affected the mobility of the system.¹⁸ However, the transient absorption (TA) studies provide strong evidence that both polaron formation and decay remain unaffected by doping. This firmly contradicts the earlier hypothesis. Instead, our current results clearly show that the observed behavior is primarily a consequence of the absence of bound excitons. Moreover, if the role of polaron formation was involved the mobility intensity would not show an upsurge as observed in this case. Here, the carriers that were trapped in the bound exciton state could

not directly participate at early time scales in the pristine system and thus lead to a lower value of photoconductivity. But, as we substitute the system and add the precursor EuBr_3 it leads to passivation of Br^- vacancies thus, no bound exciton (state observed due to defect state of Br^- vacancies) is observed. Apart from this, the mobility is also calculated (**Figure 7.5 c,d**), and it has been observed that the mobility plot is slower in the doped system. Rather, the later growth is more readily explained by how mobility gets affected by the changes in hot carriers. Previously such an effect has been witnessed by various reports in perovskites as well as GaAs-based systems.^{43,44} The observed slower rise in transient mobility plot can then be initially attributed to the slower hot carriers cooling in the doped system. The "hot" charge carriers and exciton go through a cooling process with excess energy loss pathways via carrier-phonon inelastic scattering. In CsPbBr_3 these hot carriers subsequently populate the bound exciton state present just below the VB and lead to quicker recovery of carriers. Reducing the bound exciton, which in turn reduces the population of these hot carriers to the defect state may explain the increase in the initial time photoconductivity in the doped system. Thus, the carrier photoconductivity was found to be increased and the mobility was also transiently slower as a consequence of this slower hot carrier cooling.

7.3 Conclusion

To conclude, we have successfully synthesized the Eu-CsPbBr_3 NCs using the hot injection method and the carrier dynamics have been deeply investigated employing ultrafast transient absorption and terahertz spectroscopy. The excitation energy-dependent transient absorption study shows that hot carrier cooling is found to be retarded in Eu-CsPbBr_3 system. However, the polaron formation and decay time is found to be intact, which rules out the possibility of slower hot carrier cooling because of polaron formation. The low-temperature TA study clearly suggests that this is an effect of absence of the bound exciton due to passivation of Br^- vacancies. Further, photoconductivity is found to be increased along with slow transient mobility at early time scales as depicted by the OTP studies, which was an outcome of slower hot carrier cooling in Eu-CsPbBr_3 . Altogether our findings demonstrate that Eu-CsPbBr_3 is a superior alternative to the traditional CsPbBr_3 system for hot carrier photovoltaic devices.

7.4 References

- (1) Zhou, Z.; He, J.; Frauenheim, T.; Prezhd, O. V; Wang, J. Control of Hot Carrier

- Cooling in Lead Halide Perovskites by Point Defects. *J. Am. Chem. Soc.* **2022**, *144* (39), 18126–18134.
- (2) Mix, L. T.; Yarotski, D. A.; Ghosh, D.; Tisdale, J.; Lee, M. C.; O’Neal, K. R.; Sirica, N.; Neukirch, A. J.; Nie, W.; Taylor, A. J.; Prasankumar, R. P.; Tretiak, S. Hot Carrier Cooling and Recombination Dynamics of Chlorine-Doped Hybrid Perovskite Single Crystals. *J. Phys. Chem. Lett.* **2020**, *11* (19), 8430–8436.
- (3) Wang, T.; Jin, L.; Hidalgo, J.; Chu, W.; Snaider, J. M.; Deng, S.; Zhu, T.; Lai, B.; Prezhdo, O.; Correa-Baena, J. P.; Huang, L. Protecting Hot Carriers by Tuning Hybrid Perovskite Structures with Alkali Cations. *Sci. Adv.* **2020**, *6* (43).
- (4) Conibeer, G.; Ekins-Daukes, N.; Guillemoles, J.-F.; König, D.; Cho, E.-C.; Jiang, C.-W.; Shrestha, S.; Green, M. Progress on Hot Carrier Cells. *Sol. Energy Mater. Sol. Cells* **2009**, *93* (6), 713–719.
- (5) Ross, R. T.; Nozik, A. J. Efficiency of Hot-carrier Solar Energy Converters. *J. Appl. Phys.* **1982**, *53* (5), 3813–3818.
- (6) Jin, Z.; Peng, Y.; Fang, Y.; Ye, Z.; Fan, Z.; Liu, Z.; Bao, X.; Gao, H.; Ren, W.; Wu, J. Photoinduced Large Polaron Transport and Dynamics in Organic–Inorganic Hybrid Lead Halide Perovskite with Terahertz Probes. *Light Sci. Appl.* **2022**, *11* (1), 209.
- (7) Shockley, W. The Shockley-Queisser Limit. *J. Appl. Phys.* **1961**, *32* (3), 510–519.
- (8) Ehrler, B.; Alarcón-Lladó, E.; Tabernig, S. W.; Veeken, T.; Garnett, E. C.; Polman, A. Photovoltaics Reaching for the Shockley–Queisser Limit. *ACS Energy Lett.* **2020**, *5*, 9,3029–3033.
- (9) Krogstrup, P.; Jørgensen, H. I.; Heiss, M.; Demichel, O.; Holm, J. V.; Aagesen, M.; Nygard, J.; Fontcuberta i Morral, A. Single-Nanowire Solar Cells beyond the Shockley–Queisser Limit. *Nat. Photonics* **2013**, *7* (4), 306–310.
- (10) Queisser, H. J. Slip Patterns on Boron-doped Silicon Surfaces. *J. Appl. Phys.* **1961**, *32* (9), 1776–1780.
- (11) Li, M.; Fu, J.; Xu, Q.; Sum, T. C. Slow Hot-Carrier Cooling in Halide Perovskites: Prospects for Hot-Carrier Solar Cells. *Adv. Mater.* **2019**, *31* (47), 1–17.
- (12) Nelson, C. A.; Monahan, N. R.; Zhu, X.-Y. Exceeding the Shockley–Queisser Limit in Solar Energy Conversion. *Energy Environ. Sci.* **2013**, *6* (12), 3508–3519.
- (13) Tisdale, W. A.; Williams, K. J.; Timp, B. A.; Norris, D. J.; Aydil, E. S.; Zhu, X.-Y. Hot-Electron Transfer from Semiconductor Nanocrystals. *Science* **2010**, *328* (5985), 1543–

- 1547.
- (14) Nozik, A. J.; Beard, M. C.; Luther, J. M.; Law, M.; Ellingson, R. J.; Johnson, J. C. Semiconductor Quantum Dots and Quantum Dot Arrays and Applications of Multiple Exciton Generation to Third-Generation Photovoltaic Solar Cells. *Chem. Rev.* **2010**, *110* (11), 6873–6890.
- (15) Kaur, G.; Justice Babu, K.; Ghorai, N.; Goswami, T.; Maiti, S.; Ghosh, H. N. Polaron-Mediated Slow Carrier Cooling in a Type-1 3D/0D CsPbBr₃@ Cs₄PbBr₆ Core–Shell Perovskite System. *J. Phys. Chem. Lett.* **2019**, *10* (18), 5302–5311.
- (16) Shukla, A.; Kaur, G.; Justice Babu, K.; Ghorai, N.; Goswami, T.; Kaur, A.; N. Ghosh, H. Effect of Confinement on the Exciton and Biexciton Dynamics in Perovskite 2D-Nanosheets and 3D-Nanocrystals. *J. Phys. Chem. Lett.* **2020**, *11* (15), 6344–6352.
- (17) Justice Babu, K.; Kaur, G.; Shukla, A.; Kaur, A.; Goswami, T.; Ghorai, N.; Ghosh, H. N. Concurrent Energy- and Electron-Transfer Dynamics in Photoexcited Mn-Doped CsPbBr₃ Perovskite Nanoplatelet Architecture. *J. Phys. Chem. Lett.* **2021**, *12* (1), 302–309.
- (18) Justice Babu, K.; Kaur, G.; Shukla, A.; Saha, R.; Kaur, A.; Sachdeva, M.; Yadav, D. K.; Ghosh, H. N. Fast Polaron Formation and Low Carrier Mobility in Defect-Free Polyhedral CsPbBr₃ Perovskite Nanocrystals. *ACS Photonics* **2022**, *9*(3), 969–978.
- (19) Chen, J.; Messing, M. E.; Zheng, K.; Pullerits, T. Cation-Dependent Hot Carrier Cooling in Halide Perovskite Nanocrystals. *J. Am. Chem. Soc.* **2019**, *141* (8), 3532–3540.
- (20) Yamada, Y.; Kanemitsu, Y. Electron-Phonon Interactions in Halide Perovskites. *NPG Asia Mater.* **2022**, *14* (1), 48.
- (21) Ghosh, D.; Welch, E.; Neukirch, A. J.; Zakhidov, A.; Tretiak, S. Polarons in Halide Perovskites: A Perspective. *J. Phys. Chem. Lett.* **2020**, *11* (9), 3271–3286.
- (22) Mir, W. J.; Mahor, Y.; Lohar, A.; Jagadeeswararao, M.; Das, S.; Mahamuni, S.; Nag, A. Postsynthesis Doping of Mn and Yb into CsPbX₃ (X = Cl, Br, or I) Perovskite Nanocrystals for Downconversion Emission. *Chem. Mater.* **2018**, *30* (22), 8170–8178.
- (23) Pan, G.; Bai, X.; Yang, D.; Chen, X.; Jing, P.; Qu, S.; Zhang, L.; Zhou, D.; Zhu, J.; Xu, W.; Dong, B.; Song, H. Doping Lanthanide into Perovskite Nanocrystals: Highly Improved and Expanded Optical Properties. *Nano Lett.* **2017**, *17* (12), 8005–8011.
- (24) Meinardi, F.; Akkerman, Q. A.; Bruni, F.; Park, S.; Mauri, M.; Dang, Z.; Manna, L.; Brovelli, S. Doped Halide Perovskite Nanocrystals for Reabsorption-Free Luminescent

- Solar Concentrators. *ACS energy Lett.* **2017**, 2 (10), 2368–2377.
- (25) Milstein, T. J.; Kluherz, K. T.; Kroupa, D. M.; Erickson, C. S.; De Yoreo, J. J.; Gamelin, D. R. Anion Exchange and the Quantum-Cutting Energy Threshold in Ytterbium-Doped CsPb (Cl_{1-x} Br_x)₃ Perovskite Nanocrystals. *Nano Lett.* **2019**, 19 (3), 1931–1937.
- (26) Pan, G.; Bai, X.; Yang, D.; Chen, X.; Jing, P.; Qu, S.; Zhang, L.; Zhou, D.; Zhu, J.; Xu, W. Doping Lanthanide into Perovskite Nanocrystals: Highly Improved and Expanded Optical Properties. *Nano Lett.* **2017**, 17 (12), 8005–8011.
- (27) Wang, S.; Xu, Y.; Chen, R.; Zhu, M.; Wang, M.; Cao, M.; Liu, Y.; Ding, H.; Zhang, S.; Bai, J.; Ren, J.; Xuan, T.; Li, H. Highly Efficient and Stable Eu³⁺-Doped CsPbBr₃/Cs₄PbBr₆ Perovskites for White Light-Emitting Diodes. *Coatings* **2022**, 12 (4), 512.
- (28) Lin, C. Y.; Yang, S. H.; Lin, J. L.; Yang, C. F. Effects of the Concentration of Eu³⁺ Ions and Synthesizing Temperature on the Luminescence Properties of Sr_{2-x}Eu_xZnMoO₆ Phosphors. *Appl. Sci.* **2017**, 7 (1), 30.
- (29) Li, Q.; Liu, Y.; Chen, P.; Hou, J.; Sun, Y.; Zhao, G.; Zhang, N.; Zou, J.; Xu, J.; Fang, Y.; Dai, N. Excitonic Luminescence Engineering in Tervalent-Europium-Doped Cesium Lead Halide Perovskite Nanocrystals and Their Temperature-Dependent Energy Transfer Emission Properties. *J. Phys. Chem. C* **2018**, 122 (50), 29044–29050.
- (30) Wu, J.; Bai, H.; Qu, W.; Cao, G.; Zhang, Y.; Yu, J. Preparation of Eu³⁺-Doped CsPbBr₃ Quantum-Dot Microcrystals and Their Luminescence Properties. *Opt. Mater.* **2019**, 97, 109454.
- (31) Kaur, G.; Babu, K. J.; Ghosh, H. N. Temperature-Dependent Interplay of Polaron Formation and Hot Carrier Cooling Dynamics in CsPbBr₃ Nanocrystals: Role of Carrier – Phonon Coupling Strength. **2020**, 11, 6206-6213.
- (32) Shah, J. *Ultrafast Spectroscopy of Semiconductors and Semiconductor Nanostructures*; Springer Science & Business Media, 2013; Vol. 115.
- (33) Leheny, R. F.; Shah, J.; Fork, R. L.; Shank, C. V.; Migus, A. Dynamics of Hot Carrier Cooling in Photo-Excited GaAs. *Solid State Commun.* **1979**, 31 (11), 809–813.
- (34) Kaur, G.; Babu, K. J.; Ghosh, H. N. Temperature-Dependent Interplay of Polaron Formation and Hot Carrier Cooling Dynamics in CsPbBr₃ Nanocrystals: Role of Carrier–Phonon Coupling Strength. *J. Phys. Chem. Lett.* **2020**, 11 (15), 6206–6213.
- (35) Justice Babu, K.; Kaur, G.; Shukla, A.; Kaur, A.; Goswami, T.; Ghorai, N.; Ghosh, H. N. Concurrent Energy- and Electron-Transfer Dynamics in Photoexcited Mn-Doped CsPbBr₃

- Perovskite Nanoplatelet Architecture. *J. Phys. Chem. Lett.* **2021**, *12* (1), 302–309.
- (36) Ihly, R.; Dowgiallo, A.-M.; Yang, M.; Schulz, P.; Stanton, N. J.; Reid, O. G.; Ferguson, A. J.; Zhu, K.; Berry, J. J.; Blackburn, J. L. Efficient Charge Extraction and Slow Recombination in Organic–Inorganic Perovskites Capped with Semiconducting Single-Walled Carbon Nanotubes. *Energy Environ. Sci.* **2016**, *9* (4), 1439–1449.
- (37) Wang, Y.; Zhang, Y.; Zhang, P.; Zhang, W. High Intrinsic Carrier Mobility and Photon Absorption in the Perovskite $\text{CH}_3\text{NH}_3\text{PbI}_3$. *Phys. Chem. Chem. Phys.* **2015**, *17* (17), 11516–11520.
- (38) Tailor, N. K.; Yukta; Ranjan, R.; Ranjan, S.; Sharma, T.; Singh, A.; Garg, A.; Nalwa, K. S.; Gupta, R. K.; Satapathi, S. The Effect of Dimensionality on the Charge Carrier Mobility of Halide Perovskites. *J. Mater. Chem. A* **2021**, *9* (38), 21551–21575.
- (39) Motta, C.; El-Mellouhi, F.; Sanvito, S. Charge Carrier Mobility in Hybrid Halide Perovskites. *Sci. Rep.* **2015**, *5* (1), 12746.
- (40) Stoumpos, C. C.; Malliakas, C. D.; Peters, J. A.; Liu, Z.; Sebastian, M.; Im, J.; Chasapis, T. C.; Wibowo, A. C.; Chung, D. Y.; Freeman, A. J. Crystal Growth of the Perovskite Semiconductor CsPbBr_3 : A New Material for High-Energy Radiation Detection. *Cryst. Growth Des.* **2013**, *13* (7), 2722–2727.
- (41) Bala, A.; Kumar, V. Stability of the Eu^{2+} Dopant in CsPbBr_3 Perovskites: A First-Principles Study. *J. Phys. Chem. C* **2019**, *123* (12), 6965–6969.
- (42) Yettapu, G. R.; Talukdar, D.; Sarkar, S.; Swarnkar, A.; Nag, A.; Ghosh, P.; Mandal, P. Terahertz Conductivity within Colloidal CsPbBr_3 Perovskite Nanocrystals: Remarkably High Carrier Mobilities and Large Diffusion Lengths. *Nano Lett.* **2016**, *16* (8), 4838–4848.
- (43) Bretschneider, S. A.; Ivanov, I.; Wang, H. I.; Miyata, K.; Zhu, X.; Bonn, M. Quantifying Polaron Formation and Charge Carrier Cooling in Lead-Iodide Perovskites. *Adv. Mater.* **2018**, *30* (29), 1707312.
- (44) Monti, M.; Tao, S. X.; Staniforth, M.; Crocker, A.; Griffin, E.; Wijesekara, A.; Hatton, R. A.; Lloyd-Hughes, J. Efficient Intraband Hot Carrier Relaxation in the Perovskite Semiconductor $\text{Cs}_{1-x}\text{Rb}_x\text{SnI}_3$ Mediated by Strong Electron–Phonon Coupling. *J. Phys. Chem. C* **2018**, *122* (36), 20669–20675.

Chapter 8

Conclusion & Future Prospects

8.1. Conclusion

The main goal of this thesis was to develop a thorough understanding of the charge carrier dynamics in perovskite materials. We used transient absorption and terahertz spectroscopy to accomplish this goal. Additionally, in order to investigate the material's inherent qualities throughout a range of temperatures, we performed temperature dependent TA experiments. Due to the frequent exposure of photovoltaic devices to extremely high temperatures while operating, this study of temperature-dependent properties is extremely important. Understanding the carrier cooling processes is vital as it plays a pivotal role in advancing photovoltaic devices based on perovskite material. **Chapter 1** highlights the significance of solar energy and advances in photovoltaic devices, focusing on perovskite materials' rapid rise. It explores perovskite classifications, especially Lead Halide Perovskites (LHPs), and investigates how phase transitions, doping, and crystal morphology influence carrier cooling. The chapter also examines factors like polaron formation, carrier-phonon coupling, Auger heating, and defect states in affect the carrier cooling. **Chapter 2**, discusses the Synthesis procedure and instrumentation techniques used throughout my thesis work placing a strong foundation for the subsequent chapters' research. **Chapter 3** demonstrates how the carrier cooling in perovskite solar cells can be significantly influenced by the confinement of the perovskite crystals. The fundamental mechanisms have been clarified through a thorough analysis of the samples excited at various energies. Furthermore, in both 2D and 3D systems, the exciton and biexciton dynamics of charge carriers show a slower carrier cooling at higher energy excitations. The injection of carriers into higher energy levels, necessitates a relaxation period towards the band-edge position. A noteworthy finding of the experiment is the

fascinating difference between the hot carrier cooling rates of 2D NSs and 3D NCs. The reduced Fröhlich interaction, due to increased surface-volume ratio in 2D system's leads to faster carrier cooling. We also observed that the rate of biexciton formation (indicative of intraband cooling) is quicker in the 2D NSs compared to the 3D NCs. This fascinating property allows for quicker energy dissipation into the surrounding medium. This in-depth investigation advances our fundamental knowledge of how dimensionality affects charge carrier relaxation dynamics and lays the path for the creation of innovative optoelectronic devices.

In **Chapter 4**, we tuned the facets, and a novel synthesized polyhedral dodecahedron was formed. In our thorough study, we created the perovskite dodecahedron-CsPbBr₃ and compared its properties with the convention cube-CsPbBr₃ perovskite. The steady-state optical studies show that the absorbance features were the same in both the systems but, the PLQY was increased from 22 % in cube-CsPbBr₃ to 92% in the dodecahedron-CsPbBr₃. Further, the TRPL studies show an almost 4-fold increment in PL lifetime in dodecahedron-CsPbBr₃. To comprehend the photophysical properties in both systems, TA studies were conducted. The TA studies revealed that dodecahedron-CsPbBr₃ displays prolonged carrier cooling and a remarkable 20-30% enhancement in biexciton yield compared to cube-CsPbBr₃. According to low-temperature PL experiments, where no additional PL emission towards lower energy regime due to bound excitons was observed. Thus, slower carrier cooling in the dodecahedron-CsPbBr₃ can be attributed to the absence of bound excitons. Furthermore, temperature-dependent TA investigations demonstrate that polaron sizes in dodecahedron-CsPbBr₃ is greater than those in cube-CsPbBr₃ as a result of the quicker formation of polarons within 0.25 ps in dodecahedron-CsPbBr₃ in contrast to the cube-CsPbBr₃(0.55 ps). The slower bleach growth and decay compared to cube-CsPbBr₃ may be due to the increase in polaron size from 34.7 (cube-CsPbBr₃) to 39.6 (dodecahedron-CsPbBr₃). Further, the terahertz time-domain spectroscopy (THz-TDS) investigation clearly demonstrates that the carrier mobility at very early time scales (a few picoseconds) in the dodecahedron-CsPbBr₃ system is roughly twice as low as it is in the cube-CsPbBr₃ system. This observation further supports the fact that the lower mobility in the dodecahedron-CsPbBr₃ system at early time scales is due to the faster polaron formation which leads to slower carrier cooling. Our research findings provide a solid foundation for the intriguing possibility of utilizing the advantages of dodecahedron-CsPbBr₃

in highly effective device applications. With additional facets and retarded carrier cooling, we firmly believe that dodecahedron-CsPbBr₃ is a better alternative to conventional cube-CsPbBr₃.

Inorganic lead halide perovskites have become a cutting-edge material for solar cell applications in the field of photovoltaic research, particularly as an absorbent layer. In **Chapter 5** we introspected the photophysical properties of CsPbCl₃, which has received constant attention for its capacity to emit strong blue light and has the prospective to be doped or stacked with a different complimentary material. CsPbCl₃ is an interesting perovskite for understanding the behavior of carriers when the crystal exhibits. However, there is still a lack of knowledge regarding its photophysical characteristics in respect to temperature and phase transitions. So in this study, we aimed to decipher the photophysics of CsPbCl₃ nanocrystals (NCs) utilizing ultrafast transient absorption (TA) and terahertz (THz) spectroscopy with change in temperature and excitation energy. Our spectroscopic investigation also sheds light on the temperature-dependent carrier dynamics through the orthorhombic to monoclinic phase transition. Moreover, there is a direct correlation between carrier relaxation, carrier temperature, and energy loss during phase transitions. The excitation energy-dependent OPTP measurements, reveal a noteworthy trend as the excitation energy decreases, the initial mobility decay rate slows down significantly. This phenomenon can be attributed to a reduction in Auger recombination and increased penetration depth. Understanding the temperature dependent carrier dynamics is crucial because the photovoltaic devices operate under varying temperature conditions. The insights gained from this study regarding the relaxation processes in relation to excitation energy and temperature offer valuable guidance for the development of advanced optoelectronic devices based on CsPbCl₃ perovskite nanocrystals.

As the introduction of RE³⁺ doping in CsPbCl₃ has revolutionized the field of optoelectronics, offering exciting opportunities to explore and manipulate optical, magnetic, and charge carrier transport properties, we further doped rare earth ions (RE³⁺) in the lattice of CsPbCl₃ in **Chapter 6**. Since the absorption, as well as PL spectrum of CsPbCl₃, are constrained in the UV region, if we dope the crystal with RE³⁺, it will extend the PL to the VIS region, where we now see distinct PL peaks peaking at 598, 616, and 700 nm. Here, we have used state-of-the-art methods including femtosecond fluorescence upconversion and transient absorption (TA)

spectroscopy to explore the complex photophysical transfer processes from the band edge of the host material, CsPbCl₃, to the europium ion (Eu³⁺). We observe an intriguing defect-mediated cascading energy transfer phenomenon from CsPbCl₃ to Eu³⁺, accompanied by intriguing cross-relaxation interactions among different states of Eu³⁺ revealing two distinct characteristic traits. One of these traits, peaking at 592 nm originating from magnetic dipole (MD) transition, exhibits faster growth and decay. While the other trait, attributed to electric dipole transition (ED), grows at a slower rate at 616 nm. Furthermore, our TA studies provide compelling evidence of charge transfer occurring from the band edge of CsPbCl₃ to shallow defect states induced by the Eu³⁺ doping. Additionally, we made a remarkable observation of two-photon absorption in our study, and intriguingly, we found no compromise in the efficiency of energy and charge transfer processes. This compelling result indicates that Eu-CsPbCl₃ not only demonstrates PL in the visible region but also has the capability to harness the solar energy spectrum within this range. By effectively utilizing visible and UV wavelengths, this material holds great promise for advancing solar energy conversion and driving significant advancements in optoelectronic applications.

In the last project, i.e., **Chapter 7**, our focus shifted to the study of Eu-doped CsPbBr₃ to explore the effects of doping on a different halide member, namely CsPbBr₃. This investigation delved into the spectroscopic properties of both CsPbBr₃ and Eu-CsPbBr₃. Our observations from transient absorption studies revealed a striking difference: the doped counterpart, Eu-CsPbBr₃, displayed significantly slower carrier cooling, which was contrary to what we observed in the case of CsPbCl₃. Interestingly, the formation and decay time of polaron remained unchanged. Further examination at low temperatures indicated that this phenomenon could be attributed to the absence of bound excitons, a result of Br-vacancy passivation. Additionally, our optical pump-terahertz probe studies demonstrated that this effect extended to impact carrier mobility and photoconductivity. As a consequence, Eu-CsPbBr₃ exhibited higher photoconductivity but slower transient mobility. The slow transient mobility in Eu-CsPbBr₃ is an outcome of retarded carrier cooling rate, primarily due to the absence of bound excitons. This absence of bound exciton means that an additional pathway through which carriers used to populate is no longer available, ultimately leading to the deceleration of carrier cooling. The implications of our research unequivocally highlight that the slower cooling of

hot carriers and the enhanced photoconductivity in Eu-CsPbBr₃ position it as a superior candidate for applications in photovoltaics.

8.2. Future Prospects

The future prospects for perovskite materials in the field of advanced technology are incredibly promising. Perovskite solar cells have garnered significant attention for their potential to revolutionize the renewable energy sector. Beyond photovoltaics, perovskites have shown great potential in optoelectronics, LEDs, and sensors, offering enhanced performance and versatility. As research continues to address stability and scalability challenges, perovskite materials are likely to play a crucial role in shaping the future of sustainable energy, electronics, and various cutting-edge technologies. In this thesis, we have initiated strategies aimed at moderating the rate of carrier cooling while concurrently improving the material properties which can assist in developing a more efficient photovoltaic device. The strategies encompass; changing the dimensionality, altering crystal morphology, doping, and temperature. These approaches offer valuable insights into material behavior and lay the foundation for understanding how the manipulation of material properties through chemical strategies can influence carrier cooling dynamics.

Further, understanding the temperature-dependent behavior of perovskite materials is crucial for optimizing their performance, especially in the context of carrier cooling. This behavior relates to how perovskites respond to changes in temperature and how carriers (electrons and holes) lose excess energy and return to their equilibrium state. In more detail, various strategies can be employed to efficiently control and manipulate carrier cooling, as outlined in my thesis.

Two primary strategies to consider are doping, where doping the material, and the designing of heterostructures, which involves combining different semiconductor materials to tune carrier cooling rates. These strategies can have a significant impact on the efficiency and speed at which carriers cool down in perovskite materials. Doping CsPbX₃ with lanthanides tunes the properties of perovskite materials and holds the potential to shift the PL properties into the NIR region. By introducing these lanthanide dopants, it becomes possible to extend the PL range of emitted light, thereby enabling the generation of a white light-emitting material. This approach involves manipulating the electronic structure and energy levels within the perovskite lattice,

which can result in the emission of a broader spectrum of colors. Doping perovskites with lanthanides, including ytterbium, is a promising avenue to explore for achieving these goals.

Additionally, synthesizing heterojunctions of CsPbX₃ materials with the semiconductor material offers a promising approach to further delay the carrier cooling process. This can be accomplished by combining CsPbX₃ perovskites with another semiconductor material to take advantage of the diverse carrier dynamics in different materials. By engineering this heterojunction, we can influence the carrier recombination and energy transfer processes, ultimately slowing down carrier cooling. Additionally, if we can expand the absorption range of CsPbX₃ from the UV-VIS spectrum to the NIR region, it would be helpful for various applications, such as photodetectors and solar cells, as it would enable the utilization of a broader range of incident light wavelengths for energy conversion.

These strategies hold significant potential for enhancing the performance of perovskite-based devices and opening up new opportunities for their application in a wide range of optoelectronic technologies. In the years to come, it is imperative to conduct comprehensive research on these systems in order to improve the PV performance of perovskite material.

List of Publications (Included in Thesis)

1. Effect of confinement on the exciton and biexciton dynamics in perovskite 2D-nanosheets and 3D-nanocrystals. **Ayushi Shukla**[#], Gurpreet Kaur[#], K Justice Babu, Nandan Ghorai, Tanmay Goswami, Arshdeep Kaur, Hirendra N Ghosh J. Phys. Chem. Lett. 2020, 11, 15, 6344–6352.
2. Fast Polaron Formation and Low Carrier Mobility in Defect-Free Polyhedral CsPbBr₃ Perovskite Nanocrystals. **Ayushi Shukla**[#], Kaliyamoorthy Justice Babu[#], Gurpreet Kaur[#], Ramchandra Saha, Arshdeep Kaur, Manvi Sachdeva, Dharmendra Kumar Yadav, and Hirendra N. Ghosh ACS Photonics 2022, 9, 3, 969–978.
3. Spectroscopic Investigation of Structural Perturbations in CsPbCl₃ Perovskite Nanocrystals: Temperature and Excitation Energy Dependent Study. **Ayushi Shukla**, Gurpreet Kaur, Kaliyamoorthy Justice Babu, and Hirendra Ghosh ACS Photonics 2023, 10, 6, 1906–1915.
4. Defect-Interceded Cascading Energy Transfer and Underlying Charge Transfer in Europium-Doped CsPbCl₃ Nanocrystals. **Ayushi Shukla**, Gurpreet Kaur, Kaliyamoorthy Justice Babu, Arshdeep Kaur, Dharmendra Kumar Yadav, and Hirendra N. Ghosh J. Phys. Chem. Lett. 2022, 13, 1, 83–90.
5. Retarded Hot Carrier Relaxation and Augmented Photoconductivity in Europium doped CsPbBr₃ Nanocrystals. **Ayushi Shukla**, Gurpreet Kaur, Kaliyamoorthy Justice Babu, Himanshu Bhatt, Vikas kumar and Hirendra N. Ghosh. (to be communicated)

List of Publications (Not included in thesis)

1. Probing the charge transfer mechanisms in type-II $\text{Cs}_2\text{AgBiBr}_6\text{-CdSe}$ composite system: ultrafast insights **Ayushi Shukla**[#], Gurpreet Kaur[#], Kaliyamoorthy Justice Babu, Himanshu Bhatt and Hirendra Ghosh Nanotechnology 2022.
2. Mapping the Real-Time Vibrational Infrastructure of Cs_2SnI_6 Nanocrystals through Coherent Phonon Dynamics Gurpreet Kaur, **Ayushi Shukla**, Kaliyamoorthy Justice Babu, and Hirendra N. Ghosh ACS Photonics 2022
3. Gurpreet Kaur, **Ayushi Shukla**, Arijit Sinha, Koyendriila Debnath, Kaliyamoorthy Justice Babu, Himanshu Bhatt, Umesh V. Waghmare, and Hirendra Nath Ghosh. "Ultrafast Glimpses of the Excitation Energy-Dependent Exciton Dynamics and Charge Carrier Mobility in Cs_2SnI_6 Nanocrystals." Nanoscale (2023).
4. Chemically Engineered Avenues: Opportunities for Attaining Desired Carrier Cooling in Perovskites Gurpreet Kaur, **Ayushi Shukla**, K. Justice Babu, Hirendra N. Ghosh The Chemical Record, e202200106
5. Temperature driven charge transfer process in quantum confined two-dimensional Mn-doped CsPbBr_3 perovskite nanoplatelets. K. Justice Babu, **Ayushi Shukla**, Gurpreet Kaur, Arshdeep Kaur, Himanshu Bhatt and Hirendra N. Ghosh Chemical Communications, 58(100), 13899-13902.
6. Influence of Molecular Separation on Through-Space Intervalence Transient Charge Transfer in Metal-Organic Frameworks with Cofacially arranged Redox Pair. Akashdeep Nath, Vikas Kumar, **Ayushi Shukla**, Hirendra Nath Ghosh, Sukhendu Mandal, Angewandte Chemie, 2023, e202308034.
7. In situ CsPbBr_3 architecture engineered in electrospun fibers and its ultrafast charge-transfer dynamics Kaliyamoorthy Justice Babu, Gurpreet Kaur, **Ayushi Shukla**, Arshdeep Kaur, Himanshu Bhatt, Nandan Ghorai, Goutam De, Hirendra N Ghosh Mater. Adv., 2022, 3, 6566-6576
8. Concurrent Energy- and Electron-Transfer Dynamics in Photoexcited Mn-doped CsPbBr_3 Perovskite Nanoplatelet Architecture Kaliyamoorthy Justice Babu, Gurpreet Kaur, **Ayushi Shukla**, Arshdeep Kaur, Tanmay Goswami, Nandan Ghorai, and Hirendra N. Ghosh, J. Phys. Chem. Lett. 2021, 12, 1, 302–309

9. Unravelling the Underlying Hot Carrier Transfer and Relaxation Pathways in Type-1 CsPbBr₃-PbS System Gurpreet Kaur, Ramchandra Saha, K. Justice Babu, **Ayushi Shukla**, and Hirendra N. Ghosh *J. Phys. Chem. C* 2021, 125, 10516–10525.
10. Ultrafast Hot Electron Transfer and Trap-State Mediated Charge Carrier Separation toward Enhanced Photocatalytic Activity in g-C₃N₄/ZnIn₂S₄ Heterostructure Himanshu Bhatt, Tanmay Goswami, Dharmendra Kumar Yadav, Nandan Ghorai, **Ayushi Shukla**, Gurpreet Kaur, Arshdeep Kaur, and Hirendra N. Ghosh. *J. Phys. Chem. Lett.* 2021, 12 (49), 11865–11872.
11. Enhanced Charge Carrier Separation and Improved Biexciton Yield at the p–n Junction of SnSe/CdSe Heterostructures: A Detailed Electrochemical and Ultrafast Spectroscopic Investigation Arshdeep Kaur, Tanmay Goswami, Sachin R. Rondiya, Yogesh A. Jadhav, K. Justice Babu, **Ayushi Shukla**, Dharmendra Kumar Yadav, and Hirendra N. Ghosh *J. Phys. Chem. Lett.* 2021, 12, 10958–10968.
12. Defect-Mediated Slow Carrier Recombination and Broad Photoluminescence in Non-Metal-Doped ZnIn₂S₄ Nanosheets for Enhanced Photocatalytic Activity Tanmay Goswami, Dharmendra Kumar Yadav, Himanshu Bhatt, Gurpreet Kaur, **Ayushi Shukla**, K. Justice Babu, and Hirendra N. Ghosh *J. Phys. Chem. Lett.* 2021, 12, 20, 5000–5008.
13. Probing Ultrafast Charge Separation in CZTS/CdS Heterojunctions through Femtosecond Transient Absorption Spectroscopy Arshdeep Kaur, Tanmay Goswami, K. Justice Babu, Nandan Ghorai, Gurpreet Kaur, **Ayushi Shukla**, Sachin R. Rondiya, and Hirendra N. Ghosh *J. Phys. Chem. C* 2020, 124, 36, 19476–19483.
14. Efficient Hot Electron Transfer and Extended Separation of Charge Carriers at the 1P Hot State in Sb₂Se₃/CdSe p–n Heterojunction, Arshdeep Kaur, Tanmay Goswami, K. Justice Babu, **Ayushi Shukla**, Himanshu Bhatt, and Hirendra N. Ghosh. *The Journal of Physical Chemistry Letters* 13, no. 48 (2022): 11354-11362.
15. Unveiling the Ultrafast Electron Transfer Dynamics in Epitaxial Dodecahedron CsPbBr₃/Au Heterostructure. Samaresh Samanta, Kaliyamoorthy Justice Babu, **Ayushi Shukla**, Gurpreet Kaur, Arshdeep Kaur, and Hirendra N. Ghosh**ChemPhotoChem*, doi.org/10.1002/cptc.202300242

Conferences attended/ Oral and Poster presentations

1. Presented a poster entitled on “*Elucidating the Cascading Energy and Charge Transfer Progressions in Europium-Doped Perovskite Nanocrystals*” and completed online the “Winter College on Optics: Terahertz Optics and Photonics” held at The Abdus Salam International Centre for Theoretical Physics, (6th - 17th February 2023).
2. Attended the “*Winter College on Optics: Terahertz Optics and Photonics*” online at The Abdus Salam International Centre for Theoretical Physics, (6th - 17th February 2023).
3. Oral presentation entitled on “*Unraveling the Carrier Cooling Mechanisms in Perovskite Materials: A Spectroscopic Investigation*” in Research Scholar Day (RSD) on 22nd and 23rd May, 2023, held at Institute of Nano Science and Technology, Mohali, Punjab India.
4. Delivered on Oral presentation entitled “*Exploring the Carrier Cooling Mechanisms in Perovskite Materials: A spectroscopic Investigation*” in National Conference on Futuristic materials (NCFS-2023) on 4th march 2023.
5. Presented a poster entitled on “*Unravelling the accelerated exciton and biexciton cooling in two-dimensional perovskite nanosheets*” at the 7th Theme Meeting on Ultrafast Sciences 2021 (UFS-2021) on 12th-14th November 2021.
6. Presented a poster entitled on “*Elucidating the Cascading Energy and Charge Transfer Progressions in Europium Doped Perovskite Nanocrystals*” in Ultrafast Sciences (UFS), held at IISER Thiruvananthapuram (IISER TVM) on 3rd-5th November 2022.
7. Presented a poster entitled on “*Unveiling the Temperature-Dependent Carrier Relaxation Processes in CsPbCl₃ Perovskite Nanocrystals*” in Perovskite Society of India Meet (PSIM-2023) held at Indian Institute of Technology Roorkee on 01st- 03rd, March 2023.
8. Presented a poster entitled on “*Unveiling the Temperature-Dependent Carrier Relaxation Processes in CsPbCl₃ Perovskite Nanocrystals*” in Perovskite Society of India Meet (UFS-2023) held at CSIR-National Physical Laboratory (CSIR-NPL), New Delhi on 25-27th November 2023.
9. Participated in International Conference on Advanced Characterization Techniques (ACT-2023) conducted online on 18th August 2023.

Copyright from Journals to Reuse the Content in Thesis



RightsLink

[Sign in/Register](#)



Effect of Confinement on the Exciton and Biexciton Dynamics in Perovskite 2D-Nanosheets and 3D-Nanocrystals

Author: Ayushi Shukla, Gurpreet Kaur, K. Justice Babu, et al

Publication: Journal of Physical Chemistry Letters

Publisher: American Chemical Society

Date: Aug 1, 2020

Copyright © 2020, American Chemical Society

PERMISSION/LICENSE IS GRANTED FOR YOUR ORDER AT NO CHARGE

This type of permission/license, instead of the standard Terms and Conditions, is sent to you because no fee is being charged for your order. Please note the following:

- Permission is granted for your request in both print and electronic formats, and translations.
- If figures and/or tables were requested, they may be adapted or used in part.
- Please print this page for your records and send a copy of it to your publisher/graduate school.
- Appropriate credit for the requested material should be given as follows: "Reprinted (adapted) with permission from {COMPLETE REFERENCE CITATION}. Copyright {YEAR} American Chemical Society." Insert appropriate information in place of the capitalized words.
- One-time permission is granted only for the use specified in your RightsLink request. No additional uses are granted (such as derivative works or other editions). For any uses, please submit a new request.

If credit is given to another source for the material you requested from RightsLink, permission must be obtained from that source.

[BACK](#)

[CLOSE WINDOW](#)



Fast Polaron Formation and Low Carrier Mobility in Defect-Free Polyhedral CsPbBr₃ Perovskite Nanocrystals

Author: Kaliyamoorthy Justice Babu, Gurpreet Kaur, Ayushi Shukla, et al

Publication: ACS Photonics

Publisher: American Chemical Society

Date: Mar 1, 2022

Copyright © 2022, American Chemical Society

PERMISSION/LICENSE IS GRANTED FOR YOUR ORDER AT NO CHARGE

This type of permission/license, instead of the standard Terms and Conditions, is sent to you because no fee is being charged for your order. Please note the following:

- Permission is granted for your request in both print and electronic formats, and translations.
- If figures and/or tables were requested, they may be adapted or used in part.
- Please print this page for your records and send a copy of it to your publisher/graduate school.
- Appropriate credit for the requested material should be given as follows: "Reprinted (adapted) with permission from {COMPLETE REFERENCE CITATION}. Copyright {YEAR} American Chemical Society." Insert appropriate information in place of the capitalized words.
- One-time permission is granted only for the use specified in your RightsLink request. No additional uses are granted (such as derivative works or other editions). For any uses, please submit a new request.

If credit is given to another source for the material you requested from RightsLink, permission must be obtained from that source.

[BACK](#)

[CLOSE WINDOW](#)

Defect-Interceded Cascading Energy Transfer and Underlying Charge Transfer in Europium-Doped CsPbCl₃ Nanocrystals



Author: Ayushi Shukla, Gurpreet Kaur, Kaliyamoorthy Justice Babu, et al

Publication: Journal of Physical Chemistry Letters

Publisher: American Chemical Society

Date: Jan 1, 2022

Copyright © 2022, American Chemical Society

PERMISSION/LICENSE IS GRANTED FOR YOUR ORDER AT NO CHARGE

This type of permission/license, instead of the standard Terms and Conditions, is sent to you because no fee is being charged for your order. Please note the following:

- Permission is granted for your request in both print and electronic formats, and translations.
- If figures and/or tables were requested, they may be adapted or used in part.
- Please print this page for your records and send a copy of it to your publisher/graduate school.
- Appropriate credit for the requested material should be given as follows: "Reprinted (adapted) with permission from {COMPLETE REFERENCE CITATION}. Copyright {YEAR} American Chemical Society." Insert appropriate information in place of the capitalized words.
- One-time permission is granted only for the use specified in your RightsLink request. No additional uses are granted (such as derivative works or other editions). For any uses, please submit a new request.

If credit is given to another source for the material you requested from RightsLink, permission must be obtained from that source.

[BACK](#)

[CLOSE WINDOW](#)

Spectroscopic Investigation of Structural Perturbations in CsPbCl₃ Perovskite Nanocrystals: Temperature- and Excitation-Energy-Dependent Study



Author: Ayushi Shukla, Gurpreet Kaur, Kaliyamoorthy Justice Babu, et al

Publication: ACS Photonics

Publisher: American Chemical Society

Date: Jun 1, 2023

Copyright © 2023, American Chemical Society

PERMISSION/LICENSE IS GRANTED FOR YOUR ORDER AT NO CHARGE

This type of permission/license, instead of the standard Terms and Conditions, is sent to you because no fee is being charged for your order. Please note the following:

- Permission is granted for your request in both print and electronic formats, and translations.
- If figures and/or tables were requested, they may be adapted or used in part.
- Please print this page for your records and send a copy of it to your publisher/graduate school.
- Appropriate credit for the requested material should be given as follows: "Reprinted (adapted) with permission from {COMPLETE REFERENCE CITATION}. Copyright {YEAR} American Chemical Society." Insert appropriate information in place of the capitalized words.
- One-time permission is granted only for the use specified in your RightsLink request. No additional uses are granted (such as derivative works or other editions). For any uses, please submit a new request.

If credit is given to another source for the material you requested from RightsLink, permission must be obtained from that source.

[BACK](#)

[CLOSE WINDOW](#)